Millimeter-wave Impedance Spectroscopy for High Sensitivity and Selectivity Biomolecular Detection

Luya Zhang
Ali Niknejad

Millimeter-wave Impedance Spectroscopy for
High Sensitivity and Selectivity Biomolecular Detection

by

Luya Zhang

A dissertation submitted in partial satisfaction of the

requirements for the degree of

Doctor of Philosophy

in

Engineering - Electrical Engineering and Computer Sciences

in the

Graduate Division

of the

University of California, Berkeley

Committee in charge:

Professor Ali M. Niknejad, Chair
Professor Vladimir Stojanović
Professor Costas P. Grigoropoulos

Summer 2021

Millimeter-wave Impedance Spectroscopy for
High Sensitivity and Selectivity Biomolecular Detection

Abstract

Millimeter-wave Impedance Spectroscopy for
High Sensitivity and Selectivity Biomolecular Detection

by

Luya Zhang

Doctor of Philosophy in Engineering - Electrical Engineering and Computer Sciences

University of California, Berkeley

Professor Ali M. Niknejad, Chair

An integrated biosensor is a miniaturized device which performs biochemical analysis normally handled by a laboratory equipment. By incorporating signal processing electronics, it automates the massive processing of biological samples, avoids noise and interferences from wiring and interfacing with other systems and enables real-time detection of biochemical reactions. With these numerous benefits, integrated biosensors are poised to change the face of chemical and biological analysis and eventually revolutionize the pharmaceutical industry.

Among different types of biosensing techniques, impedance spectroscopy is peculiarly attractive for the purpose of integration. It is fully electronic in nature, since the sensing frontend can be simply an electrode pair or an inductor coil, which are native to the standard CMOS processes and can be readily adapted into various IC building blocks. Recent years have seen a tremendous advancement in integrated impedance biosensing, a handful of which have already pervaded people's daily lives. Nevertheless, the majority of the impedance biosensors focus on dc-MHz frequency range even though the transistor cut off frequency is approaching half terahertz.

To fulfill the frequency gap, this thesis aims to develop mmWave integrated impedance spectrometers for biomolecular sensing. Operating at mmWave frequencies offers additional advantages. For example, biomolecules interact with EM fields very differently at mmWave frequencies, which allows the discovery of new biochemical fingerprints. In the first part of the thesis, an oscillator-based dielectric sensor is developed which allows the characterization of biomolecules around 40 GHz with sub-ppm sensitivity. It is integrated with single-photon-avalanche-diode based optical sensors to allow highly selective sensing by creating a high-dimensional sample dataset. The second part of the thesis presents an integrated electron paramagnetic resonance spectrometer for *in vivo* applications. Several design challenges related to *in vivo* mmWave frequency sensing and detection are discussed and addressed.

To my parents

Contents

List of Figures

List of Tables

Acknowledgments

First and foremost, I would like to express my deepest appreciation to my research advisor, Professor Ali M. Niknejad, for his excellent technical guidance and project support. I feel very fortunate to work with Ali as he gives me the freedom to decide the research directions that I want to explore. During my entire PhD, Ali always encourages me to think creatively and helps solidify my ideas based on his vast knowledge and expertise in engineering, physics and mathematics. His virtuosity on circuit design, enthusiasm about daily life and altruism for other people have constantly motivated me to become a better person, a big fortune from which I will continue to benefit in the future.

During my six years at Berkeley, I have also had the opportunity to interact with many great faculty members. I want to thank Professor Bernhard Boser for his technical and personal advice which helped me through my first year as a graduate student in a foreign country. I would also like to acknowledge Professor Vladimir Stojanović and Professor Mekhail Anwar for their insightful feedbacks in numerous design reviews and project discussions. Special thanks go to Professor Costas Grigoropoulos for his interest in my research and unreserved support for my laser experiments. I am also grateful to Professor Chunlei Liu for his constructive input when he was on my master thesis and PhD qualifying exam committee. I have enjoyed a couple of wonderful courses taught at Berkeley and thank Ali, Bernhard, Vladimir, Professor Clark Nguyen, Professor Ming Wu, Professor Jonathan Shewchuk and Professor Osama Shanaa for their efforts.

My time at Berkeley has been enriched by my friends and colleagues from BWRC and Swarm Lab. I want to thank all members in our group for their valuable comments during the group meetings. I am especially thankful to Lorenzo Iotti, Bo Zhao, Andrew Townley, Greg Lacaille, Nai-Chung Kuo, Yi-An Li, Nima Baniasadi, Ali Ameri and Benyuanyi Liu in our group for countless discussions that help advance my projects. Thanks to Jun-Chao Chien, Siva Thyagarajan and Sriramkumar Venugopalan, although we don't overlap at Berkeley, for all the helpful conversations. I want to extend my special thanks to people from Boser's group, Hao-yen Tang, Efthymios Papageorgiou, Burak Eminoglu, Behnam Behroozpour and Pramod Murali, who always treat me as part of the group and offer me lots of support. In addition, stimulating technical discussions with Zhongkai Wang, Sidney Buchbinder, Christos Adamopoulos, Panagiotis Zarkos, Letian Wang, Joy Jiang, and Sashank Krishnamurthy have always been helpful. Aside from hardwork, I am also grateful to Angie Wang, Pengpeng Lu, Yongjun Li, Emily Naviasky, Joshua Kay, Meng Wei, Yikuan Chen, Rohit Braganza, Hossein Najafi, Sijun Du, Zhaokai Liu, Ruocheng Wang, Sean Huang, Yue Dai, Zhenghan Lin, Rebecca Zhao, and Yi-Hsuan Shih, for their friendship.

I must also greatly acknowledge all the staff members, Brian Richards, Fred Burghardt, Greg Pearson, James Dunn, Anita Flynn, Candy Corpus, Mikaela Cavizo-Briggs, Melissa Trevizo and Yessica Bravo from BWRC, Paul Lum for QB3 facility and Bill William King from Cory machine shop. Thank you for the incredible amount of work behind the scenes.

Of course, I want to reserve my utmost gratitude to my parents. It is their love, support and trust that gives me the strength to flourish and makes me what I am today.

Chapter 1

Introduction

1.1 Impedance Spectroscopy in the New Era

Impedance spectroscopy, conventionally known as electrochemical impedance spectroscopy (EIS), measures the impedance of an electrolytic solution by applying a small sinusoidal perturbation, usually voltage, to the system. Solid-state EIS sensors, ever since its earliest development in 1970s [1], have gained significant popularity due to the benefits of cost reduction, sensitivity enhancement and quality control improvement in a batch production. Among the most successful commercialized solid-state EIS biosensors are the blood glucose meters for diabetes, which accounts for more than $12.64 billion market size in 2020, and is expected to reach $19.6 billion by 2028 [2]. Other applications include the detection of many important biomolecules such as DNA, proteins, and aptamers. [3] provides a good review on this topic.

The fundamental principle of EIS can be illustrated with the equivalent circuit model of the electrode-electrolyte system, as shown in Fig. 1.1. The most efficient way to detect the impedance
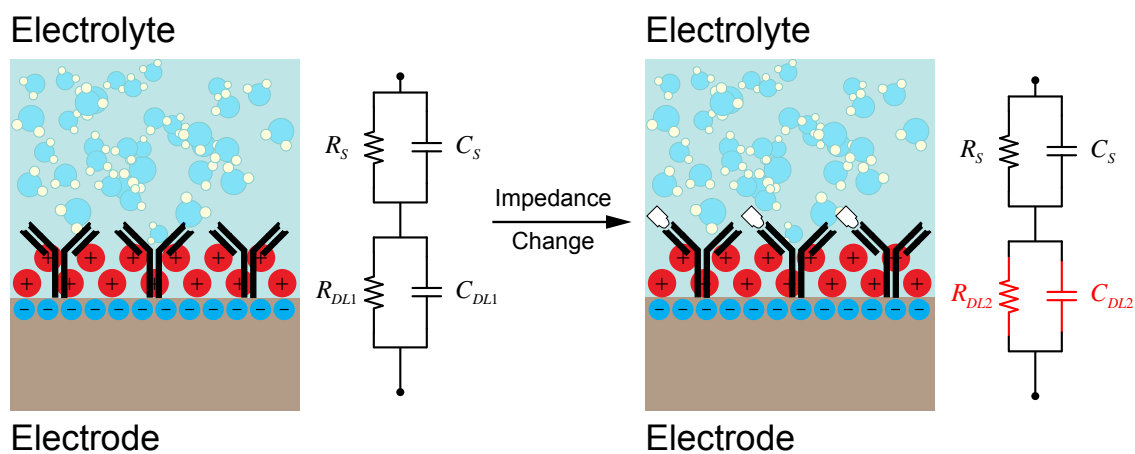
Figure 1.1: A simple equivalent circuit model for the electrode-electrolyte system.
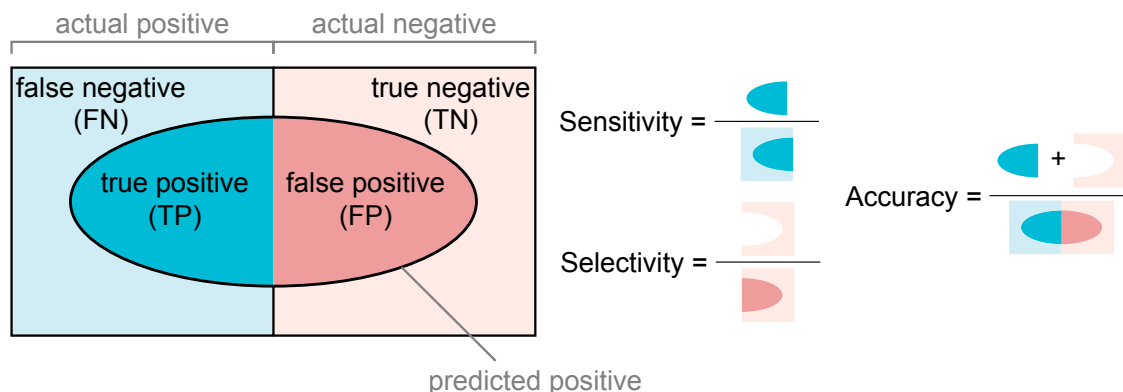
Figure 1.2: Sensitivity and selectivity[11].

change is by embedding this electrode-electrolyte system into a CMOS circuit block. Indeed recent years have seen a tremendous research efforts devoted into CMOS biosensors [4–8], some of which have been transformed into products. The majority of these biosensors operate at dc-MHz frequency range and thereby are only sensitive to the bio-chemical processes which takes place at the electrode/electrolyte interface (modeled as R_{DL} and C_{DL} in Fig. 1.1).

With the aggressive transistor scaling, the cut-off frequency of today's CMOS technologies has reached beyond $250-300$ GHz. Blessed with such high speed devices, it is time to build beyond-10 GHz impedance biosensors to investigate biomolecular interactions in the electrolyte (modeled as R_S and C_S in Fig. 1.1). For example, the biological functions of many macromolecules (proteins, lipids, DNA and etc.) depend on their interaction with water molecules through hydrogen bonds, which are usually observed in the frequency range of $1-100$ GHz [9]. In the cell culture media, going beyond 10 GHz also bypasses the cell membrane so that the biomolecular processes inside cells can be accessed [10]. In addition to characterizing the electrical properties, there also exist some interesting magnetic properties associated with certain biomolecules at this frequency range that can be detected by impedance sensors (e.g. electron paramagnetic resonance). The scope of EIS is thereby expanded to include magnetic sensing, and the term impedance spectroscopy better describes the focus of this thesis.

1.2 It Takes Two to Tango: Sensitivity and Selectivity

Sensitivity and selectivity (or specificity) are both statistical terms which are used to quantify the performance of a binary test. Using Fig. 1.2 for reference, sensitivity, also known as true positive rate, is the proportion of true positives among all the positive predictions. On the other hand, selectivity, known as true negative rate, is the proportion of true negatives among all the negative predictions. If it were a diagnostic test, sensitivity measures the test's capability to determine the patient cases correctly whereas selectivity measures its capability to determine healthy cases correctly.

People have long understood the significance of sensitivity in the sensing applications and

thereby researchers are constantly pushing down the detection limit to new record levels. However, the value of selectivity has not been emphasized enough, at least in the engineering community. To illustrate how important it is, an extreme example could be an all-true test which always predicts positive regardless of the input. By definition its sensitivity is 100% but it is useless. Ultimately it is the accuracy that matters. In other words, what proportion of the positive predictions are truly positive *and* what proportion of the negative predictions are truly negative? In the case of the diagnostic test, a clinically useful sensor needs to be sensitive enough to identify all the patients and selective enough not to misclassify any healthy people. It takes two to tango.

1.3 Thesis Organization

The goal of this thesis is to develop mmWave frequency impedance biosensors, with the focus on various circuit and system techniques that simultaneously achieve high sensitivity and high selectivity. Chapter 2 introduces a quadrature oscillator based dielectric biosensor with very high sensitivity. The selectivity issue associated with the dielectric sensor is subsequently addressed by the integration of multiple sensing modalities, which is discussed in Chapter 3. Chapter 4 explores electron paramagnetic resonance (EPR) as a new sensing modality that by itself achieves superior selectivity. The EPR signal is detected with a low-power highly-sensitive impedance sensor. A further development is made in Chapter 5 by converting the EPR spectrometer into an implant. Several design challenges are discussed and resolved. Chapter 6 concludes this thesis and suggests directions for future research.

Chapter 2

Quadrature Oscillator based Dielectric Relaxation Spectroscopy

Dielectric relaxation spectroscopy (DRS) studies the interaction between the electric field and matter in the frequency range of 10^{-6} Hz to 10^{12} Hz. The types of matter-field interaction characterized by DRS include [12]: (a) microscopic fluctuations of molecular dipoles, i.e, dipole polarization, (b) translational diffusion of mobile charges, i.e, ionic polarization, and (c) the separation of charges at interfaces between dielectric layers (Maxwell-Wagner polarization) or conductor layers (electrode polarization).

The polarization of molecules is reflected at the macroscopic scale as the material's complex permittivity. On the other hand, at the microscopic scale, take the dipole polarization as an example. In the presence of an alternating field, the molecular dipoles tend to orient along with the field to reduce the electric energy potential of the material. At low frequencies, the dipoles are able to follow exactly the change of the field polarity. However, at sufficiently high frequencies, the dipoles can no longer keep track with the field alternation and eventually relax to random orientations. The relaxation process is characterized as a peak-shape function of the imaginary permittivity ϵ'' versus frequency, and a step-like decrease in the real part ϵ'. The turning frequency point where the molecules relax not only depends on the molecular structure of the dipole, but also its interactions with other neighboring molecules or functional groups within the same molecule. The dielectric relaxation spectroscopy is thereby a very important tool in determining molecular dynamics and interactions.

Starting from the pioneering works of Debye [13], Onsager [14] and Oncley [15], DRS has been used extensively to characterize the dielectric properties of different biological solutions, cell suspensions, polymers and solutions of polyelectrolytes. Covering such an extraordinarily wide frequency range, DRS is sensitive to a diverse range of biological processes, from slow macromolecular movements, to relatively fast reorientations of small molecules and side chain groups [16], as shown in Fig. 2.1. Therefore, it plays an important role in biological and pharmaceutical sciences, such as studying protein dynamical structures (e.g., intramolecular motions, conformational transitions and hydration), monitoring membrane properties of normal and pathological cells, investigating the states of water in the pharmaceutical materials, and so on.
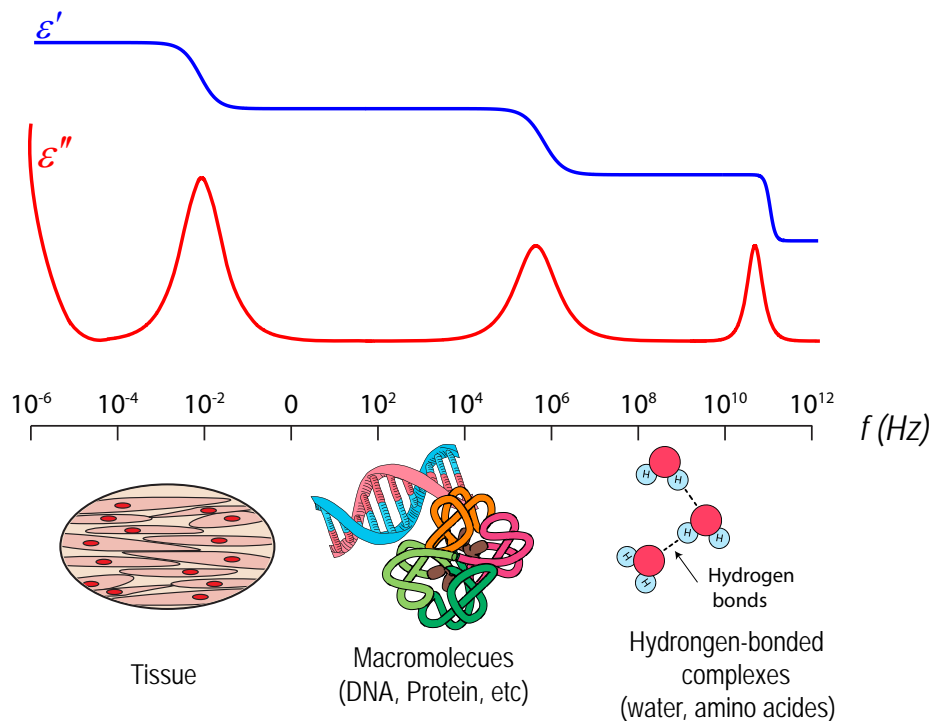
Figure 2.1: Dielectric relaxation spectroscopy of biomolecules.

Measurements of material dielectric properties can be performed either in the time domain (time-domain spectroscopy, TDS) or in the frequency domain (frequency-domain spectroscopy, FDS). TDS is based on the transmission line theory, where the sample under characterization is used to terminate a predefined transmission line. A voltage step is applied to the line and the reflected wave is recorded. By comparing the reflection with the incident wave, the complex permittivity of the sample can be extracted. TDS is extremely rapid for broadband measurements in that no frequency sweep is required. The main challenge is the need of a ultra-fast and low-noise sampler, which limits its miniaturization at high frequencies.

On the other hand, FDS measures the dielectric properties at discrete frequency points with a sinusoidal excitation. Conventionally, FDS is performed using a vector network analyzer (VNA). However, the sensitivity is considerably limited by the VNA noise, as well as the residual artifacts due to imperfect de-embedding. This motivates the development of integrated impedance analyzers [4, 17–20]. As shown in Fig. 2.2(a), the impedance analyzer consists of a voltage source, a pair of sensing electrodes, a transimpedance amplifier (TIA), an I/Q demodulator and ADCs. With the driven voltage source known as V_{drive} and the sensing current measured as I_{sense}, the absolute value of the sensor impedance can be derived as $Z_{\mathrm{sense}} = V_{\mathrm{drive}}/I_{\mathrm{sense}}$. Moving above 10-GHz frequencies, oscillators provide a much simpler scheme for capacitance measurements by translating the change of the capacitance into the change of the oscillation frequency [21–25], as shown in Fig. 2.2(b). Usually only the real part of the permittivity is obtained directly, whereas the imaginary part needs

(a)

(b)
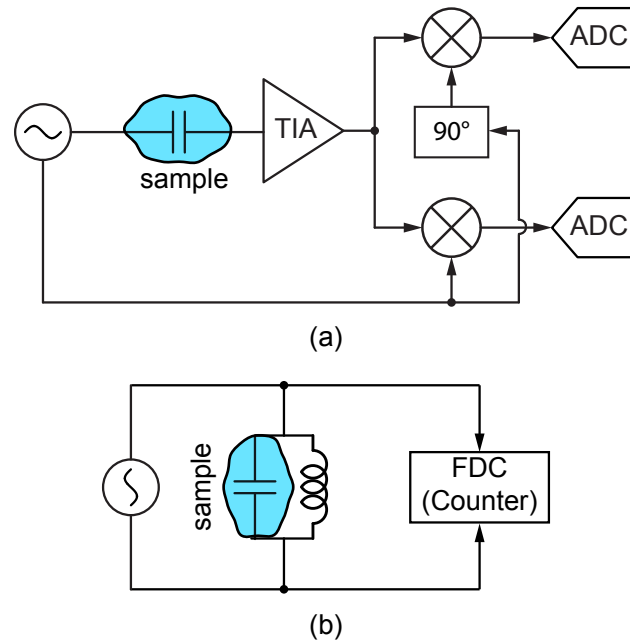
Figure 2.2: Integrated impedance analyzers for dielectric spectroscopy.

to be computed via the Kramers-Kronig relations.

In this chapter, a quadrature oscillator based dielectric spectrometer is presented [26]. Instead of using a counter to measure the oscillation frequency [22–25], two mutually coupled oscillators are utilized as the sensing frontend, which converts the frequency change to a phase signal. This introduces a 'free' signal boost equal to the tank quality factor Q. Additionally, the flicker noise contributed by the cross-coupled pair is also attenuated to further enhance the sensitivity.

This chapter is organized as follows. Section 2.1 provides a theoretical analysis on the proposed quadrature oscillator used for this dielectric spectrometer. Section 2.2 explains the operation mechanism of the sensor and its noise performance. Section 2.3 describes the circuit building blocks. Section 2.4 and Section 2.5 cover the electrical and biological measurements, respectively. Section 2.6 concludes this chapter.

2.1   Quadrature Oscillator Design

Generally speaking, obtaining accurate quadrature signals at millimeter-wave frequencies is critical for both wireless and wired communication systems, as it enables direct conversion architectures [27], provides phase interpolation for phased-array transceivers [28], and generates clock phases for half-rate clock and data recovery (CDR) circuits [29]. Compared with quadrature generation using poly-phase filters, quadrature hybrids, and divide-by-2 frequency dividers, quadrature coupled oscillators (QVCOs) offer superior power and area efficiency at mmW frequencies [30–33].
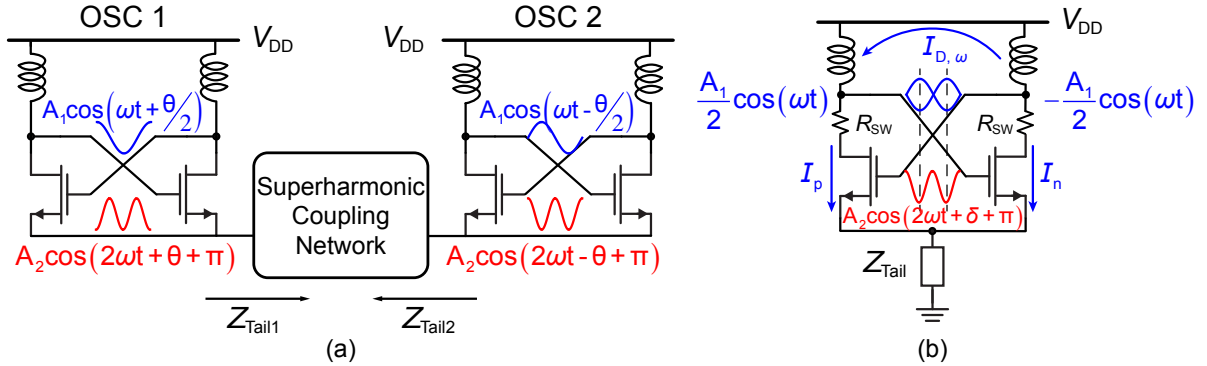
Figure 2.3: (a) Conceptual model of superharmonic coupled oscillators and (b) the corresponding half circuit.

Key performance specifications for a QVCO include phase accuracy, phase noise and frequency tuning range. It has been recognized that off-resonance locking degrades the phase noise and tuning range performance [34], which is an issue with the parallel (P-QVCO [35–38]) and series (TS-QVCO and BS-QVCO [39, 40]) coupling schemes. Alternatively, an explicit 90° phase shift can be introduced when coupling the quadrature nodes to achieve in-phase injection locking [41–46] for a better noise performance. Yet phase-shifting couplers add direct loading to the LC tank and impair the tuning range. Moreover, these circuits either contribute extra noise (active-device-based [41, 42]) or suffer from a limited coupling strength (passive-device-based [43–46]), which poses a direct trade-off between phase noise and phase accuracy.

Instead of coupling through fundamental nodes, quadrature locking can be realized by enforcing a 180° phase difference between the second harmonics extracted from the IQ oscillator common-mode nodes, i.e., superharmonic coupling [47–50]. Theoretically speaking, a superharmonic QVCO can achieve even more than 3 dB lower phase noise than a single VCO thanks to the tail filtering effect [51] without impacting the tuning range. Despite these benefits, superharmonic coupling is predominantly used in sub-10GHz QVCOs with only moderate phase accuracy, and a complete analysis on its locking mechanism is still missing.

In this section, the performance limiting factors of existing superharmonic architectures are revealed with a proposed tail impedance theory, based on which a new superharmonic network optimized for mmW QVCOs is proposed. Moreover, the phase noise and quadrature error performance of the proposed QVCO is also analyzed.

2.1.1 Superharmonic Network Impedance Theory

2.1.1.1 Effective Negative-G_m due to the Second Harmonic

Superharmonic injection locking relies on the boosted second harmonics at the coupling nodes to ensure phase lock. Consider the conceptual model of two identical oscillators superharmonically coupled together through the common-source tail nodes, as shown in Fig. 2.3(a), where the oscillation

frequency is ω and the relative phase difference equals θ. The second harmonic oscillation at the source of the cross-coupled pair is boosted by the coupling network, which strongly modulates transistor g_m value through device nonlinearities. The influence of g_m-modulation is profound since it directly affects the oscillator loop-gain, start-up condition and phase noise performance. More importantly, as shall be proven later, the superharmonic coupling network stimulates a variable tail impedance to each oscillator based upon their relative phase difference θ, which will vary the second harmonic magnitude A_2 (and thereby g_m). Since the steady-state phase relation θ_{ss} is the one with the highest g_m, arbitrary phase relation can be realized with a proper superharmonic network design. Quadrature phase relation ($\theta_{ss} = 90°$) is one such special case.

To calculate the effective negative transconductance of the cross-coupled pair (denoted as $G_m = -g_m/2$) due to the second harmonic modulation, consider the half circuit model of the tail-coupled superharmonic oscillators in Fig. 2.3(b), where Z_{Tail} represents the total tail impedance associated with the coupling node, including both the parasitic capacitance from the oscillator itself and the impedance stimulated by the coupling network. The oscillator operates in the voltage-limited regime for optimal phase noise performance. Therefore the second harmonic voltage minima at the tail node aligns with the fundamental output extrema (maxima and minima) with a small phase offset δ[52]. This phase offset δ originates from the tail reactance, $j\mathrm{Im}(Z_{Tail})$, and equals zero at the steady state with an optimal superharmonic network design.

Referring to Fig. 2.3(b), denote the differential output of a VCO as $A_1\cos(\omega t)$ and the voltage at the coupling tail node can be approximated as a sinusoid at the frequency of 2ω: $A_2\cos(2\omega t + \delta + \pi)$ where $\delta \simeq 0$. Assuming a square-law I-V characteristic for now, and taking into account of the second harmonic oscillation at the common source node, the transistor current of each branch can be modeled as

$$I_{\mathrm{p,n}} = \frac{1}{2}K_n\left(V_{OV0} \mp \frac{A_1}{2}\cos(\omega t) - A_2\cos(2\omega t + \delta + \pi)\right)^2 \tag{2.1}$$

where $K_n = \mu_n C_{ox}\frac{W}{L}$ and V_{OV0} is the DC overdrive voltage. From (2.1), the differential current flowing into the oscillator tank at ω is calculated by

$$\begin{aligned} I_{D,\omega} &= \left.\frac{I_{\mathrm{p}} - I_{\mathrm{n}}}{2}\right|_\omega \\ &\simeq -\frac{1}{2}K_n\left(V_{OV0} + \frac{A_2}{2}\cos(\delta)\right)A_1\cos(\omega t). \end{aligned} \tag{2.2}$$

The effective negative-G_m of the cross-coupled pair is therefore derived as

$$G_m = -\frac{1}{2}K_n\left(V_{OV0} + \frac{A_2}{2}\cos(\delta)\right). \tag{2.3}$$

For completeness, consider a more generic I-V characteristic of a transistor under large signal excitation (e.g. LC oscillators):

$$I_{\mathrm{p,n}} = \alpha_0 + \alpha_1 V_{OVp,n} + \alpha_2 V_{OVp,n}^2 + \alpha_3 V_{OVp,n}^3 + \ldots, \tag{2.4}$$

where

$$V_{\text{OVp,n}} = V_{\text{OV0}} \mp \frac{A_1}{2}\cos(\omega t) - A_2\cos(2\omega t + \delta + \pi). \tag{2.5}$$

In the square-law special case, $\alpha_2 = \frac{1}{2}K_n$ and $\alpha_{n\neq 2} = 0$. With the same derivation yields a more generic negative-G_m expression:

$$
\begin{aligned}
G_m \simeq & -\frac{\alpha_1}{2} - \alpha_2\left(V_{\text{OV0}} + \frac{A_2}{2}\cos(\delta)\right) \\
& - \frac{\alpha_3}{2}\left(\frac{3}{16}A_1^2 + 3V_{\text{OV0}}^2 + \frac{3}{2}A_2^2 + 3V_{\text{OV0}}A_2\cos(\delta)\right)
\end{aligned}
\tag{2.6}
$$

It is clear from (2.3) and (2.6) that the second harmonic A_2 plays an important role in setting the oscillator effective negative-G_m, the start-up condition and most importantly, the steady-state oscillation mode in the case of coupled oscillators.

2.1.1.2 Arbitrary Phase Relationship Realization

Back to the original model in Fig. 2.3(a), suppose the second harmonic magnitude A_2 is a function of the relative phase difference θ between the coupled oscillators, i.e. $A_2=A_2(\theta)$. If $A_2(\theta)$ has a single maximum value at $\theta = \theta_{ss}$ for both oscillators, there will only exist one stable oscillation mode which is θ_{ss}, as it produces the largest loop gain and predominates over all the other modes during the initial startup.

From the circuit implementation perspective, $A_2(\theta)$ can be realized by engineering the tail impedance, i.e. $Z_{\text{Tail}}(\theta)$. To quantify the relationship between A_2 and Z_{Tail}, treat the half-circuit model in Fig. 2.3(b) as a voltage-commutative mixer up-converting from the drain to the source, where R_{SW} is the average on-resistance of the switches.

With a voltage division, the mixer output at the upper sideband, i.e. A_2, is

$$A_2 = \frac{1}{2}\frac{Z_{\text{Tail}}}{Z_{\text{Tail}} + R_{\text{SW}}}\frac{A_1}{2} = \frac{A_1}{4}\frac{Z_{\text{Tail}}}{Z_{\text{Tail}} + R_{\text{SW}}} \tag{2.7}$$

From (2.3) and (2.7), two conclusions can be drawn regarding Z_{Tail}. First, increasing $\|Z_{\text{Tail}}\|$ increases the second harmonic A_2 and thereby the effective negative-G_m. Second, since phase offset δ in (2.3) arises from $\angle Z_{\text{Tail}}$, reducing the tail reactance improves the effective negative-G_m and loop gain as well. Moreover, in-phase injection lock happens when Z_{Tail} is real.

Therefore, in order to achieve an arbitrary locking phase at $\theta = \theta_{ss}$, one can engineer $Z_{\text{Tail}}(\theta)$ so that it has *exactly one strict maxima* at θ_{ss} for *both* oscillators over all possible θ values. As a validation, transient simulations were performed on the circuit model in Fig. 2.3(a) with different tail impedance characteristics (peaking at $\theta = 30°$, $60°$ and $90°$). Fig. 2.4 plots the simulated initial transient for three different cases in which the oscillators are forced to start in phase. From left to right in each subfigure plots $Z_{\text{Tail}}(\theta)$ characteristics, simulated relative phase difference between the two coupled VCOs and the oscillation frequency, respectively. The value of $Z_{\text{Tail}}(\theta)$ over the interval $\theta \in [-\pi, 0]$ is zero-padded and not shown.
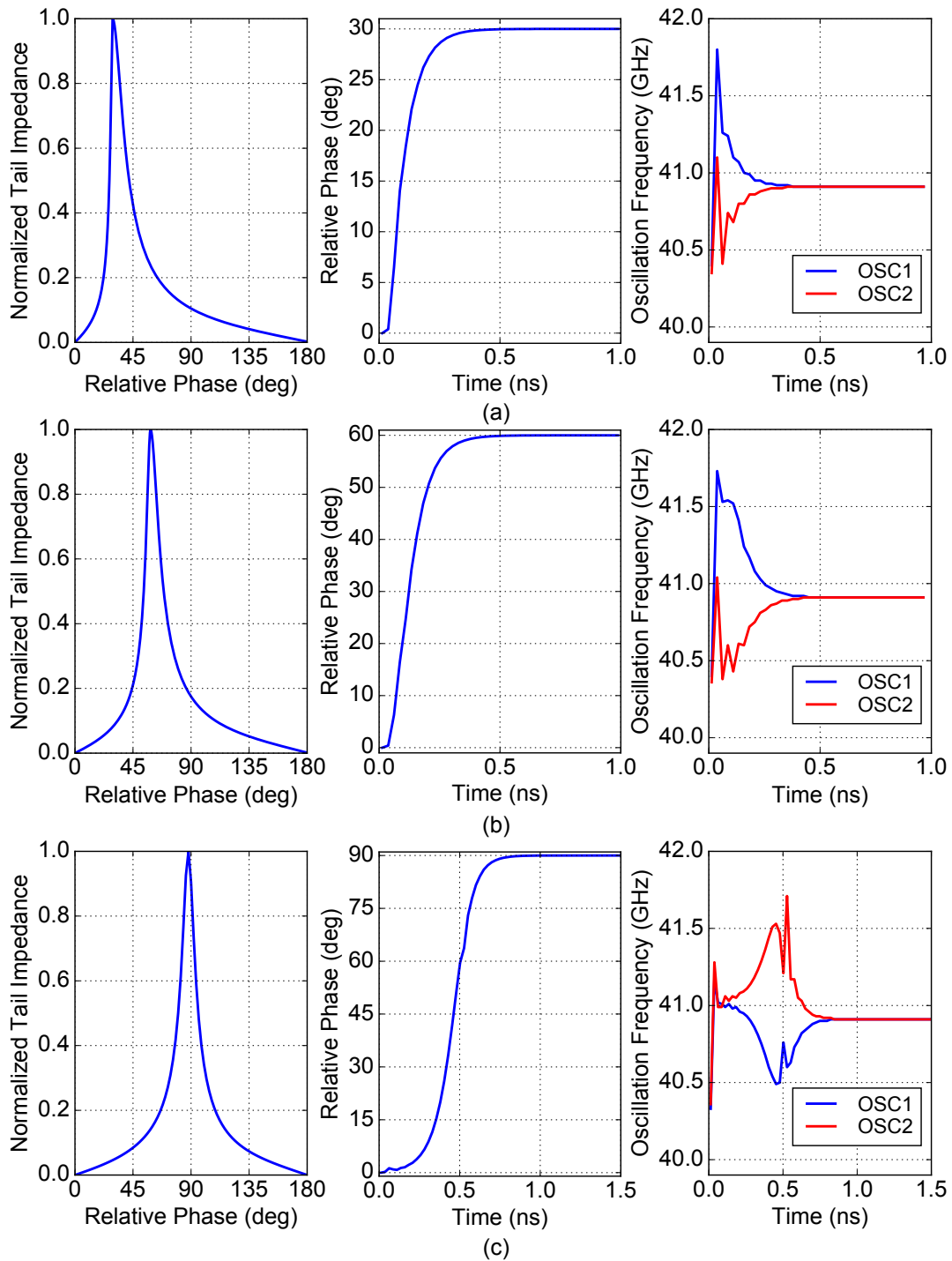
Figure 2.4: Simulated start-up transients of 40GHz superharmonically coupled oscillators achieving a predefined phase relationship of (a) $\theta_{ss} = 30°$, (b) $\theta_{ss} = 60°$ and (c) $\theta_{ss} = 90°$ through Z_{Tail} engineering.
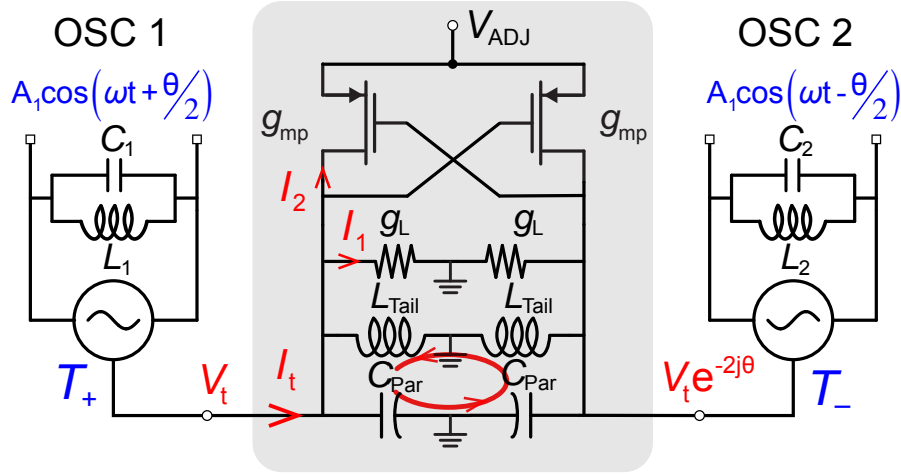
Figure 2.5: Proposed superharmonic coupling network optimized for mm-Wave QVCOs.

As expected, they all converge to the phase where $Z_{\text{Tail}}(\theta)$ is maximized. The oscillation frequency is set by the LC tank and not affected by the coupling network. An example circuit that can achieve arbitrary tail impedance peaking characteristics is provided and discussed 2.1.1.3.

2.1.1.3 Proposed mmW Quadrature Coupling Network

As the primary focus of this work, using superharmonic coupling network to create a quadrature phase relation via tail impedance engineering is exploited here. As discussed in [53], although a transformer [47] or a capacitively-cross-coupled pair [49] can be used to stimulate a variable tail impedance which peaks at the quadrature phase relation, they suffer from degraded quadrature accuracy when scaling to mmW frequencies. Hence a new superharmonic coupling structure optimized for mmW QVCOs is proposed here (Fig. 2.5).

The proposed coupling network is composed of a PMOS cross-coupled pair and an inductor L_{Tail}, whereas g_L and C_{Par} represent the total resistive loss and capacitive parasitics associated with the coupling nodes $T_{+,-}$. Unlike [49], no dedicated bias network is needed. The inductor L_{Tail} is used to resonate out C_{Par} at 2ω. For mm-Wave QVCOs, L_{Tail} is small thanks to the doubled operation frequency and relatively large source capacitance in the practical layout. With reactance cancellation, the negative-g_{mp} cell can maximize Z_{Tail} at $\theta = 90°$.

To gain some intuition, two extreme cases where $\theta = 0°$ (in-phase lock) and $\theta = 90°$ (quadrature lock) are considered first. At $\theta = 0°$, the second harmonics of the coupled oscillators are common-mode signals, which converts the cross-coupled PMOS to the diode-connected fashion and yields

$$Y_{\text{Tail}_{+/-}} = g_L + g_{\text{mp}} \tag{2.8}$$

where $Z_{\text{Tail}_{+/-}} = 1/Y_{\text{Tail}_{+/-}}$. On the contrary, at $\theta = 90°$, the second harmonics are purely differential,

which generates a much larger $Z_{\text{Tail}_{+/-}}$:

$$Y_{\text{Tail}_{+/-}} = g_{\text{L}} - g_{\text{mp}} \tag{2.9}$$

Note that the proposed superharmonic QVCO is completely different from the divide-by-2 quadrature generation. Although the superharmonic coupling network may seem to be an oscillator at first sight, it does not need to oscillate by itself at all. In fact, the nominal control voltage V_{ADJ} (Fig. 2.5) is around 400mV–450mV, only slightly higher than the PMOS threshold. Therefore the proposed coupling network is also very power-efficient and can be scaled to even higher frequencies.

A complete $Z_{\text{Tail}}(\theta)$ over the entire range of $\theta \in (-\pi, \pi]$ at 2ω can be derived by solving KCL (see Fig. 2.5). Assuming the node voltages at $T_{+,-}$ are V_t and $V_t e^{-2j\theta}$ respectively,

$$Y_{\text{Tail}_{+/-}}(\theta) = -g_{\text{mp}} \cdot e^{\mp 2j(\theta - \pi/2)} + g_{\text{L}} \tag{2.10}$$

Fig. 2.6 plots the calculated and simulated tail impedance values at nodes T_+ and T_-. Like other superharmonic QVCOs [47–50], the proposed coupling network doesn't select $\theta = +90°$ or $-90°$ as Z_{Tail} is maximized in both cases. An auxiliary coupling network [54] with minimally sized transistors can be added to direct the oscillation phase without any appreciable loading effects. In addition, as θ moves away from $\pm 90°$, not only does $\|Z_{\text{Tail}}\|$ drop, but the phase $\angle Z_{\text{Tail}}$ also quickly deviates from $0°$. According to (2.3), the effective negative-G_m reduces even faster, which promotes the quadrature mode.

To lock the two oscillators with an arbitrary phase relationship, Fig. 2.7(a) provides an example circuit that achieves arbitrary tail impedance peaking characteristics. It utilizes two delay blocks inserted at the gate of the cross-couple PMOS pairs which offset the second harmonic input by $\pm\phi$. The tail impedance of OSC1 is given by

$$Y_{\text{tail}} = \frac{g_{\text{L}}}{2} \cdot \left(1 - e^{-2j\theta}\right) + g_{\text{mp}} \cdot e^{-2j\theta - j\phi} \tag{2.11}$$

Fig. 2.7(b) illustrates the optimal solution for g_{mp} and ϕ that minimizes Y_{tail}, which is

$$\begin{aligned} g_{\text{mp}} &= g_{\text{L}}\sin(\theta) \\ \phi &= \frac{\pi}{2} - \theta \end{aligned} \tag{2.12}$$

2.1.2 QVCO Performance Characteristics

2.1.2.1 Phase Noise

This section focuses on how the superharmonic coupling network influences the QVCO phase noise performance. Major noise contributors of the proposed QVCO include: two cross-coupled NMOS pairs, one PMOS pair, and resistances in the two fundamental tanks and one second-harmonic tank. Due to the circuit symmetry, only one quarter of the above noise sources (i.e. the entire I_+ side
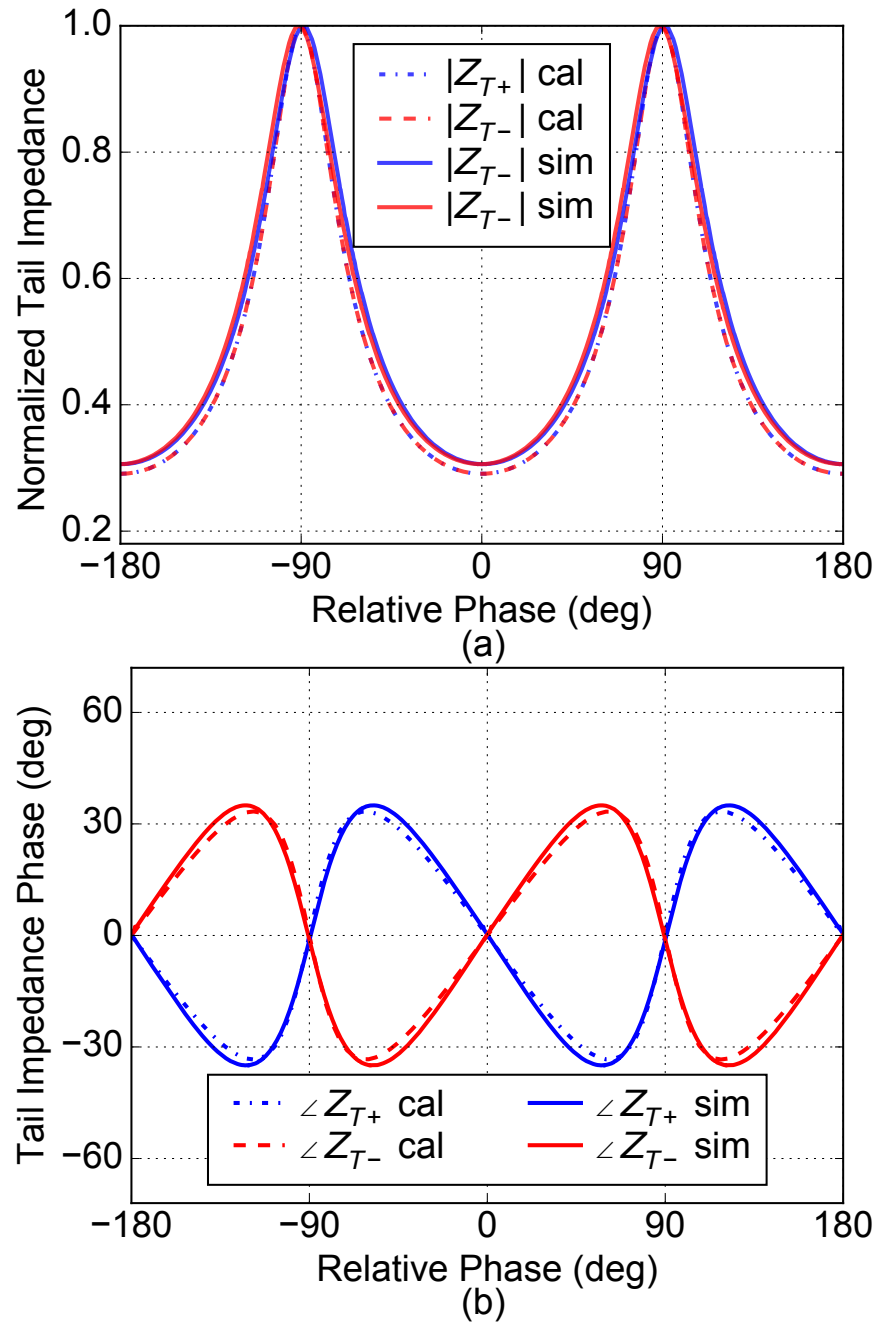
Figure 2.6: Calculated and simulated (a) normalized magnitude and (b) phase of the tail impedance $Z_{\text{Tail}}(\theta)$ at nodes $T_{+/-}$ and frequency 2ω, which is stimulated by the proposed superharmonic network.
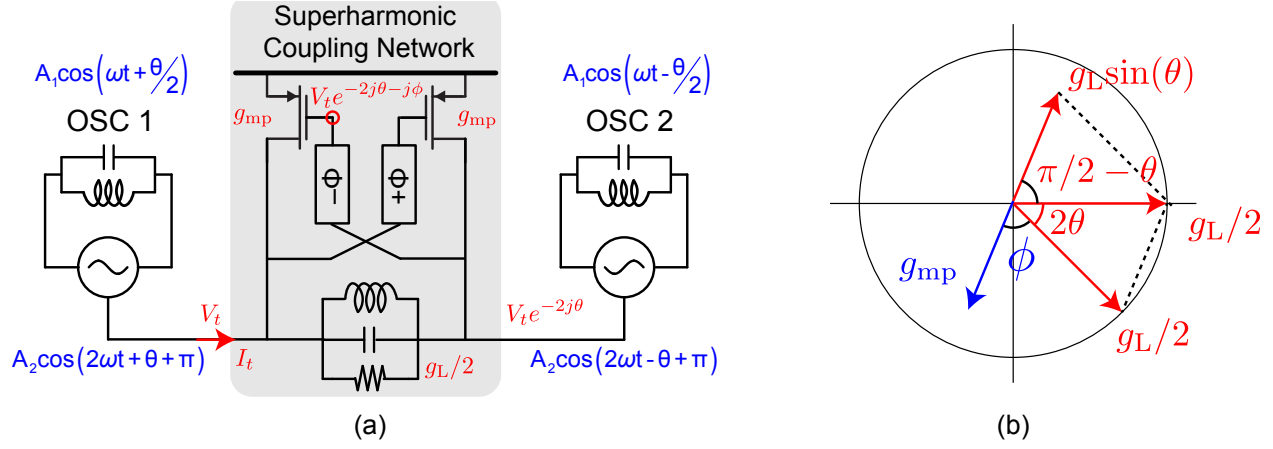
Figure 2.7: Example circuit diagram that achieves arbitrary $Z_{\mathrm{Tail}}(\theta)$ peaking characteristics.

and one half of the T_+ side) are considered, as shown in Fig. 2.8(a). The total noise is 4× as high. Moreover, noise of mutually coupled oscillators is synchronized across all the nodes [34], i.e.

$$\Delta \widetilde{\phi}_{I_{+/-}} = \Delta \widetilde{\phi}_{Q_{+/-}} = \Delta \widetilde{\phi}_{T_{+/-}}/2 \tag{2.13}$$

where $\Delta \widetilde{\phi}_j$ represents the noise induced excess phase at node j. Therefore only the phase noise at the node I_+ is analyzed.

Following the ISF (Impulse Sensitivity Function) theory by [55–57], the phase noise contributed by the noise sources in Fig. 2.8(a) at a given frequency offset $\Delta\omega$ is

$$\mathcal{L}(\Delta\omega) = 10\log\left(\sum_j \frac{\Gamma^2_{j,\mathrm{rms}}}{q^2_{\mathrm{max}}} \cdot \frac{\overline{i^2_j}}{2\Delta\omega^2} \right) \tag{2.14}$$

where $q_{\mathrm{max}} = A_1 C_{\mathrm{T}}/2$ is the maximum dynamic charge at I_+ and $\Gamma^2_{j,\mathrm{rms}}$ is the RMS power of the ISF Γ_j associated with the current noise $\widetilde{i}_j$, which is defined as (let $\phi = \omega t$)

$$\Gamma^2_{j,\mathrm{rms}} = \frac{1}{2\pi} \int_{-\pi}^{\pi} \left| \Gamma_j(\phi) \right|^2 d\phi \tag{2.15}$$

To compute $\Gamma_j(\phi)$, Fig. 2.8(a) is simplified and rearranged into Fig. 2.8(b), and the NMOS drain noise $\overline{i^2_n}$ is modeled as two fully correlated noise sources $\widetilde{i_{n1}} = \widetilde{i_{n2}} = \widetilde{i_n}$. Clearly the ISF of node **1** and **2** ($\Gamma_1(\phi)$, $\Gamma_2(\phi)$) are sufficient to characterize the ISFs for all four noise sources:

$$\Gamma_{p/2}(\phi) = \Gamma_2(\phi),\ \Gamma_n(\phi) = \Gamma_1(\phi) + \Gamma_2(\phi)$$
$$\Gamma_{G_T}(\phi) = \Gamma_1(\phi),\ \Gamma_{g_{L}/2}(\phi) = \Gamma_2(\phi) \tag{2.16}$$

and the following analysis will focus on these two ISFs.
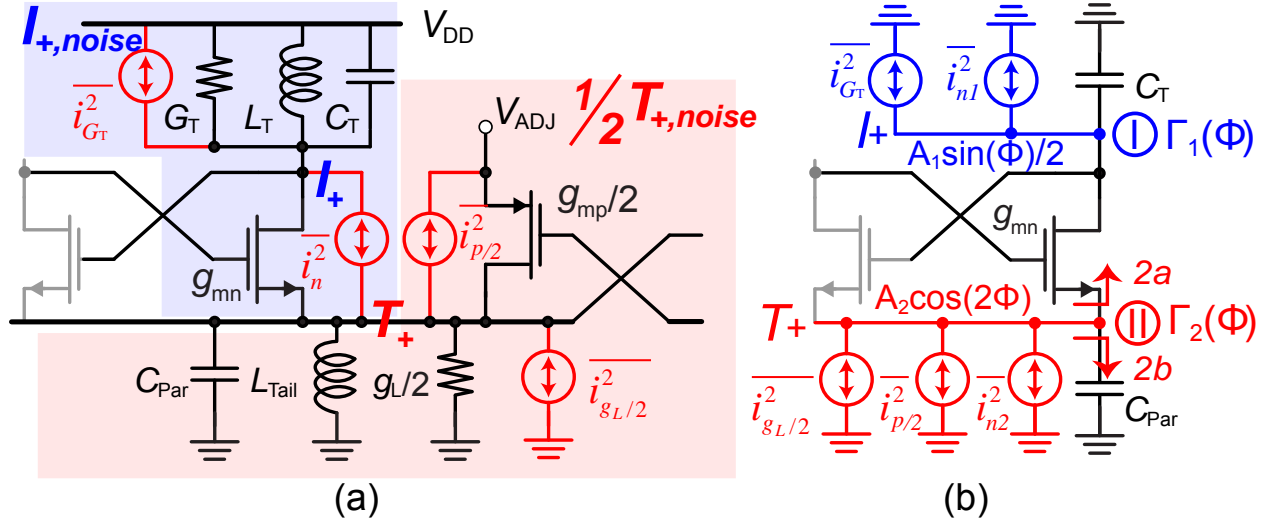
Figure 2.8: Quarter circuit of the proposed QVCO with noise sources annotated, (a) original and (b) rearranged for ISF calculation. All the node capacitors and inductors remain unaltered for proper charge sharing when deriving ISFs.

$\Gamma_1(\phi)$ is well studied as the ISF of the tank resistor noise[55]. As $V_{I_+} = \frac{A_1}{2}\sin(\phi)$,

$$\Gamma_1(\phi) = \frac{1}{N}\sin(\phi + \frac{\pi}{2}) = \frac{1}{N}\cos(\phi) \tag{2.17}$$

where $N = 4\left(1 + \frac{8C_{Par}A_2^2}{C_T A_1^2}\right)$ for a QVCO with a tail tank [34, 58].

As for $\Gamma_2(\phi)$, charges injected at the node **2** are split into $\Gamma_{2a}(\phi)$ and $\Gamma_{2b}(\phi)$ [Fig. 2.8(b)], and

$$\Gamma_2(\phi) = \frac{C_{eff}(\phi)}{C_{eff}(\phi) + C_{Par}}\Gamma_{2a}(\phi) + \frac{C_{Par}}{C_{eff}(\phi) + C_{Par}}\Gamma_{2b}(\phi) \tag{2.18}$$

where $C_{eff}(\phi) = 2C_T$ when both NMOS transistors are on, otherwise $C_{eff}(\phi) = C_T$.

$\Gamma_{2a}(\phi)$ was derived in [56, Eq. (66)], as the ISF of tail current noise of a bare-bones VCO without the tail tank. It doubles the frequency of $\Gamma_1(\phi)$ (as plotted in Fig. 2.9(a)), and can be approximated as

$$\Gamma_{2a}(\phi) = \frac{K_\Phi}{N}\sin(2\phi) \tag{2.19}$$

where $K_\Phi \in (0, 1)$, set by the NMOS bias condition, and $N = 4$.

For $\Gamma_{2b}(\phi)$, a unit charge impulse taking the path 2b disturbs the tail tank first at the node $V_{T_+} = A_2\cos(2\phi)$, and produces an excess phase [55, Eq. (10)]

$$\Delta\widetilde{\phi}_{T_+} = \frac{\cos(2\phi + \frac{\pi}{2})}{N_2 \cdot q_{Tail,max}} \tag{2.20}$$

where $q_{\text{Tail,max}} = A_2 C_{\text{Par}}$ and $N_2 = 2$ since the tail tank is differential. According to (2.13), *IQ* nodes will then be synchronized to the tail nodes:

$$\Delta\widetilde{\phi}_{T_+}/2 = \Delta\widetilde{\phi}_{I_{+/-}} = \frac{\Gamma_{2b}(\phi)}{q_{\max}} \tag{2.21}$$

which yields

$$\Gamma_{2b}(\phi) = -\frac{A_1}{8A_2}\frac{C_{\text{T}}}{C_{\text{Par}}}\sin(2\phi) \tag{2.22}$$

Combining (2.18)–(2.22) yields the rms power of $\Gamma_2(\phi)$ (assume $C_{\text{eff}}(\phi) = C_{\text{T}}$ for simplicity):

$$\Gamma_{2,\text{rms}}^2 = \frac{1}{32}\left(\frac{C_{\text{T}}}{C_{\text{T}} + C_{\text{Par}}}\right)^2\left|\frac{A_1}{2A_2} - K_\Phi\right|^2 \tag{2.23}$$

The calculated and simulated $\Gamma_2(\phi)$ (using the method by [59]) waveforms are shown in Fig. 2.9(a). Note that the sign inversion between $\Gamma_{2a}(\phi)$ and $\Gamma_{2b}(\phi)$ always holds and can be utilized to minimize $\Gamma_2(\phi)$ with proper biasing and tank design. More importantly, based on (2.23), without affecting the main oscillator operation, increasing C_{Par} (and reducing L_{Tail} to maintain a 2ω tail tank) can attenuate $\Gamma_{2,\text{rms}}^2$-related phase noise, which includes $\overline{i_p^2}$ and $\overline{i_{g_L}^2}$ from the coupling network, as well as $\overline{i_n^2}$ from the NMOS pair according to (2.16). As a validation, the QVCO phase noise induced by a constant tail tank loss $\overline{i_{g_L}^2}$ is calculated and simulated (see Fig. 2.9(b)), which decreases when C_{Par} is sized up. In practice, as increasing C_{Par} does not change the main oscillator design, the optimal C_{Par} is mostly determined by the tail inductor fabrication limit and the potentially increased g_L when L_{Tail} shrinks down.

In addition to $\Gamma_2(\phi)$ minimization, the coupling network also reduces the NMOS phase noise contribution by attenuating $\overline{i_n^2}$. Unlike tank resistors, NMOS channel noise is periodically modulated by V_{GS} and is thus cyclostationary, i.e. $\overline{i_n^2} = \overline{i_{n0}^2} \cdot \alpha_n^2(\phi)$, where $\overline{i_{n0}^2} = 4k_B T \gamma g_{\text{ds0}}$ is the peak noise power and $\alpha_n(\phi)$ is the noise modulation function (NMF) [55].

Fig. 2.10 depicts typical node voltages of a cross-coupled NMOS and its NMF $\alpha_n(\phi)$ [60]. $\overline{i_{n0}^2} = 4k_B T \gamma g_{\text{ds0}}$ is defined at $V_{\text{D}} = V_{\text{G}}$ where $\alpha_n(\phi)$ peaks, and g_{ds0} is the peak channel conductance at this V_{GS} point with zero V_{DS} [61], which is

$$g_{\text{ds0}} = K_n(V_{\text{GS}} - V_{\text{th}}) = K_n(V_{\text{OV0}} - A_2) \tag{2.24}$$

In a bare-bones oscillator (Fig. 2.10(b)), $A_2 \simeq 0$ and g_{ds0} takes the familiar term: g_m. On the other hand, A_2 is boosted in a superharmonic QVCO (Fig. 2.10(a)), which reduces g_{ds0} and thereby the NMOS channel noise. Note that g_{ds0} reduction is not contradictory to the increase of negative-G_m as the physical origins of g_m and g_{ds0} are completely different.

Therefore, the proposed superharmonic network not only helps reduce the phase noise contributed by the NMOS-pairs in the main oscillators (via $\Gamma_2(\phi)$ and g_{ds0}), but also minimizes its own noise contribution (via $\Gamma_2(\phi)$), which makes it a good candidate for low-noise QVCOs.
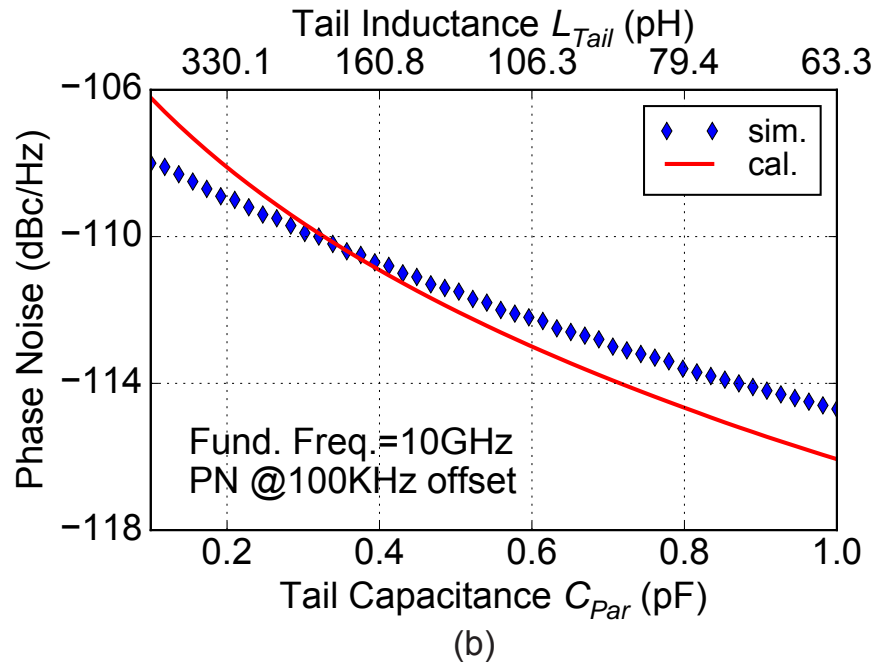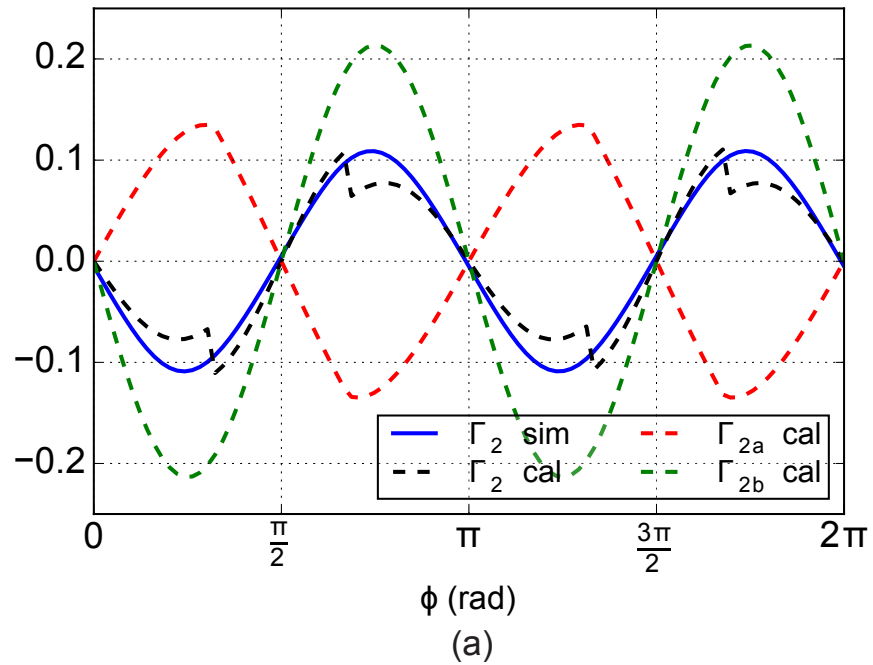
Figure 2.9: Calculated and simulated (a) $\Gamma_2(\phi)$ waveforms at C_{Par} =0.6pF, and (b) phase noise contributed by g_{L} =1kΩ (see Fig. 2.5) at different C_{Par}; f_{osc} =10GHz, C_{T} =0.2pF, V_{DD} =0.75V and the tail tank is tuned to stay at 20GHz. As $\Gamma_2(\phi)$ is frequency-independent, the QVCO is designed at 10GHz not 40GHz for a better illustration of the impact of C_{Par}.
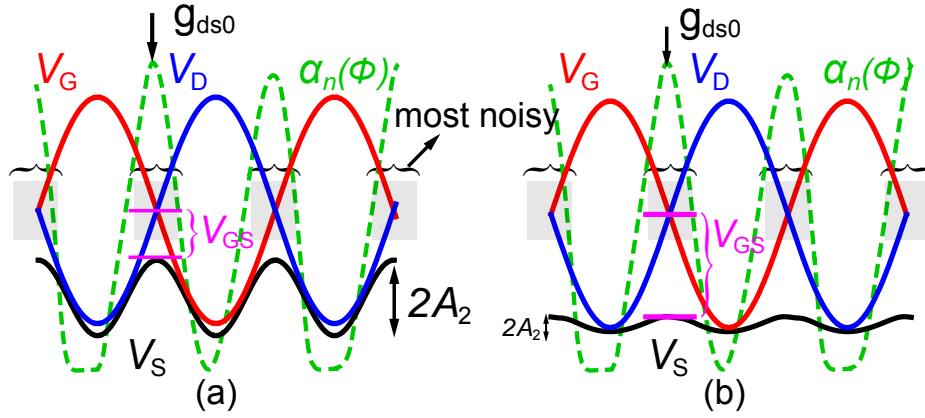
Figure 2.10: Illustration of g_{ds0} reduction with node waveforms (V_G, V_D, V_S) and NMF $\alpha(\phi)$ of a transistor in an oscillator (a) with and (b) without boosted second harmonic at V_S.

2.1.2.2 Quadrature Accuracy

Mismatch between the coupled oscillators produces phase error and amplitude imbalance, which affects the image rejection and should be minimized. The amplitude imbalance is not an issue here since the oscillator operates in the voltage-limited regime. On the other hand, phase error reduction through direct tank tuning requires auxiliary feedback [50], which complicates the system design significantly. An alternative way to reduce the phase error is by increasing the oscillator coupling strength. Nevertheless, most existing QVCO architectures are faced with strict trade-off between phase accuracy and phase noise when changing the coupling strength, which requires the optimization to be performed during the design phase and thereby they do not offer any phase accuracy tunability [40–42].

As an important feature, the proposed coupling network can adjust quadrature accuracy by changing g_{mp} with almost no phase noise penalty. Using the proposed tail impedance theory, a closed-form solution of the phase error θ_e as a function of g_{mp} under a given mismatch is derived.

Assume in Fig. 2.5 ($\theta = 90°$), the natural frequency of OSC1 and OSC2 deviates to $\omega_{OSC1} = \omega + \delta\omega$ and $\omega_{OSC2} = \omega - \delta\omega$ ($\delta\omega > 0$) due to mismatches. Mutual injection forces them to lock back to ω with a new phase difference $\theta' = 90° + \theta_e$ ($\theta_e > 0$). For OSC1, the tank capacitive and inductive energy are given by

$$E_C = \frac{1}{2}C_1 A_1^2$$

$$E_L = \frac{1}{2}L_1\left(\frac{A_1}{\omega L_1}\right)^2 = \frac{1}{2}C_1 A_1^2 \frac{\omega_{OSC1}^2}{\omega^2} = E_C\left(1 + 2\frac{\delta\omega}{\omega}\right)$$

(2.25)

The inductive energy is higher as OSC1 runs below its natural frequency ($\delta\omega > 0$). Since the tank reactive energy needs to be balanced, it needs to borrow an extra capacitance $\delta C = 2\sqrt{\frac{C_1}{L_1}}\frac{\delta\omega}{\omega^2}$, which
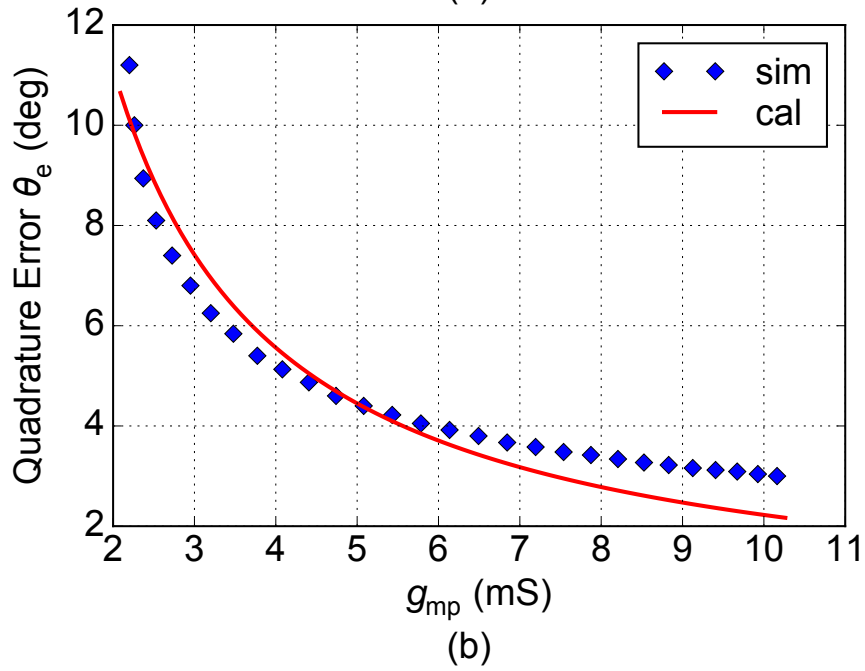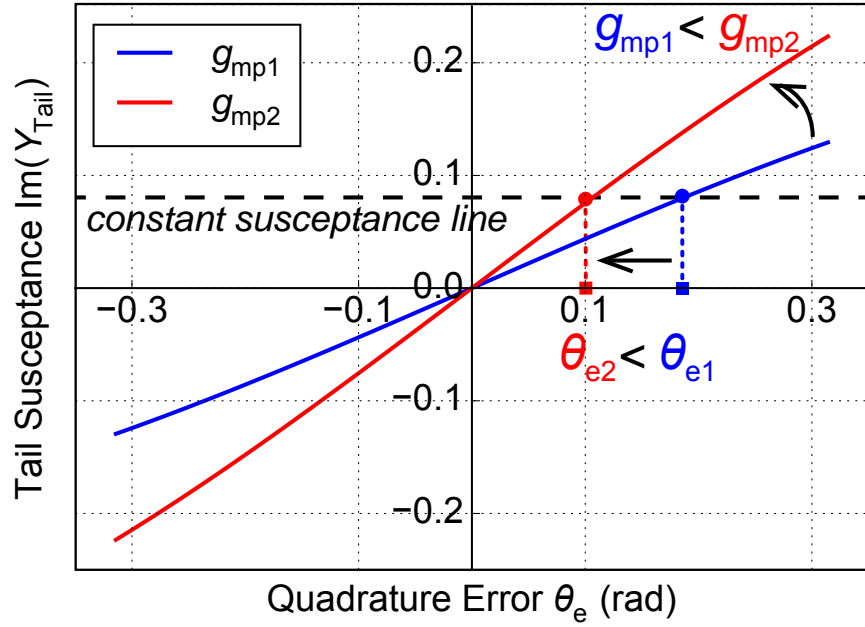
Figure 2.11: Quadrature error reduction mechanism (a) explained with constant tail susceptance line and (b) verified by simulation (f_{osc} =40GHz, C_1 =100fF, Q_1 =15, Φ_C =0.32, $\frac{\delta C}{C}$ =1%).

is provided by the tail node T_+. Based on (2.10), the tail susceptance at $\theta' = 90° + \theta_e$ is

$$B_{\text{Tail}_+} = \text{Im}(Y_{\text{Tail}_+}) = g_{mp} \sin(2\theta_e) \tag{2.26}$$

Taking into account the conversion loss Φ_C during the borrowing process (like a mixer) yields $B_{\text{Tail}_+} \Phi_C = \omega \, \delta C$. Therefore the quadrature error θ_e at a given mismatch is approximated as

$$\theta_e = \frac{\delta\omega}{\omega} \sqrt{\frac{C_1}{L_1}} \frac{1}{g_{\text{mp}} \, \Phi_C} \tag{2.27}$$

The same applies for OSC2, except that it needs a $-\delta C$ from the node T_-, provided by $B_{\text{Tail}_-} = -g_{\text{mp}} \sin(2\theta_e)$.

From (2.27), it is clear that increasing g_{mp} reduces θ_e. For better intuition, Fig. 2.11(a) plots $\text{Im}\big(Y_{\text{Tail}_+}(\theta_e)\big)$ at two different g_{mp}. Since the required δC is constant at a given mismatch (depicted as a constant susceptance line), increasing g_{mp} will push θ_e back to 0 (reduces phase error). Simulation results agrees very well with (2.27), as shown in Fig. 2.11(b).

It is true that increasing g_{mp} raises the PMOS noise contribution. However, the tail impedance $\|Z_{\text{Tail}}\|$ increases simultaneously, leading to a stronger second harmonic A_2. Based on (2.24), the NMOS noise contribution is thus reduced. Since the NMOS sizing is larger than PMOS, this compensation can be significant. This is verified with the simulated phase noise and phase error at different V_{ADJ} (a higher V_{ADJ} increases g_{mp}) in Fig. 2.12(a), and thermal noise contribution breakdown in Fig. 2.12(b). The $\|Z_{\text{Tail}}\|$-boosted second harmonic effect places the NMOS noise and PMOS noise on the opposite side of a seesaw to yield a relatively flat phase noise response, which highlights the phase accuracy tunability of the proposed coupling network.

The analysis so far assumes the resonance frequency of the tail tank ω_2 equals the second harmonic of the IQ oscillators 2ω. Now consider the existence of harmonic mismatch but no IQ mismatch, i.e. $\omega_2 = 2\omega + \delta\omega_2$ and $\omega_{\text{OSC1}} = \omega_{\text{OSC2}} = \omega$. The tail susceptance in (2.10) is modified as

$$Y_{\text{Tail}_{+/-}}(\theta) = -g_{\text{mp}} \cdot e^{\mp 2j(\theta - \pi/2)} + g_L - j\sqrt{\frac{C_{\text{Par}}}{L_{\text{Tail}}}} \frac{\delta\omega_2}{\omega} \tag{2.28}$$

Fig. 2.13 plots the complex $Z_{\text{Tail}_{+/-}}$ as a function of IQ phase difference, assuming 2.5% harmonic mismatch. Unlike Fig. 2.6, the $\|Z_{\text{Tail}}\|$ maxima of the two oscillators split apart due to harmonic mismatches. Therefore, OSC1 and OSC2 tend to drag θ_e along opposite directions to maximize their own loop gain. Since the two oscillators are matched, the drag force is balanced at the green circle in Fig. 2.13, corresponding to equal Z_{Tail} and zero quadrature error ($\theta_e = 0$). This can be verified by the steady-state simulation results in Fig. 2.14, where both oscillators see the same $Z_{\text{Tail}_{+/-}}$ and produce no phase error regardless of the harmonic mismatch level. However, if there is IQ mismatch, the drag force cannot be exactly balanced, which leads to different $Z_{\text{Tail}_{+/-}}$ and adds to the existing IQ imbalance. Through the same phase error reduction mechanism as above, increasing g_{mp} helps improve the quadrature accuracy.
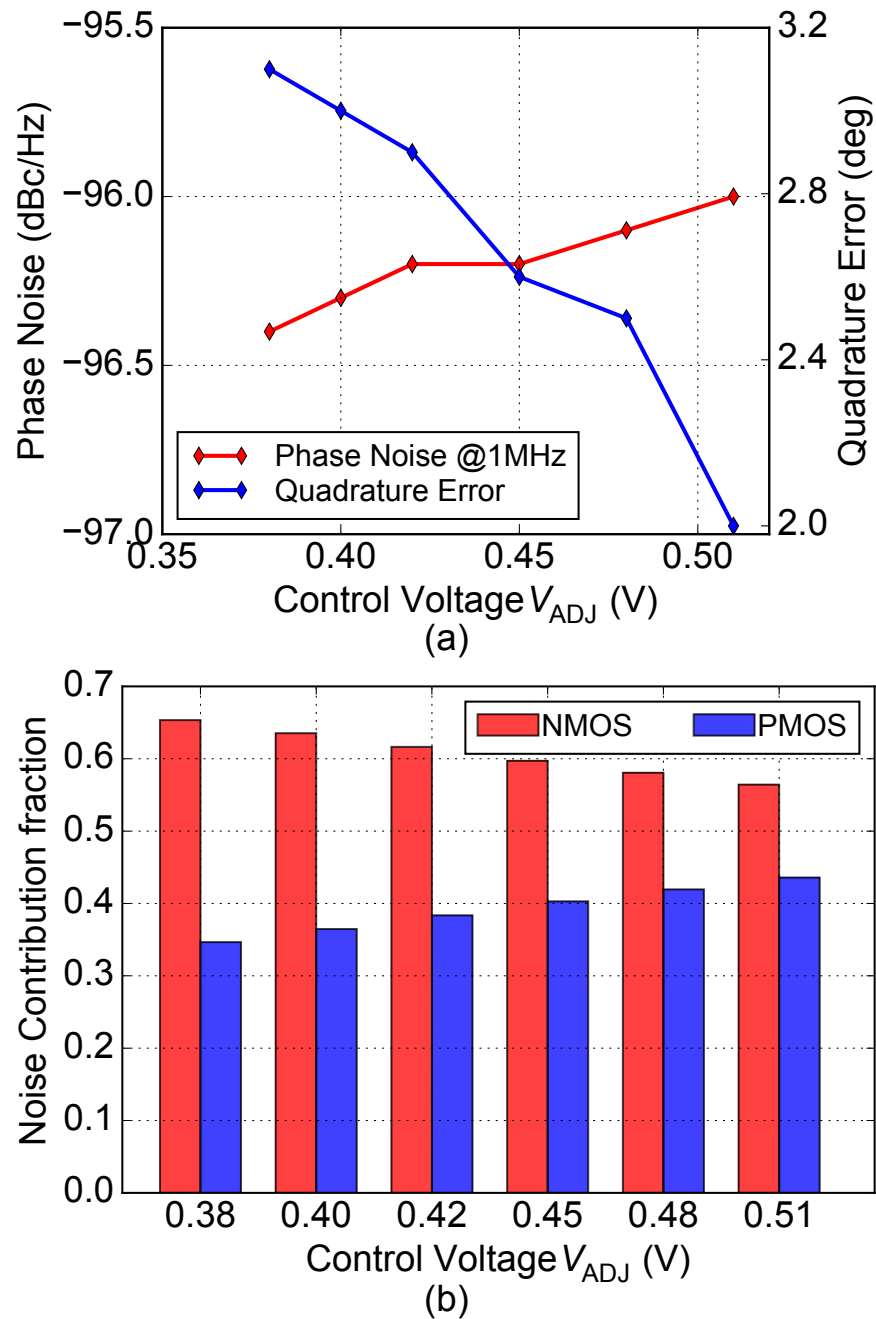
Figure 2.12: Simulated (a) phase noise and quadrature error, and (b) transistor thermal noise contribution breakdown at different V_{ADJ} (at 1MHz offset from a 40GHz carrier, assuming $\frac{\delta C}{C}$=1%).

2.2   QVCO-based Dielectric Sensing

2.2.1   Sensing Scheme

Oscillators are particularly popular in above-GHz reactance sensing [23, 62–64] through the measurement of the oscillation frequency shift. As analyzed in [65], the oscillator $1/f^3$ phase
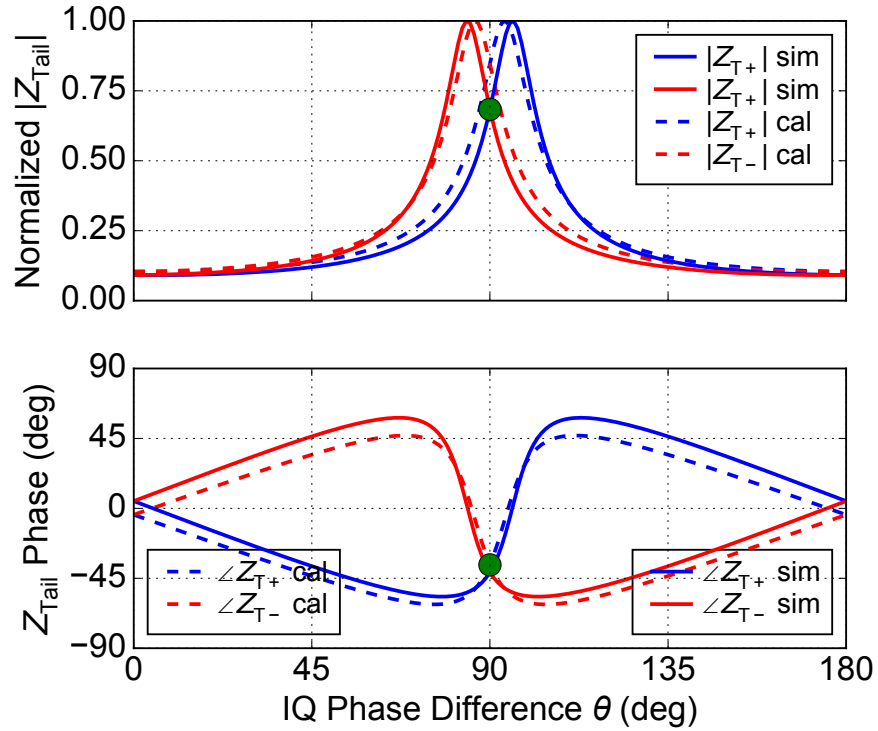
Figure 2.13: Calculated and simulated $Z_{\text{Tail}_{+/-}}(\theta)$ stimulated by the coupling network ($\theta = \pi/2 + \theta_e$), assuming 2.5% mismatch between ω_2 and 2ω.

noise limits the minimum detectable signal (MDS) and affects the long-term frequency stability. To suppress the $1/f^3$ phase noise, [65] introduced a correlated double counting (CDC) technique [see Fig. 2.15(a)], where a replica reference tank is added and shares the same active core with the sensing tank to form two oscillators with correlated $1/f^3$ phase noise. The noise can be attenuated by switching between the two tanks and taking the frequency difference. However, CDC faces two major limitations when used in dielectric detection. First, large switches are required to avoid tank quality factor degradation, which in turn contribute excessive capacitive parasitics and decrease sensitivity. Second, to isolate the reference tank from the biomedium, a protection layer (e.g. PDMS, SU-8) must be applied. Since the permittivity of the protection layer ($\epsilon_{\text{PDMS}} = 2.3$, $\epsilon_{\text{SU-8}} = 4.1$) is much smaller than water, the two tanks respond differently to the same (correlated) noise charge injection Q_n, as illustrated in Fig. 2.15(b), which decorrelates the two oscillators and leads to only partial noise cancellation.

Fig. 2.16 shows the simplified sensing architecture proposed in this work, where the sensing oscillator is divided into two mutually coupled oscillators *equally* exposed to the biomedium. To facilitate measuring the tank capacitance in a $1/f^3$-phase-noise-free regime, an additional varactor
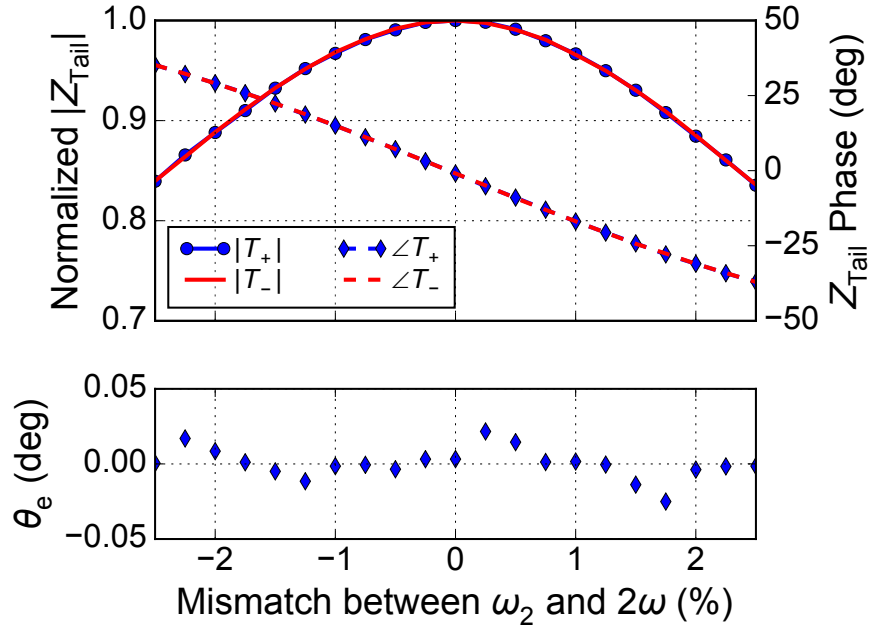
Figure 2.14: Simulated steady-state tail impedance $Z_{\text{Tail}_{+/-}}$ (top) and quadrature error θ_{e} (bottom) as a function of harmonic mismatch. The fluctuation of θ_{e} comes from the simulation residual error.

is included in each oscillator, and their values are modulated differentially at ω_{m},

$$C_{\text{VAR1,2}} = C_{\text{VAR,CM}} \pm \delta C_{\text{VAR}} \cdot \cos(\omega_{\text{m}}t), \tag{2.29}$$

so that the *free-running* frequencies of the two oscillators are also modulated differentially,

$$\omega_{1,2} = \omega_0\left(1 \mp \frac{\delta C_{\text{VAR}}}{2C_{\text{T}}} \cdot \cos(\omega_{\text{m}}t)\right)$$

$$= \omega_0 \mp \omega_\Delta \cdot \cos(\omega_{\text{m}}t). \tag{2.30}$$

With a shallow modulation depth ω_Δ, injection locking maintains the *operating frequency* of the two oscillators at ω_0 and converts the modulated frequency difference into a differential phase signal, to be measured by the subsequent phase detector. The gist is that the tank capacitance C_{T} is encoded in the phase signal and is not corrupted by $1/f^3$ phase noise as long as ω_{m} is beyond the flicker corner frequency ω_{C}.

The quantitative relationship between the tank capacitance and the phase signal can be established via Adler's equation [66–68]. The phase dynamics of an oscillator under injection is given by

$$\frac{d\theta_i}{dt} = \omega_i - \omega_{\text{inj}} + K_{\text{inj}}\frac{\omega_i}{2Q}\sin(\theta_{\text{inj},i} - \theta_i), \tag{2.31}$$
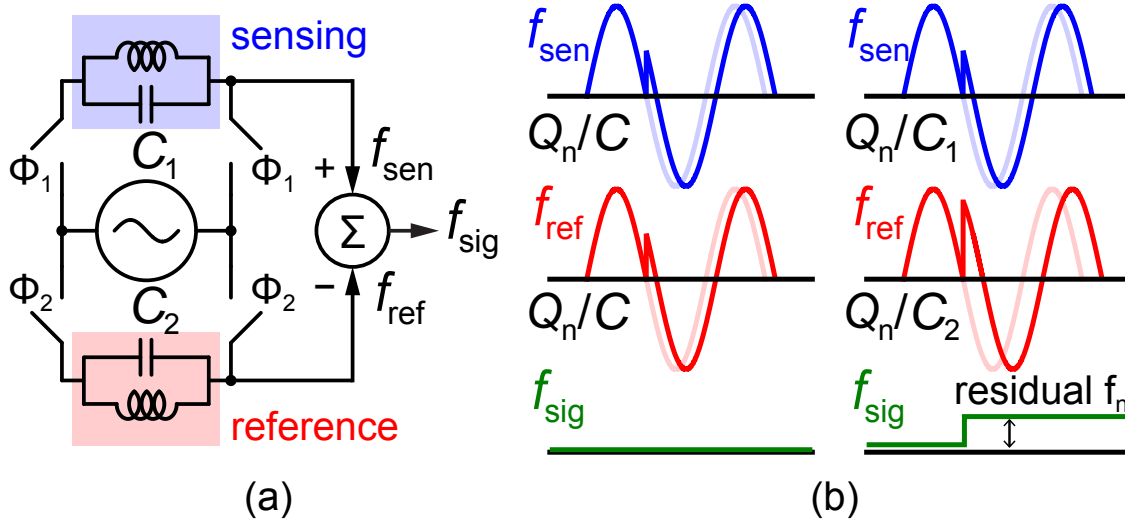
Figure 2.15: Oscillator-based sensor using CDC to attenuate $1/f^3$ phase noise. (a) Sensor architecture, and (b) CDC efficiency for $C_1 = C_2$ (left) and $C_1 \neq C_2$ (right). The time-interleaved operation is ignored for illustration simplicity.
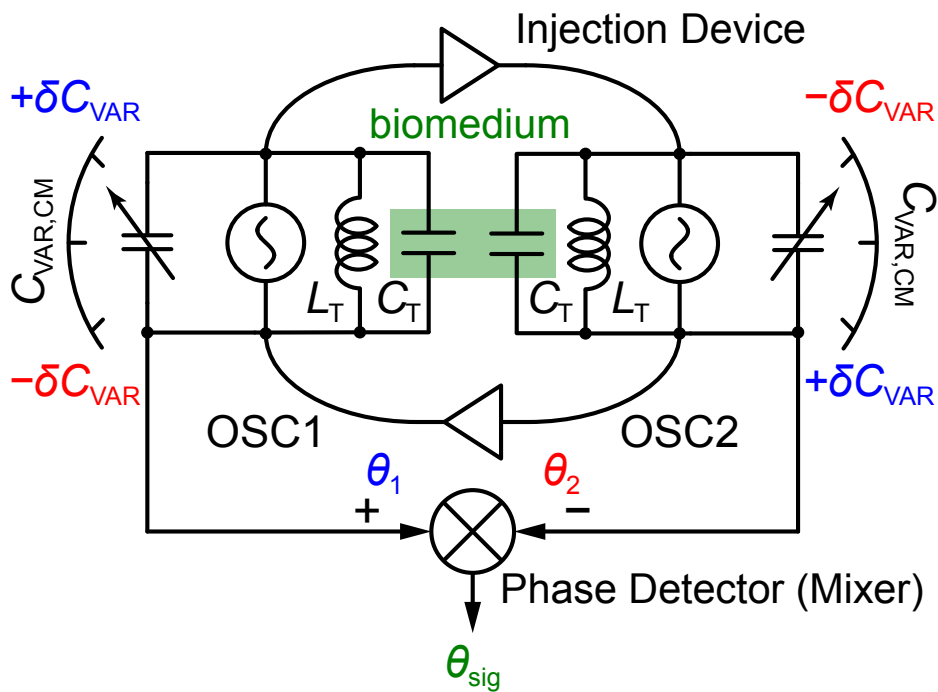
Figure 2.16: Proposed permittivity sensor architecture.
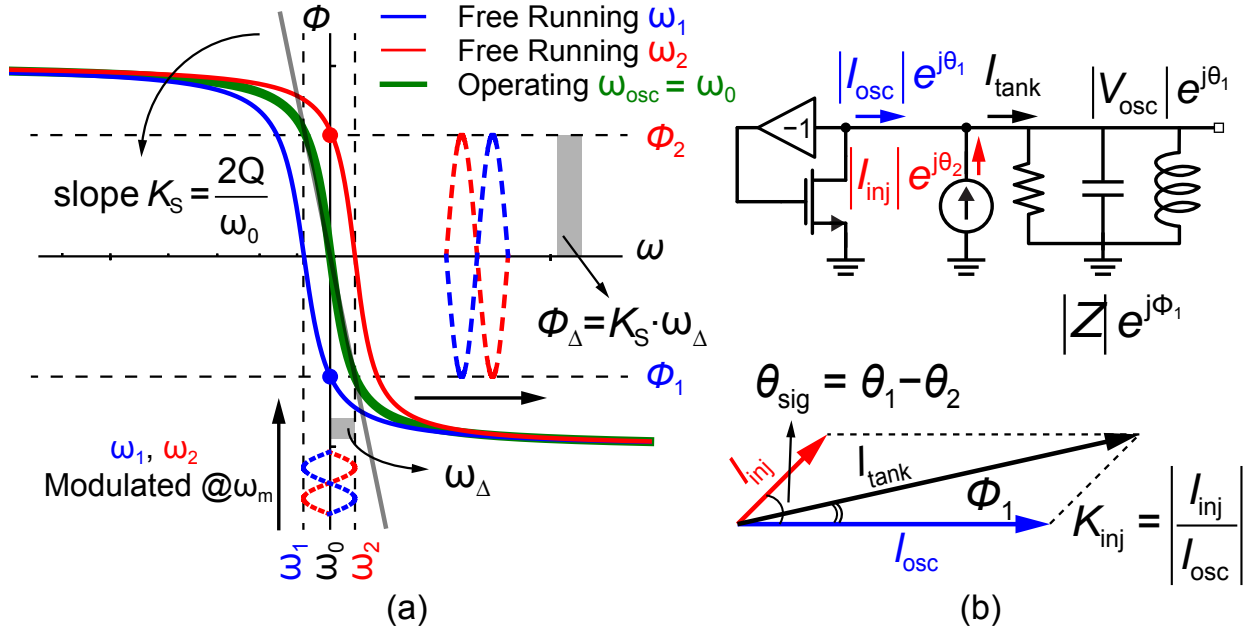
Figure 2.17: Proposed sensing scheme. (a) Tank impedance phase spectrum showing the modulation principle, and (b) injection phasor diagram showing $|\theta_{\text{sig}}| \approx \Phi_{1,2}/K_{\text{inj}}$.

where θ_i = oscillation phase, $\theta_{\text{inj},i}$ = injection phase, ω_i = oscillator free-running frequency, ω_{inj} = injection frequency, K_{inj} = injection strength, Q = tank quality factor and $i = 1, 2$. At steady state, the two oscillators are locked to ω_{osc} so that $d\theta_i/dt = 0$ and $\omega_{\text{inj}} = \omega_{\text{osc}}$. Assume the injection signal is in-phase with the injection source, i.e., $\theta_{\text{inj},1} = \theta_2$ and vice versa. It follows from (2.31) that,

$$
\begin{aligned}
\omega_{\text{osc}} &= \omega_1 + K_{\text{inj}}\frac{\omega_1}{2Q}\sin(\theta_2 - \theta_1) \\
&= \omega_2 + K_{\text{inj}}\frac{\omega_2}{2Q}\sin(\theta_1 - \theta_2).
\end{aligned}
\tag{2.32}
$$

Combining (2.30) and (2.32) validates that two oscillators lock back to $\omega_{\text{osc}} = \omega_0$, and yields the solution to the phase signal θ_{sig}.

$$
\omega_{\text{osc}} = \frac{2\omega_1\omega_2}{\omega_1 + \omega_2} = \omega_0 - \frac{\omega_\Delta^2}{\omega_0}\cos^2(\omega_m t) \approx \omega_0
\tag{2.33}
$$

$$
\sin(\theta_{\text{sig}}) = \sin(\theta_1 - \theta_2) = -\frac{\delta C_{\text{VAR}}}{C_T}\frac{Q}{K_{\text{inj}}}\cos(\omega_m t)
\tag{2.34}
$$

It is apparent from (2.34) that the tank capacitance C_T manifests itself through the amplitude of the modulated phase signal, with an amplification factor of $\delta C_{\text{VAR}} \cdot Q/K_{\text{inj}}$. Consequently, increasing δC_{VAR} and reducing injection strength K_{inj} improve the signal quality, given that the shallow modulation assumption still holds (which sets the limits to δC_{VAR} and K_{inj}).
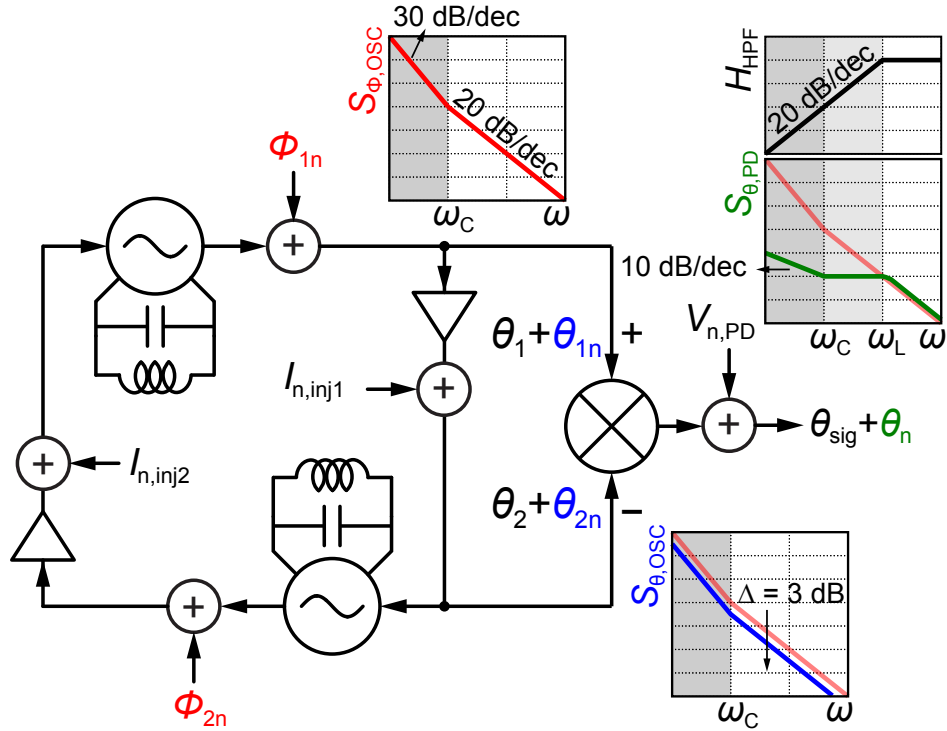
Figure 2.18: The noise model of the permittivity sensor.

The proposed sensing scheme is in fact a derivative spectroscopy, which can be visualized in Fig. 2.17(a). When the two oscillators are injection locked at ω_0 (green), their free-running frequencies are modulated differentially around ω_0 (blue and red), which leads to the tank impedance phases $\phi_{1,2}$ being modulated as well. If ω_Δ is small, the output amplitude ϕ_Δ is proportional to the derivative of the tank impedance phase spectrum, $d\phi/d\omega = 2Q/\omega_0$. Based on the injection phasors in Fig. 2.17(b), the phase signal θ_{sig} is simply ϕ_Δ boosted by $1/K_{\text{inj}}$. That is, by modulating the free-running frequencies of the two coupled sensing oscillators, the biomedium dielectric constant, encoded in the tank impedance phase spectrum, can be measured at a frequency beyond the flicker corner.

2.2.2   Noise Analysis

One common fallacy is to presume that the phase noise of the two mutually coupled oscillators are completely canceled through self-mixing, so that the above modulation technique is unnecessary. Starting from Adler's equation, it shall be shown that injection locking and mixing only performs a first-order high-pass filtering to the $1/f^3$ phase noise, mandating the use of modulation.

Fig. 2.18 shows the sensor noise model, including the oscillator phase noise (uncoupled), $S_{\phi,\text{OSC1,2}}$, injection noise $I_{\text{n,inj1,2}}$ and phase detector noise $V_{\text{n,PD}}$. Since $I_{\text{n,inj1,2}}$ strongly depends on
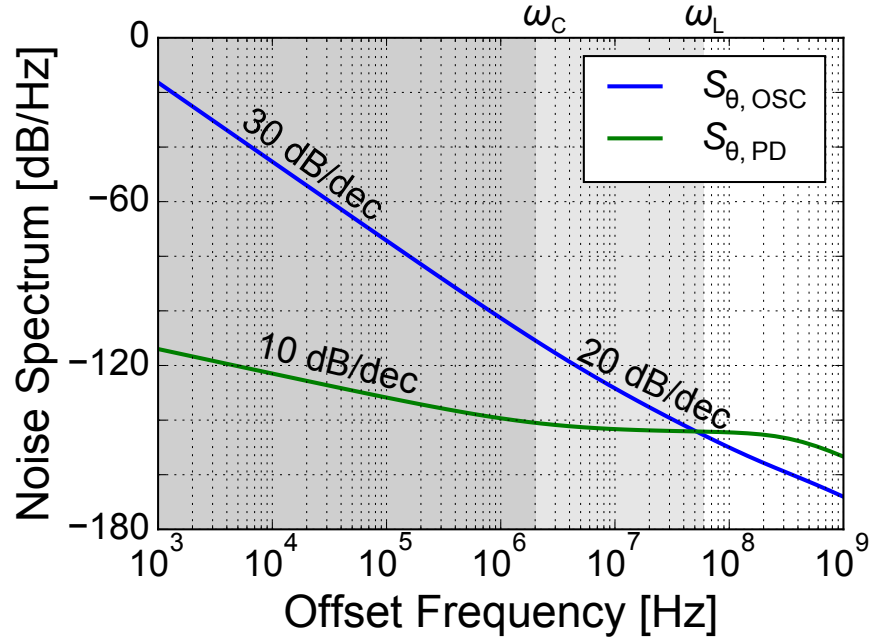
Figure 2.19: Simulated noise power spectrum, relative to the carrier (40 GHz) for $S_{\theta,\mathrm{OSC}}$ and DC for $S_{\theta,\mathrm{PD}}$ (ω_{C} = flicker corner, ω_{L} = lock range).

the coupling method and can be absorbed into $S_{\phi,\mathrm{OSC}1,2}$, while $V_{\mathrm{n,PD}}$ is simply additive, the focus here will be $S_{\phi,\mathrm{OSC}1,2}$.

For noise analysis, (2.31) is perturbed by $\theta_i \Rightarrow \theta_i + \theta_{i,\mathrm{n}}$ and $\omega_i \Rightarrow \omega_i + d\phi_{i,\mathrm{n}}/dt$, where $\theta_{i,\mathrm{n}}$ and $\phi_{i,\mathrm{n}}$ ($i = 1, 2$) are oscillator phase fluctuations with and without injection locking, respectively. At steady state, assuming shallow modulation and in-phase injection, (2.31) becomes

$$
\begin{aligned}
\frac{d\theta_{1\mathrm{n}}}{dt} &= \omega_1 + \frac{d\phi_{1\mathrm{n}}}{dt} - \omega_0 - K_{\mathrm{inj}}\frac{\omega_1}{2Q}\sin(\theta_{\mathrm{sig}} + \theta_{1\mathrm{n}} - \theta_{2\mathrm{n}}) \\
\frac{d\theta_{2\mathrm{n}}}{dt} &= \omega_2 + \frac{d\phi_{2\mathrm{n}}}{dt} - \omega_0 + K_{\mathrm{inj}}\frac{\omega_2}{2Q}\sin(\theta_{\mathrm{sig}} + \theta_{1\mathrm{n}} - \theta_{2\mathrm{n}}).
\end{aligned}
\tag{2.35}
$$

Therefore the signal noise $\theta_{\mathrm{n}} = \theta_{1\mathrm{n}} - \theta_{2\mathrm{n}}$ can be derived as

$$
\begin{aligned}
\frac{d\theta_{\mathrm{n}}}{dt} &= \frac{d\phi_{1\mathrm{n}}}{dt} - \frac{d\phi_{2\mathrm{n}}}{dt} - K_{\mathrm{inj}}\frac{\omega_0}{Q}\sin(\theta_{\mathrm{sig}} + \theta_{\mathrm{n}}) - 2\omega_\Delta\cos(\omega_{\mathrm{m}}t) \\
&\simeq \frac{d\phi_{1\mathrm{n}}}{dt} - \frac{d\phi_{2\mathrm{n}}}{dt} - K_{\mathrm{inj}}\frac{\omega_0}{Q}\theta_{\mathrm{n}}.
\end{aligned}
\tag{2.36}
$$

Laplace transforming (2.36) yields

$$
\Theta_{\mathrm{n}}(s) = \frac{s}{s + \omega_{\mathrm{L}}}\left(\Phi_{1\mathrm{n}}(s) - \Phi_{2\mathrm{n}}(s)\right),
\tag{2.37}
$$

where $\omega_L = K_{inj} \cdot \omega_0/Q$ is the overall lock range [69]. (2.37) validates such first-order high-pass filtering with $\omega_{3\,dB} = \omega_L$. In other words, mutual coupling only attenuates the $1/f^3$ phase noise in θ_n by 20 dB/dec, and chopping is thereby required for higher sensitivity. Note that mutual injection locking alone does not provide any noise filtering effect, only lowering it by 3 dB, i.e., $S_{\theta,OSC1,2} = S_{\phi,OSC1,2}/2$ [70]. The conceptual noise spectrums are plotted in Fig. 2.18. For validation, the simulated noise spectrums are shown in Fig. 2.19.

In this work, quadrature locked oscillators are selected over in-phase locked oscillators to maximize the conversion gain for small θ_{sig}. After switching to a QVCO, one needs to examine if the derived equations still hold. This can be done through validation of the only assumption made during the derivation, i.e., in-phase injection ($\theta_{inj,1} = \theta_2$ and vice versa). Thanks to the superharmonic network, the fundamental injection is delayed by 90° through the inversion of the second harmonic. Suppose the output voltages of IQ oscillators are $\sin(\omega_0 t + \theta_1)$ and $\cos(\omega_0 t + \theta_2) = \sin(\omega_0 t + \theta_2 + 90°)$, respectively (Fig. 2.20). The signal injected into OscI is thereby $\theta_{inj,1} = \theta_2 + 90° - 90° = \theta_2$, which validates the assumption.

2.3 Circuit Implementation

For verification, a 40 GHz QVCO sensor prototype was fabricated in the TSMC 28 nm bulk CMOS process. Fig. 2.20 shows the complete circuit diagram of the dielectric sensor. Fig. 2.21(a) shows the detailed circuit diagram of the proposed superharmonic QVCO. Each individual VCO uses a 3-bit thermometer-coded switched-MOM capacitor bank for discrete frequency tuning, along with an accumulation-mode varactor for continuous tuning. The NMOS transistor in the cross-coupled cell is sized as 10.8μm/28nm to ensure a start-up loop-gain of 2.2 over PVT variations. In the superharmonic coupling network, a PMOS cross-coupled pair (sized as 10.8μm/28nm) is utilized for tail impedance boosting and quadrature locking. PMOS is selected since it consumes zero voltage headroom and allows completely independent tuning. The control voltage for phase accuracy tuning is set around V_{ADJ}=450mV for optimal g_{mp}-V_{ADJ} sensitivity. A third varactor is included in the coupling network for tail tuning. Although the frequency mismatch between the tail tank and the second harmonic of the IQ VCOs will not cause quadrature error if the two VCOs are matched, such harmonic mismatch should still be minimized as it reduces the second harmonic strength, which degrades the phase noise and phase accuracy in the presence of IQ mismatch.

The tank inductors are laid out using the top metal for optimal quality factor and self resonance frequency (Fig. 2.21(b)). A nominal metal stack is employed without any ultra-thick metal layers. The tail inductor is very small compared with the tank inductors, which yields a compact layout. A complete EM simulation is performed to characterize the inductive mutual coupling and the return path of fundamental and second harmonic signals (both common-mode and differential-mode). The simulated tank inductance $L_{I,Q} = 265$ pH with $Q = 12$ and the tail inductance $L_T = 110$ pH with $Q = 12.5$.

To characterize the quadrature accuracy, the DC product of IQ self-mixing is used, i.e., $\cos(\omega t - \theta_e/2) \cdot \sin(\omega t + \theta_e/2)\big|_{DC} \rightarrow \sin(\theta_e)$. A double-balanced voltage-commutative passive mixer followed by a chopper amplifier is employed for such purpose, as shown in Fig. 2.22(b). A
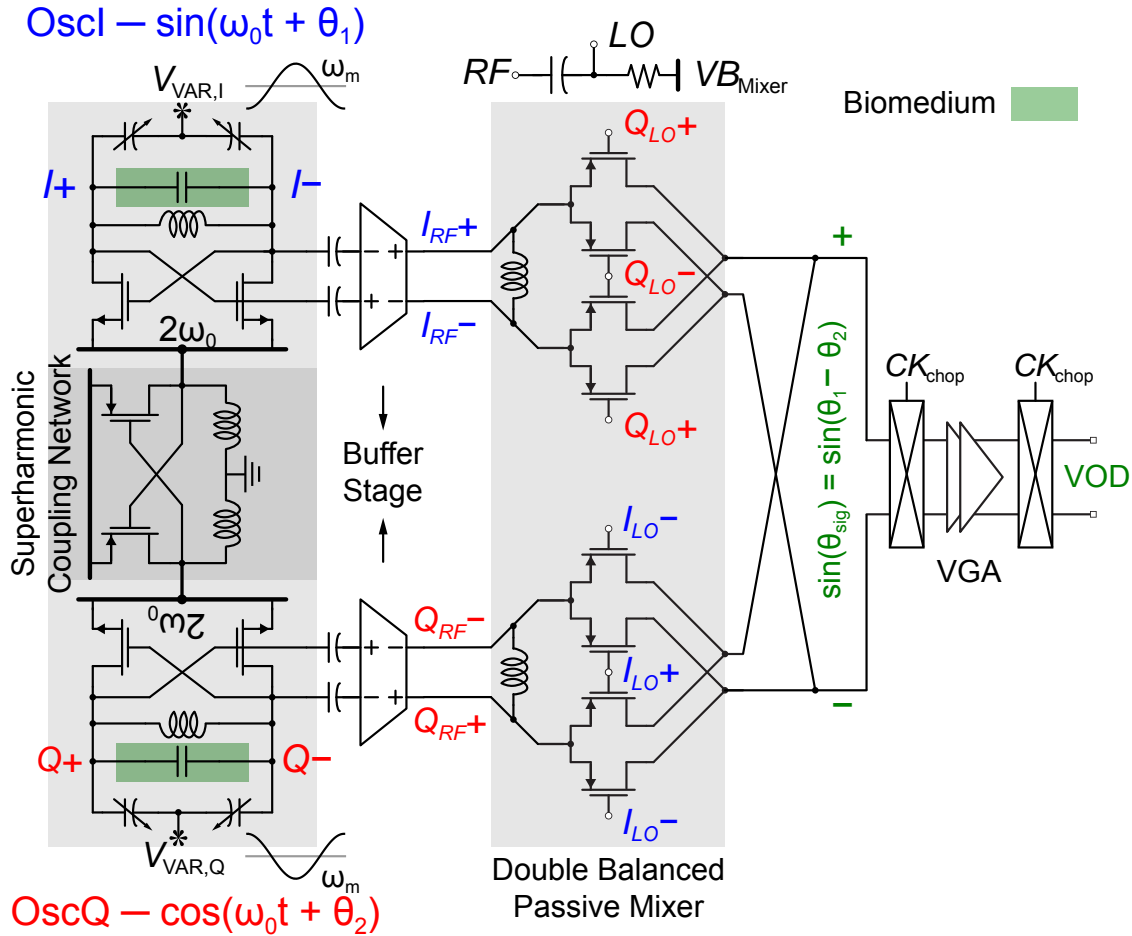
Figure 2.20: Permittivity sensor circuit block diagram.

tuned buffer stage (Fig. 2.22(a)) is inserted between the QVCO and the mixer for isolation. It also provides the DC bias for the chopper amplifier input common mode through $V_{DD, BUF}$=650 mV. Chopping at 10 MHz is sufficient to remove the amplifier's DC offset and flicker noise. The PMOS mixer gate is biased at 400 mV to avoid DC current and thereby its flicker noise contribution. To allow back-calculating the phase error from the measured differential V_{OD}, post-layout simulations are performed to extract the transfer curve from the quadrature error θ_e at the buffer input to V_{OD}, as plotted in Fig. 2.22(c)).

For the purpose of biomolecular sensing, HFSS simulations are performed, indicating that the QVCO tank inductor $Q = 9.5$ in phosphate-buffered saline (PBS, $\epsilon_r = 20$, $\sigma_0 = 2$ S/m). With 1% $\Delta\epsilon_r$ in PBS, each oscillator picks up 5.22 aF ΔC (out of $C_T = 54$ fF), creating 48.3 ppm frequency shift. The signal is up-converted from dc by modulating the individually accessible varactor control voltages differentially at ω_m around a common bias $V_{VAR,CM}$. It is then readout by the passive mixer and baseband VGA.
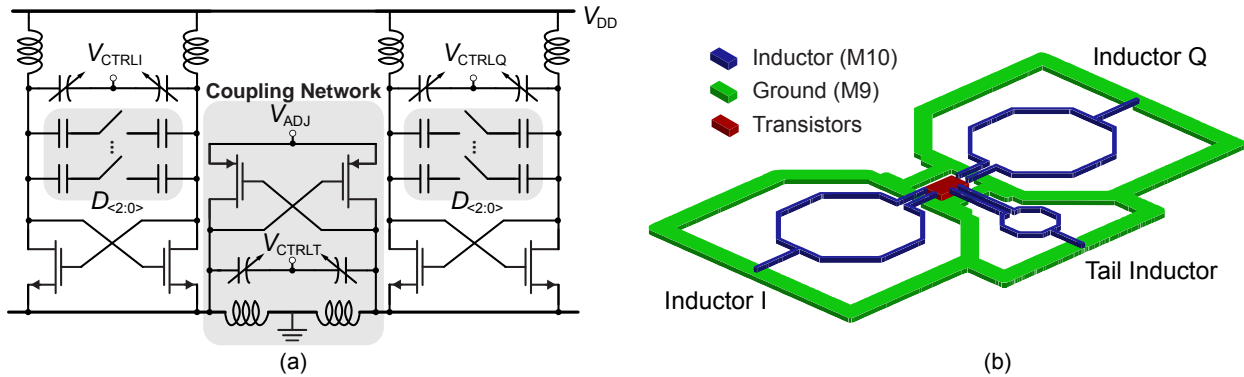
Figure 2.21: (a) Complete schematic of the proposed superharmonic QVCO and (b) 3D view of the inductor model in EM simulations (not to scale).
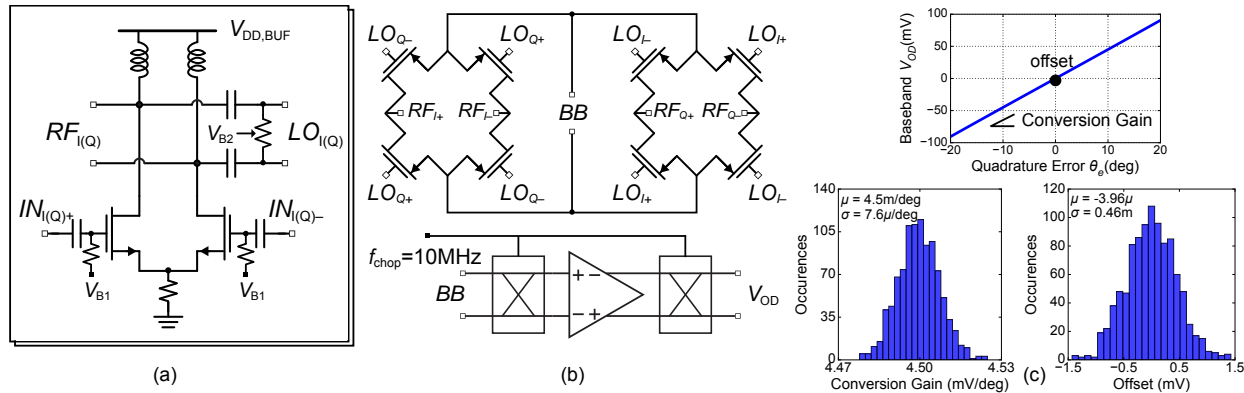
Figure 2.22: Schematic of (a) the tuned buffer stage and (b) the double-balanced voltage-commutative passive mixer with the chopper amplifier, (c)(top) extracted V_{OD}–θ_e transfer curve from post-layout simulations, and (bottom) 1000 post-layout Monte-Carlo simulation results of conversion gain and offset, including mismatch data from the mixer and the baseband stage.

2.4 Electrical Characterization

The chip is fabricated in the TSMC 28 nm bulk CMOS process. The QVCO occupies 0.068 mm^2 and consumes 8.4 mW at V_{DD}=0.75 V. The sensing capacitors are configured as part of the inductor feeds using top metal layers (M10 and AP). A bio-cavity is created by aligning a slab of drilled Polydimethylsiloxane (PDMS) to the sensor chip on the PCB. Adhesion bonding and mechanical pressure are used to prevent medium leakage. Fig. 2.23 shows the chip photo and packaging.

Measurements were performed to study both the QVCO performance (tuning range, phase noise and quadrature accuracy) and the sensor performance (lock range, noise and sensitivity). The results are summarized in the following two sub-sections.
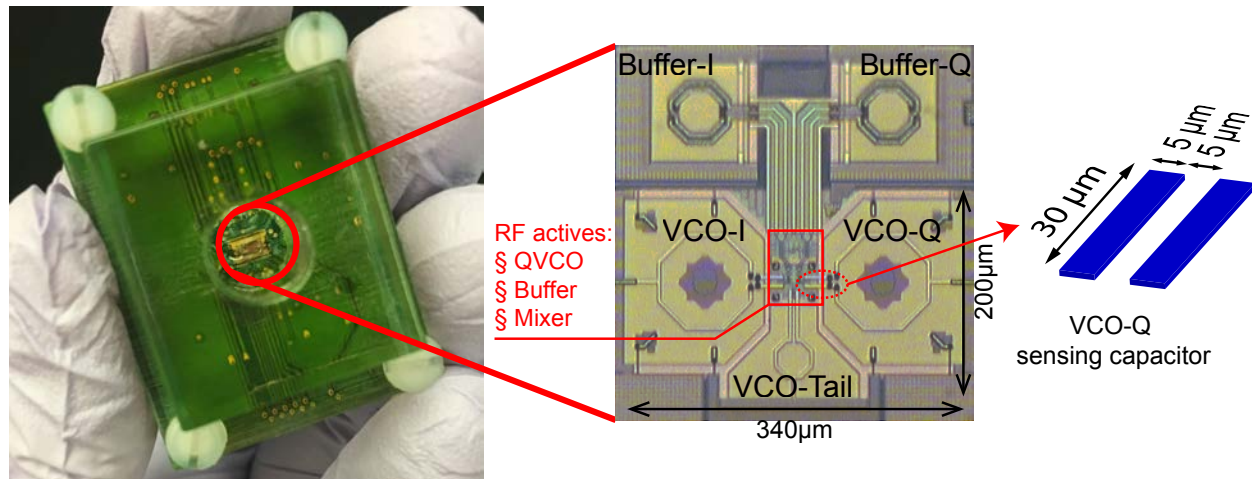
Figure 2.23: Chip micrograph and packaging.

2.4.1 QVCO Performance

Tuning range and phase noise measurements are performed through on-wafer probing. The near-field signal was captured by a SG probe (Cascade Microtech ACP40-W-SG-150), and then amplified to about 0 dBm by a two-stage LO amplifier before being fed into the spectrum analyzer (Agilent N9030A). The LO amplifier has an overall gain of 65 dB and 6 dB noise figure, which ensures a reliable phase noise measurement down to -100 dBc/Hz. The QVCO can be tuned from 37.5 GHz to 45.1 GHz, exhibiting a tuning range of 18.4% (see Fig. 2.24). Fig. 2.25 shows the phase noise measurement at the center frequency and across tuning range. At 40.7 GHz, the phase noise at 1 MHz offset is -94.32 dBc/Hz, which corresponds to a FoM of -177.4 dBc/Hz. The measured flicker corner is around 1.6 MHz.

Quadrature accuracy is characterized following the procedure described in the previous section and the measurement result at different phase tuning voltage V_{ADJ} is plotted in Fig. 2.26(a). An external ADC is used for digitization and the total integrated output noise is 0.2 mV, corresponding to a minimal detectable phase error of $0.04°$. At V_{ADJ}=0.45 V, a phase error of $0.18°$ is achieved. The back-calculation accuracy is subject to the buffer and mixer offsets as well as the $\theta_e - V_{\text{OD}}$ conversion gain fluctuation due to process variations. The buffer offset is lumped into part of the quadrature error, while the mixer offset and conversion gain variation are estimated with Monte-Carlo simulations (Fig. 2.22(c)). Taking into account 3-σ outliers, the worst-case phase error is $0.48°$. Fig. 2.27 shows the measured quadrature accuracy across frequency tuning range. The increased phase error near the edge of the tuning range is caused by the harmonic mismatch. Moreover, increasing V_{ADJ} attenuates the phase error: a 36× phase error reduction is achieved over the measurement range with only 2 dB phase noise variation, as shown in Fig. 2.26. Interestingly, when V_{ADJ} is less than 430 mV, the measured phase noise trend in Fig. 2.26(b) does not match the simulation in Fig. 2.12(a). The excessive phase noise is caused by off-resonance locking due to mismatches when the coupling is weak. Specifically, when the coupled VCOs are locked off-resonance, the effective tank Q drops
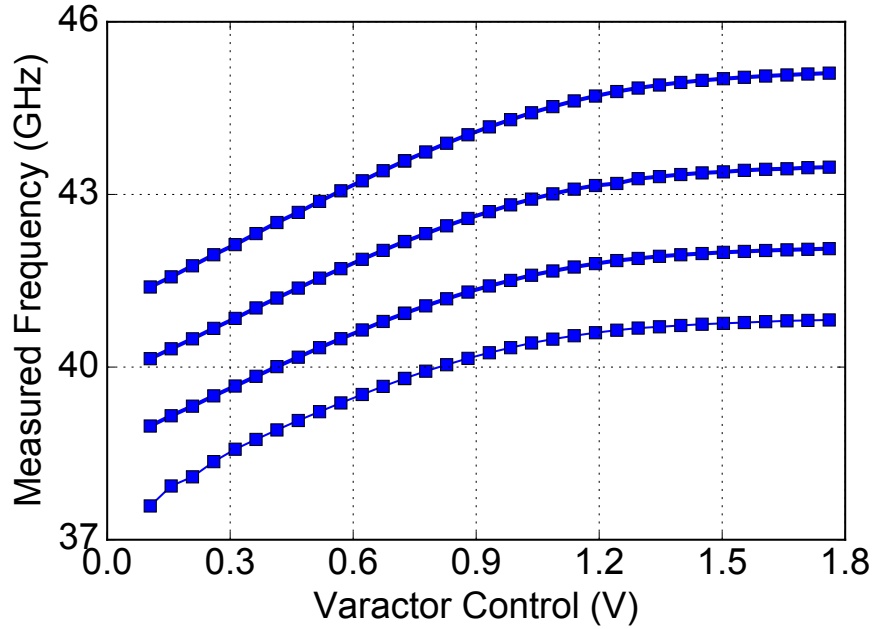
Figure 2.24: Measured frequency tuning curves.

at the rate of $\cos(\phi_{\text{off\_res}})$, where $\phi_{\text{off\_res}} \simeq \theta_e/2$, which induces extra phase noise[71, 72]. This is verified by Fig. 2.28(b), which will be discussed in a moment.

To further validate the phase accuracy tunability, artificial offsets are created between the two VCOs with individually-accessible varactor control voltages. Fig. 2.28(a) shows the measured V_{OD} as a function of ΔV_{CTRL} (which reflects the amount of IQ mismatch) at different V_{ADJ}. Clearly increasing V_{ADJ} reduces the quadrature error. Phase noise degradation due to off-resonance locking is verified in Fig. 2.28(b) with the aid of ΔV_{CTRL}. More importantly, the excessive phase noise caused by IQ mismatch is attenuated when V_{ADJ} is increased.

Table 2.1 summarizes and compares our work with the state-of-art mm-Wave QVCOs. Offering a tunable phase accuracy with almost no phase noise degradation, the proposed superharmonic QVCO achieves 0.18° phase error with a competitive tuning range and phase noise performance.

2.4.2 Sensor Performance

To study the performance of using QVCO as a dielectric sensor, measurements were performed in both air and PBS. The frequency tuning range [Fig. 2.29(a)] and lock range [Fig. 2.29(b)] are characterized by coupling the oscillator near-field to the SG probe and the signal is captured by a spectrum analyzer, sharing the same setup as in the previous subsection. When measuring the lock range, the varactor control voltages of IQ oscillators are offset differentially from $V_{\text{VAR,CM}}$ by $V_{\text{VAR,DM}}$. The value of $V_{\text{VAR,DM}}$ when pulling is observed denotes the lock range.

Table 2.1: Performance Comparison with the State-of-the-art mm-Wave QVCOs

Reference	Coupling Method	CMOS Tech.	Freq. (GHz)	TR (%)	Power (mW)	Phase Error (deg)	PN @1MHz (dBc/Hz)	FoM* (dBc/Hz)	FoM$_T$** (dBc/Hz)	Phase Accuracy Tunability
[36]'08	Parallel	90 nm	48	16.7	22.7	0.4	-85	-165	-170	No
[30]'11	Transformer	65 nm	58	7.5	22	1.5	-96	-178	-175	No
[40]'13	Bottom series	65 nm	25	2.8	14.4	1.8	-109	-185	-174	No
[48]'14	Superharmonic	40 nm	58	16.2	30	2	-92.5	-173	-177	No
[41]'14	NMOS diode	65 nm	63	16.6	11.4	0.7	-94.2	-180	-184	No
[44]'14	Transformer	65 nm	56	24	16	0.5-4.5	-89.8	-173	-180	No
[42]'15	Bidirectional diode	65 nm	26	15.4	11.8	0.36	-99	-176	-180	No
[45]'16	Transformer	65 nm	54	9.1	24	2	-95.5	-180	-179	No
[46]'16	Transformer	28 nm	74	6.4	35.6	1.5	-93.5	-175	-171	No
[37]'17	Bidirectional parallel	90 nm	67	6.6	91	0.46	-105.8	-183	-179	No
[38]'18	Parallel	90 nm	58	4.1	18	0.3	-83.2	-166	-158	No
This Work	**Superharmonic**	**28 nm**	**41**	**18.4**	**8.4**	**0.18±0.3***	**-94.3**	**-177**	**-183**	**Yes**

*FoM=PN$-20\log_{10}\left(\frac{f_0}{\Delta f}\right)+10\log_{10}\left(\frac{P_{DC}}{1mW}\right)$, **FoM$_T$=FoM$-20\log_{10}\left(\frac{\text{Tuning Range}[\%]}{10}\right)$, both @1MHz, ***back-calculated, ±3-σ process mismatches.
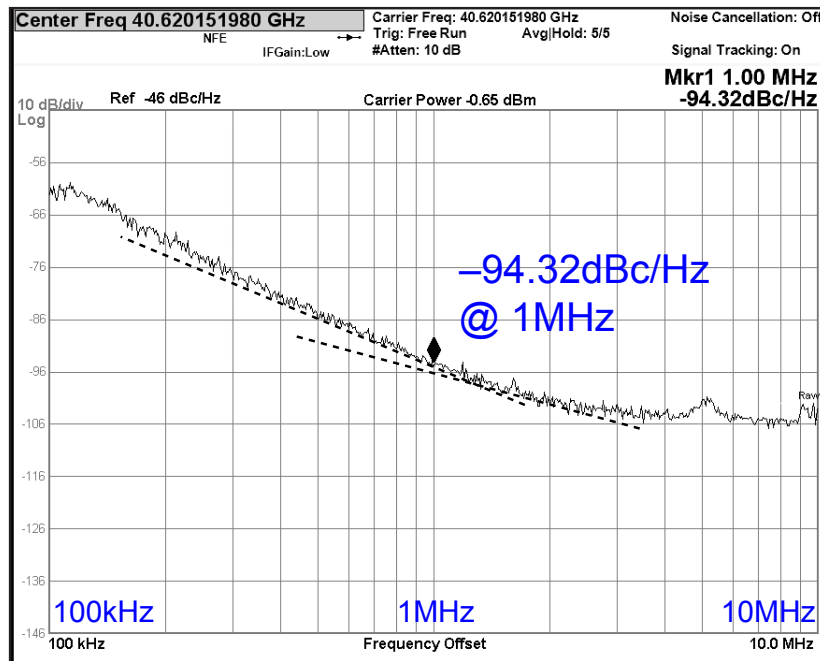
(a)
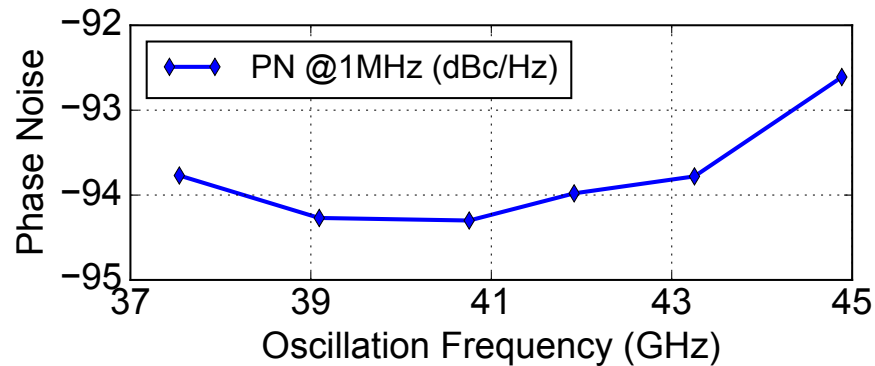
(b)

Figure 2.25: Measured phase noise (a) at 40.7 GHz, and (b) over tuning range at 1 MHz frequency offset, V_{ADJ}=450 mV.

To validate the noise analysis and prove the necessity of modulation, the major flicker source is sorted out by inspecting the sensor output noise spectrums as follows. First, the noise spectrums are measured when the VGA chopper pair (Fig. 2.20) is enabled (at 10 MHz) and disabled (both with $V_{VAR,DM} = 0$). As shown in the top subplot of Fig. 2.30, the contribution of the VGA flicker noise is imperceptible. For further verification, the noise spectrum of the VGA alone was also measured and shown in the bottom subplot of Fig. 2.30, which is indeed much lower than the overall sensor
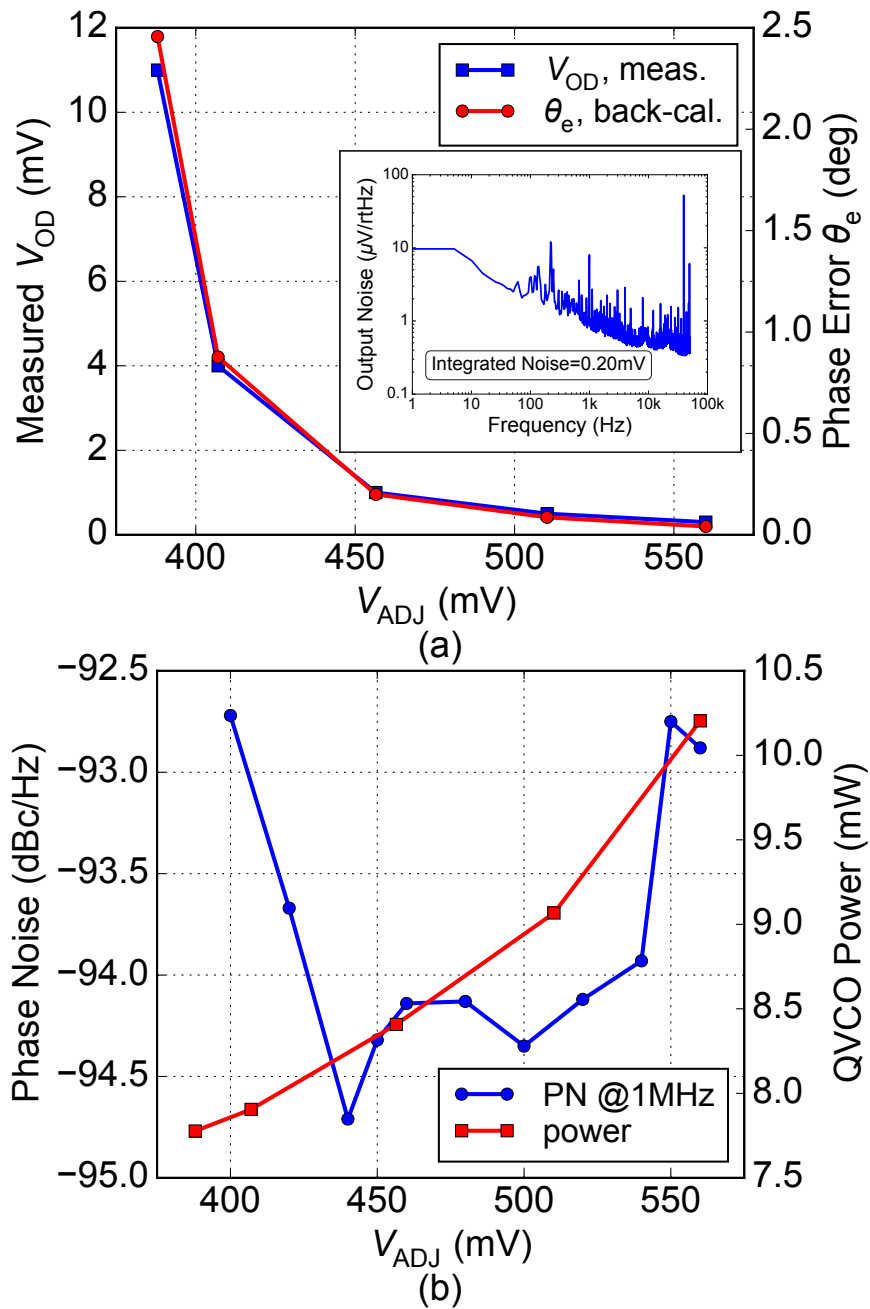
Figure 2.26: Measured (a) quadrature accuracy (inset, measured V_{OD} noise PSD), (b) phase noise (at 1 MHz offset) and power consumption at different V_{ADJ}. The measured oscillation frequency remains at 40.7 GHz.

noise level. However, once the two oscillators are unlocked with a large $V_{VAR,DM}$, the output noise
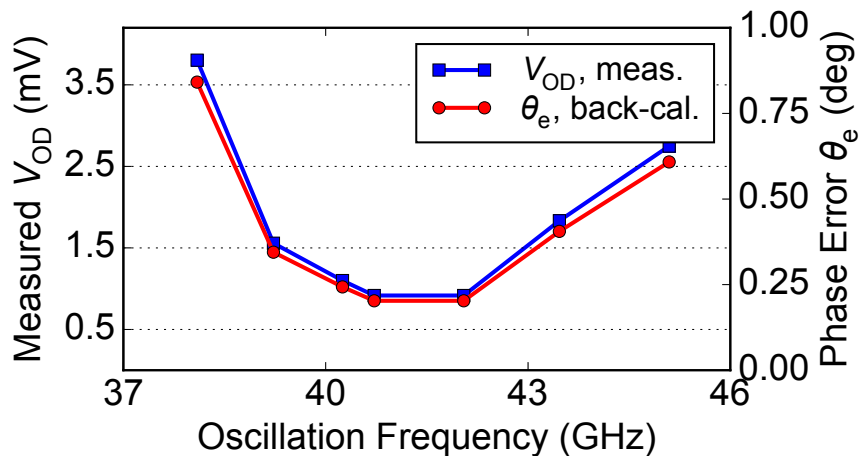
Figure 2.27: Measured quadrature accuracy across tuning range, V_{ADJ}=450 mV.
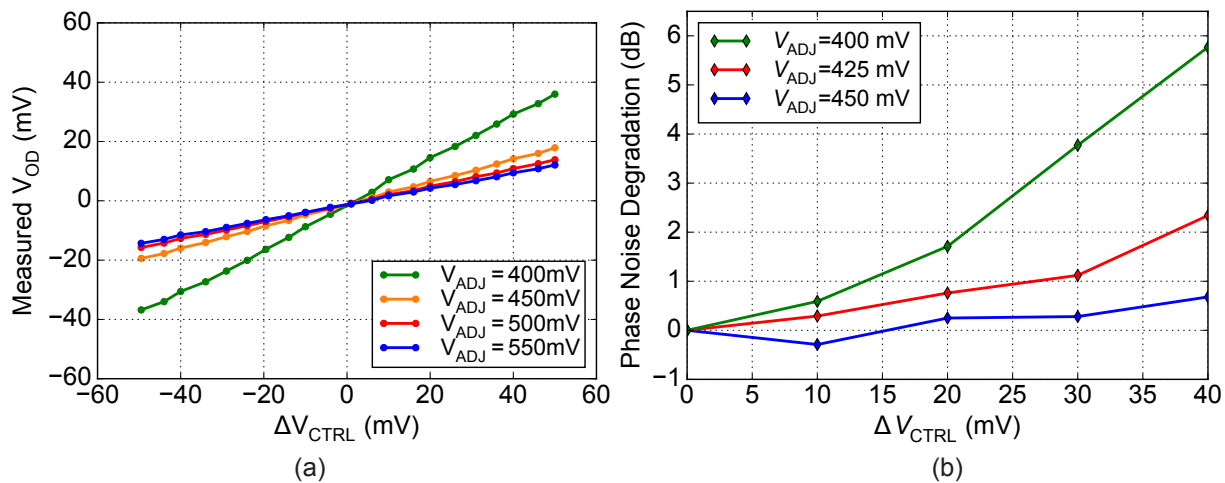
Figure 2.28: Measured (a) I/Q self-mixing differential DC output and (b) phase noise degradation (at 1MHz offset) decreases as V_{ADJ} increases at given ΔV_{CTRL}, $V_{CTRL,CM}$=1.2 V.

spectrum, down-converted from the oscillator far-out f^0 phase noise [73], is flattened out, indicating that the QVCO virtually contributes all the flicker noise. This is expected since the QVCO transistor size is much smaller than the VGA.

Chopping is performed by modulating the varactor control voltages differentially with $\delta_m \cdot \cos(\omega_m t)$ around a common bias voltage $V_{VAR,CM} = 1.35$ V. The modulation frequency is 1 MHz, above the flicker noise corner (about 900 kHz, Fig. 2.30). The optimal modulation depth should be the largest δ_m that satisfies shallow modulation requirements to ensure good linearity and close-in
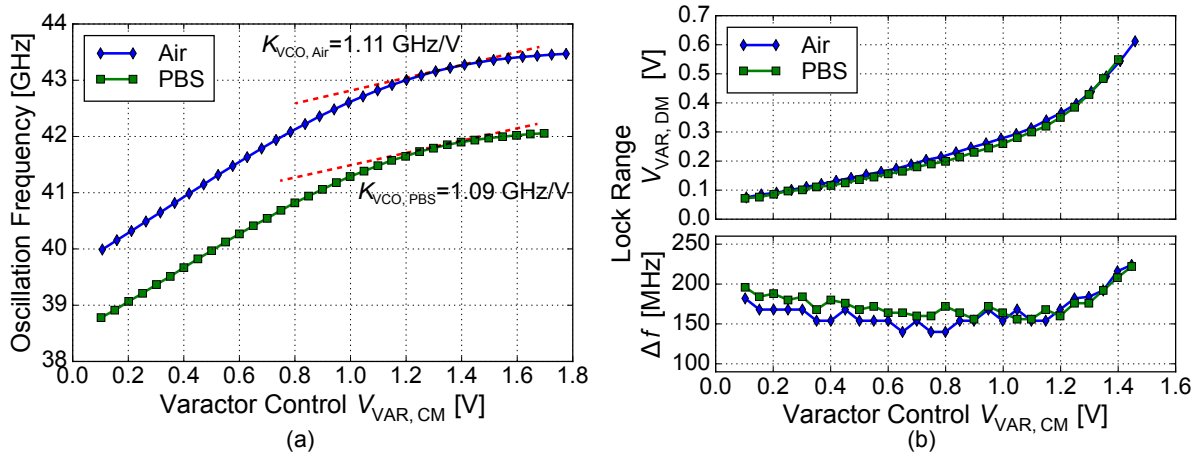
Figure 2.29: Measured QVCO (a) frequency tuning range and (b) lock range, denoted by (top) varactor control voltage difference at the edge of lock, and (bottom) the correspondent frequency reduction from the nominal oscillation frequency, as predicted by (2.33).

noise performance. Specifically, according to (2.34), a large δ_m (large δC_{VAR}) is desirable for a higher signal gain. However, as δ_m increases, the second-order nonlinear term $-\frac{\omega_\Delta^2}{\omega_0}\cos^2(\omega_m t)$ in (2.33) becomes appreciable, which causes the oscillation frequency to drop [see Fig. 2.31(a)]. Moreover, it also modulates the locking frequency at $2\omega_m$ and distorts the output waveform severely [Fig. 2.31(b)], as the two oscillators cannot lock to a fixed frequency but a variable one. Another impediment that arises from the modulation of the locking frequency is flicker noise up-conversion. As shown in Fig. 2.32, when $\delta_m = 50$ mV, although the overall noise spectrum seems unaltered, the close-in band (shaded area) incurs clear flicker noise up-conversion, which counteracts the benefits of a higher signal gain and degrades the SNR. $\delta_m = 10$ mV is selected as a good compromise.

To characterize the sensor sensitivity in terms of $\delta f/f_0$ from the measured noise spectrum, $V_{VAR,CM}$ is employed as an intermediate variable, as adapted from [74]. Denote the VGA output as $V_{OD} = S_m \cdot \cos(\omega_m t)$. The following two quantities,

$$K_{VCO} = \frac{\partial f_0}{\partial V_{VAR,CM}}, \quad K_{TR} = \frac{1}{\delta_m}\frac{\partial S_m}{\partial V_{VAR,CM}} \tag{2.38}$$

are measurable from the frequency tuning curve [Fig. 2.29(a)] and the modulation gain plot [Fig. 2.33(a)]. The measured noise v_n in S_m can thereby be converted to the frequency noise f_n through a simple division,

$$f_n = \frac{K_{VCO}}{K_{TR}}\frac{v_n}{\delta_m/\sqrt{2}} \tag{2.39}$$

Normalizing f_n by f_0 gives the frequency sensitivity. As shown in Fig. 2.33(b), the thermal noise limited MDS is 0.2 ppm/$\sqrt{Hz}$ for air and PBS. This corresponds to a minimal detectable capacitance change of 0.0216 aF/$\sqrt{Hz}$ in PBS at 42 GHz. Despite a lower tank Q in PBS, its integrated noise is similar to air, since the QVCO $1/f^2$ noise is filtered out.
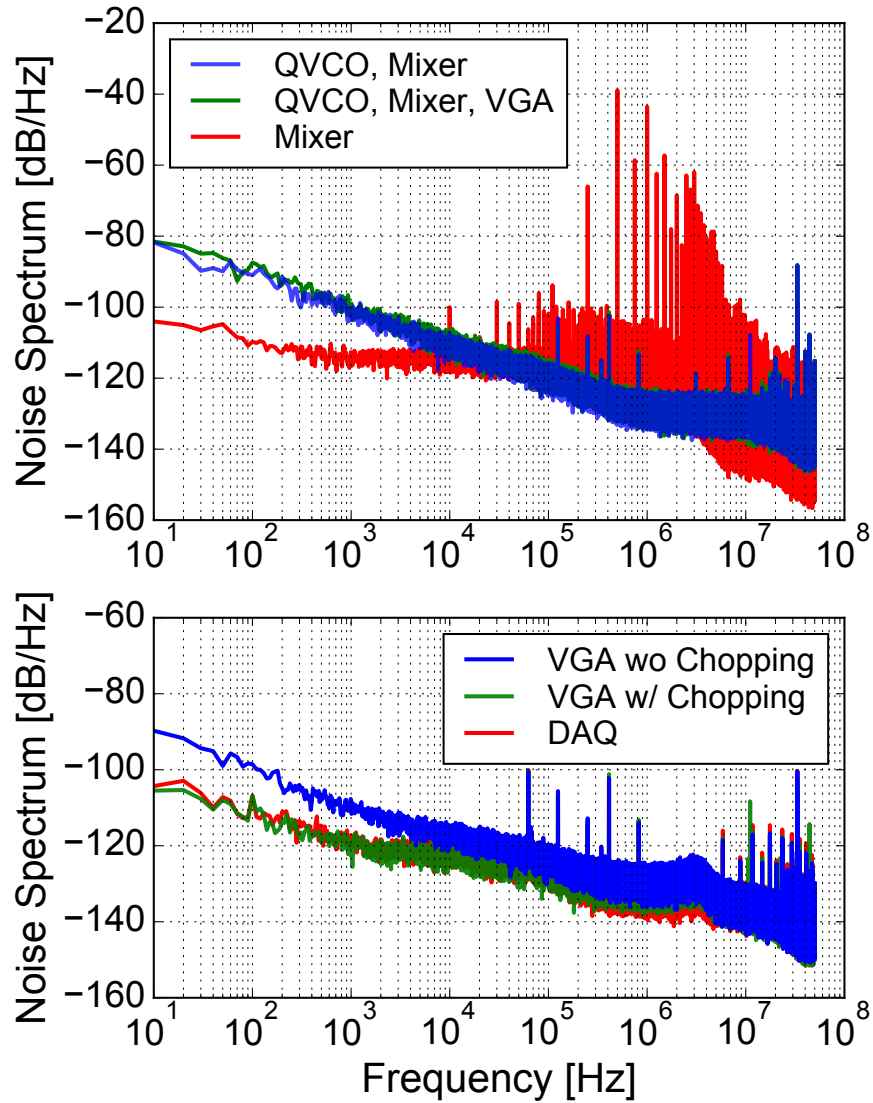
Figure 2.30: Measured output noise spectrums: (top) the entire permittivity sensor, when (blue) in lock & chopper on, (green) in lock & chopper off and (red) out of lock; and (bottom) VGA only, where the residual flicker noise comes from the off-chip data acquisition tool (DAQ).
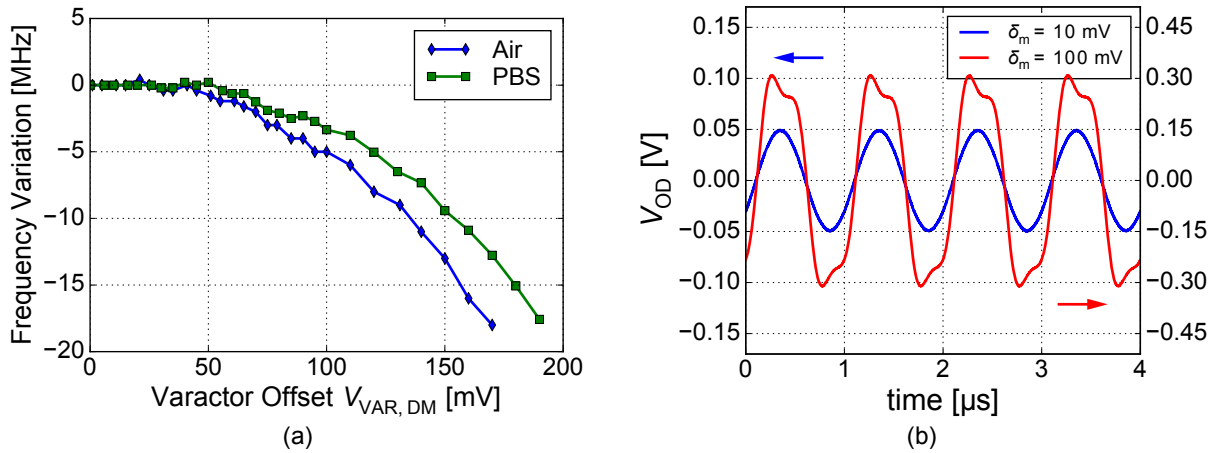
Figure 2.31: Measured (a) variation of the oscillation frequency as the varactor control difference increases ($V_{VAR,CM} = 1.35$ V), and (b) sensor output waveforms.
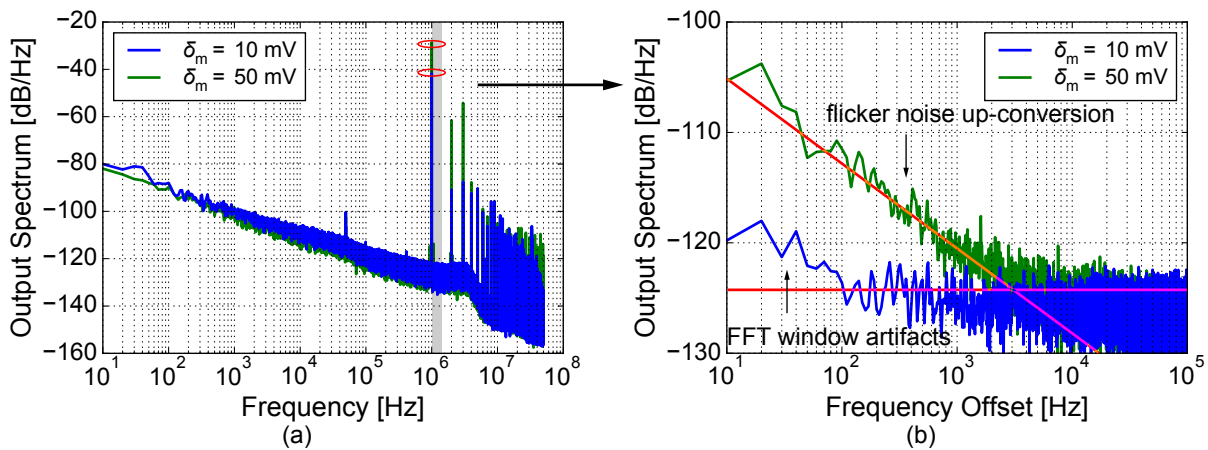
Figure 2.32: Measured sensor output spectrum at two different modulation depths, plot relative to (a) DC and (b) the modulation frequency (1 MHz).
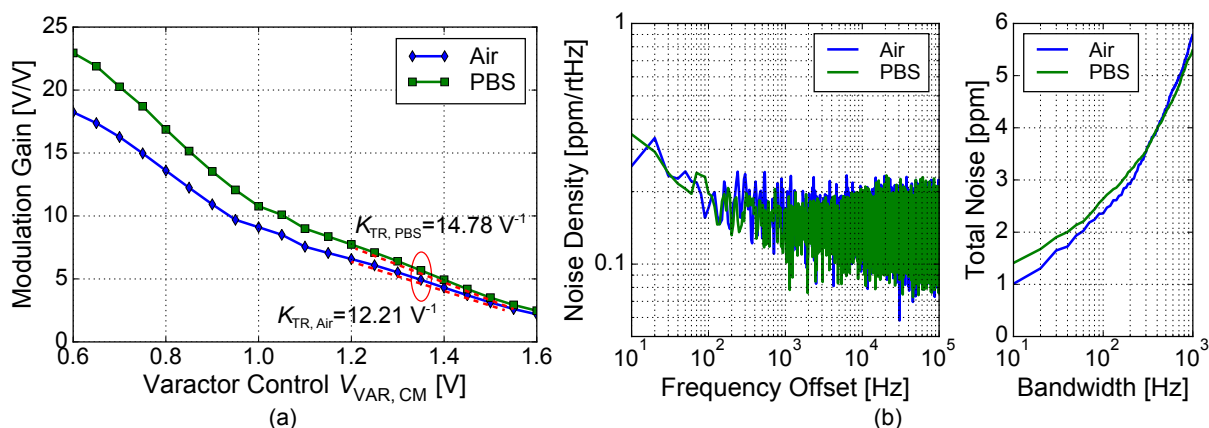
Figure 2.33: Measured (a) modulation gain S_m/δ_m, and (b) frequency noise PSD, integrated noise over different filter bandwidths.

The dynamic range of an injection-locked-oscillator based reactance sensor is determined by the lock range [21, 75], which is generally narrow. A feedback-around-sensor structure was utilized in [75] to extend the dynamic range with elevated system complexity. Here both sensing oscillators are equally exposed to the biomedium, so that their oscillation frequencies shift together when there is a dielectric change. The dynamic range is thereby decoupled from the lock range. When the measurement condition changes from air & $V_{\text{VAR, CM}} = 1.7$ V to PBS & $V_{\text{VAR, CM}} = 0.1$ V [Fig. 2.29(a)], a frequency shift of 4.7 GHz is supported by the sensing topology, corresponding to a dynamic range of more than 115 dB.

To summarize, a new QVCO-based permittivity sensing architecture is proposed, accompanied by a novel chopping technique to achieve a sensitivity level of 0.2 ppm/$\sqrt{\text{Hz}}$. Table 2.2 summaries its performance metrics and compares them with the state-of-the-art oscillator-based reactance sensors.

2.5 Biomolecular Experiments

To perform *in vitro* experiments, samples are dispensed from a pipette onto the chip. Bondwires are protected with a bio-compatible UV curable epoxy (EPO-TEK OG116-31). A small amount of the adhesive is dipped from the PCB side, which will flow towards the bondwires and cure in 30 seconds under UV light exposure to avoid contaminating the sensors.

The dispersion properties of four chemical liquids, including de-ionized water (DIW), dimethyl sulfoxide (DMSO), ethylene glycol (EG) and isopropyl alcohol (IPA), were characterized at different frequency bands by varying the cap-DAC codes. The results are summarized in Fig. 2.34. The measured sensor output in air is also provided in Fig. 2.34(a). The air value decreases as the frequency increases due to the reduction of the tank quality factor Q, even though the total tank capacitance C_T is smaller at higher frequencies. Since for air, $\epsilon' = 1$ and $\epsilon'' = 0$, the measured

Table 2.2: COMPARISON WITH OSCILLATOR-BASED REACTANCE SENSORS

Reference	Freq. [GHz]	Type	CMOS Tech.	Approach	Sensitivity [ppm]	Dynamic Range [dB]	Bandwidth [Hz]	Power [mW]
[22]'12	7-9	Dielectric	90 nm	PLL	222*	49.1	-	16.5
[23]'13	10.4	Dielectric	90 nm	PLL	15	72.3	1000	22
[75]'16	16	Dielectric	65 nm	Unilateral Injection + Phase/Field Modulation	0.57	99.3	10	16
[24]'16	60/120	Complex Dielectric	65 nm	Freq. Counting	2.67/2.87	-	100	12.2/34.8
[76]'17	0.98-6	Complex Dielectric	180 nm	Freq. Counting + CDS	2.1	-	4	10 - 24
[77]'18	1.4/3.7	Magnetic	65 nm	Freq. Counting	0.35	>62	1	5
This Work	**42**	**Dielectric**	**28 nm**	**Mutual Injection + Varactor Modulation**	**0.2**	**115**	**1**	**11.5**

*Calculated from reported $\Delta f_{\min} = 2$ MHz.
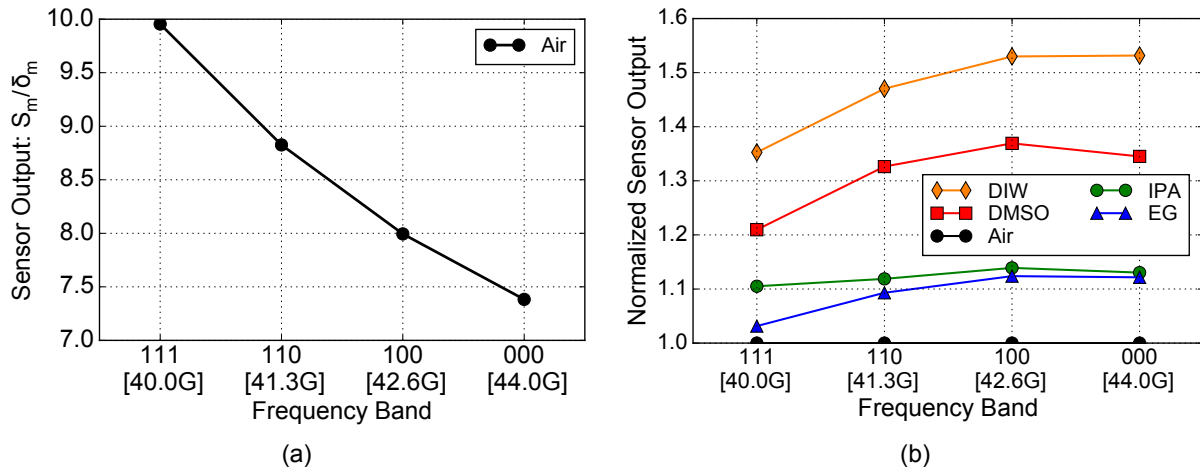
Figure 2.34: Measured dispersion characteristics of four different chemical liquids. The annotated frequency band values are measured in air.

changes across different frequencies are intrinsic to the oscillator itself, not related to the chemical liquids. Therefore, to remove such artifacts, the sensor output (S_m/δ_m) of the above four different liquids are normalized as follows

$$\frac{S_{m,\text{Air}}/\delta_{m,\text{Air}}}{S_{m,\text{liquid}}/\delta_{m,\text{liquid}}} = \frac{C_{T,\text{liquid}}}{C_{T,\text{air}}} \cdot \frac{Q_{\text{air}}}{Q_{\text{liquid}}} \tag{2.40}$$

and then plot in Fig. 2.34(b).

Another bimolecular experiment was performed to distinguish the same macromolecule (hyaluronic acid) of different molecular weight. Hyaluronic acid (HA) is a major glycosaminoglycan of the extracellular matrix, and plays an important role in various cellular interactions and physiological functions. Interestingly, the exact biological properties and physiological functions of HA depend heavily on its molecular weight. For example, high molecular weight HA (HMW-HA) is anti-inflammatory, whereas low molecular weight HA (LMW-HA) promotes inflammation. HMW-HA is effective for treating the sepsis-induced lung injury and ozone-induced AHR, whereas LMW-HA increase AHR and cause many lung disorders [78]. HA with different molecular weights can be differentiated using the multi-angle laser light-scattering method as they exhibit different refractive index increment properties [79]. It is thereby believed that they also have different dielectric properties and can be differentiated with the proposed oscillator-based dielectric sensor. To verify, HA with MW = 1.75−2 MDa (HMW-HA) and MW = 0.75−1 MDa (LMW-HA) were dissolved to 5mg/1.5mL weight concentration, and then loaded onto the sensor for characterization. As shown in Fig. 2.35, at all frequency bands they show different dielectric properties. The same experiment was repeated several times at the 40 GHz band to show such distinction is repeatable.
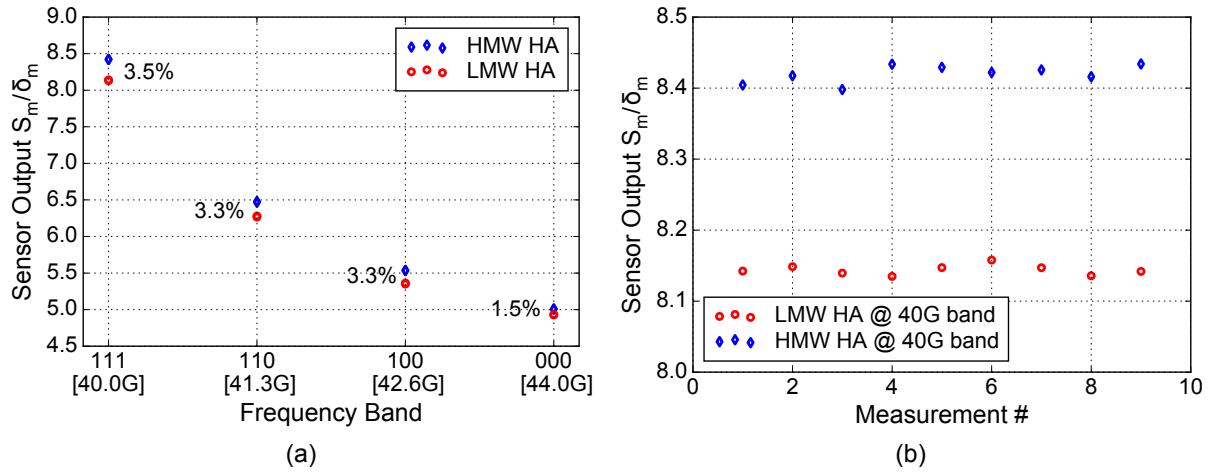
Figure 2.35: Hyaluronic acid of different molecular weights can be distinguished by the dielectric sensor.

2.6 Chapter Summary

This chapter focuses on the theoretical analysis, circuit design and performance characterization of a QVCO-based dielectric sensor. This chapter started with analyzing the operation mechanism of the proposed superharmonic QVCO architecture with an emphasis on its phase noise and quadrature accuracy performance. Following the QVCO circuit analysis, it proceeded to explain how the QVCO serves as a dielectric sensor, as well as its achievable sensitivity. Electrical measurements to characterize its circuit performance and biological experiments to demonstrate its functionality were conducted and the results were provided.

Chapter 3

Dual Modality Biomolecular Sensor

Selectivity measures the ability for a biosensor to distinguish the target analyte from other species in a complex biological medium. The best illustration of selectivity is the antigen-antibody interaction. Despite the superior sensitivity offered by oscillator-based dielectric sensors [22, 24, 75, 76], they generally suffer from a poor selectivity due to the lack of specific dielectric labels. One may argue that the broadband dielectric spectrum (10^{-6} Hz $- 10^{12}$ Hz) of different analytes must be different and thereby a good selectivity can be realized with a broadband measurement. In reality, not all the frequency ranges are equally available. For example, the low frequency signals of a conductive system are almost completely screened by the electrode polarization and Maxwell-Wagner polarization. Moreover, the biological media usually contain complex analytes so that it is not uncommon for them to share similar dielectric properties with different combinations of biological samples.

Fortunately, technology advancements permit same-chip integration of multiparametric biosensors to create a multi-dimensional fingerprint for the target analytes, which enhances the sensor selectivity and classification capabilities greatly [80–82]. For instance, [80] developed a dual-modality microfluidic device, which measures cell elongation length, deformability and electrical impedance to better classify different types of cells. A further step towards lab-on-CMOS [83–87] offers a complete system integration on a miniaturized platform to reduce parasitics and interferences. More importantly, various signal processing techniques can be applied *in situ* to enhance the sensor sensitivity. Examples include chopper stabilization in a flow cytometer [74] to alleviate sensor offsets and flicker noise, correlated double sampling (CDS) in a bioluminescence chip [88] to suppress the dark current, and Σ-Δ modulation in a fluorescence DNA chip [89] to extend the dynamic range.

Since many biomolecular interactions involve light emission with rich information, adding optical sensors helps to improve the selectivity. Compared with conventional photodiodes, single photon avalanche diodes (SPADs) are favored as they can also resolve photon arrival times with sub-ns precision, adding an additional dimension.

In this chapter, a dual-modality dielectric-optical biomolecular sensor is demonstrated. The dielectric sensor has already been introduced in Chapter 2. This chapter begins with the discussion of the overall system-level specification in Section 3.1. It then focuses on the implementation and characterization of the SPAD-based optical sensor in Section 3.2 and Section 3.3, respectively. *In*
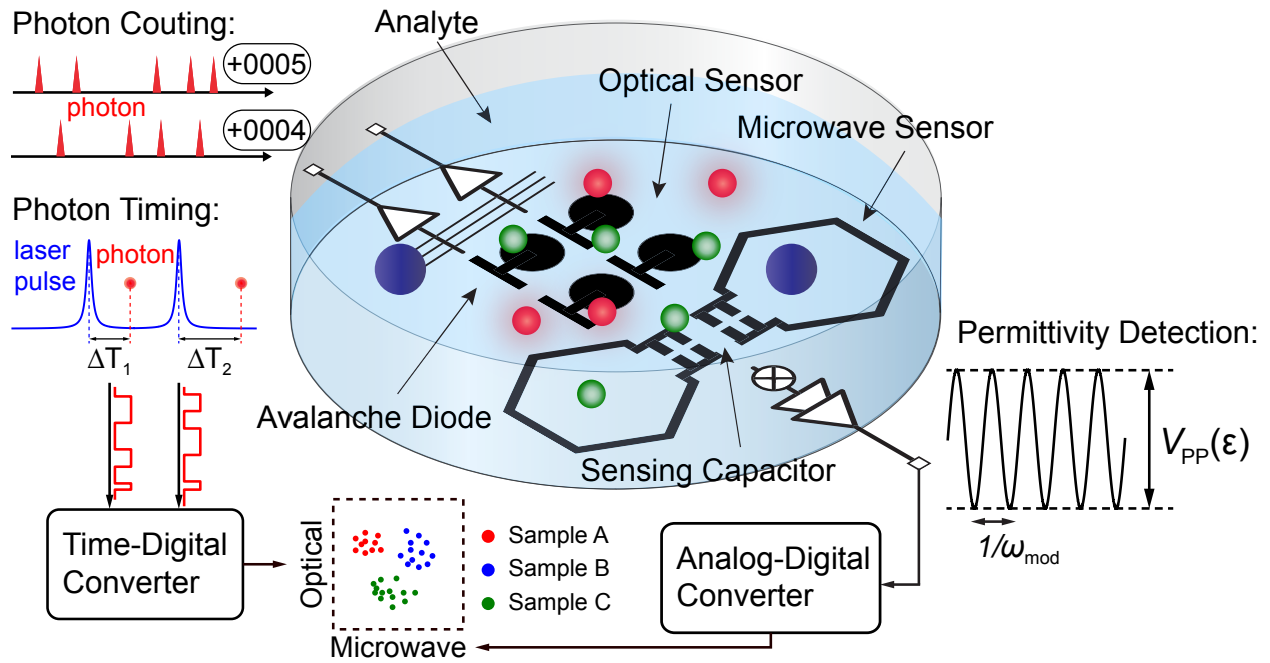
Figure 3.1: Proposed dual-modality microwave-optical biomolecular sensor.

Table 3.1: SYSTEM SPECIFICATIONS

	Dielectric Sensor	**Optical Sensor**
Transducer Type	Oscillator	Avalanche Diode
Signal Type	Permittivity	Fluorescence Lifetime
Signal Level	$\Delta\epsilon = 0.1\%$ $(\epsilon_{\text{water}} = 20$ [90])	$\tau = 1 - 30$ ns [91]
Noise Requirement	$(f_n/f)_{\text{rms}} < 4$ ppm	$t_{\text{jitter}} < 0.5$ ns

vitro experiments performed using this dual-modality biomolecular sensor are described in Section 3.4. Section 3.5 concludes this chapter.

3.1   System Architecture

Fig. 3.1 illustrates the system-level diagram of the dielectric-optical biosensing platform. The dielectric sensor utilizes a pair of sensing capacitors as part of the QVCO tank to detect the analyte permittivity, as described in the previous chapter. Meanwhile, the SPAD-based optical sensors detects the bioluminescence intensity and fluorescence lifetime to further improve the sensor selectivity. A SPAD can be viewed as an optical latch, which is triggered upon a photon absorption, so that both photon quantities and their arrival times can be measured.

To allow detection of biomolecules and their interactions, Table 3.1 lists the design specifications for each sensing modality. The minimal signal level during the biomedium analysis determines the sensor noise floor. Based on EM simulations, 1% of $|\Delta\epsilon|$ in an aqueous solution (at 40 GHz, $\epsilon_{\text{water}} = 20$) leads to $|\Delta C| = 5.22$ aF. With 54 fF total tank capacitance in this design, a 4.83 ppm frequency change needs to be resolved for measurement of 1% dielectric change with 20 dB SNR, or 0.1% change with 0 dB SNR, which sets the sensor noise floor. Similarly, since the typical fluorescence lifetimes of standard dyes are 1−30 ns, the timing jitter of the optical sensor should be kept below 0.5 ns, i.e., half of the minimal lifetime.

3.2 Optical Sensor

3.2.1 Device Implementation

A single photon avalanche diode is a p-n junction reversely biased over its breakdown voltage V_{BD} by V_{EX} (the excess bias voltage). Upon absorption of a photon, a substantial amount of current is created through impact ionization. With proper control logic, a digital transition edge is triggered at the onset of breakdown. The avalanche process is then quenched to allow detection of the next photon. Important performance metrics of SPADs are dark count rate (DCR), photon detection efficiency (PDE) and impulse response. A higher V_{EX} improves both PDE and impulse response, to the extent where the simultaneously increased DCR starts impairing SNR. In advanced processes, transistor oxide breakdown voltages limit V_{EX} as well.

Fig. 3.2 shows the cross-section view of the fabricated SPAD in 28 nm CMOS. The multiplication region is formed with p-well/deep n-well, surrounded by a native p-substrate region as the guard ring. Highly doped layers should be avoided as they increase DCR and even promote tunneling breakdown (not photon-sensitive) due to the increased defect density. The relatively stronger electric field at the edge of the junction can cause premature breakdown[92], which pushes the photon-sensitive region back to the thin junction borderline. A lower-doped guard ring is thereby employed to reduce the edge field. The device is circularly shaped for the same reason to prevent strong corner fields, which forms a 6×6 μm^2 multiplication region. The multiplication region is free of the poly-Si layer (fabricated as SiGe or metal in advanced processes) to avoid PDE reduction, which prevents making large-area SPADs due to the strict poly-Si density design rule.

3.2.2 Circuit Implementation

SPADs are biased at a high negative voltage V_{A} through the anodes to operate in the Geiger mode. The schematic of the pixel-level control logic and the signal timing diagram are shown in Fig. 3.3. The excessive bias voltage, V_{EX}, which is defined as the voltage across the SPAD in excess of its breakdown voltage V_{BD}, should be maximized for the best noise and photon detection efficiency performance. The maximal achievable V_{EX} in Fig. 3.3 is given by $V_{\text{DD}} - V_{\text{A}} - V_{\text{BD}} = V_{\text{DD}}$ since the SPAD must be turned off when $V_{\text{C}} = 0$ V. Thick-oxide transistors are used to interface with SPADs to extend the available V_{EX} to 1.8 V. An external clock CK is fed to the chip and generates
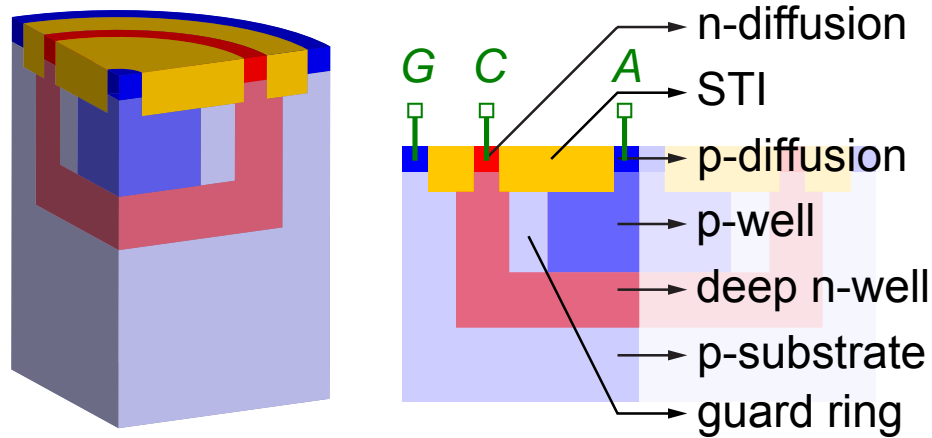
Figure 3.2: Cross-section view of the fabricated SPAD. The three contacts are A = anode, external node to a high voltage bias (negative) V_A, C = cathode, internal node (V_C in Fig. 3.3) to the readout circuit, and G = ground.

two non-overlapping phases ϕ_1 and ϕ_2 to activate/deactivate the SPAD periodically. This *CK* can also be synchronized to a pulsed laser to perform fluorescent lifetime measurements. An 8-bit delay unit ($\Delta t = 300$ ps) is inserted to allow finer timing alignment.

The pixel control circuit contains three key units: an NMOS quencher M_N, a PMOS pre-charger M_P and an edge-triggered positive feedback loop. The operation principle is as follows. As shown in Fig. 3.3(b, i), after ϕ_1 turns off M_N, the SPAD is activated by ϕ_2 through M_P. When an avalanche event starts, the current spike begins to discharge the cathode V_C, which reduces the SPAD built-in electric field, avalanche current, and eventually quenches the device. Meanwhile, through the DFF, the falling edge of V_C triggers the positive feedback to turn off M_P and turn on M_N, which expedites the quenching process to sharpen the transition edges. Moreover, the SPAD is kept off until the next activation cycle to prevent after-pulsing (which worsens DCR). If no event occurs during a preset detection window [Fig. 3.3(b, ii)], ϕ_1 will deactivate the SPAD through M_N. Both V_{Cd} and V_T can be configured for photon counting and photon timing [Fig. 3.3(b, iii and iv)]. V_{Cd} compares with its leading rising edge to measure photon arrival times, while V_T uses its trailing rising edge (created by the DFF asynchronous set S) as the reference. To reduce the counting window size, V_{Cd} is preferred when most photons arrive closer to the beginning of the detection window whereas V_T is better suitable for late photons.

3.3 Electrical Characterization

The chip is fabricated in the TSMC 28 nm bulk CMOS process, and occupies 1.2×1.0 mm^2. The prototype contains one QVCO-dielectric sensor and eight SPAD-optical sensors. The sensing capacitors are configured as part of the inductor feeds using top metal layers (M10 and AP). A
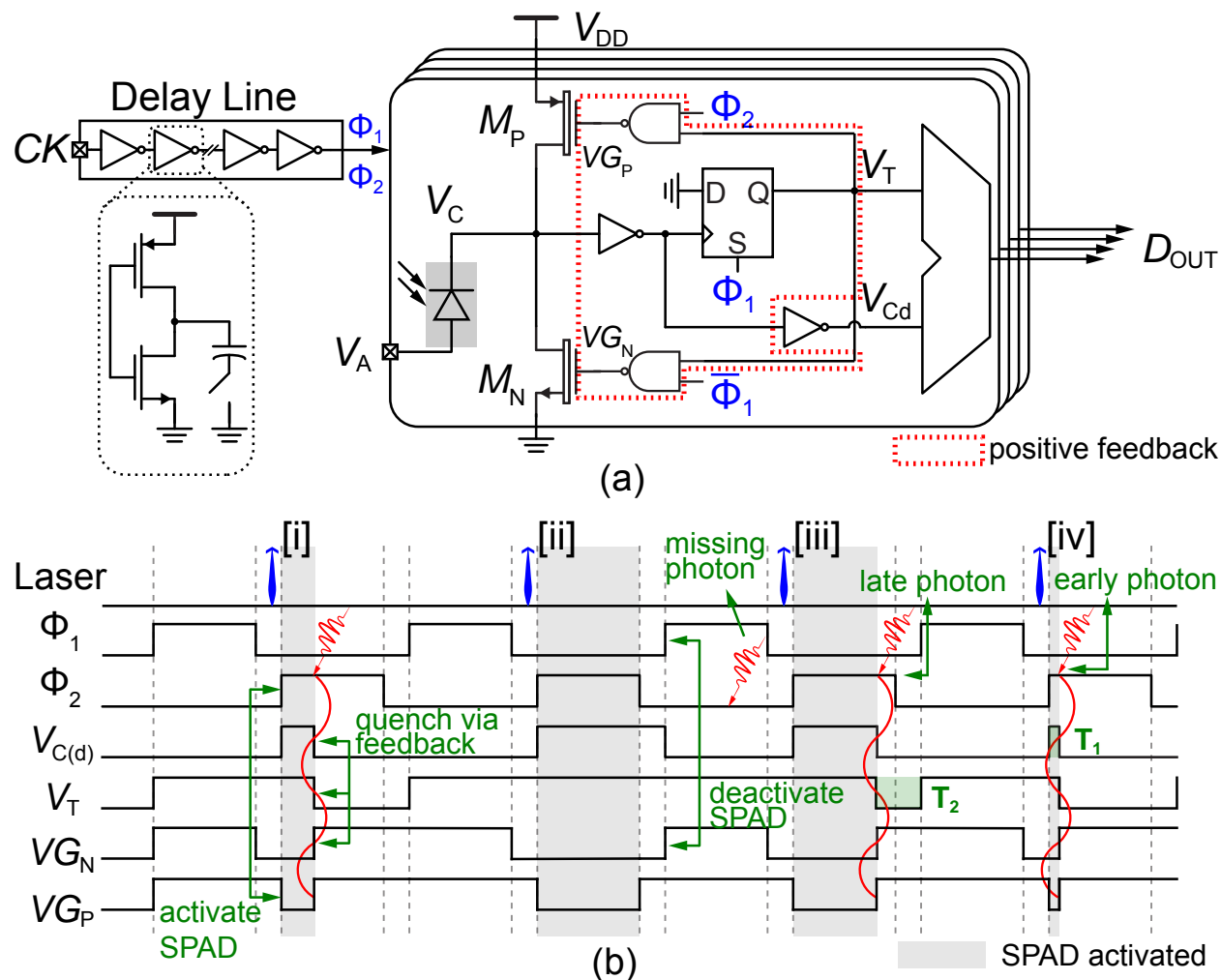
Figure 3.3: (a) SPAD circuit block diagram and (b) operation timing diagram.

bio-cavity is created by aligning a slab of drilled Polydimethylsiloxane (PDMS) to the sensor chip on the PCB. Adhesion bonding and mechanical pressure are used to prevent medium leakage. Fig. 3.4 shows the chip photo and packaging.

Since the electrical performance of the QVCO-based dielectric sensor has been provided in Chapter 2, this chapter focuses on the characterization of the SPAD-based optical sensor.

The I-V curve of the fabricated SPADs was characterized using a semiconductor analyzer (Keysight B1500A), showing a breakdown voltage of 15.3 V at room temperature.

The dark count rate (DCR) is measured at different excess biases V_{EX} by varying the anode voltage V_A. The SPAD is gated with 70% on-cycle by a 1 MHz CK signal [Fig. 3.3(a)] and an accumulated 10-second measurement is performed to allow a reliable extraction of DCR. The reported DCR in Fig. 3.5 corresponds to the measured count rate divided by 70% to calibrate out the dead time. Using the same setup, the photon detection efficiency (PDE) is measured under
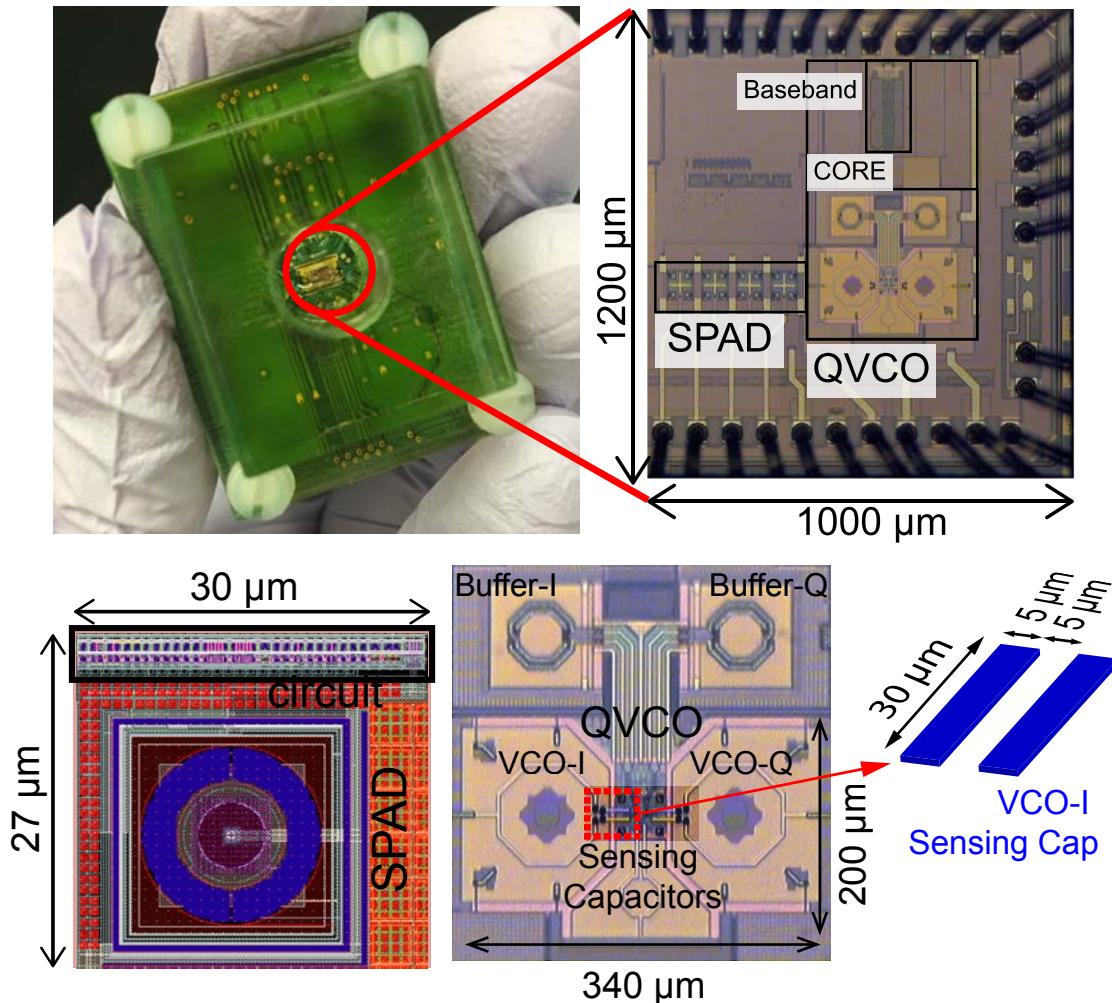
Figure 3.4: Chip micrograph and PCB packaging for bio-experiments.

three different wavelengths. The laser power is heavily attenuated by a neutral density filter before reaching the SPAD. The result is summarized in Fig. 3.6. At $V_{EX} = 1$ V, the SPAD has a DCR of 500/second and a PDE of 11.5% at $\lambda = 520$ nm.

The timing jitter of SPADs is quantified by the FWHM of its instrumentation response function (IRF), which can be characterized by repeatedly illuminating the device with a δ-like picosecond laser pulse. The time interval between the laser excitation and the SPAD output triggering edge (V_{Cd}, see Fig. 3.3) is recorded, and the resulting histogram is shown in Fig. 3.7 as the device IRF. The measurement was performed using a 300-fs laser source (IMRA FCPA μJewel D-400, frequency doubled to 522 nm) at 1 MHz repetition rate. The IRF shows a FWHM = 300 ps, representing a convolved timing uncertainty of the SPAD, readout circuits and the laser synchronization equipments. In addition to the Gaussian response, which corresponds to the photons absorbed in the multiplication region, the jitter histogram also exhibits an exponential tail, since it takes time for the carriers
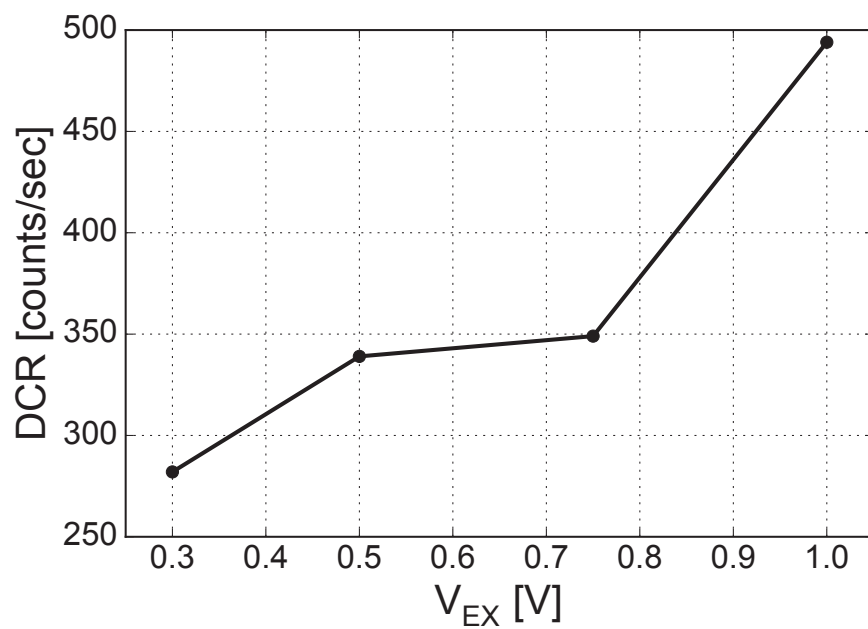
Figure 3.5: Measured dark count rates (DCR).
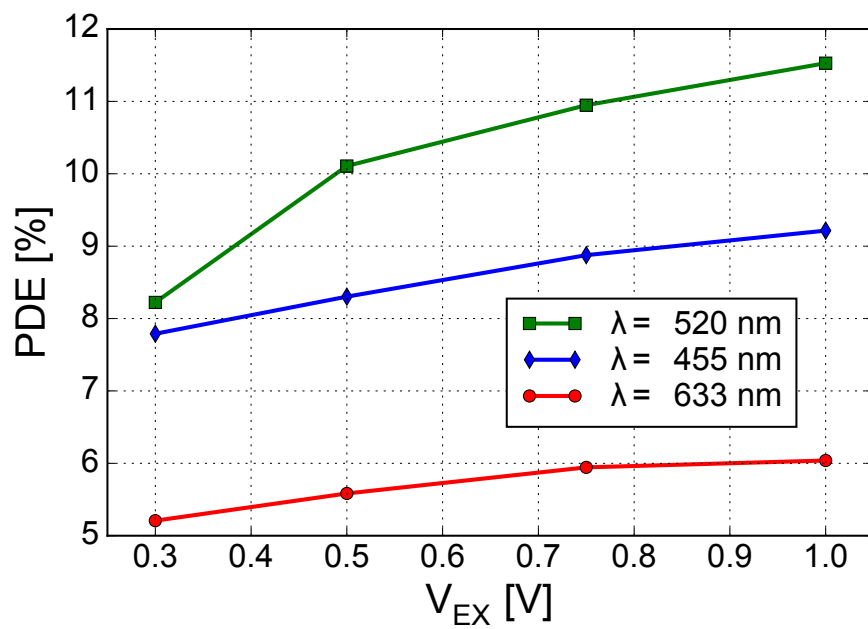
Figure 3.6: Measured photon detection efficiency (PDE).
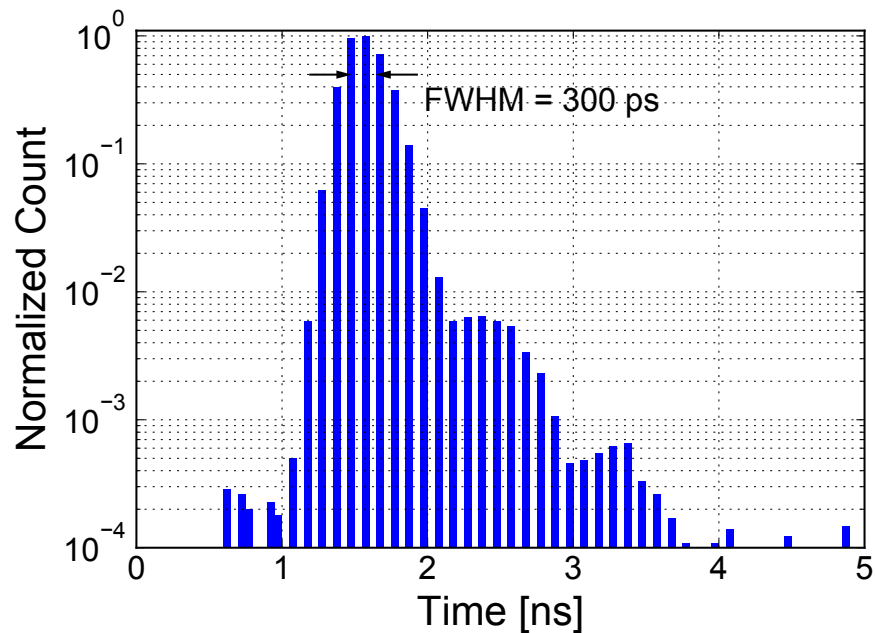
Figure 3.7: Measured impulse response function (IRF) at $V_{EX} = 1$ V.

generated outside the multiplication region to diffuse into the active region and trigger the avalanche process.

It is worth mentioning that the SPAD-based optical sensor is a first time demonstration in the 28 nm bulk CMOS process. Compared with the prior art implemented in sub-100 nm CMOS processes, it exhibits better DCR, equivalent PDE and jitter performance without any process modifications, as summarized in Table 3.2.

3.4 Biomolecular Experiments

As depicted in Fig. 3.1, both dielectric and optical signals of the same sample are collected simultaneously, which helps to improve the sensor selectivity by combining results from both sensing modalities. The dielectric signal and the photon timing information were extracted through off-chip analog-to-digital and time-to-digital conversion. All the experiments were performed in the ambient environment with an external voltage regulator.

3.4.1 Protein Denaturation

Denaturation of proteins involves the change of their three-dimensional structures and the loss of functionalities. An *in vitro* experiment is performed to demonstrate that the sensor has (i) a

Table 3.2: COMPARISON WITH SPAD IN SUB-100 NM CMOS PROCESS

Reference	Technology	Device Layer	Diameter	Breakdown voltage	DCR [cps] (V_{EX})	PDE (V_{EX})	IRF [ps]
[93]'11	90 nm Bulk	Ndiff–Psub	8 μm	10.4 V	8100 (0.13 V)	12% (0.15 V)	435
[94]'13	65 nm Bulk	Ndiff–Pwell	8 μm	9.1 V	500k (0.25 V)	5.5% (0.25 V)	235
[95]'17	40 nm Bulk*	Pwell–Deep Nwell	5.4 μm	15.5 V	50 (1 V)	30% (1 V)	170
[96]'18	28 nm FD-SOI	Pwell–Deep Nwell	25 μm	9.6 V	28k (0.3 V)	-	-
This Work	**28 nm Bulk**	**Pwell–Deep Nwell**	**6 μm**	**15.3 V**	**500 (1V)**	**11.5% (1 V)**	**300**

*Process tailored for SPAD performance, microlenses included.
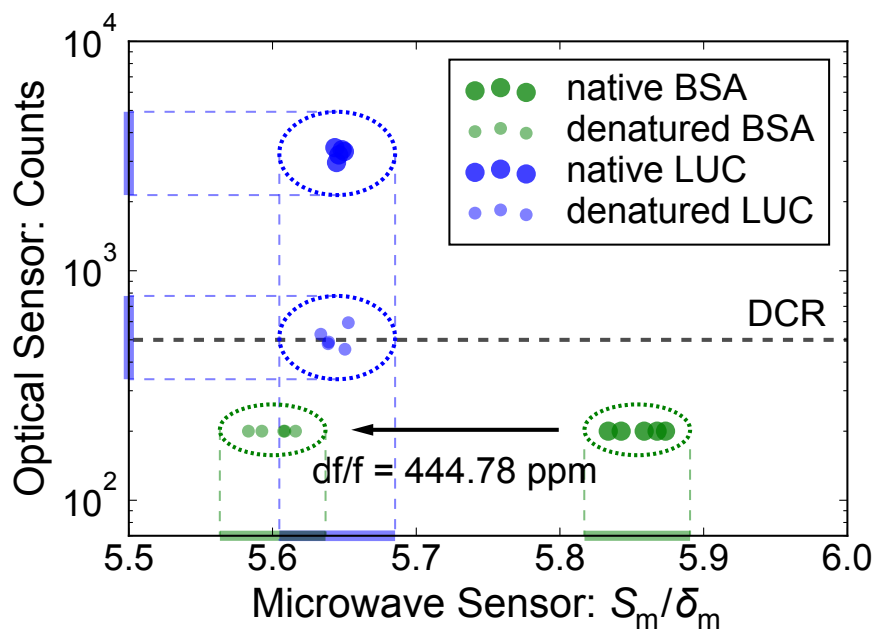
Figure 3.8: Protein thermal denaturation, BSA (x-axis) and LUC (xy-axes).

good sensitivity capable of detecting protein structural changes, and (ii) an enhanced selectivity thanks to the use of the dual-modality sensing scheme. Bovine serum albumin (BSA, 66 kDa) is dissolved in PBS to 10% weight concentration and heat-inactivated at 90°C in a sealed container. The protein solution is loaded onto the sensor before and after heating to take measurements (both at room temperature). As shown in Fig. 3.8, a frequency shift of 444.78 ppm is induced due to BSA unfolding. On the other hand, the unfolding of the enzyme luciferase (LUC, 61 kDa) is not observable because of its extremely low working concentration (0.02% weight concentration in this experiment). Alternatively, LUC catalyzes luciferin oxidation to emit light at its native state only, which allows identifying the denatured LUC with the optical sensor by measuring the luminescence intensity change (Fig. 3.8). The above experiment is repeated five times and shows consistent results. As depicted by the four clusters in Fig. 3.8, compared with using a single sensing modality, the four types of proteins (native/denatured BSA/LUC) can be completely distinguished from one another by combining the experimental data from both modalities. In other words, a multimodal strategy improves the overall sensor selectivity.

3.4.2 Fluorescence Lifetime Measurement

In addition to detecting the relative bioluminescent light intensity, the SPAD sensor also measures the absolute fluorescence lifetime to further improve the sensor selectivity. A fluorescence lifetime standard, rhodamine 6G (Rh6G) iodide solution, is used to characterize the sensor timing accuracy.
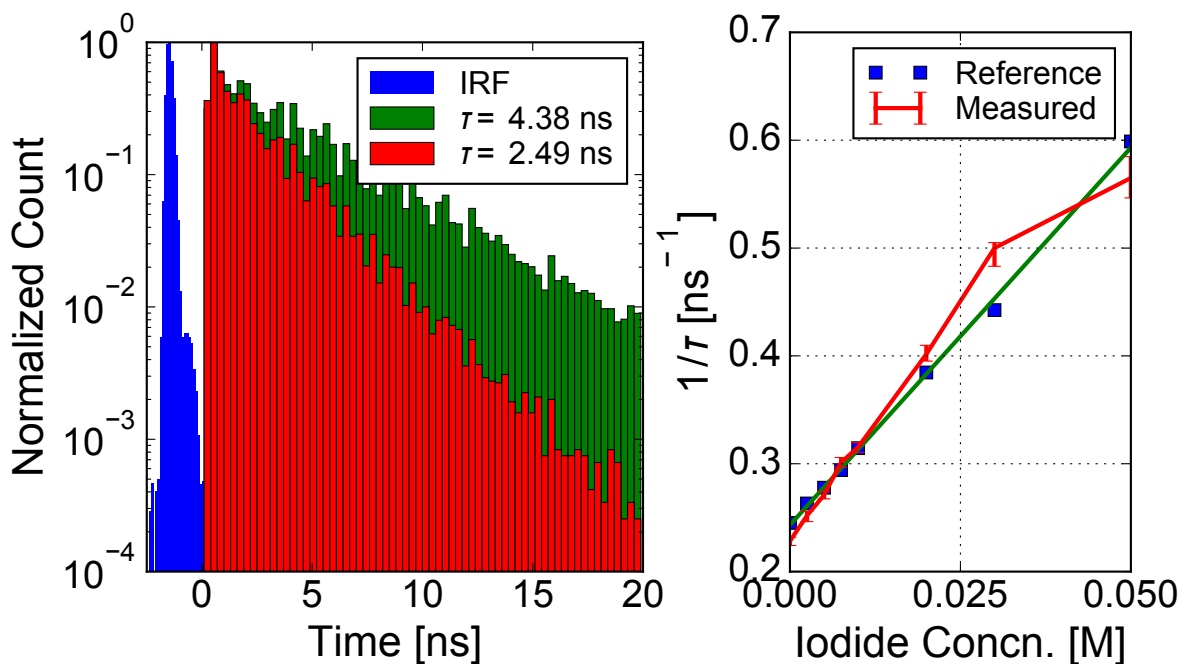
Figure 3.9: Rh6G fluorescence lifetime measurement.

Rh6G lifetime is varied from 1 to 5 ns with different potassium iodide concentrations (the overall ionic strength maintained at 0.2 M by adjusting the potassium chloride concentration). The measured lifetime values at different iodide concentrations are shown in Fig. 3.9, which closely match the literature standards in [97], since the device IRF is much narrower compared with the fluorescence exponential decay.

3.5   Chapter Summary

Given the predominant role of sensitivity and selectivity in the biosensing applications, this work presents a dual-modality dielectric-optical biosensor, which measures the permittivity change, bioluminescence intensity and fluorescence lifetime. A new QVCO-based permittivity sensing architecture is proposed, accompanied by a novel chopping technique to achieve a sensitivity level of 0.2 ppm/$\sqrt{\text{Hz}}$. The SPAD-based optical sensor is a first time demonstration in the 28 nm bulk CMOS process. Compared with the prior art, it exhibits better DCR, equivalent PDE and jitter performance without any process modifications. A protein thermal denaturation experiment confirms the sensitivity and selectivity enhancement of the dual-modality biosensing platform.

Chapter 4

Ultralow-Power Electron Paramagnetic Resonance (EPR) Spectroscopy

Although oscillator-based dielectric sensor demonstrates supreme sensitivity, a concern still exists with regard to its lack of discrimination among different species inducing permittivity changes through non-specific interactions with the constituents of the surrounding media. Adding multiple sensing modalities improves the overall sensor selectivity but also increases the system complexity. Therefore it is desirable to develop a single modality sensor that is both highly sensitive and selective.

To understand what it takes to make a highly selective sensor, use antibody-antigen interaction as an example. An antibody is a large Y-shaped protein produced by B-cells to identify and neutralize foreign objects such as bacteria and viruses. The antibody recognizes a specific part of the foreign object called the antigen. Each tip of the Y antibody has a specific site called the paratope (analogous to a lock) which only mates with one particular site (called epitope, analogous to a key) on the antigen. Such 'lock-and-key' recognition makes the antibody a biosensor with exquisite selectivity.
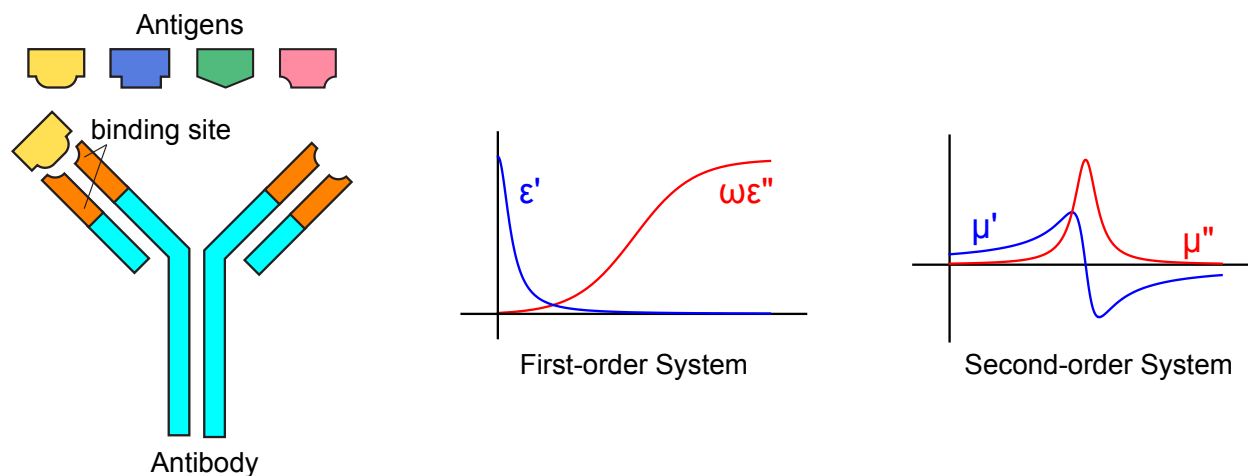
Figure 4.1: Sensor selectivity versus system order.

Mathematically, the 'lock-and-key' relationship can be represented by an impulse function, with biomolecules as the input and the sensor signal as the output. This explains why the dielectric relaxation spectroscopy is inherently of poor selectivity since it is only a first-order system, as shown in Fig. 4.1. Clearly a highly selective sensor must at least possess a second-order response, showing a resonance peak when the target is detected. However, the dielectric resonance processes typically take place in the infrared and optical portion of the spectrum (1 THz and above) for common materials [98], which makes it difficult to measure using the CMOS electronics.

Electron paramagnetic resonance (EPR) studies the interaction between the electromagnetic field and magnetic dipoles (unpaired electrons) in the presence of a static magnetic field. It exhibits a second-order resonance characteristic in the frequency range of 1−100 GHz, and the shape and location of the resonance line is uniquely determined by the target sample. Therefore, by definition, it is highly selective. EPR is widely used in various biological, medical and scientific studies, such as direct detection of radical metabolites, reactive oxygen species, determination of pO_2 level, identification of paramagnetic transition metals, etc. The EPR spectrum can be measured through impedance spectroscopic methods.

In this chapter, an ultralow-power integrated EPR spectrometer is demonstrated with high sensitivity and selectivity. Section 4.1 gives an overview of the basic concepts of EPR, with a special focus on the phenomenological equations of Bloch, which provides the theoretical support for using impedance spectroscopy to measure the EPR signal. Section 4.2 motivates the efforts of developing low-power EPR spectroscopic techniques. The system architecture, circuit implementation and measurement results of the proposed design are described in Section 4.3 and 4.4. Section 4.5 concludes this chapter.

4.1 EPR Basics

Electron paramagnetic resonance (EPR), also known as electron spin resonance (ESR) is a spectroscopic technique that studies materials with unpaired electrons. The underlying mechanism is the same as nuclear magnetic resonance (NMR), except that it detects magnetically induced splitting of electron spin states while NMR detects the splitting of nuclear spin states. This section reviews some of the fundamental concepts of the EPR spectroscopy that are pertinent to the focus of this chapter. For readers interested in this topic, a comprehensive treatise can be found in [99, 100].

4.1.1 An Isolated Spin in the Magnetic Field

4.1.1.1 Classical Treatment

Strictly speaking, 'spin' is purely a quantum mechanical quantity with no direct classical analogue. It is used here simply because this quantity associates a charged particle with the concept of both magnetic moment $\vec{\mu}$ and angular momentum $\vec{J}$.

First consider a point charge in a circular motion, which produces a current loop, as shown in Fig. 4.2. In the far field the current loop appears as a magnetic dipole with the magnetic moment $\vec{\mu}$
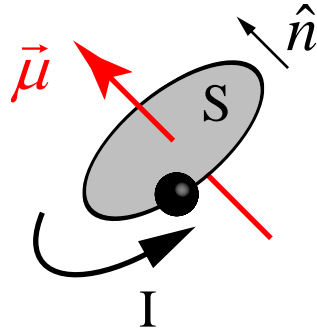
Figure 4.2: A point charge in circular motion.

given by

$$
\begin{aligned}
\vec{\mu} &= \text{current} \cdot \text{loop area} \cdot \hat{n} \\
&= \frac{qv}{2\pi r} \cdot \pi r^2 \cdot \hat{n} \\
&= \gamma \vec{J}
\end{aligned}
\tag{4.1}
$$

where $\vec{J} = mvr \cdot \hat{n}$ is the angular momentum and $\gamma = \frac{q}{2m}$ is called the gyromagnetic ratio. It is worth mentioning that for an isolated electron, the classical expression of γ does not hold exactly. In fact, the gyromagnetic ratio of a self-spinning electron is almost twice of the value for an orbiting electron. Therefore the correct γ_e is given by

$$
\gamma_e = \frac{e}{2m_e} g_e = \frac{g_e \mu_B}{\hbar}
\tag{4.2}
$$

where μ_B is the Bohr magneton and the electron g-factor $g_e = 2.0023193043617(15)$.

Now take this magnetic dipole into a static magnetic field $\vec{B_0}$, which is uniformly distributed and constant in time. According to the classical theory of electromagnetism, the magnetic field $\vec{B_0}$ will produce a torque $\vec{\tau} = \vec{\mu} \times \vec{B_0}$ on the magnetic dipole $\vec{\mu}$ and change its angular momentum at the same rate, i.e.

$$
\frac{d\vec{J}}{dt} = \vec{\tau} = \vec{\mu} \times \vec{B_0}
\tag{4.3}
$$

Combining (4.1) and (4.3), the motion of the magnetic dipole is given by

$$
\frac{d\vec{\mu}}{dt} = \gamma \vec{\mu} \times \vec{B_0}
\tag{4.4}
$$

(4.4) can be solved by transforming to a rotating coordinate system. Let S' be a second coordinate frame that rotates at an angular velocity of $\vec{\Omega}$ relative to the laboratory frame S. According to the general law of relative motion, the relationship between the time derivative of an arbitrary vector $\vec{A}$
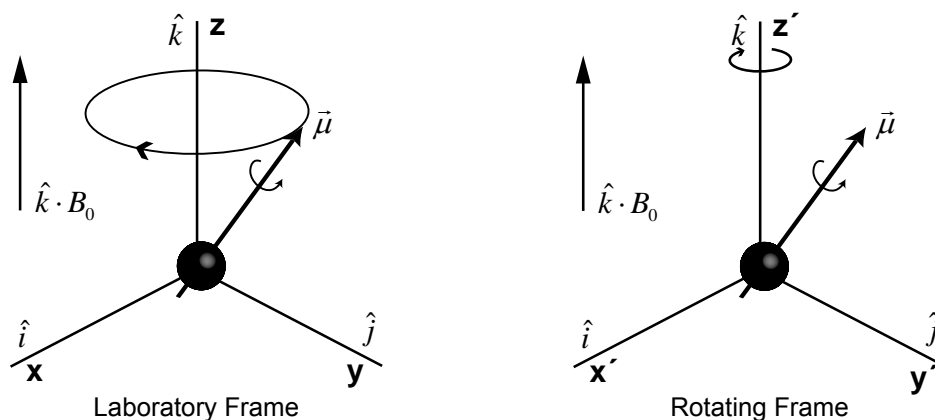
Figure 4.3: Change of coordinate frame.

computed in the laboratory frame S, denoted as $d\vec{A}/dt$, and the one computed in the rotating frame S', denoted as $\partial\vec{A}/\partial t$ is given by

$$\frac{d\vec{A}}{dt} = \frac{\partial\vec{A}}{\partial t} + \vec{\Omega} \times \vec{A} \tag{4.5}$$

Therefore, in the rotating frame S', (4.4) can be rewritten as

$$\frac{\partial\vec{\mu}}{\partial t} + \vec{\Omega} \times \vec{\mu} = \gamma\vec{\mu} \times \vec{B_0}$$

$$\text{or} \quad \frac{\partial\vec{\mu}}{\partial t} = \gamma\vec{\mu} \times \left(\vec{B_0} + \frac{\vec{\Omega}}{\gamma}\right) \tag{4.6}$$

Since $\vec{B_0} = \hat{k}B_0$ is a static field, by choosing $\vec{\Omega} = -\gamma B_0\hat{k}$, (4.6) is simplified as $\partial\vec{\mu}/\partial t = 0$. In other words, the magnetic dipole moment is held 'still' in the rotating frame, indicating that it precesses at an angular velocity of $\vec{\Omega} = -\gamma B_0\hat{k}$ in the laboratory frame. Specifically, such precession is called the 'Larmor precession' and the angular velocity γB_0 is called the 'Larmor frequency'. It is one of the most important definitions in EPR and NMR, since an rf energy packet of the exact same frequency is needed to excite the magnetic resonance, according to the quantum theory (an incredible coincidence!).

4.1.1.2 Quantum Mechanical Treatment

A rigorous quantum mechanical derivation is beyond the scope of this dissertation. Instead, a qualitative quantum mechanical picture of the spin dynamics is drawn here to provide a better intuition on the underlying principles of the magnetic resonance.

In quantum mechanics, the angular momentum is quantized. For instance, the total angular momentum of a rotating diatomic molecule can be any of the following value

$$J_{tot} = \left(I(I+1)\right)^{1/2}\hbar \tag{4.7}$$
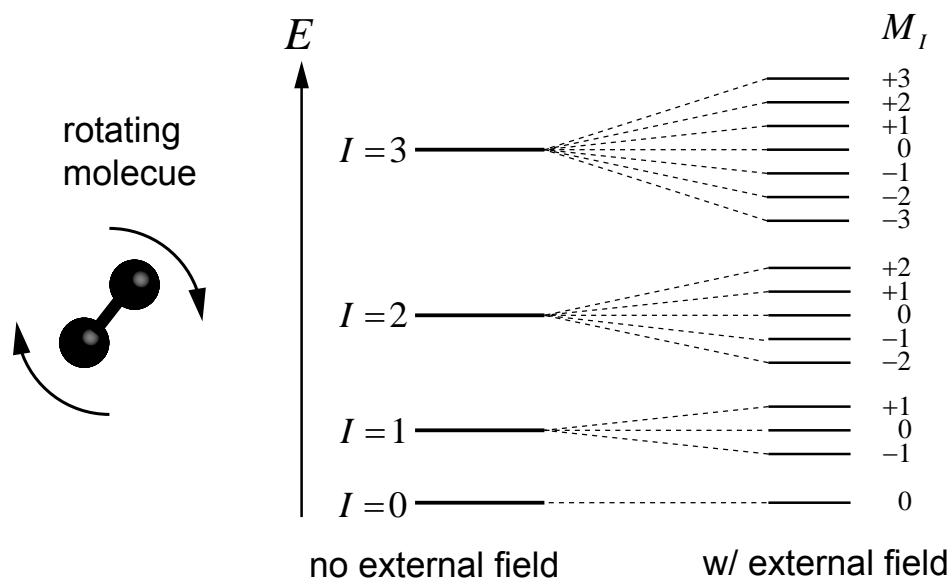
Figure 4.4: Illustration of the quantized energy levels of a rotating diatomic molecule, the degenerate states without external fields and the Zeeman splitting under an external field.

where $I = 0, 1, 2 \ldots$, and the associated rotational energy is also quantized, which takes

$$E_I = BI(I + 1) \tag{4.8}$$

where B is the rotational constant for that specific molecule. Moreover, at each energy level I, there exist a total of $(2I + 1)$ sub-states with different directions of rotation. They are specified by a second quantum number M_I which takes the values of $M_I = -I, -I + 1, \ldots, +I$. In the absence of an external field, all $(2I + 1)$ sub-states with the same I but different M_I have the same energy, meaning that they are degenerate.

Introducing an external static magnetic field will break the degeneracy, causing the $(2I + 1)$ sub-states to split into different energy levels. This is called the Zeeman splitting. Although particles tend to populate the lower energy level as explained by the Boltzmann distribution, they can be excited to the higher energy level if the correct amount of energy is provided. The transition only takes place at certain frequency values, which gives the name of magnetic resonance.

Spin is another form of angular momentum. It is the intrinsic property of the particle and always exists regardless of motion of the particle. The total angular momentum for a particle with spin takes the form of

$$J_{tot} = \left(S(S + 1)\right)^{1/2}\hbar \tag{4.9}$$

where S can either be an integer or a half-integer. For electrons, $S = 1/2$, called 'spin-1/2'.

Since a state with spin S is $(2S + 1)$-fold degenerate, the electron ground state will split into two sub-levels under an external magnetic field B_0, as sketched in Fig. 4.5. The energy difference between the two Zeeman states can be derived by solving the time-independent Schrödinger equation.
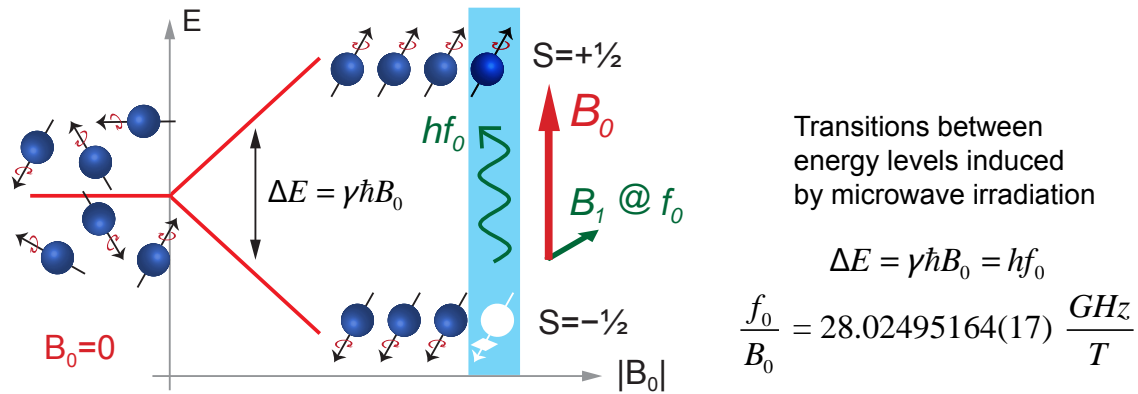
Figure 4.5: Illustration of the Zeeman splitting for a spin-1/2 system with unpaired electrons under an external magnetic field $\vec{B_0}$. The transition only happens when the frequency of the microwave energy B_1 equals to the energy gap between the two Zeeman states.

The result is directly presented here as

$$\Delta E = E_{+1/2} - E_{-1/2} = \gamma \hbar B_0 = g_e \mu_B B_0 \tag{4.10}$$

To trigger the electron paramagnetic resonance, one can apply an electromagnetic field B_1 with the frequency specified as

$$f_0 = \frac{\Delta E}{h} = \frac{\gamma}{2\pi} \cdot B_0 \tag{4.11}$$

which is the so-called Larmor frequency. Since $\gamma_e/(2\pi)$ = 28.02495164(17) GHz/T, EPR spectroscopy typically operates at 10s−100s GHz. Note that for the transition to happen, B_1 must orient perpendicular to the B_0 field, which is not obvious from this qualitative picture but can be proven with a quantitative quantum mechanical treatment.

4.1.2   Bloch Equations - A Macroscopic Perspective

In practice, the material under study contains a large number of spins and therefore a macroscopic picture that describes the magnetic resonance of spin ensembles is needed. The vector sum of the magnetic moments of all the spins is the net magnetization, i.e.,

$$\vec{M} = \sum \vec{\mu} \tag{4.12}$$

Hence (4.4) becomes,

$$\frac{d\vec{M}}{dt} = \gamma \vec{M} \times \vec{B_0} \tag{4.13}$$

However, (4.13) only holds when the spin interactions are ignored, which is not a realistic assumption.

In 1946, Felix Bloch, co-discover of NMR, proposed a set of very simple equations to describe the magnetic resonance properties for spin ensembles. Although the Bloch equations are derived

from phenomenological arguments, it provides insights for most of the magnetic resonance processes with correct quantitative predictions. It constitutes the following four heuristic arguments.

First, if the spin interactions are ignored, the motion of the net magnetization is given by $d\vec{M}/dt = \gamma \vec{M} \times \vec{B_0}$, which is the same as (4.13).

Second, in the presence of a static external field $\vec{B_0} = \hat{k}B_0$, it is reasonable to assume that M_z (where $\vec{M} = \hat{i}M_x + \hat{j}M_y + \hat{k}M_z$) tends to establish its thermal equilibrium through the following process

$$\frac{dM_z}{dt} = \frac{M_0 - M_z}{T_1} \tag{4.14}$$

where $M_0 = (\chi_0/\mu_0)B_0 = \chi_0 H_0$ is the thermal equilibrium magnetization and T_1 is called the longitudinal relaxation time or the spin-lattice relaxation time. In the expression of M_0, χ_0 represents the material static magnetic susceptibility, which can be expressed as following according to the Curie's law,

$$\chi_0 = \frac{N\gamma^2\hbar^2 I(I+1)}{3k_B T} \tag{4.15}$$

where N is called spin density (total number of spins per unit volume), k_B is the Boltzmann constant, T is the absolute temperature, and I refers to the total angular momentum quantum number ($I = 1/2$ for electrons if the orbital angular momentum is negligible).

Third, under the influence of the applied ac magnetic field $\vec{B_1} = \hat{i}B_1\cos(\omega t)$, the inter- and intra-spin interactions will inevitable cause the transverse magnetization M_x and M_y to decay, which is given by

$$\begin{aligned}\frac{dM_x}{dt} &= -\frac{M_x}{T_2}\\\frac{dM_y}{dt} &= -\frac{M_y}{T_2}\end{aligned} \tag{4.16}$$

where T_2 is called the transverse relaxation time or the spin-spin relaxation time. Usually $T_1 \approx T_2$ in liquids whereas $T_1 \gg T_2$ in solids.

The fourth argument is linear superposition. It states that in the presence of an external static dc field $\vec{B_0}$ and a much weaker ac magnetic field $\vec{B_1}$, the above three motions can be superposed, which gives rise to

$$\frac{d\vec{M}}{dt} = \gamma \vec{M} \times \vec{B} - \frac{M_x\hat{i} + M_y\hat{j}}{T_2} - \frac{M_z\hat{k} - M_0\hat{k}}{T_1} \tag{4.17}$$

Note that $\vec{B}$ is the sum of both the dc field and the ac field, i.e., $\vec{B} = \hat{k}B_0 + \hat{i}B_1\cos(\omega t)$.

Again, (4.17) can be solved by transforming to a coordinate frame S' that rotates at $\vec{\Omega} = \hat{k}\Omega_z$. The choice of Ω_z is made based on the following observation. The ac magnetic field $\vec{B_1} = \hat{x}B_1\cos(\omega t)$ can be decomposed into two rotating components, with one rotating clockwise and one counterclockwise,
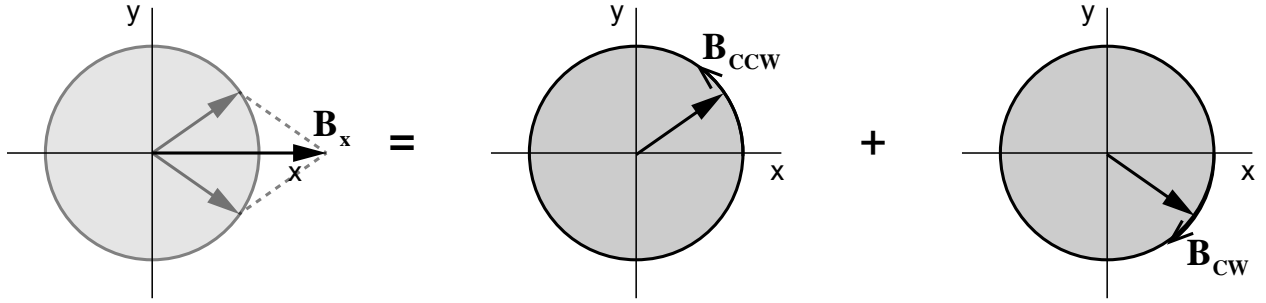
Figure 4.6: Decomposition of a linear oscillating field into two rotating fields.

as shown in Fig. 4.6

$$\vec{B}_{\mathrm{CW}} = \frac{B_1}{2}\left(\hat{i}\cos(\omega t) - \hat{j}\sin(\omega t)\right)$$
$$\vec{B}_{\mathrm{CCW}} = \frac{B_1}{2}\left(\hat{i}\cos(\omega t) + \hat{j}\sin(\omega t)\right)$$

(4.18)

Since one of the components will rotate in the same direction as the Larmor procession where the other one will be in the opposite direction, it can be shown that near magnetic resonance, the influence from the antirotating component can be neglected. Therefore, in the following discussion, only $\vec{B}_{\mathrm{CW}}$ is considered for simplicity and the angular velocity of the rotating frame S' is set to $\Omega_z = -\omega$ so that it rotates clockwise as well.

In S', the Bloch equations can be written as

$$\frac{dM_{x'}}{dt} = \gamma\left(\vec{M} \times \vec{B}_{\mathrm{eff}}\right)_{x'} - \frac{M_{x'}}{T_2}$$
$$\frac{dM_{y'}}{dt} = \gamma\left(\vec{M} \times \vec{B}_{\mathrm{eff}}\right)_{y'} - \frac{M_{y'}}{T_2}$$
$$\frac{dM_{z'}}{dt} = \gamma\left(\vec{M} \times \vec{B}_{\mathrm{eff}}\right)_{z'} - \frac{M_{z'} - M_0}{T_1}$$

(4.19)

where $\vec{B}_{\mathrm{eff}} = \hat{k}'B_0 + \hat{i}'\frac{B_1}{2} + \vec{\Omega}/\gamma$. Opening the vector cross product in (4.19) leads to

$$\frac{dM_{x'}}{dt} = +\gamma M_{y'} \cdot \left(B_0 + \frac{\Omega_z}{\gamma}\right) - \frac{M_{x'}}{T_2}$$

(4.20a)

$$\frac{dM_{y'}}{dt} = +\gamma\left(M_{z'} \cdot \frac{B_1}{2} - M_{x'}\left(B_0 + \frac{\Omega_z}{\gamma}\right)\right) - \frac{M_{y'}}{T_2}$$

(4.20b)

$$\frac{dM_{z'}}{dt} = -\gamma M_{y'} \cdot \frac{B_1}{2} - \frac{M_{z'} - M_0}{T_1}$$

(4.20c)

As $B_1 \to 0$, the transverse magnetization $M_{x'}$ and $M_{y'}$ will vanish when a sufficiently long time has elapsed. From (4.20c), the longitudinal magnetization $M_{z'}$ at the steady state only differs

from M_0 by an infinitesimal of order B_1^2. With the weak ac field assumption, i.e., $B_1 \ll B_0$, it is safe to replace $M_{z'}$ in (4.20b) by M_0. Additionally, (4.20) can be further simplified by introducing $M_+ = M_{x'} + iM_{y'}$ and adding (4.20a) to $i \times$(4.20b), which leads to

$$\frac{dM_+}{dt} = -M_+ \cdot \left(i\gamma \left(B_0 + \frac{\Omega_z}{\gamma} \right) + \frac{1}{T_2} \right) + i\gamma M_0 B_1 / 2 \tag{4.21}$$

This can be readily solved, which yields

$$M_+ = A e^{-\alpha t} + \frac{i\gamma M_0 B_1 / 2}{1/T_2 + i(\gamma B_0 + \Omega_z)} \tag{4.22}$$

where $\alpha = 1/T_2 + i(\gamma B_0 + \Omega_z)$. Neglect the exponential decay term, define $\omega_0 = \gamma B_0$, and use $M_0 = (\chi_0/\mu_0)B_0$, $\Omega_z = -\omega$, the steady state solution of (4.22) can be written as

$$\begin{aligned}
M_{x'} &= \chi_0 \frac{\frac{1}{2}\omega_0 \Delta\omega T_2^2}{1 + (T_2\Delta\omega)^2} \cdot \frac{B_1}{\mu_0} \\
M_{y'} &= \chi_0 \frac{\frac{1}{2}\omega_0 T_2}{1 + (T_2\Delta\omega)^2} \cdot \frac{B_1}{\mu_0}
\end{aligned} \tag{4.23}$$

where $\Delta\omega = \omega_0 - \omega$. The transverse magnetization is static in the rotating reference frame S' and thereby rotates in the laboratory frame at the rate of $\Omega_z = -\omega$. To transition back to the laboratory frame, use

$$M_x = M_{x'}\cos(\omega t) + M_{y'}\sin(\omega t) \tag{4.24}$$

In addition, since the complex magnetic susceptibility $\chi = \chi' - i\chi''$ is defined as

$$M_x = \left(\chi'\cos(\omega t) + \chi''\sin(\omega t) \right) \frac{B_1}{\mu_0} \tag{4.25}$$

Combining (4.23), (4.24) and (4.25) yields

$$\chi' = \frac{\chi_0}{2} \frac{\omega_0 \Delta\omega T_2^2}{1 + (T_2\Delta\omega)^2} \tag{4.26a}$$

$$\chi'' = \frac{\chi_0}{2} \frac{\omega_0 T_2}{1 + (T_2\Delta\omega)^2} \tag{4.26b}$$

To this point, with the Bloch equations, it is shown that the spin ensembles will possess an ac magnetic susceptibility when they are exposed to an oscillating magnetic field B_1 and a static magnetic field B_0, provided that B_1 and B_0 are orthogonal to each other, and that the oscillation frequency of B_1 satisfies $\omega = \omega_0 = \gamma B_0$, which is the 'Larmor frequency'. The ac magnetic susceptibility also emerges in the vicinity of the Larmor frequency. Fig. 4.7 illustrates the shape of the complex magnetic susceptibility.
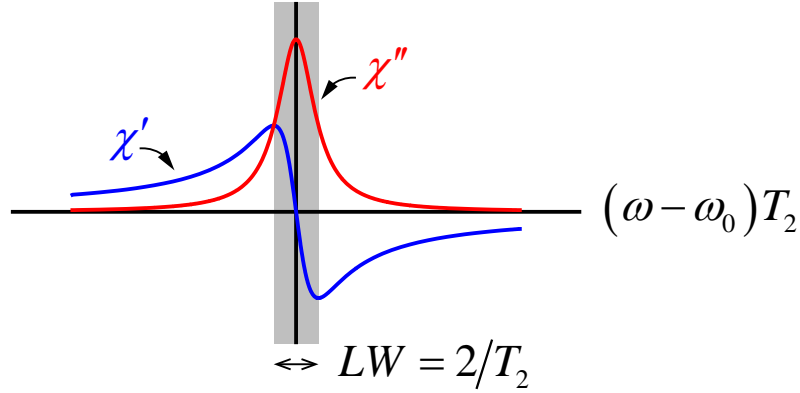
Figure 4.7: Complex susceptibility of spin ensembles from the Bloch equations.

More importantly, (4.26) essentially provides a theoretical basis for using impedance spectroscopy to detect the magnetic resonance. Specifically, if an inductor coil is filled with an ensemble of spins, with an external dc magnetic field B_0, its inductance L will become

$$L = L_0\big(1 + \chi(\omega)\big) \tag{4.27}$$

where L_0 is the inductance in the absence of B_0. Taking the coil resistance R_0 into account, the coil impedance Z can be written as

$$
\begin{aligned}
Z &= i\omega L_0(1 + \chi' - i\chi'') + R_0 \\
  &= i\omega L_0(1 + \chi') + (\omega L_0 \chi'' + R_0)
\end{aligned}
\tag{4.28}
$$

Since χ' and χ'' are always related, only one of the two quantities needs to be measured and the other one can be computed accordingly. According to (4.28), χ' can be directly obtained if the coil inductance can be measured in the vicinity of the Larmor frequency, which falls into the regime of impedance spectroscopy.

On the other hand, it is also possible to obtain χ'' first through the absorption spectroscopy. Assume the magnetic field B_1 produced by the current $i = I\cos(\omega t)$ that flows in the inductor coil is uniform and takes a volume of V_c. The peak energy stored in this volume is given by

$$\frac{1}{2}L_0 I^2 = \frac{1}{2\mu_0}B_1^2 V_c \tag{4.29}$$

Therefore the average power dissipated in the spin ensembles is

$$
\begin{aligned}
\overline{P} &= \frac{1}{2}I^2 \cdot (\omega L_0 \chi'') \\
&= \frac{1}{2\mu_0}\omega\chi'' B_1^2 V_c
\end{aligned}
\tag{4.30}
$$

This equation provides a direct connection between the absorbed power, χ'' and the strength of the alternating field, which is widely used as the basis of calculating χ'' in the existing laboratory EPR instrumentation. Obviously it is difficult to scale down this second method to the integrated CMOS platform, whereas the first method of direct assessment of the coil inductance can be realized with a thoughtful design, which will be discussed in the following sections.

4.1.3   Spin-Orbit Interaction

The analysis so far places the spin ensembles in the free space, neglecting all the surrounding particles of different kinds. To study the EPR spectrum of a particular molecule, one needs to put the electron back to the molecule and consider the interaction between the electron and atomic nucleus. Since the electron will orbit around the atomic nucleus, it also possesses some orbital angular momentum $\vec{L}$, in addition to its intrinsic spin angular momentum $\vec{S}$. Its total angular momentum $\vec{J}$ changes to $\vec{J} = \vec{L} + \vec{S}$.

For electrons in free space, $\vec{J} = \vec{S}$, with (4.1) and (4.2), it results in

$$\vec{\mu}_{\mathbf{S}} = \frac{\mu_B}{\hbar} g_e \vec{S} \tag{4.31}$$

For electrons in the molecule, $\vec{J} = \vec{L} + \vec{S}$, the angular momentum becomes

$$\begin{aligned}
\vec{\mu}_{\mathbf{J}} &= \vec{\mu}_{\mathbf{S}} + \vec{\mu}_{\mathbf{L}} \\
&= \frac{\mu_B}{\hbar} \left(g_e \vec{S} + g_L \vec{L} \right) \\
&= \frac{\mu_B}{\hbar} g_J \vec{J}
\end{aligned} \tag{4.32}$$

where g_J is the Landé g-factor. It is common practice to assume that the spin-orbit coupling induced angular momentum $\vec{L}$ is proportional to $\vec{S}$, and (4.32) can be reorganized as

$$\vec{\mu}_{\mathbf{J}} = \frac{\mu_B}{\hbar} (g_e + \delta g) \vec{S} = \frac{\mu_B}{\hbar} g \vec{S} \tag{4.33}$$

The Zeeman transition energy in (4.10) becomes

$$\Delta E = g \mu_B B_0 = (g_e + \delta g) \mu_B B_0 \tag{4.34}$$

and thereby the resonance Larmor frequency changes. The magnitude of δg depends on the size of the atomic nucleus. The $g-$factors of organic free radicals with only C, N, O and H atoms will be very close to g_e, whereas transition metals can have a $g-$factor that is much larger than g_e.

The exact value of the $g-$factor, measured by the resonance Larmor frequency at a given dc magnetic field, can be used to identify different molecules, making EPR a molecular analytical tool with supreme selectivity. In addition to the $\vec{L} - \vec{S}$ coupling, other types of interactions, such as hyperfine coupling (a stronger version of spin-orbit interaction) and spin-spin coupling, are not uncommon. As a result, the EPR resonance frequency and the shape of the spectrum (e.g., linewidth, number of peaks and etc.) provide fruitful information for the study of molecular properties.

4.2 Motivation

EPR has been established as the most powerful technique for studying free radicals and other paramagnetic species, such as reactive oxygen species and transition metal ions, in the biological systems. It is capable of providing various physiological and metabolic information from tissues, such as redox status, cell viability and tissue perfusion. Sharing similar detection principles with magnetic resonance imaging (MRI), EPR offers several orders of magnitude higher sensitivity by operating at a higher frequency.

Despite these advantages, EPR is predominantly used in the scientific laboratories and has not yet advanced to the clinical practices. One major obstacle is associated with the existing EPR instrumentation, which is bulky, expensive and extremely complicated to operate, and thereby restricts its deployment to many clinical settings, such as point-of-care or body implants.

With the rapid development of (Bi)CMOS technologies, several integrated EPR spectrometers have been demonstrated [63, 101, 102]. In [101], an RF transceiver was implemented to detect the absorption of microwave energy by EPR. However, it consumes 2W of power, which causes significant heating and undesired interference with the radical EPR responses. On the other hand, oscillator-based EPR spectrometers [63, 102] were reported with a better energy efficiency. In the latter case, it measures the change of the radical magnetic permeability caused by EPR, which is manifested as the change of the oscillation frequency. The sensitivity, however, is affected by the temperature drift and transistor flicker noise, which also change the oscillation frequency.

A clinically useful EPR spectroscopy demands both high sensitivity and high energy efficiency. To meet these goals, this chapter proposes a new sensing topology to simultaneously improve the detection limit and power efficiency. To minimize the transducer noise contribution, a passive *LC* resonator is employed to measure the EPR induced magnetic permeability change. An RF source is capacitively injected to the resonator to excite EPR, and then a self-mixing interferometric phase detection is performed to extract the EPR signal as well as to cancel out the noise from the RF source. The low-frequency temperature drift and flicker noise from the readout circuity are canceled by on-off modulating the injection source. As a validation, a 14 GHz EPR spectrometer prototype was fabricated in the 28 nm CMOS process, which achieves 6.1×10^8 spins/rtHz sensitivity with only 1.12 mW power consumption, over 10× better than the existing single-chip EPR spectrometers.

4.3 System Architecture

One of the key conclusion drawn from the Bloch equations in the previous section is that the EPR spectrum of a paramagnetic species can be expressed as an ac magnetic susceptibility χ' in the vicinity of the Larmor frequency. Furthermore, χ' can be obtained by measuring the inductance variation of a sensing coil positioned in contact with the paramagnetic species, as shown in Fig. 4.8.

To measure the change of inductance around f_0 (14 GHz in this work) with a high sensitivity, a capacitively coupled *LC* tank is utilized as the sensing frontend, which is shown in Fig. 4.9. The tank capacitor C_T and the injection capacitor C_{IJ} in parallel resonate with the sensing inductor L at f_0, which forces a quadrature relation between the tank output V_{LC} and the injection input V_{IJ}. At
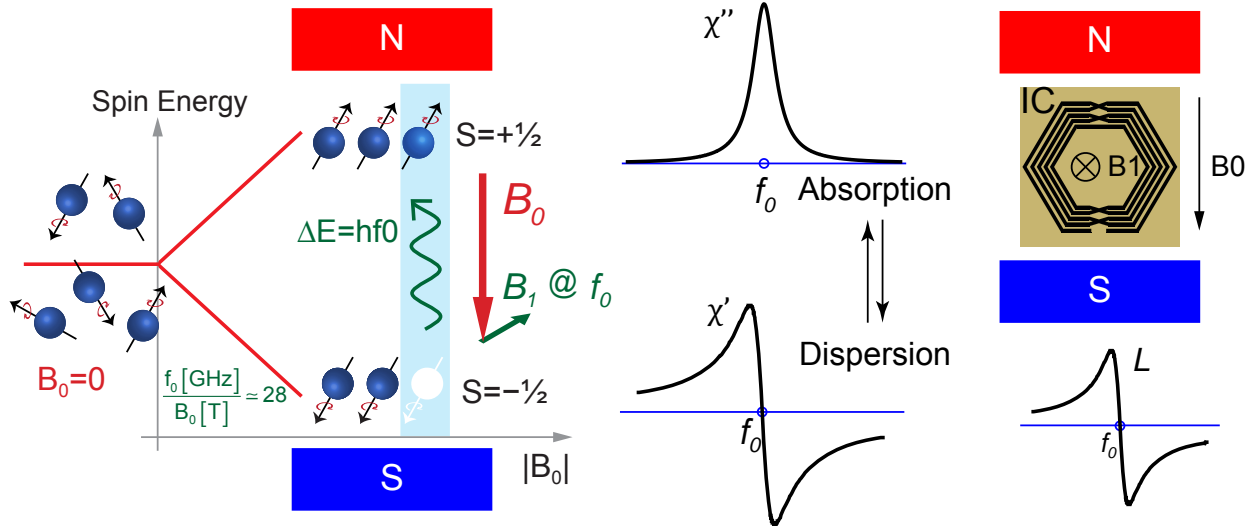
Figure 4.8: Principle of EPR spectroscopy and the equivalence between the absorption EPR spectrum and the dispersion EPR spectrum. The latter allows EPR to be measured as the change of the inductance.

$f = f_0 + \delta f$, the relation between V_{LC} and V_{IJ} around f_0 can be derived as

$$\left\| \frac{V_{LC}}{V_{IJ}} \right\| = Q \frac{C_{IJ}}{C_T} \tag{4.35}$$

and

$$\angle \frac{V_{LC}}{V_{IJ}} = Q\left(\frac{\delta f}{f_0} + \frac{\delta L}{2L_0} \right) + \frac{\pi}{2} \tag{4.36}$$

where $\delta L = L_0 \cdot \chi\prime$.

As the frequency of V_{IJ} is swept in the vicinity of f_0, the relative phase difference between V_{LC} and V_{IJ} deviates from 90° by a quantity that is proportional to both δL and δf, multiplied by a gain-boosting factor equal to the tank qualify factor Q, as indicated in (4.36). In this work, the simulated $Q = 20.8$.

Because the inductance only changes in the presence of B_0, two measurements with $B_0 = 0$ T and $B_0 = 0.5$ T are sufficient to extract the EPR signal $\chi\prime$, i.e.,

$$\theta_{B_0 \neq 0} = Q\left(\frac{\delta f}{f_0} + \frac{\delta L}{2L_0} \right)$$
$$\theta_{B_0 = 0} = Q\left(\frac{\delta f}{f_0} \right) \tag{4.37}$$

where θ is the quadrature difference between V_{LC} and V_{IJ}, and the sensor output is proportional to $\sin(\theta)$, as depicted in Fig. 4.9.

To extend the sensing volume, L should be maximized without sacrificing the tuning range. Moreover, according to (4.35), the ratio between C_{IJ} and C_T should be selected to equalize the
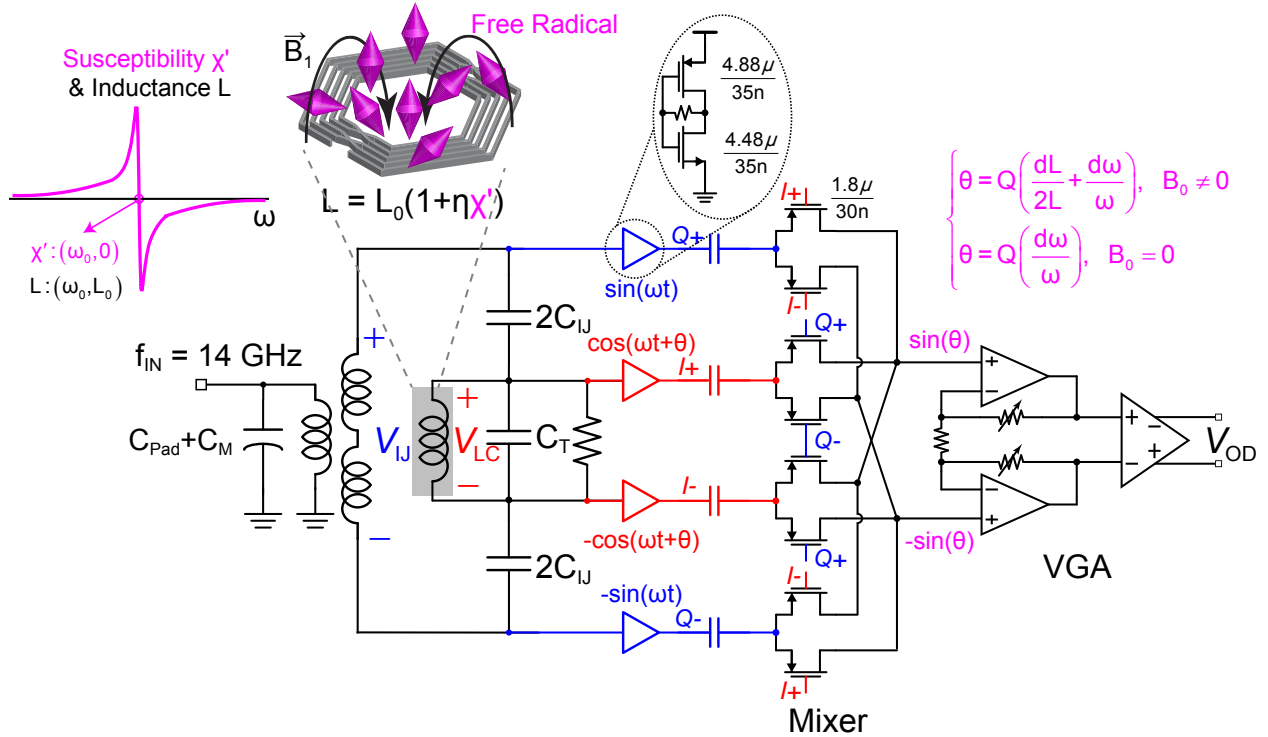
Figure 4.9: System block diagram.

relative amplitude between V_{IJ} and V_{LC}, so that the propagation delays of the subsequent mixer drivers are matched to avoid introducing extra phase error. In this work, $L = 1$ nH and $C_T/C_{IJ} = 20$. A double-balanced voltage-commutative passive mixer is employed to convert the aforementioned phase signal into voltage, which is then amplified by a VGA and fed to an external ADC.

Compared with oscillator-based inductor sensing solutions [63, 102–104], the proposed method eliminates the noisy transistors, thereby exhibiting a much better sensitivity and immunity against the temperature and supply variations. In addition, self-mixing based phase detection [26] is performed, which not only brings a free transducer gain of Q before any amplifier stages, but also cancel out the phase noise from the injection source. In addition, since the EPR signal is down-converted to dc, the offset and flicker noise from the mixer and VGA are of great concern. To avoid SNR degradation, system-level chopping is applied by on-off modulating the 14 GHz injection signal at 50 kHz to shift the signal frequency above the flicker corner. The residual noise is solely the thermal noise of the coil and mixer/VGA, which can be attenuated by averaging.

In addition to noise, another critical factor that affects SNR is the orientation of B_0. Since EPR demands that B_1 be perpendicular to B_0, while the B_1 fields created by a planar inductor extend to all directions, as depicted in Fig. 4.10, a filling factor η is introduced ($\delta L = L_0 \cdot \eta \chi\prime$, $\eta < 1$) to account for the signal loss. EM simulations were used to identify the optimal B_0 direction that maximizes η. It was found that when B_0 orients along the inductor feeds (the y axis in Fig.4.10), η reaches $\eta_{max} = 0.32$. Moreover, the effective sensing volume can be estimated from the distribution
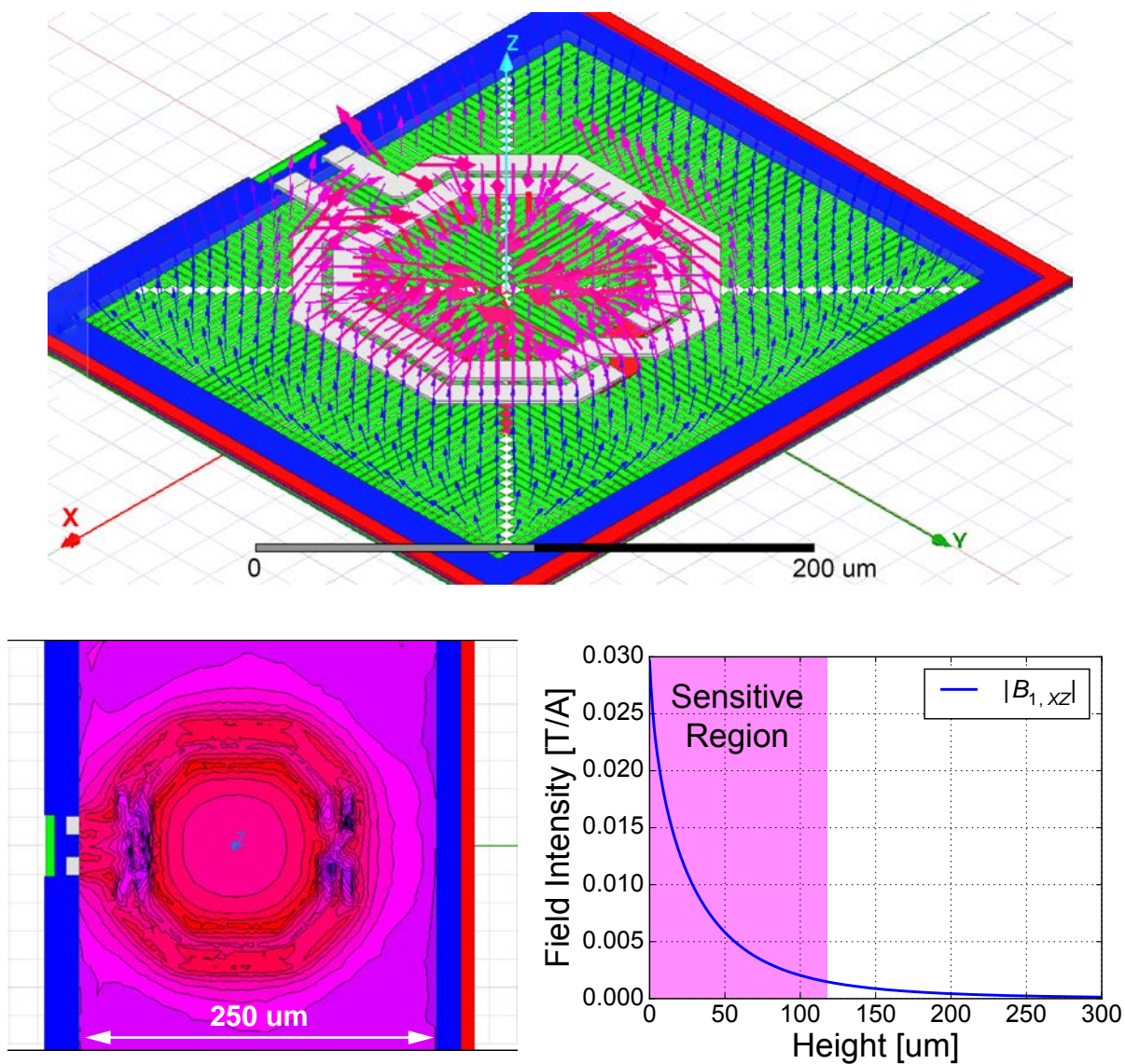
Figure 4.10: HFSS simulation results of the 3-dimensional B_1 fields created by the sensing coil (top), and the distribution of B_{1x}, B_{1z} components (bottom), which illustrates the effective sensitivity volume.
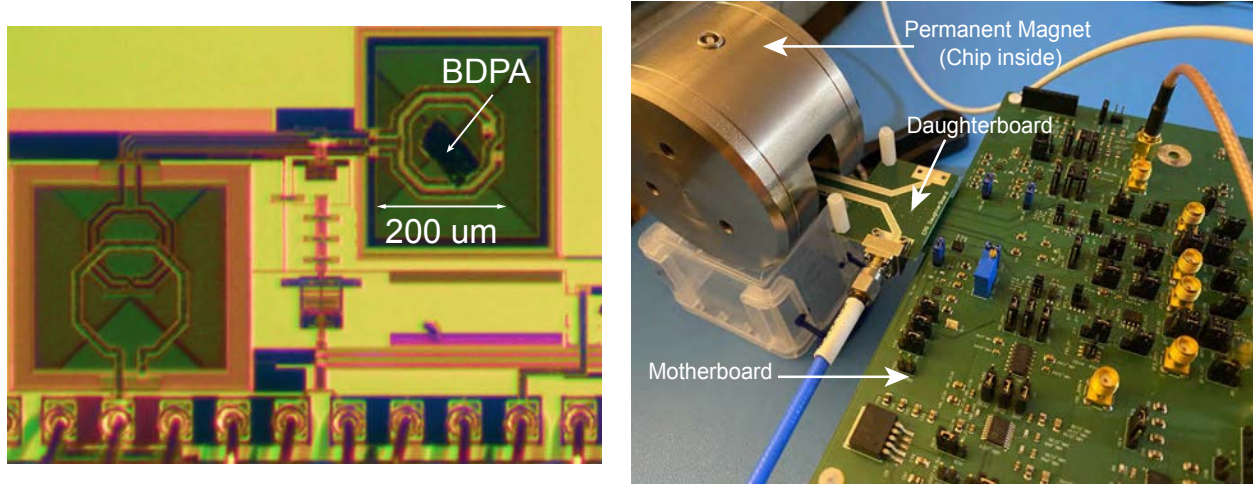
Figure 4.11: Chip micrograph with a BDPA sample (left) and measurement setup (right). Sample deposited in the center of the sensing inductor following the procedure in [105].

of B_{1x} and B_{1z}, as shown in Fig. 4.10, which is approximately 7.5 nL.

4.4 Measurement Results

A sensor prototype was fabricated in the 28 nm CMOS process. Fig. 4.11 gives the chip micrograph and the experimental setup. For optimal power and linearity performance, the supply voltage of the RF and BB domains are set to 0.6 V and 1.2 V, respectively. The entire chip consumes 1.12 mW. A compact 0.5 T permanent magnet ($80\times80\times55$ mm^3) is used to provide a uniform B_0 field. The chip was positioned inside the magnet with a proper orientation according to the above description. A 50 kHz 9 dBm pulse-modulated injection signal was generated off-chip and coupled to the sensor through a wide-band on-chip transformer. The chip was back-lapped to a thickness of 150 μm to reduce the bond-wire inductance. HFSS/Spectre co-simulation was performed to include the bond-wire impact, the estimated differential amplitude of the injection signal at the sensor input V_{IJ} (Fig. 4.9) is 0.85 V.

An *in-vitro* bio-experiment was performed using crystalline BDPA, an organic radical. BDPA was deposited at the center of the sensing inductor prior to the experiment. To characterize its EPR properties, two measurements with and without the permanent magnet were conducted. The injection frequency was swept around $f_0 = 14.33$ GHz at a step size of 1 MHz during the measurement. The EPR spectrum of BDPA can then be extracted by taking the difference between the two measurements. The results are summarized in Fig. 4.12.

To examine the sensor sensitivity level, its output power spectrum density (PSD) was measured, as shown in Fig. 4.13. For noise analysis, the PSD is elevated by 3 dB due to the subtraction operation when obtaining the EPR spectrum. The noise density around the signal frequency (50 kHz) is about 0.71 μV/rtHz. Following the method given by [103], with a BDPA sample of known
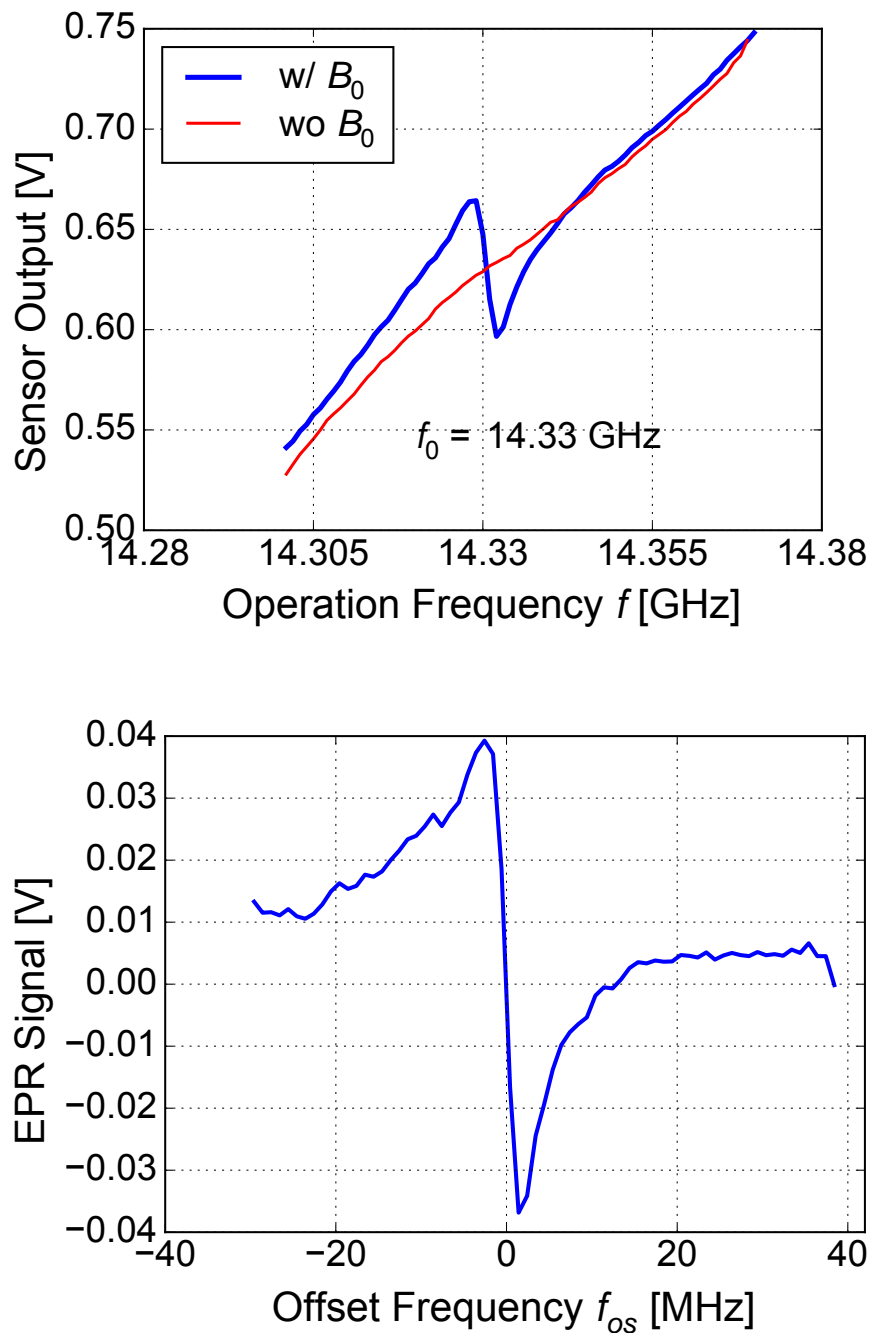
Figure 4.12: Measured EPR spectrum of a BDPA crystal.
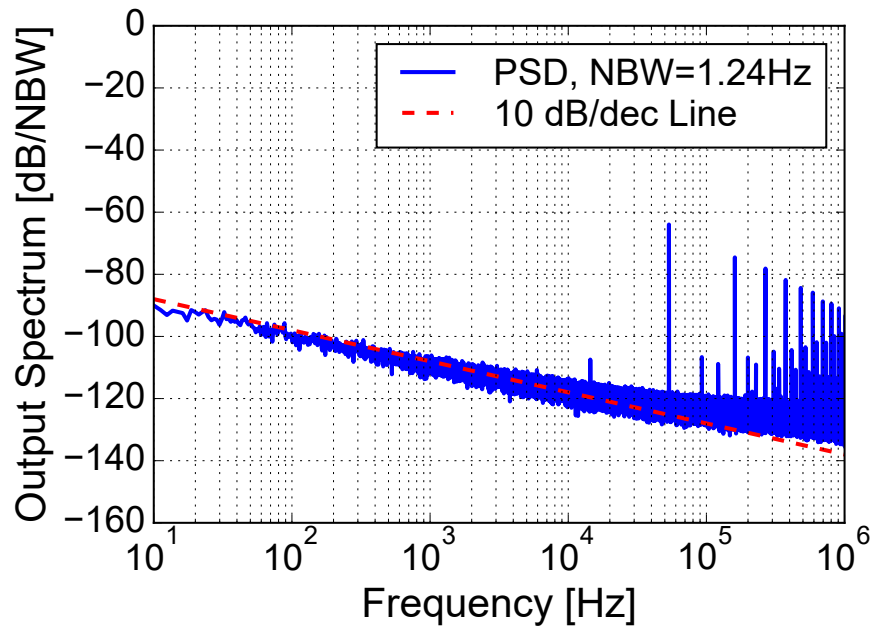
Figure 4.13: Measured output (V_{OD}, see Fig. 4.9) power spectrum density (PSD), with a system-level chopping at 50 kHz.

size ($110\times40\times5$ μm^3) and known spin density (1.57×10^{27} spins/m^3), the sensor can achieve a spin sensitivity of 6.1×10^8 spins/rtHz.

4.5 Chapter Summary

In this chapter, electron paramagnetic resonance spectroscopy is explored as a powerful sensing technique with supreme selectivity. The basic principles of magnetic resonance are revisited from both classical and quantum mechanical viewpoints. Bloch equations establish the relation between the magnetic resonance spectrum and the ac magnetic susceptibility of the spin ensembles, which makes it possible to measure EPR spectrum using the impedance spectroscopic methods.

Based off the Bloch equations, an ultralow-power CMOS inductance sensor for clinical electron paramagnetic resonance (EPR) spectroscopy was designed and fabricated. The key performance metrics of the sensor are summarized in Table 4.1, and compared with the state-of-the-art integrated EPR spectrometers. It demonstrates the best energy efficiency and almost the highest spin sensitivity. Although a slightly better sensitivity was shown in [103], it consumed much more power and required an AM modulation of the B_0 field, which substantially increases the system complexity and cost. The sensitivity volume can be further enlarged by arraying the sensing coils. It is worth mentioning that the entire sensor array can share the same excitation source, which provides a much

better power scaling compared with active oscillator based sensor topologies. Overall, offering a high sensitivity and power efficiency, this work paves the way for EPR to be translated into routine clinical practice, as described in the next chapter.

Table 4.1: COMPARISON WITH THE STATE-OF-THE-ART INTEGRATED EPR SPECTROMETERS

	This Work	ISSCC'18 [3]	ISSCC'16 [2]	TMTT'15 [1]	JMR'12 [4]	Rev. Sci.'08 [5]
Field Strength B_0 [T]	**0.5**	0.5	0.5	0.15	0.96	0.35
Operation Frequency [GHz]	**11.2-14.5**	11.8-14.2	13.2-14.3	3.8-4.8	27	9
Spin Sensitivity [spins/rtHz]	**6.1×10^8**	8×10^9	4×10^9	Not specified	2×10^8	1×10^{10}
Sensitivity Volume [nL]	**7.5**	15/channel*	27	10000**	1	1
ASIC Power [mW]	**1.12**	15/channel*	15	2000	75	160
Technology	**28 nm CMOS**	130 nm CMOS	130 nm CMOS	130 nm BiCMOS	130 nm CMOS	350 nm CMOS
EPR Spectrum	**Dispersion**	Dispersion	Dispersion	Absorption	Dispersion	Dispersion
Tolerance to PVT Variations	**High**	Low	Low	High	Low	Low
System Size and Complexity	**Low**	Low	Low	Low	High	High

* Eight channels in total.
** Used an off-chip resonator on the PCB.

Chapter 5

Galvanically Coupled EPR Spectrometer for *In Vivo* Applications

In this chapter, we dive into an exciting emerging field of electron paramagnetic resonance spectroscopy, *in vivo* EPR.

In 1944, EPR was first discovered by Soviet physicist Yevgeny Zavoisky. About the same time, Edward Purcell at Harvard and Felix Bloch at Stanford successfully demonstrated NMR for condensed matter in 1946. Since then, NMR has flourished and become an indispensable, if not the most important, technique for the non-invasive investigation of human anatomy, physiology and pathophysiology. To date, the Nobel Prize has been awarded five times for the development of NMR and MRI, but has never gone to EPR. Despite the fact that EPR is arguably the best tool for quantitative assessment of free radicals in the biological system, the development of *in vivo* EPR is much less impressive, as there are several technical obstacles which need to be solved. Namely, most biologically relevant free radicals, such as reactive oxygen species (ROS), reactive nitrogen species (RNS) and reactive sulfur species have very short relaxation times, making the spectra linewidth too wide to be visible. The concentrations of endogenous free radicals in living tissues are usually very low, sometimes below the current EPR detection limit. This directly links to the third challenge, where the optimal EPR operation frequency is so high (>10 GHz) that the signal is mostly absorbed by the human tissue before reaching the external detector.

Recent developments and the remaining challenges faced by *in vivo* EPR are discussed in Section 5.1, which motivate our work. Specifically, to address the non-resonant absorption of EPR signal by human tissue, a galvanically coupled EPR spectrometer for implantable usage is demonstrated. Section 5.2 presents the overall system architecture, which consists of a galvanic human body channel for the propagation of the incoming reference frequency (Section 5.3), a subsampling phase lock loop for the generation of EPR excitation frequency (Section 5.4) and the EPR sensor core (Section 5.5). Measurement results are provided in Section 5.6 and 5.7. Finally, Section 5.8 concludes this chapter.

5.1 Introduction

5.1.1 Opportunities

Although direct detection of many naturally occurring paramagnetic species using *in vivo* EPR still remains far-fetched, researchers have managed to synthesize exogenous paramagnetic species which are used as 'spying probes' to obtain useful physiologic and metabolic information. Simply put, by infusing or injecting these spin probes inside the tissue, the change of their EPR line shapes will be correlated to certain physiologic processes, and can be monitored in real-time to track the dynamics.

Recent years have seen significant progress in developing various functional spin probes to quantitatively characterize the chemical property of the tumor microenvironment (TME), including tissue hypoxia, acidosis, high reducing capacity, elevated intracellular glutathione (GSH) levels and interstitial inorganic phosphate [106, 107], among which tumor hypoxia imaging by *in vivo* EPR has been proven to be very promising and gained lots of momentum.

5.1.1.1 Tumor Hypoxia

Hypoxia is a physiological condition characterized by a deficiency of tissue oxygen levels, i.e., lower than normal partial pressure of oxygen (pO$_2$), which arises from an imbalance between oxygen delivery and oxygen consumption. It has been estimated that 50% to 60% of solid tumors exhibit hypoxia due to structural abnormalities of tumor micro-vessels and disturbed micro-circulation [108], as shown in Table 5.1. Recurring tumors are even more susceptible to hypoxia than primary tumors [109, 110]. Additionally, when radiation is administered to patients with cancer, radio-sensitivity is progressively limited when pO$_2$ in a tumor is less than 25-30 mmHg, which severely compromises the clinical outcome [111, 112]. In other words, hypoxia is not only a hallmark feature of a solid tumor, but also significantly reduces the efficacy of both the radiotherapy and the chemotherapy, resulting in a lower survival rate.

Table 5.1: TYPICAL OXYGEN TENSIONS IN TUMORS AND THE RESPECTIVE HEALTHY TISSUES [113]

Tumor Type	# of patients	Tumor pO$_2$ [mmHg]	Tissue pO$_2$ [mmHg]
Head and neck	592	10	40-51
Lung	26	16	39
Breast	212	10	65
Pancreatic	7	2	52
Cervix	730	9	51
Prostate	190	7	20-31
Brain	104	13	54

As a result, accurate detection of hypoxia plays an important role in the identification of tumor recurrence and in the development of new treatment strategies with a better outcome.

5.1.1.2 Diagnosis of Hypoxia

Considerable efforts have been made to detect hypoxia, which are summarized in Fig. 5.1. Generally speaking, these methods can be categorized into the following three groups:

(1) *Direct*: measure oxygen concentrations through explicit interaction with O_2.
(2) *Indirect*: measure a physiological process that involves O_2, e.g., blood hemoglobin saturation curves, which relates to blood oxygen partial pressures.
(3) *Indirect*: measure endogenous markers that are over-expressed as a result of hypoxia, e.g., hypoxia-inducible factor-1α (HIF-1α).

Indirect detection of exogenous markers:
HIF-1, CAIX, GLUT-1:
cellular response to hypoxia

Invasive direct methods:
polarographic (Clack) electrodes:
oxygen level at the needle

Tissue Cells

pO_2

Low

Non-invasive direct methods:
Fluorescence quenching,
Photoacoustic lifetime imaging,
EPR
oxygen level near the probe

High

Endogenous
markers

Blood Vessels

O_2

Non-invasive indirect methods:
NIRS, BOLD MRI, Photoacoustic Tomography:
blood flow and oxygenation dynamics in blood

Figure 5.1: Techniques used for detecting hypoxia in tumors [113].

Despite the large number of detection techniques, very few are approved for clinical use and none of them have been established in the clinical routine for tumor treatment, mainly because of the following two reasons. First, the invasive nature of some of the effective techniques limits their usage to superficial tumors and requires great expertise. For example, the 'gold standard' polarographic method [114] involves insertion of an electrode into the tumor, which disrupts the tissue and makes repeated measurements extremely difficult. Second, many of the non-invasive techniques either rely on indirect evidence or fail to provide quantitative measurements, which can cause misleading predictions. Examples include blood oxygen level-dependent (BOLD) MRI, near-infrared spectroscopy (NIRS) and photo-acoustic tomography (PAT). All of them infer tissue oxygen levels through imaging hemoglobin in blood, which is not quantitative, easily affected by blood flow effects and only reveal the oxygen levels in vasculature rather than tissue [115].

To date, only EPR, fluorescence lifetime and photoacoustic lifetime imaging can perform direct pO_2 quantification in a non-invasive fashion. However, the latter two have the disadvantage of not being able to make repeated measurements [116], a huge disadvantage in most clinical practices.

5.1.1.3 EPR Oximetry
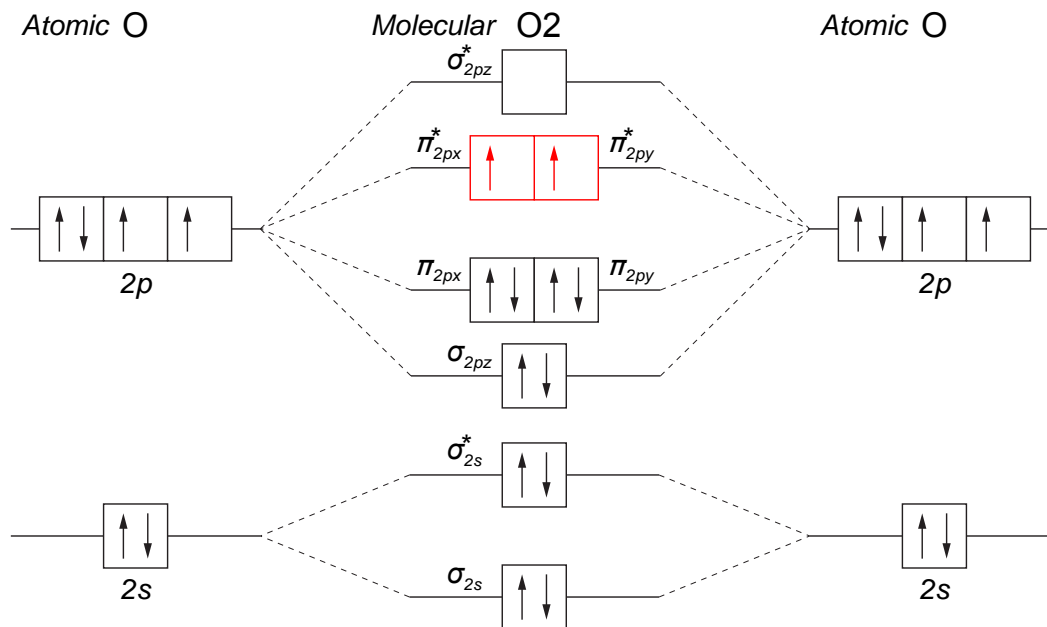
Figure 5.2: Molecular orbital energy diagram of O_2 molecule.

Molecular oxygen is a triplet that contains two unpaired electrons (see Fig. 5.2), which accounts for its paramagnetism. Direct detection of the oxygen paramagnetic spectrum is almost impossible due to its extreme wide linewidth. Instead, EPR oximetry utilizes the interaction between molecular oxygen and other paramagnetic species whose relaxation rates are accelerated as a result of such interaction [117]. The enhancement of the relaxation rate, which corresponds to a broadened EPR spectrum, usually scales linearly with the oxygen concentration, and therefore can be directly used to interpret the pO_2 level, as illustrated in Fig. 5.3. The paramagnetic spin probes can either be soluble (e.g., nitroxides) or particulate (e.g., lithium phthalocyanine (LiPc), lithium octa-*n*-butoxynaphthalocyanine (LiNc-BuO), and carbon blacks).

Substantial amount efforts have been devoted to characterize these paramagnetic probes for *in vivo* oximetry applications [119–122]. In 2020, a clinical trial [123] that involved 24 human beings who received implantation of the LiNc-BuO spin probes (called 'OxyChip') into the tumor validates the safety and feasibility of EPR oximetry for clinical usage, which signals a major breakthrough in the fight against cancer.
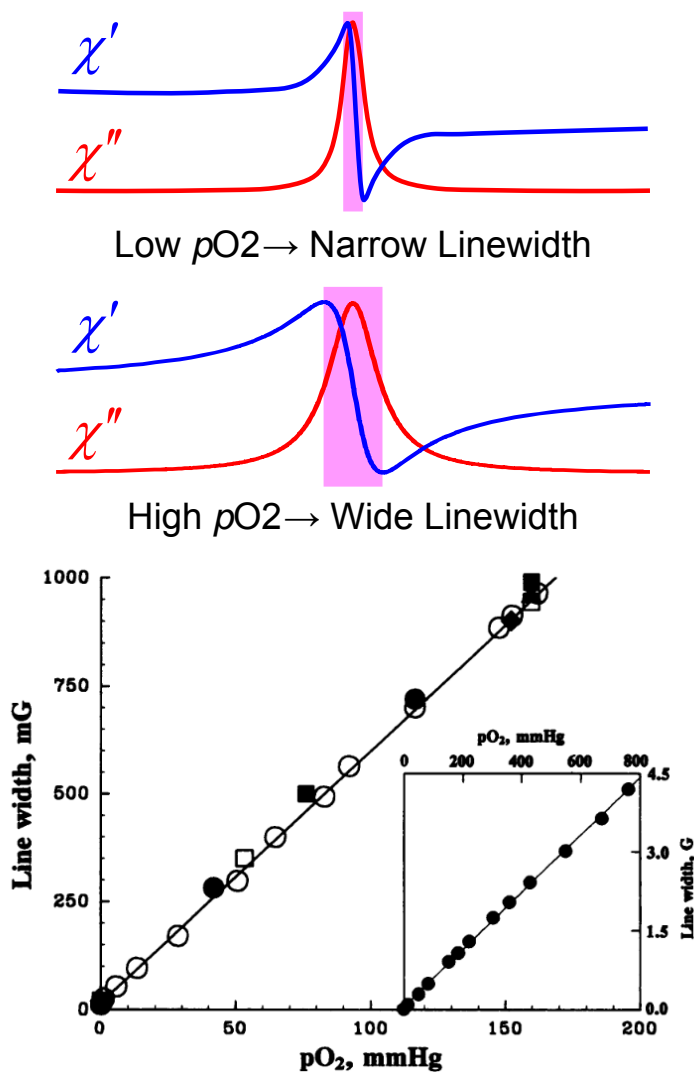
Figure 5.3: Effect of oxygen on the EPR spectra of paramagnetic materials, qualitative trend (top), and change of the EPR linewidth at different pO_2 levels for LiPc [118] (bottom).

5.1.2 Challenges

Despite this encouraging outcome, the existing clinical/pre-clinical practices predominantly use L-Band (1.2 GHz) or lower frequencies for EPR spectroscopy, which is suboptimal. Recall the expression of the complex magnetic susceptibility derived from the Bloch equations (see (4.26),

which is repeated here)

$$\chi' = \frac{\chi_0}{2} \frac{\omega_0 \Delta\omega T_2^2}{1 + \left(T_2\Delta\omega\right)^2}$$
$$\chi'' = \frac{\chi_0}{2} \frac{\omega_0 T_2}{1 + \left(T_2\Delta\omega\right)^2}$$

$$(5.1)$$

Apparently the EPR signal intensity is proportional to the operation frequency ω_0. Since the commercial EPR spectrometers all measure the absorption spectrum (χ''), whereas the human body is such an efficient absorber for radio frequency energies, most of the incident electromagnetic energy will be converted to heat rather than contribute to EPR spin flip transitions if moving beyond the L-Band or penetrating into the deeper tissue layers. Moreover, to avoid tissue damage by RF exposure, IEC (International Electrotechnical Commission) puts strict regulations on the permissible RF power so that one cannot arbitrarily raise the intensity of the applied $\vec{B_1}$ field for better SNR.

As a result, there exists a direct trade-off between the tissue penetration depth and signal-to-noise ratio. As of today, even at L-Band (1.2 GHz), OxyChip can only reach 1 cm depth [124]. A X-Band (9 GHz) *in vivo* EPR was demonstrated for finger nail dosimetry in [125] but only has a penetration depth of 2 mm. Therefore, a revolution in the EPR instrumentation must happen, otherwise it is very likely that *in vivo* EPR will by and large be restricted to superficial tissue layers despite its enormous potential.

5.2 System Architecture

To enable high-frequency deep-tissue EPR, we propose to develop an implantable EPR spectrometer which triggers and detects the paramagnetic resonance signal *in situ*, as shown in Fig. 5.4(b). Compared with the existing instrumentation [see Fig. 5.4(a)], the proposed solution avoids the devastating signal loss due to tissue absorption, so that EPR can operate at a higher frequency for better sensitivity and penetrate into a greater depth without impairing its SNR.

Since the EPR operation frequency (>10 GHz in this work) must be precisely controlled with MHz−kHz accuracy, the spectrometer implant will be wirelessly coupled an external subharmonic frequency source to minimize tissue absorption. As a result, a low-noise low-power phase lock loop (PLL) needs to be integrated onto the spectrometer for frequency multiplication. Fig. 5.5 shows the block diagram of the proposed implantable EPR spectrometer. With the static field magnetic field $B_0 = 0.5$ T, the fabricated prototype operates at 14 GHz. It consists of the following three key building blocks, which will be discussed separately in the next few sections.

(1) **Subharmonic galvanic coupling channel**. A 30 MHz ultralow-noise clock signal is generated externally to serve as the subharmonic frequency reference. Wireless coupling is made galvanically, achieving at least 5 cm penetration depth.
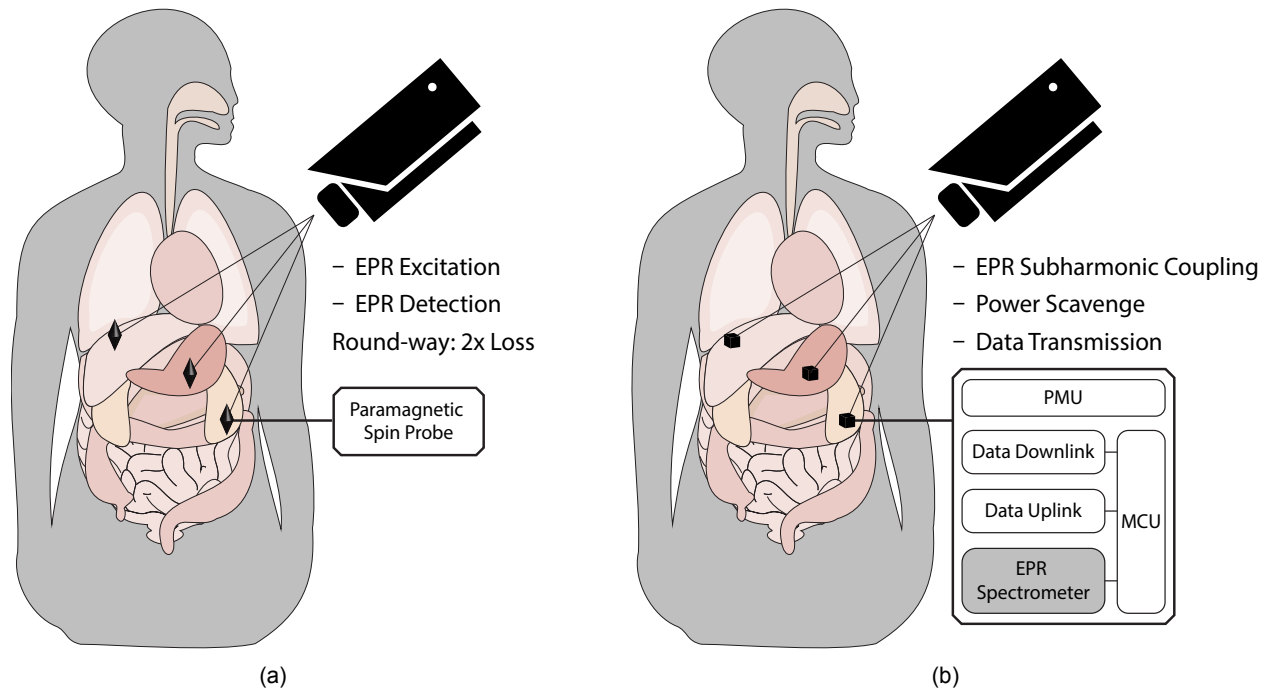
Figure 5.4: *In vivo* EPR spectroscopy, (a) existing instrumentation, with only paramagnetic spins probes implanted, and (b) proposed instrumentation, with both the spectrometer and spin probes implanted.

(2) **Subsampling phase lock loop (SSPLL)**. A very high multiplication factor ($M = 480$) is needed to synthesize the 14 GHz EPR source. Subsampling topology is selected due to its superior power-jitter performance for high M-factor PLL.

(3) **EPR sensor core**. The ultra-sensitive low-power EPR sensor introduced in Chapter 4 is reused here.

It worth mentioning that a complete EPR implant also includes the power management unit (PMU), data communication link (uplink/downlink) and a micro-controller unit (MCU), as depicted in Fig. 5.4(b). Since they are universal building blocks for all the implantable devices and do not fall within the theme of this dissertation, they were not implemented in this prototype. In order to estimate the power budget for this implantable EPR spectrometer, several ultrasonically powered medical implants are used as reference [126–128]. A power transfer depth as large as 10 cm has been demonstrated in tissue phantom and 6 cm in porcine tissue [127], with peak instantaneous current ranging from 5 mA ($V_{DD} = 12$ V) [127] to 12.4 mA ($V_{DD} = 1$ V) [126]. Therefore, with $V_{DD} = 0.9 - 1.2$ V, a peak current $I_{peak} < 10$ mA is a reasonable design budget. Note that these implantable devices are typically heavily duty-cycled to minimize the average power consumption.

In addition, biocompatibility must also be taken into consideration. Polydimethylsiloxane (PDMS) is a highly biocompatible and biostable silicon polymer, which is widely used in the medical

devices and has been approved for use in the human objects [119]. The EPR oximetry clinical trial conducted in 2020 [123] further validated the safety of PDMS. Therefore, the EPR spectrometer along with the spin probes will also be encapsulated in PDMS.
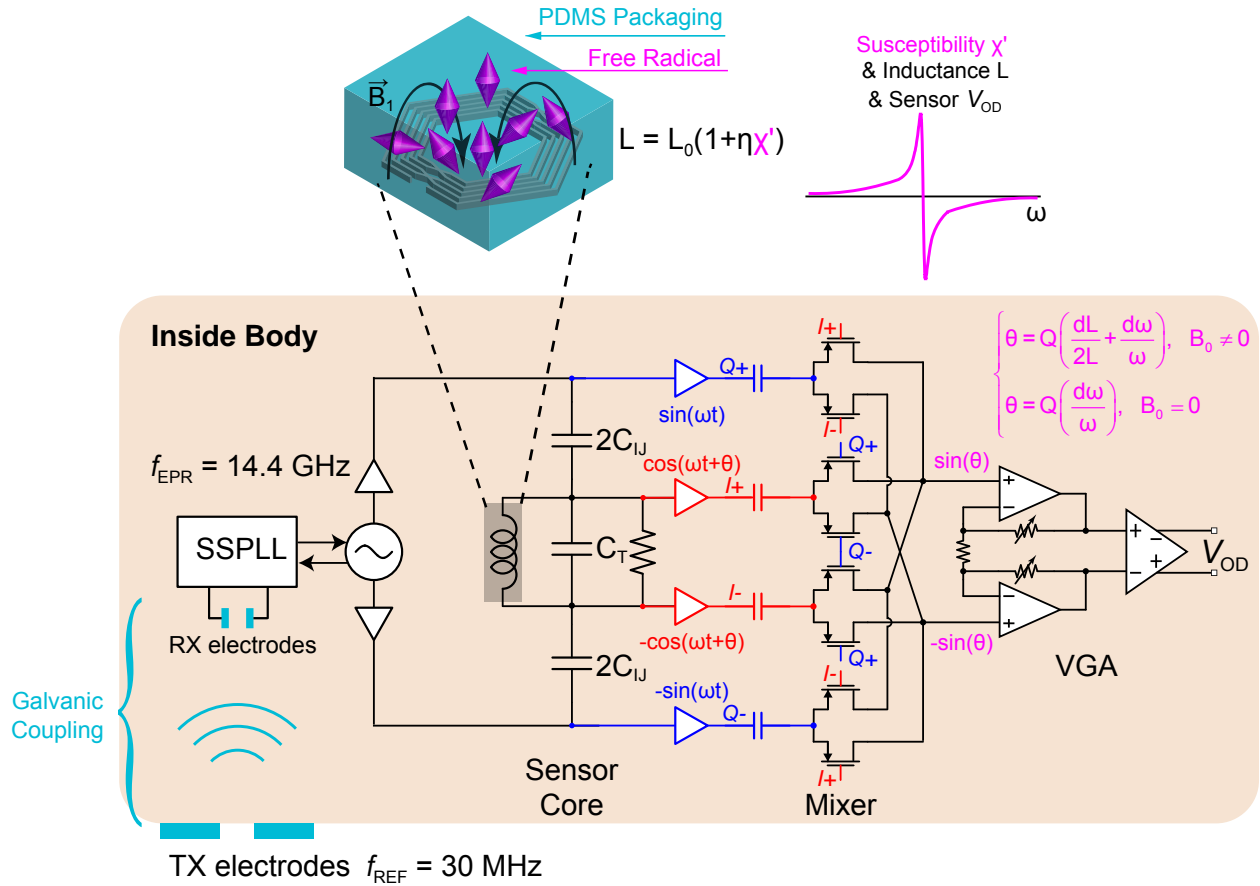
Figure 5.5: Block diagram of the proposed implantable EPR spectrometer.

5.3 Subharmonic Coupling

5.3.1 Carrier Selection

First things first, one needs to decide what types of carrier (ultrasound vs electromagnetic (EM) radiation vs alternative voltage/current), and at what frequency, will be utilized to wirelessly couple the reference clock onto the implanted EPR spectrometer. The distinction between electromagnetic radiation and alternative voltage/current is made based on how the EM wavelength in tissue compares with the coupling distance (set $D = 5$ cm). Using water for approximation [129], where the dielectric constant equals $\epsilon_r = 78$ up to 1 GHz. The EM frequency at which its wavelength $\lambda = 50$ cm, such

that $D = \lambda/10$, is around 70 MHz. Therefore, for coupling frequency below 70 MHz, the tissue can be modeled as lumped circuits and the coupled signal takes the form of alternating voltage/current, which is also referred to as capacitive coupling and galvanic coupling. On the other hand, going beyond 70 MHz will require a distributed model or a radiation model.

Although ultrasound seems to have won the battle of wireless power delivery for medical implants [126–128, 130, 131], it is not necessarily the optimal choice for wireless clocking, whose design target is to minimize the phase noise at the PLL output rather than to maximize the energy collected by the load. In this case, the objective function can be written as

$$\arg \min \mathrm{PN}_{SRC} \times M^2 + \mathrm{PN}_{BUF} \times M^2 \tag{5.2}$$

where PN_{SRC} and PN_{BUF} are the phase noise of the external signal generator and the on-chip reference buffer, respectively. M is the PLL multiplication factor.

One subtle but critical fact most people aren't aware of is that the phase noise of a signal generator does not scale up by M^2 when the carrier frequency is M times higher. Take R&S® SMA100A signal generator as an example [132]. Its phase noise at 10-100 kHz offset for a carrier frequency of 1 MHz, 10 MHz and 100 MHz are -152 dBc/Hz, -168 dBc/Hz and -156 dBc/Hz, respectively. When up-converted to 14 GHz, the correspondent in-band phase noise will be -69 dBc/Hz, -105 dBc/Hz and -113 dBc/Hz, provided that the reference buffer noise contribution is negligible. Therefore, ideally the reference frequency should be as high as possible, which gives EM coupling some leverage over the ultrasound.

The FCC and FDA have issued safety guidelines for human exposure to electromagnetic energy [133, 134] [1], and diagnostic ultrasound [135, 136], as summarized in Table 5.2. Considering the power loss due to tissue absorption, the actual voltage level that arrives at the implant can be substantially smaller when coupling at a higher frequency, so that the reference buffer phase noise in (5.2) may eventually dominate. This essentially sets the upper bound for the coupling frequency.

Four different types of coupling methods have been considered.

(1) **Ultrasound**.

Medical ultrasound devices operate in the frequency range of $1-20$ MHz. In order for the PLL to achieve an in-band phase noise of -110 dBc/Hz [2], the frequency of the ultrasonic wave must be at least 25 MHz if R&S® SMA100A is used as the reference source. Since the ultrasound attenuation in tissue is linearly proportional to the frequency [0.3 dB/(cm·MHz), see Table 5.2], passing 25 MHz sound waves through a 5 cm thick tissue layer will incur 37.5 dB loss in power. Using maximal ultrasonic power density approved by FDA (720 mW/cm^2), the electric power that arrives at the reference buffer input is only 64 μW/cm^2 assuming perfect matching at all the interfaces and 100% acoustic-electric conversion efficiency. To generate a 1 V peak-to-peak voltage swing, the resonance resistance of the piezoelectric receiver must satisfy $R_{\mathrm{res}} \geq 2 \text{ k}\Omega \cdot \text{cm}^2$. Overall, ultrasound can be an option if suitable

---

[1]These exposure limits are intended to apply to all people, with the exception of patients undergoing a procedure for medical diagnosis or treatment, see *IEC 60601-1* for RF emission guidelines from medical devices.

[2]It is typical for a free-running 14 GHz VCO to reach -110 dBc/Hz phase noise at 1 MHz frequency offset, which is thereby used to specify the in-band phase noise.

Table 5.2: Regulations for Human Exposure to Electromagnetic and Ultrasonic Energy

Electromagnetic Maximum Permissible Exposure				
Frequency [MHz]	RMS electric field strength [V/m]	RMS magnetic field strength [A/m]	RMS power density [W/m^2]	Averaging time [min]
1−30	$1842/f_M$	$16.3/f_M$	$(9000/f_M^2, 100000/f_M^2)$	6
30−100	61.4	$16.3/f_M$	$(10, 100000/f_M^2)$	6
100−300	61.4	0.163	10	6
300−3000	-	-	$f_M/30$	6
Diagnostic Medical Ultrasound Properties				
Frequency [MHz]	Speed of sound [m/s]	Wavelength [mm]	RMS power density [W/m^2]	Attenuation [dB/(cm·MHz)]
1-20	1450−2100	0.075−1.5	7200	0.3

f_M: frequency in MHz.

piezoelectric materials are used to fabricate such a receiver. [137] and [138] provide some useful guidelines for the ultrasonic receiver design.

(2) **Electromagnetic Wave**.

Compared with ultrasound, the challenge associated with using electromagnetic waves is on the opposite side of the spectrum, where the phase noise from the reference buffer becomes the bottleneck.

Consider a frequency range of 350−700 MHz (tissue wavelength λ =5−10 cm) and assume the implant occupies 1 cm^2. The receiving antenna is electrically small. For a folded dipole, its radiation resistance is

$$R_{r,D} = 4\eta\frac{\pi}{6}\left(\frac{L}{\lambda}\right)^2 \tag{5.3}$$

and for a loop antenna, the radiation resistance is

$$R_{r,L} = \eta\frac{8}{3}\pi^3\left(\frac{A}{\lambda^2}\right)^2 \tag{5.4}$$

where L and A represents the antenna length and area, respectively. η is the wave impedance in tissue, which is given by $\eta = \sqrt{\mu_0/(\epsilon_0\epsilon_r)} = 43\ \Omega$ for water with $\epsilon_r = 78$. Even at 700 MHz, the radiation resistance is only about 5 Ω for both antennas, which poses a great challenge for matching and limits the achievable voltage swing at the reference buffer input, adversely affecting the phase noise performance.

Power absorption by tissue further complicates the situation. The penetration depth, at which the field intensity reduces to 1/e, for a 700 MHz carrier is about 1.5−2.5 cm [139, 140]. Therefore with the maximal RF power regulated by FCC (1−2 mW/cm^2, see Table 5.2),

the available power at 5 cm is about 15 μW/cm^2. Even with 100% antenna efficiency, the rms voltage at the reference buffer input $V_{\text{in,rms}}$ is only 8.7 mV without additional matching network. To achieve -110 dBc/Hz phase noise, the reference buffer input referred voltage noise should be 136 dB below $V_{\text{in,rms}}$, i.e.,

$$10\log_{10}\left(\frac{4k_B T\gamma/g_m \cdot \alpha}{V_{\text{in,rms}}^2}\right) = -110 - 20\log_{10}(\frac{14\,\text{GHz}}{700\,\text{MHz}}) = -136 \tag{5.5}$$

Assuming $\gamma = 1$, $\alpha = 2$ and 200 mV overdrive voltage, the reference buffer will consume at least 2 mA current. To achieve such performance, the receiving antenna and input matching network must be optimized to use EM wave coupling, which is not trivial considering the complexity of the human body.

(3) **Alternating Voltage/Current: Galvanic Coupling**.
For frequencies below 70 MHz, the tissue layer can be modeled using lumped circuits. In the case of galvanic coupling, a pair of electrodes (TX) is placed directly in contact with the tissue and transmits voltage to a second pair of electrodes (RX), as shown in Fig. 5.6(a). Since the wave prorogation effect can be neglected, matching is not necessary and the RX load can be kept open to maximize received voltage level. The FCC sets an upper limit of 61.4 V/m RMS for the non-radiating electric field, whereas the penetration depth for an input frequency $f \leq 70$ MHz [139] is above 10 cm. The estimated voltage amplitude at the reference buffer input can be 0.5 V, which is promising. Therefore, galvanic coupling is implemented in this work since it is simple and efficient.

(4) **Alternating Voltage/Current: Capacitive Coupling**.
Capacitive coupling is very similar to galvanic coupling, except that it employs only one TX electrode and one RX electrode, as shown in Fig. 5.6(b). Since the earth ground is involved as part of the return path, it becomes very difficult to either predict or control the channel behavior and the noise performance. Thereby it is excluded from the consideration.

5.3.2 Galvanic Channel

In this prototype, the RX electrodes are sized 2.5 mm $\times$ 0.25 mm, with a center-to-center spacing of 4 mm, whereas the TX electrodes are sized 25 mm $\times$ 50 mm, with a center-to-center spacing of 70 mm, both made of copper. The dimension and relative position of the TX/RX electrodes are illustrated in Fig. 5.7.

To characterize the channel gain, a biologically equivalent phantom which mimics the dielectric properties of human tissue is fabricated and inserted in between the TX and RX electrodes. The recipe can be found in [141] and is also recommended by NIH[3]. Essentially the recipe uses deionized water as base, and tunes its conductivity and permittivity to match the actual tissue values by adding salt (NaCl) and sucrose. Agar is then used to gel the solution. For a frequency range of 10−70 MHz, the dielectric constant and conductivity of tissue can be found in [142, 143].

---

[3]Dielectric phantom recipe generator: https://www.amri.ninds.nih.gov/cgi-bin/phantomrecipe
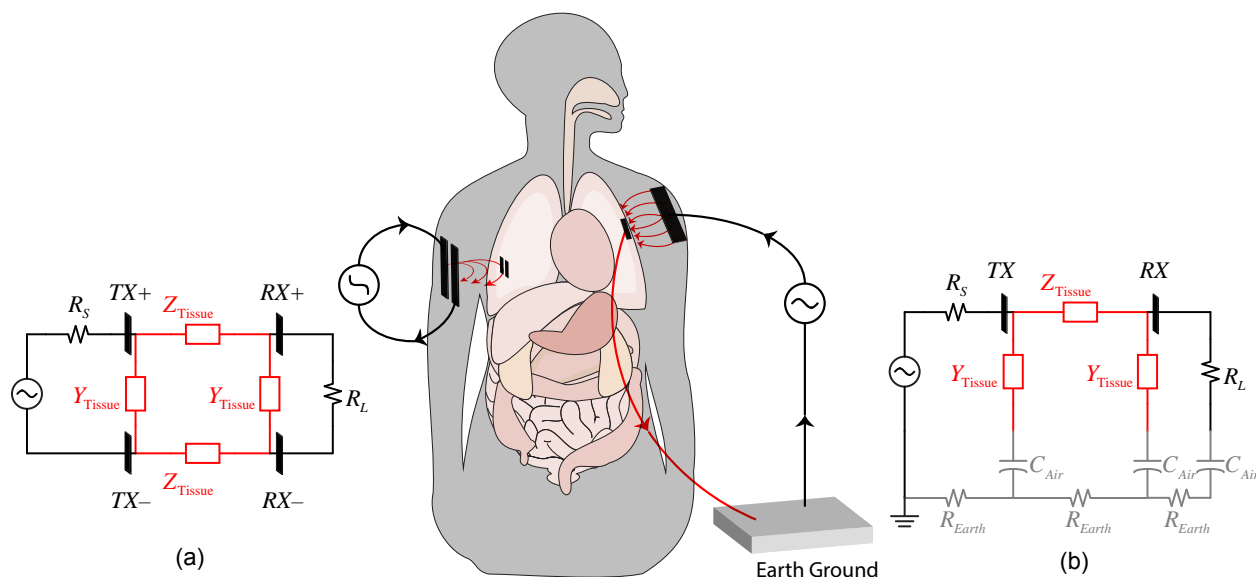
Figure 5.6: Comparison between (a) galvanic coupling and (b) capacitive coupling.
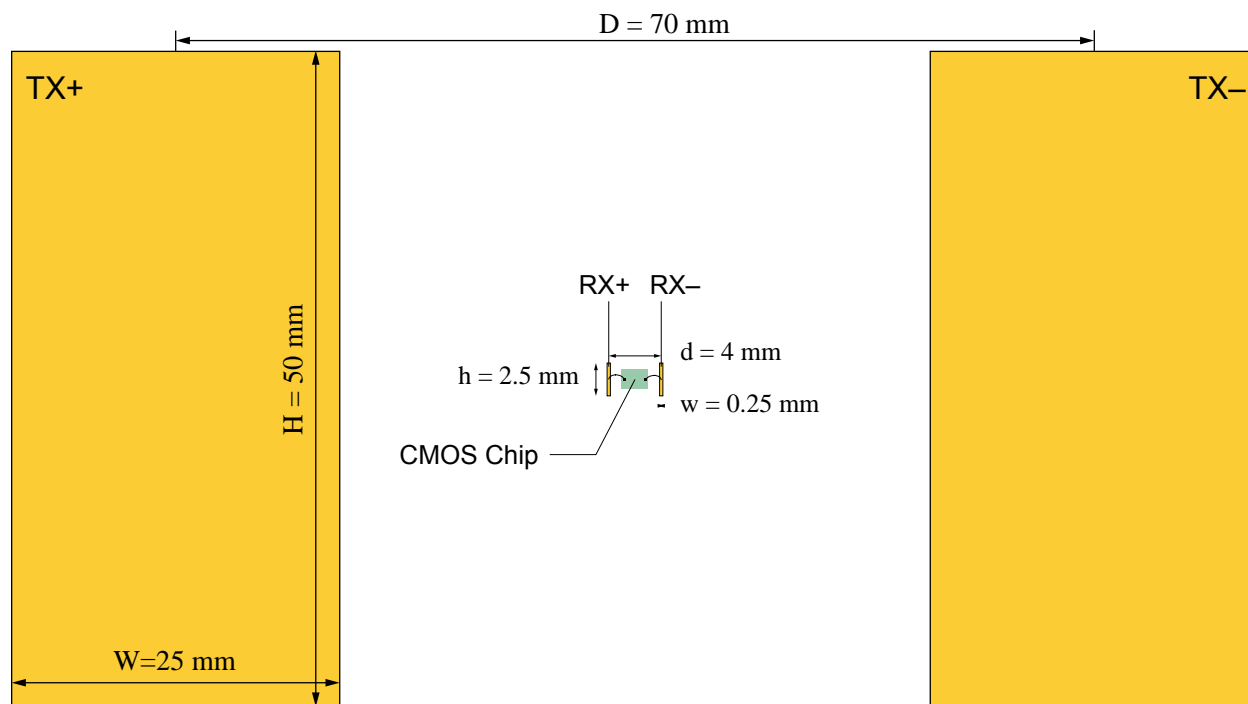
Figure 5.7: Galvanic coupling: dimension of the TX/RX electrodes (drawn to scale). The EPR spectrometer can be positioned in between the two RX electrodes.
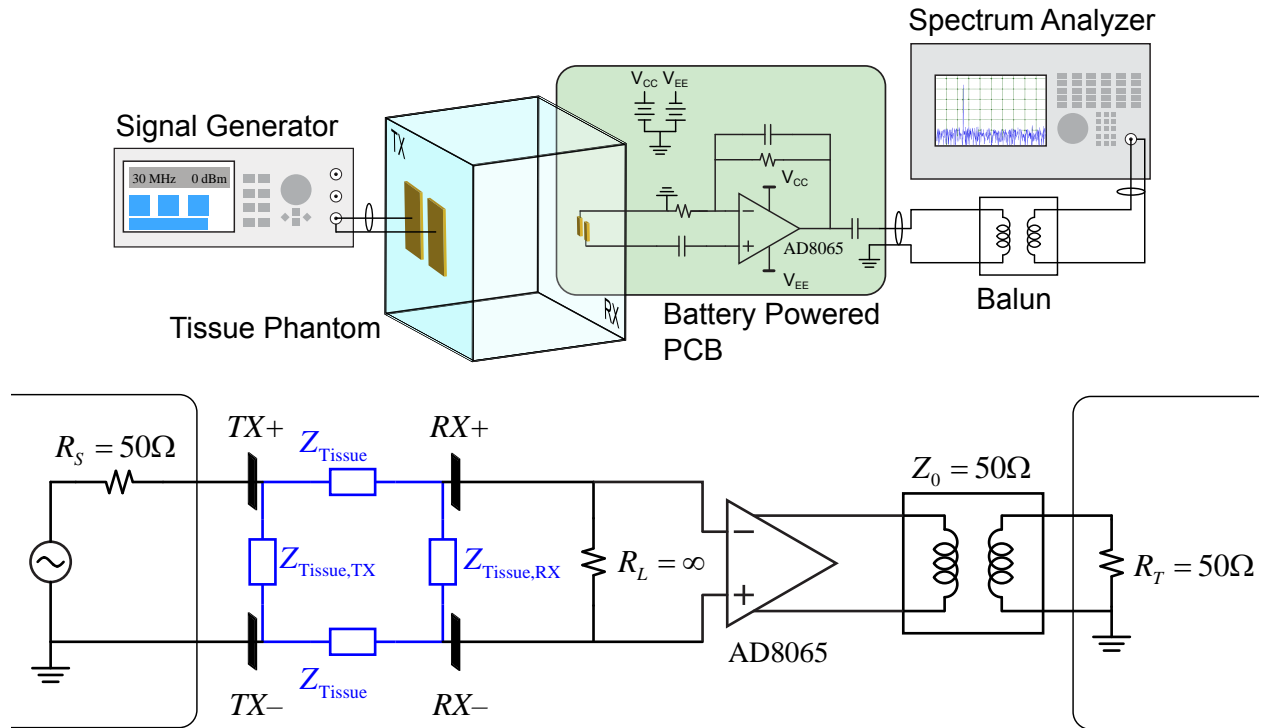
Figure 5.8: Galvanic channel gain characterization, (top) measurement setup and (bottom) equivalent circuit diagram.

Fig. 5.8 illustrates the measurement setup for the gain characterization of the galvanic channel. It is configured to imitate the actual implant. For example, a buffer amplifier with high input impedance is inserted in between the RX electrodes and the spectrum analyzer to prevent the loading effects from the analyzer input termination. In addition, the RX PCB is powered by batteries and the amplifier output connects to the spectrum analyzer through a balun (Mini-Circuits FTB-1-6) to provide isolation from the earth ground. The gain of the buffer amplifier is calibrated first using the same setup by replacing the TX/RX electrodes and the tissue phantom with a second balun (Mini-Circuits FTB-1-6).

During the actual measurements, dielectric phantoms which mimic the tissue permittivity around 30 MHz ($\epsilon = 60$, $\sigma = 0.15$ S/m) were fabricated with different thickness values ($T = 1 - 5$ cm). For each thickness value, measurements were repeated three times using phantoms fabricated at different batches. The actual phantom dielectric constant, conductivity and TX/RX electrodes alignment can have $\pm 10\%$ variations. Results were summarized in Fig. 5.9(a)-(c) and consolidated in Fig. 5.9(d). Note that the measured channel gain also includes the impact from the impedance mismatch at the TX electrodes, i.e.

$$G = \frac{V_{\mathrm{RX}}}{V_{\mathrm{TX}}} \cdot \frac{2Z_{\mathrm{TX,in}}}{Z_{\mathrm{TX,in}} + R_{\mathrm{S}}} \tag{5.6}$$

where $Z_{\mathrm{TX,in}}$ is the channel input impedance seen from the TX electrodes.
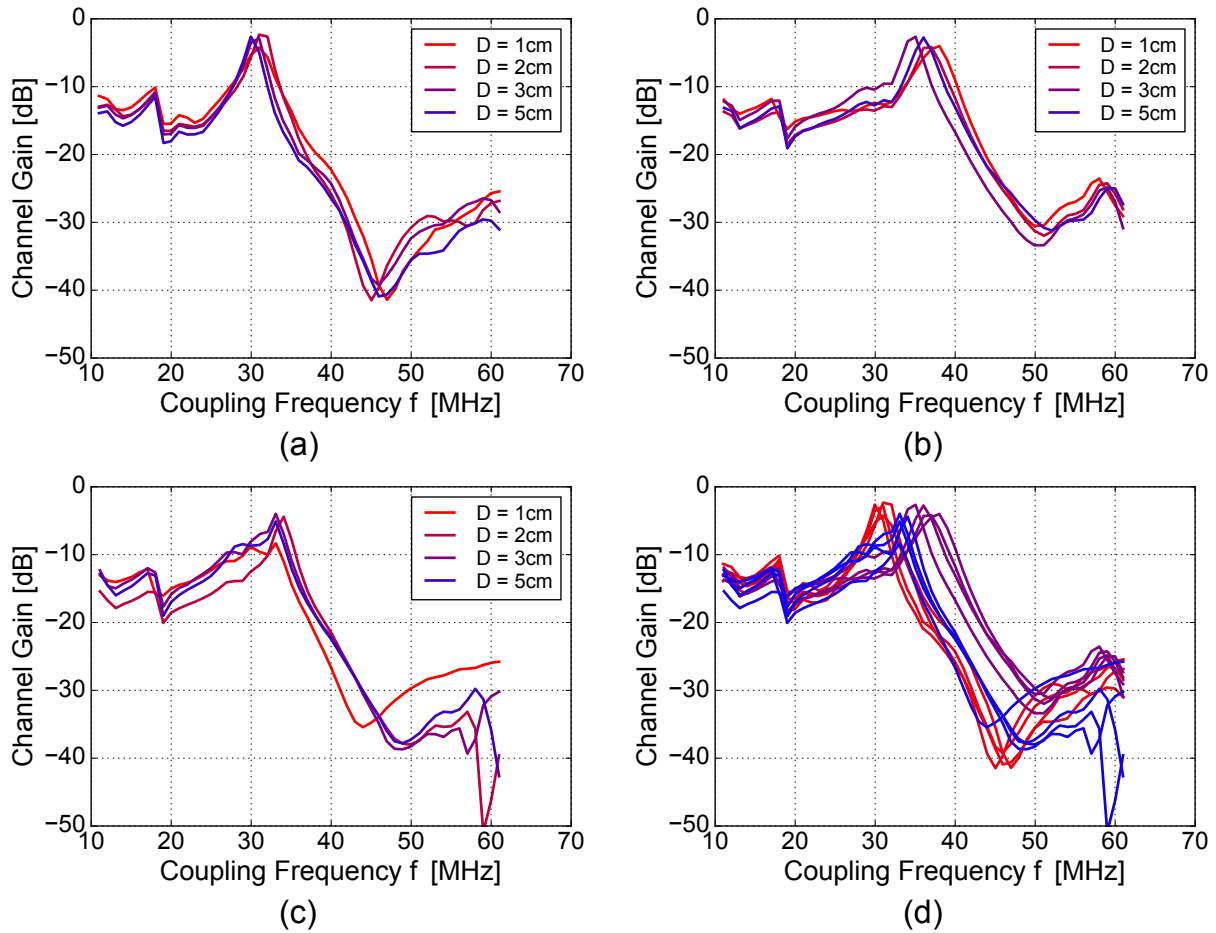
Figure 5.9: Galvanic channel gain for coupling frequencies $f = 10 - 60$ MHz, where (a)-(c) represent measurement results from three different batches and are consolidated into (d).

It can be observed that the channel performs best around $30-35$ MHz. What is interesting about Fig. 5.9 is that the channel gain remain relatively constant when the coupling distance increases from 1 cm to 5 cm. This can be explained using the equivalent circuit model shown in Fig. 5.8. Given the relative dimension of the TX/RX electrodes, there holds $Z_{\text{Tissue,TX}} \ll Z_{\text{Tissue}} \ll Z_{\text{Tissue,RX}}$, so that $Z_{\text{Tissue,TX}}$ dominates the overall channel loss. Since increasing the coupling distance only affects Z_{Tissue}, the channel gain won't be affected as long as the above inequality remains true. The TX electrodes are sized large intentionally so that the electric fringe field can have a wide coverage for RX electrodes at various depths.
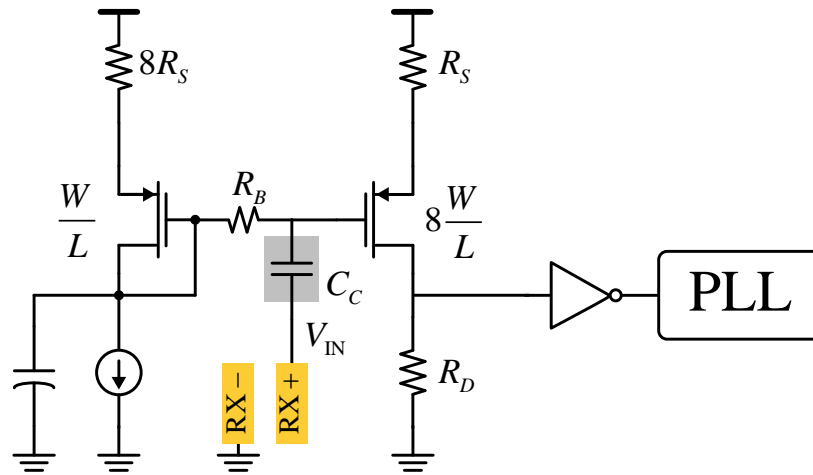
Figure 5.10: Schematic of the reference buffer.

5.3.3 Reference Buffer Design

Fig. 5.10 shows the schematic of the reference buffer. Instead of using a single inverter, a current biased common source amplifier is employed so that the buffer power consumption can be well controlled for different input amplitudes. In order to minimize the flicker noise contribution to the close-in phase noise, the input stage uses a resistor degenerated PMOS transistor. $R_B = 10$ kΩ is added to boost the input impedance seen by the RX electrodes. Fig. 5.11(a) shows the simulated phase noise (referred to the PLL output) when the input amplitudes change from 0.1 V to 1 V. A single inverter based reference buffer is designed to have comparable phase noise performance [see Fig. 5.11(b)]. However, its current consumption can jump up to 3 mA when the input signal level is 0.1 V whereas the PMOS amplifier buffer maintains 500 μA current across for 0.1−1 V input level, as shown in Fig. 5.12.

5.4   Subsampling PLL

To synthesize a 14 GHz carrier from a 30 MHz subharmonic reference, the PLL has a very large multiplication factor $M = 480$. The major design challenge is to simultaneously achieve low phase noise and low power consumption (e.g. below 10 mW), and the phase detector usually becomes the performance bottleneck for high M-factor PLLs. Although cascading PLLs helps reduce M per stage, it causes a significant power overhead and unwanted coupling between the two VCOs. In fact, direct high M-factor frequency synthesis with low phase noise and low power consumption is also a compelling topic in the communication community. Nowadays beyond-10GHz frequency synthesizers have become ubiquitous building blocks for the ever-growing wireless and wireline communication systems. To meet the stringent requirements on data rate and modulation schemes, the phase noise of the frequency synthesizers must be minimized. On the other hand, since low-noise
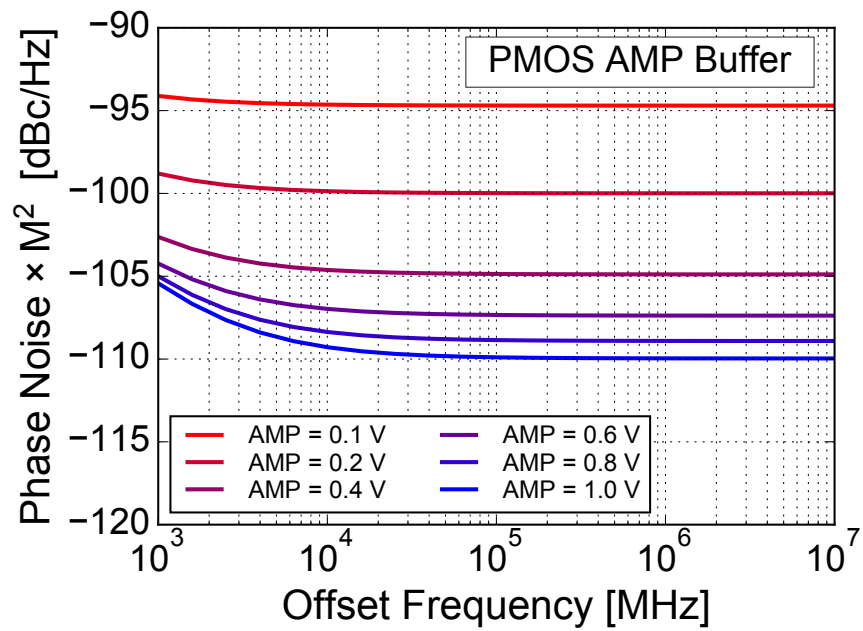
(a)
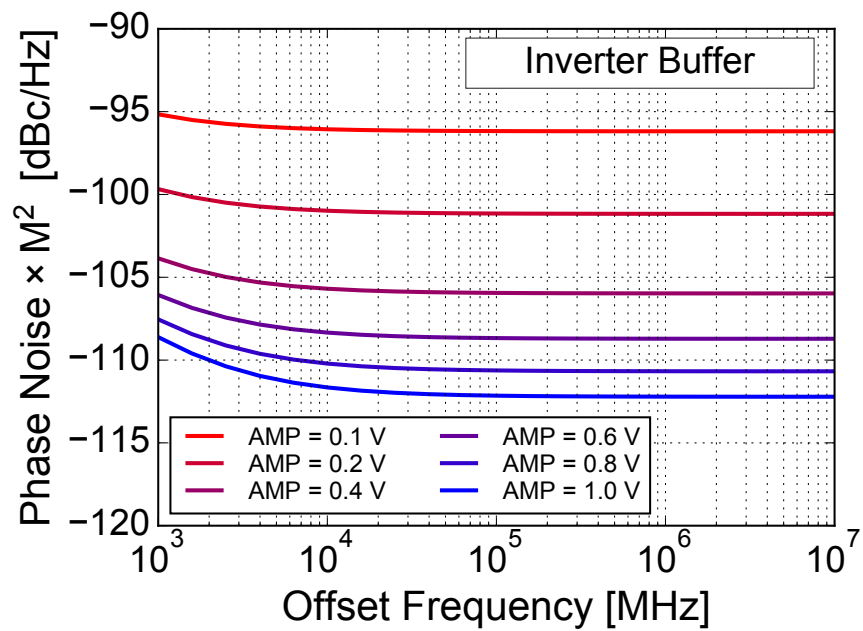
(b)

Figure 5.11: Simulated phase noise (multiplied by M^2) at different signal levels, using (a) PMOS amplifier and (b) single inverter as the reference buffer.
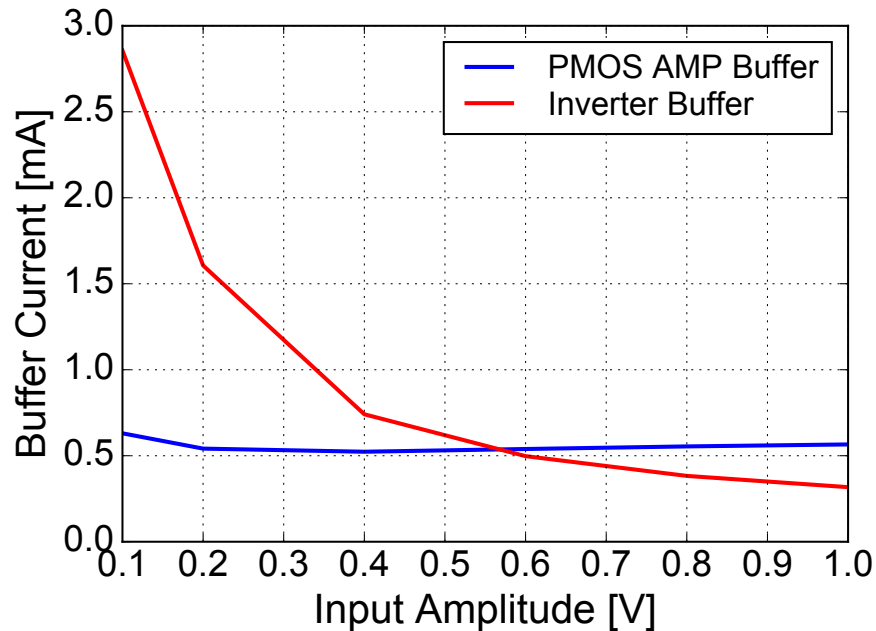
Figure 5.12: Simulated supply current at different signal levels.

and low-cost crystal oscillators operate at MHz range, a >10GHz frequency synthesizer demands a very large multiplication factor M (typically 400-1000) as well.

5.4.1   CPPLL vs SSPLL

Fig. 5.13 illustrated the block diagram and phase noise model of the classical charge pump PLL (CPPLL). Within the loop bandwidth, the PLL phase noise is dominated by the phase detector (PD), which is multiplied by M^2 when referred to the PLL output due to the multiplication factor M in the feedback path. This becomes problematic when the multiplication factor is high, and poses a direct trade-off between jitter and power.

Such an unpleasant trade-off can be mitigated by using a subsampling PLL (SSPLL). Fig. 5.14(a) shows its conceptual diagram and waveform. Basically, the differential sinusoidal waveform of the VCO is sampled by the reference clock, and the sampled voltage is then converted to current by a charge pump and integrated via the loop filter to control the VCO frequency. At the steady state, the reference clock always samples at the VCO zero-crossing, indicating that the VCO is locked. Therefore, SSPLLs are superior for generating low phase noise signals, as the divider noise is eliminated, and that the phase detector/charge pump (PD/CP) noise is not multiplied by M^2, as indicated by its noise model in Fig. 5.14(b).

To mathematically demonstrate the noise and power advantage of using SSPLL for high M-factor PLL, the phase noise of both the subsampling PD (SSPD) and the charge pump PD (CPPD) are
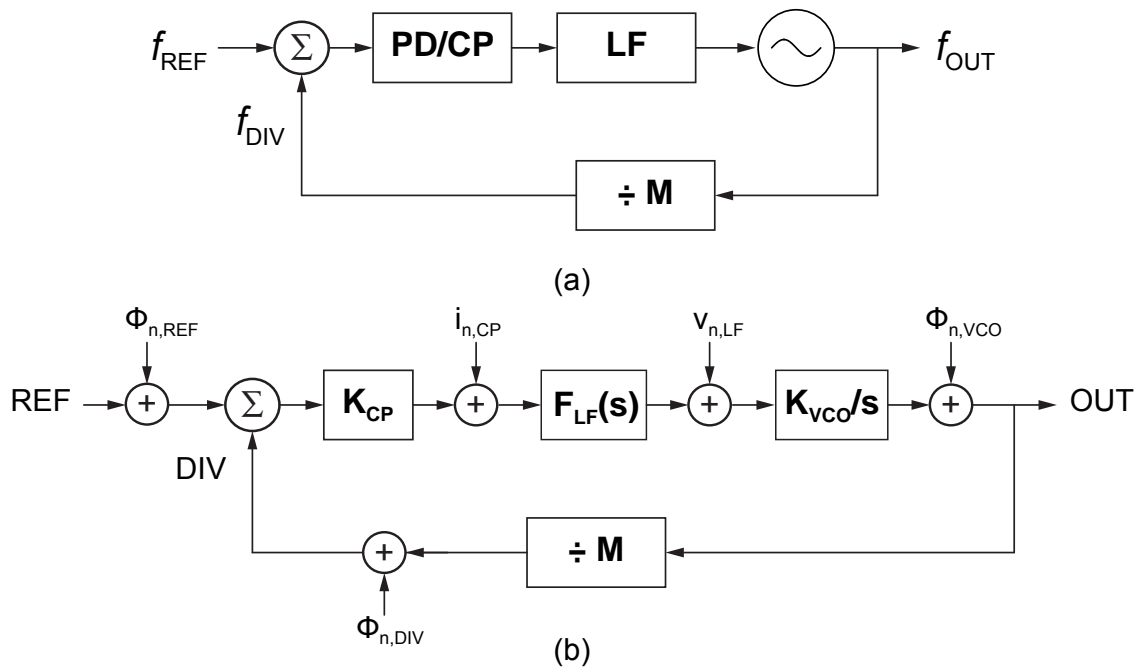
Figure 5.13: Charge pump PLL (CPPLL), (a) diagram and (b) phase noise model.
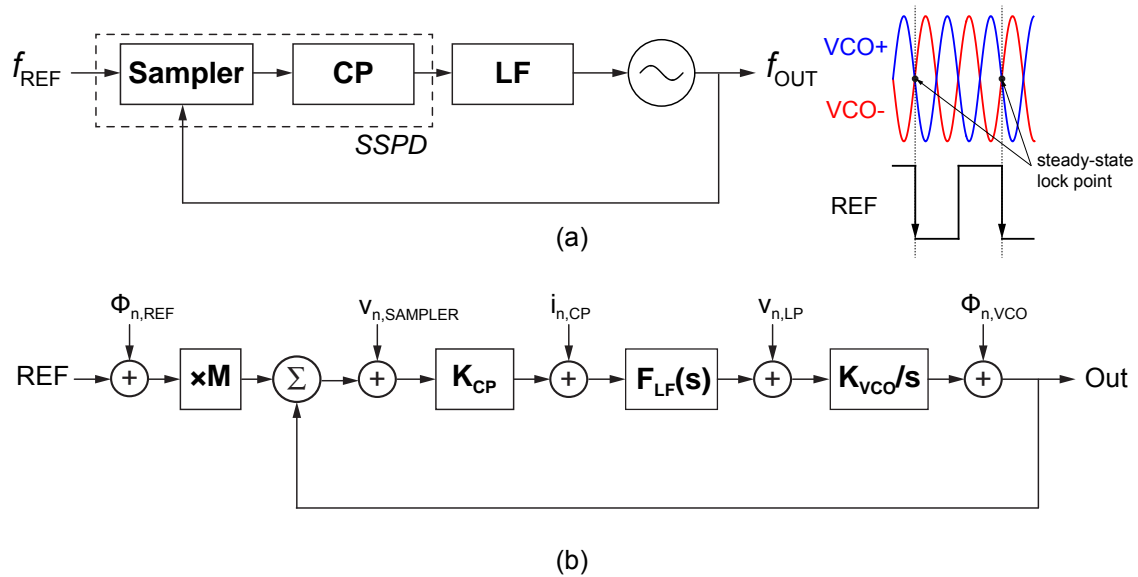
Figure 5.14: Subsampling PLL (SSPLL), (a) diagram and (b) phase noise model.

computed and compared as follows.

Using the phase noise model in Fig. 5.13(b), the CPPD phase noise transfer function can be

calculated as

$$H_{CP}(s) = \frac{\Phi_{n,OUT}}{i_{n,CP}} = \frac{F_{LF}(s) \cdot K_{VCO}/s}{1 + K_{CP} \cdot F_{LF}(s) \cdot K_{VCO}/s \cdot \frac{1}{M}} = \frac{M}{K_{CP}} \cdot H(s) \quad (5.7)$$

where $H(s)$ is the unity PLL close loop transfer function (i.e., $|H(0)| = 1$), with a 3-dB bandwidth proportional to its natural frequency of

$$\omega_{n,CP} = \sqrt{\frac{K_{CP} \cdot K_{VCO}}{M \cdot C_{1,CP}}} \quad (5.8)$$

where $K_{CP} = I_{CP}/(2\pi)$ and $C_{1,CP}$ is the CPPLL loop filter capacitor. For simplicity, consider thermal noise only. The CP current noise power, $\overline{i_{n,CP}^2}$ is given by

$$\overline{i_{n,CP}^2} = \alpha \cdot 4kT\gamma g_m \cdot \frac{T_{PFD}}{T_{REF}} \quad (5.9)$$

where α is the noise factor of the CP and T_{PFD} is the brief on-time of the PFD to eliminate the potential deadzone.

Similarly, using the phase noise model in Fig. 5.14(b), the SSPD phase noise transfer function is

$$H_{SS}(s) = \frac{\Phi_{n,OUT}}{i_{n,SS}} = \frac{F_{LF}(s) \cdot K_{VCO}/s}{1 + K_{SS} \cdot F_{LF}(s) \cdot K_{VCO}/s} = \frac{1}{K_{SS}} \cdot H(s) \quad (5.10)$$

Here assume both PLLs share the same close loop transfer function for a fair comparison. The SSPLL natural frequency is given by

$$\omega_{n,SS} = \sqrt{\frac{K_{SS} \cdot K_{VCO}}{C_{1,SS}}} \quad (5.11)$$

where $C_{1,SS}$ is the SSPLL loop filter capacitor. In the SSPD, when the charge pump samples the VCO output, it only dumps current to the loop filter for a fraction of the reference period to control the loop gain. Denote its on-time as T_{PUL}. Assuming the VCO has a differential amplitude of A_{VCO} and the charge pump transconductance is g_m, in the vicinity of the steady state, K_{SS} is given by

$$K_{SS} = A_{VCO} \cdot g_m \cdot \frac{T_{PUL}}{T_{REF}} \quad (5.12)$$

The SSPD charge pump current noise, $\overline{i_{n,SS}^2}$ can be estimated as

$$\overline{i_{n,SS}^2} = \alpha \cdot 4kT\gamma g_m \cdot \frac{T_{PUL}}{T_{REF}} \quad (5.13)$$

With (5.7), (5.8), (5.10) and (5.11), now compare the power consumption of the two charge pumps, assuming both PLLs have the same 3-dB bandwidth and in-band CP phase noise, i.e.,

$$\frac{K_{CP}}{M \cdot C_{1,CP}} = \frac{K_{SS}}{C_{1,SS}} \tag{5.14a}$$

$$\frac{M}{K_{CP}} \cdot i_{n,CP} = \frac{1}{K_{SS}} \cdot i_{n,SS} \tag{5.14b}$$

Plugging into (5.9) and (5.13), (5.14b) can be simplified as

$$\frac{I_{CP}}{I_{SS}} = \frac{\alpha_{CP}}{\alpha_{SS}} \cdot \frac{T_{PFD}}{T_{PUL}} \cdot \left(2\pi M \cdot \frac{A_{VCO}}{V_{OV}} \cdot \frac{T_{PUL}}{T_{REF}}\right)^2 \tag{5.15}$$

Since the PLL figure of merit (FoM) is defined by

$$FoM_{PLL} = 10\log_{10}\left(\frac{\sigma_{t,PLL}^2}{(1s)^2} \cdot \frac{P_{DC,PLL}}{1mW}\right), \tag{5.16}$$

the FoM improvement by SSPLL can be evaluated (approximately) with $10\log_{10}(I_{CP}/I_{SS})$. On the other hand, (5.14a) compares the silicon area cost of the two PLLs since it defines the loop capacitor ratio for the same ω_{3dB}, once the CP current ratio I_{CP}/I_{SS} and the SSCP fractional on-time T_{PUL}/T_{REF} are determined.

Now apply (5.15) in a 1-V deep sub-micron CMOS process. A reasonable assumption can be made that $T_{PFD} = 100$ ps, $A_{VCO} = 0.8$ V and $V_{OV} = 0.2$ V. Typical T_{PUL}/T_{REF} can vary from 1/100 to 1, which is greatly dependent on the actual design. $\alpha_{CP}/\alpha_{SS} \approx 0.5 - 2$, and is set to unity for simplicity. Fig. 5.15 shows the calculated FoM improvement as a function of the multiplication factor M with various SSPD fractional on-time for a 30 MHz clock reference. It is obvious that SSPLL offers a significant better FoM when M is high.

5.4.2   Conventional SSPLL: Power Stability Trade-off

A divider-less SSPLL cannot distinguish different integer numbers of reference periods due to the periodicity of the VCO sinusoidal output, and thereby is prone to false frequency acquisition and external disturbances. To address this issue, a separate frequency lock loop (FLL), which is simply a CPPLL with a deadzone PFD, is employed to ensure correct locking, as shown in Fig. 5.16. The dead-zone PFD regards the divider output and the reference clock as identical if their phase difference falls within the predefined deadzone value and thereby disables its own charge pump (FLL-CP).

Since the FLL-CP injects no current (and thereby no noise) to the loop once the PLL is locked, it has long been believed that the FLL-CP power can be minimized. However, for high M-factor SSPLLs, this can lead to severe stability issues. To understand this issue, the loop gain and phase margin of the two loops in Fig. 5.16 are derived as follows.

For the subsampling loop, the loop gain is given as

$$L_{SS}(s) = \frac{K_{SS}K_{VCO}}{C_1 + C_2} \cdot \frac{1}{s^2} \frac{1 + s/\omega_z}{1 + s/\omega_{p3}} = K_{SS} \cdot L_0(s) \tag{5.17}$$
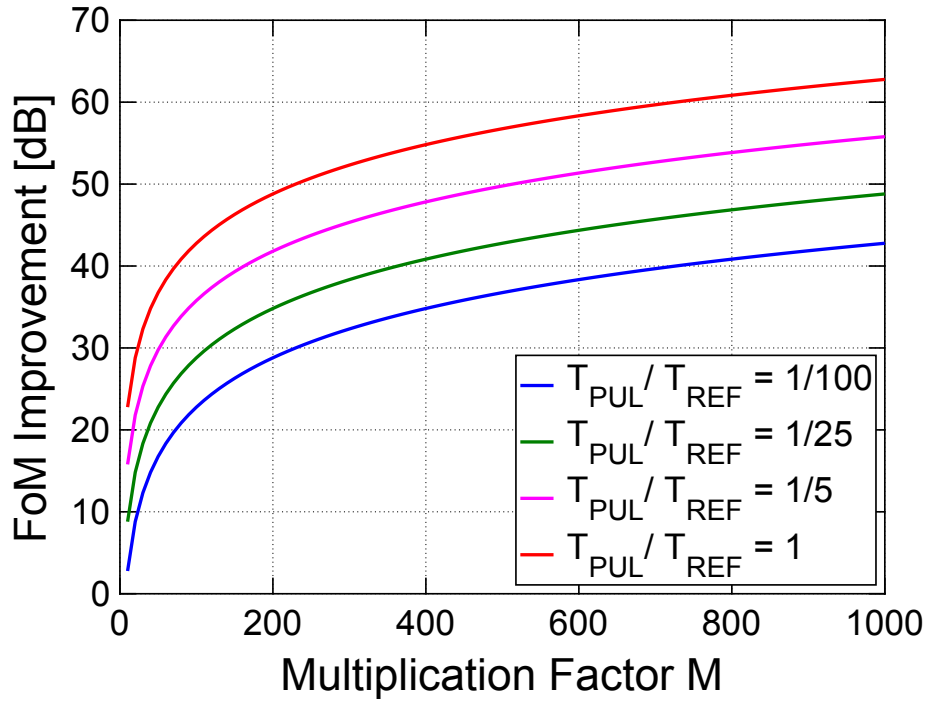
Figure 5.15: FoM improvement of SSPLL compared with CPPLL.

where $\omega_z = 1/(R_1 C_1)$, $\omega_{p3} = 1/(R_1 C_{eq})$ and $C_{eq} = C_1 C_2/(C_1 + C_2)$. For the frequency lock loop, its loop gain is

$$L_{FLL}(s) = \frac{1}{M} \cdot \frac{K_{FLL} K_{VCO}}{C_1 + C_2} \cdot \frac{1}{s^2} \frac{1 + s/\omega_z}{1 + s/\omega_{p3}} = \frac{K_{FLL}}{M} \cdot L_0(s) \tag{5.18}$$

where $K_{FLL} = I_{FLL-CP}/(2\pi)$, same as the previous definition in CPPLL. Both loops contains two poles at the origin, one zero ω_z and one out-of-band pole ω_{p3}. The phase margin of such loop can be calculated as

$$PM = \tan^{-1}\left[4\zeta^2\left(1 + \frac{1}{32\zeta^2}\right)\right] - \tan^{-1}\left[4\zeta^2 \frac{C_{eq}}{C_1}\left(1 + \frac{1}{32\zeta^2}\right)\right] \tag{5.19}$$

where the damping factor ζ of each loop is given by

$$\zeta_{SS} = \frac{R_1}{2}\sqrt{K_{SS} K_{VCO}(C_1 + C_2)} \tag{5.20a}$$

$$\zeta_{FLL} = \frac{R_1}{2}\sqrt{\frac{K_{FLL} K_{VCO}(C_1 + C_2)}{M}} \tag{5.20b}$$

Define the loop gain ratio LGR as

$$LGR = \frac{K_{SS}}{K_{FLL}/M} = \left(\frac{\zeta_{SS}}{\zeta_{FLL}}\right)^2 \tag{5.21}$$
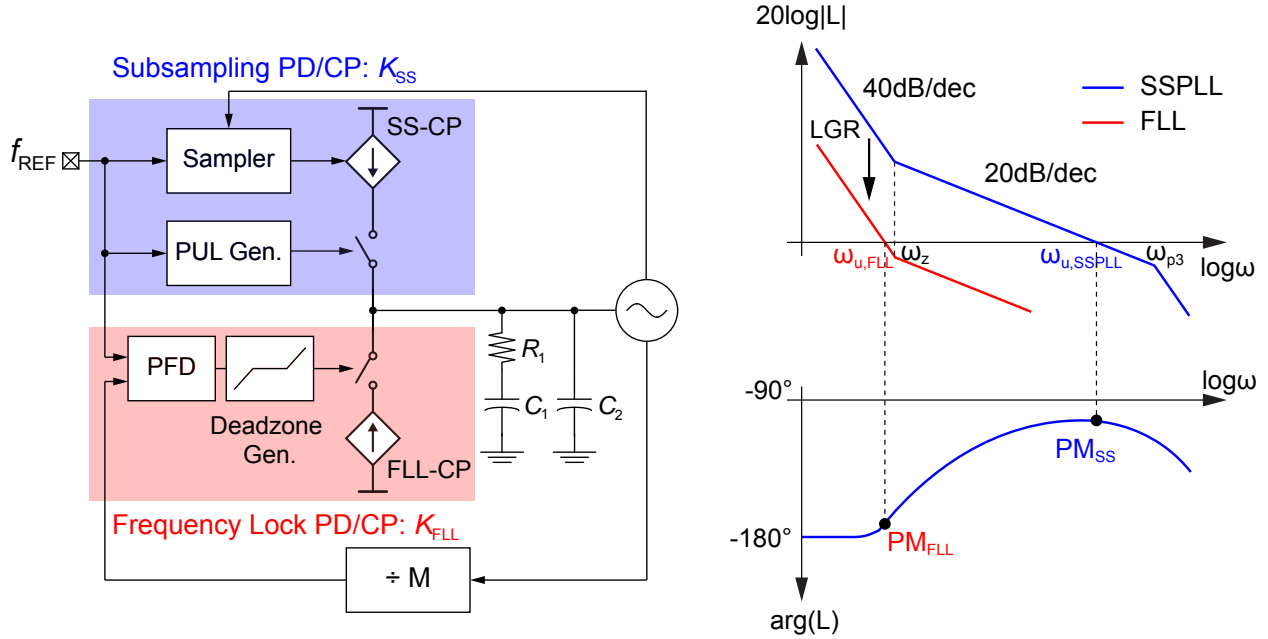
Figure 5.16: Conventional SSPLL with the frequency lock loop, showing the block diagram and stability issues for the frequency lock loop.

For a given damping factor, there exists an optimal capacitor ratio C_1/C_2 such that the phase margin is maximized [144]. That is, when $\zeta = \frac{1}{2}\sqrt[4]{C_1/C_{eq}}$, it gives

$$\mathrm{PM}_{max} = \tan^{-1}\left(\frac{C_1/C_2}{2\sqrt{1 + C_1/C_2}}\right) \tag{5.22}$$

Supposing the subsampling loop is designed with the maximized phase margin, the phase margin of the FLL for different LGRs can thereby be computed, as shown in Fig. 5.17. When LGR > 9, the phase margin of the FLL falls below 50°, causing grave stability issues. To illustrate how this affects the power consumption of the FLL, take a hypothetical SSPLL with $M = 480$ as an example. Assume the overdrive voltage $V_{OV} = 0.2\ V$, the VCO differential amplitude $A_{VCO} = 0.8\ V$ and the fractional pulse width $T_{PUL}/T_{REF} = 0.05$. Having LGR=1 requires the FLL-CP current be 600 times higher than the SS-CP current. By contrast, if the two CPs burns the same power, the LGR jumps up to 600, which pulls the PM of the FLL to below 10°, even though the subsampling loop has a better than 55° phase margin.

To save power, [145] duty-cycled the FLL aggressively, at the cost of an increase in the re-acquisition time upon a sudden lock failure. In [146], the FLL was replaced by a 150 μW disturbance correction loop, but its lock range is limited, so that the PLL may still lose lock with large disturbances.
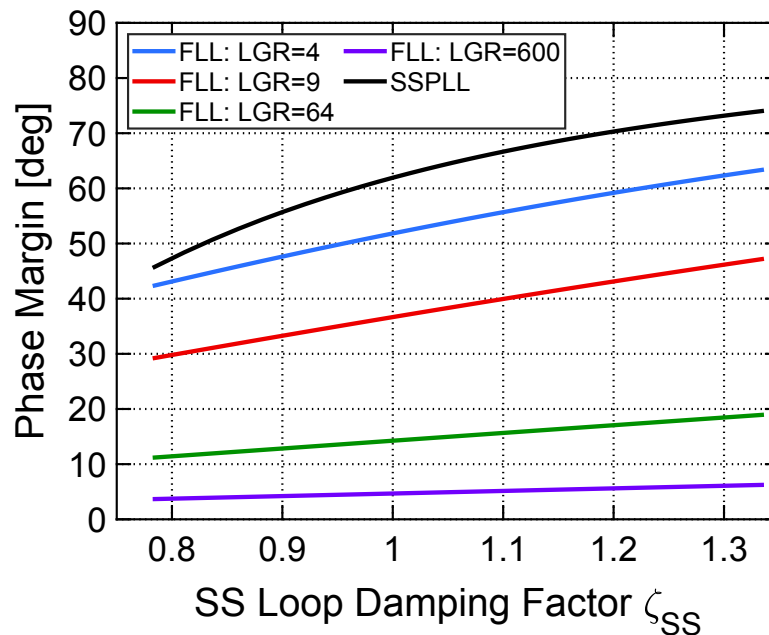
Figure 5.17: Calculated phase margin of conventional SSPLL and FLL at different LGRs.

5.4.3   Proposed SSPLL

This work presents a SSPLL operating at $13.2-17.2$ GHz with a multiplication factor $M = 480$. It dissipates only 6.6 mW including an always-on FLL and achieves an integrated jitter (1 kHz $-$ 100 MHz) of 153.4 fs. This is made possible by employing a new subsampling charge pump/loop filter (SS-CP/LF) topology, which breaks the harsh tradeoff between the loop stability and the power consumption.

5.4.3.1   Block Diagram

The stability issue associated with the conventional dual loop PLL can also be visualized in the Bode plot. As illustrated in Fig. 5.18(a), simply reducing the FLL 'dc' loop gain by LGR without changing its zero location ω_z degrades its phase margin. On the other hand, however, if the zero of the FLL is also shifted down accordingly, the PM loss of the FLL can be recovered, as shown in Fig. 5.18(b).

One naive way of reducing $\omega_{z,FLL}$ is to introduce a second loop filter for the FLL. However, the additional loop filter incurs a noise penalty even if the FLL turns off when the VCO is locked. More importantly, it also requires a second varactor, so that there will be infinite combinations of varactor control voltages $V_{CTRL,FLL}$ and $V_{CTRL,SS}$ which produce the same VCO frequency. This is undesirable since the loop may settle to a suboptimal solution.
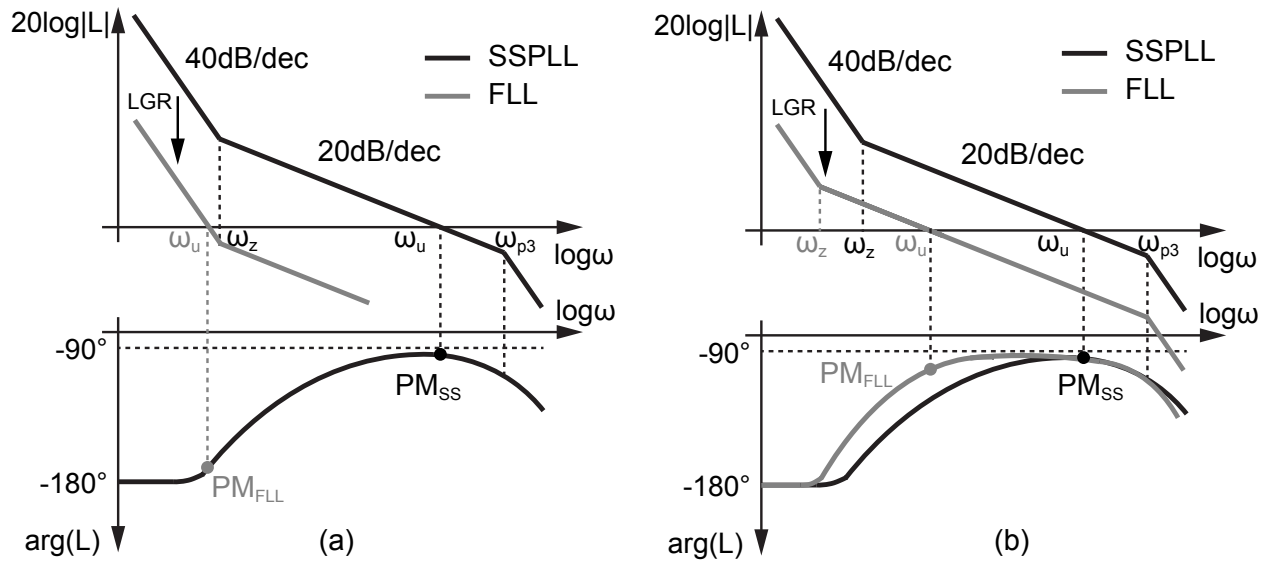
Figure 5.18: Effect of LGR on the stability of FLL, in (a) the classical case and (b) the proposed case.
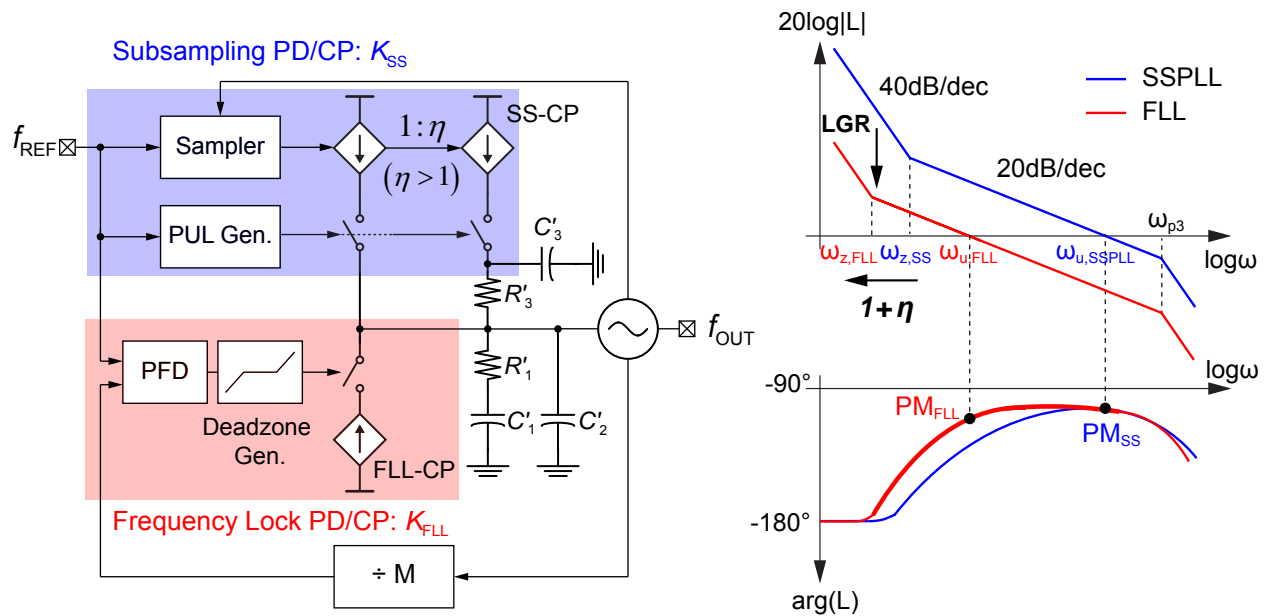
Figure 5.19: Proposed SSPLL with the frequency lock loop, showing a new charge pump/loop filter topology to solve the stability and power trade-off.

Fig. 5.19 shows the block diagram of the proposed SSPLL. The subsampling loop employs two copies of SS-CPs with a current split ratio of $1 : \eta$. They are controlled by the same VCO sampler while injecting current into two distinct nodes of the loop filter. The second injection node is created

by adding another RC leg ($R_3' C_3'$) to the loop filter, where $R_3' = R_1'$ and $C_3' = C_1'$. The FLL remains unaltered.

5.4.3.2 Loop Gain Analysis

With this new topology, the transfer functions of the subsampling loop and the FLL are re-examined. For the subsampling loop, it holds

$$L_{SS}'(s) = \frac{K_{SS}K_{VCO}}{C_1' + C_2' + C_3'} \cdot \frac{1}{s^2} \frac{1 + s/\omega_{z,SS}}{1 + s/\omega_{p3}'} \tag{5.23}$$

where $\omega_{z,SS} = (1+\eta)/(R_1' C_1')$ and $\omega_{p3}' = 1/(R_{eq}' C_{eq}')$. Note that $R_{eq}' = R_1'/2$ and $C_{eq}' = 2C_1' C_2'/(2C_1' + C_2')$, which reflects the parallel combination of all the resistors and capacitors in the loop filter.

For the frequency lock loop, its loop transfer function can be written as

$$L_{FLL}'(s) = \frac{1}{M} \cdot \frac{K_{FLL}K_{VCO}}{C_1' + C_2' + C_3'} \cdot \frac{1}{s^2} \frac{1 + s/\omega_{z,FLL}}{1 + s/\omega_{p3}'} \tag{5.24}$$

where $\omega_{z,FLL} = 1/(R_1' C_1')$. Clearly, with the proposed loop design, the subsampling loop and the FFL share the same pole locations but distinct zero locations. In addition to downshifting the FLL loop gain magnitude by a factor of LGR, its zero is also left-shifted by $(1 + \eta)$ from the subsampling loop zero, i.e., $\omega_{z,FLL} = \omega_{z,SS}/(1 + \eta)$, which alters the loop gain phase of the FLL and improve its PM. Since the loop gain magnitude falls at 40 dB/dec before the zero, the SS-CP current split ratio should be set to

$$1 + \eta = \sqrt{LGR} \tag{5.25}$$

so that the FLL PM is comparable with the subsampling loop PM.

The efficacy of the proposed SS-CP/LF topology can be validated using the hypothetical M =480 SSPLL from the previous discussion. The charge pump current ratio for different LGRs are summarized in Table 5.3. Same as Fig. 5.17, suppose the PM of the subsampling loop has been optimized for a predefined damping factor ζ_{SS}. Now the SS-CP needs to be split proportionally to compensate the FLL PM at a given LGR, which is set based off the power budget. With no action taken, the FLL PM quickly falls below $20°$ when the LGR increases, as shown in Fig. 5.17. However, if the SS-CP splits at $\eta = \sqrt{LGR} - 1$, the FLL PM is always better than the SSPLL for all LGRs, as depicted in the top subplot in Fig. 5.20.

In practice, it is desirable to keep a constant η while varying the LGR. Note that the LGR is subject to change whenever the FLL-CP current is varied (to save power or to change the FLL loop bandwidth) or the SS-CP fractional on-time T_{PUL}/T_{REF} is modified (to change the SSPLL loop bandwidth). Fig. 5.20 bottom plot shows how the FLL PM changes at various LGRs for $\eta = 4$, which is still better than $60°$ even when the LGR reaches $600-900$. This proves the flexibility and robustness of the proposed SS-CP/LF topology.

Table 5.3: CHARGE PUMP CURRENT RATIO AT VARIOUS LGR

LGR	CP Current Ratio I_{FLL-CP}/I_{SS-CP}
1	603.2
4	150.8
64	9.5
600	1
900	0.67

Assume $M = 480$, $T_{PUL}/T_{REF} = 0.05$.

5.4.3.3 Loop Filter Design

It is critical to emphasize that the proposed SS-CP/LF does not incur extra power or area penalty. Suppose that all the loop components are identical for the two PLLs in Fig. 5.16 and Fig. 5.19 except the SS-CP and the loop filter. Since the SS-CP in Fig. 5.19 is formed by splitting the Fig. 5.16 by a ratio of $1 : \eta$, the power consumption of the proposed topology remains the same. To maintain the same loop transfer function, it requires that the total loop capacitance and the pole/zero frequencies of the two SSPLLs be equal. Combining (5.17) and (5.23) yields

$$C_1 + C_2 = 2C_1' + C_2' \tag{5.26a}$$

$$\frac{1}{R_1 C_1} = \frac{1 + \eta}{R_1' C_1'} \tag{5.26b}$$

$$R_1 \cdot \frac{C_1 C_2}{C_1 + C_2} = \frac{R_1'}{2} \cdot \frac{2C_1' C_2'}{2C_1' + C_2'} \tag{5.26c}$$

and $C_3' = C_1'$, $R_3' = R_1'$. Since $C_2 \ll C_1$, (5.26) can be reduced to

$$C_1' = C_3' = C_1/2 \tag{5.27a}$$

$$C_2' = C_2/(1 + \eta) \tag{5.27b}$$

$$R_1' = R_3' = 2(1 + \eta) \cdot R_1 \tag{5.27c}$$

As the loop capacitor (and VCO) occupies the most space for a SSPLL, the proposed design almost does not cost extra area.

5.4.3.4 Phase Noise Analysis

Lastly, it is important to examine the phase noise characteristics of the proposed SS-CP/LP and its impact on the overall PLL phase noise. Fig. 5.21 depicts the equivalent noise model of the proposed SSPLL.
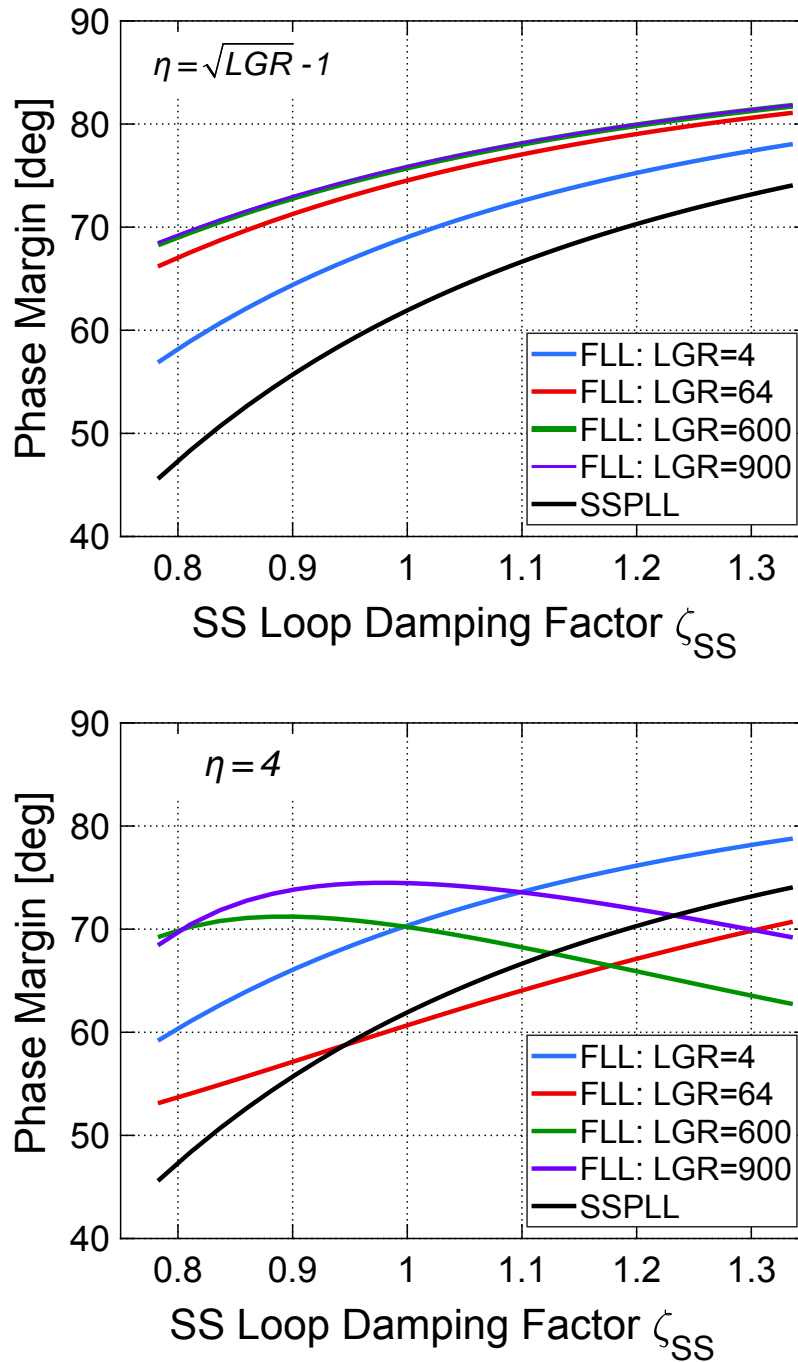
Figure 5.20: Calculated phase margin of different SSPLL loop configurations, (top) proposed SSPLL with $\eta = \sqrt{LGR} - 1$, and (bottom) proposed SSPLL with $\eta = 4$.
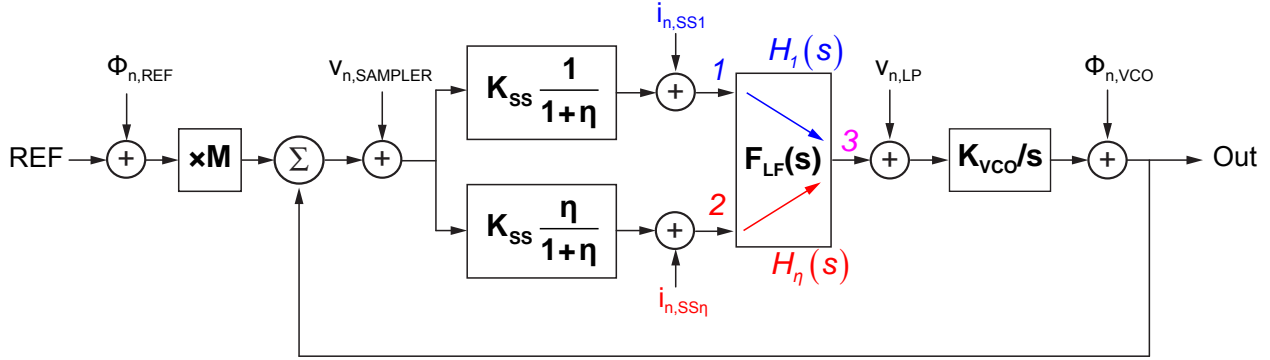
Figure 5.21: Phase noise model of the proposed SSPLL.

The current noise of two SS-CPs in Fig. 5.19 are denoted as $i_{n,SS1}$ and $i_{n,SS\eta}$ respectively by their current ratio. Based on Fig. 5.21, the noise transfer function can be derived as

$$\Phi_{n,OUT} = \frac{1}{1 + L'_{SS}(s)} \cdot \left(i_{n,SS1} H_1(s) + i_{n,SS\eta} H_\eta(s) \right) \cdot \frac{K_{VCO}}{s} \tag{5.28}$$

where $L'_{SS}(s)$ is the SSPLL loop transfer function defined in (5.23), and $H_1(s)$ and $H_\eta(s)$ represent the loop filter transimpedance for each SS-CP. (5.28) can be further expanded as

$$\Phi_{n,OUT} = \frac{1}{K_{SS}} \cdot \frac{L'_{SS}(s)}{1 + L'_{SS}(s)} \cdot \left(i_{n,SS1} \frac{1 + sR'_1 C'_1}{1 + s/\omega_{z,SS}} + i_{n,SS\eta} \frac{1}{1 + s/\omega_{z,SS}} \right) \tag{5.29}$$

The relationship between $i_{n,SS1}$, $i_{n,SS\eta}$ and $i_{n,SS}$ (defined in (5.13)) depends on whether the noise of the two SS-CPs are correlated or not, which is related to the actual circuit implementation. If $i_{n,SS1}$ and $i_{n,SS\eta}$ are fully correlated, i.e.,

$$i_{n,SS1} = i_{n,SS} \cdot \frac{1}{1 + \eta} \tag{5.30a}$$

$$i_{n,SS\eta} = i_{n,SS} \cdot \frac{\eta}{1 + \eta} \tag{5.30b}$$

(5.29) can be simplified as

$$\Phi_{n,OUT} = \frac{1}{K_{SS}} \cdot \frac{L'_{SS}(s)}{1 + L'_{SS}(s)} \cdot i_{n,SS} \tag{5.31}$$

which is the same as (5.10), indicating that the proposed SS-CP does not affect the phase noise performance. On the other hand, if $i_{n,SS1}$ and $i_{n,SS\eta}$ are completely uncorrelated, there will be

$$\overline{i_{n,SS1}^2} = \overline{i_{n,SS}^2} \cdot \frac{1}{1 + \eta} \tag{5.32a}$$

$$\overline{i_{n,SS\eta}^2} = \overline{i_{n,SS}^2} \cdot \frac{\eta}{1 + \eta} \tag{5.32b}$$

As a result, the phase noise from the two SS-CPs combined is higher. It can be approximated that the power of $\Phi_{n,OUT}$ in (5.29) increases by a factor of $(1 + \eta)$. For instance, an equal split will raise the SS-CP phase noise contribution by 3 dB, whereas $\eta = 4$ will lead to around 7 dB increase. However, the overall SSPLL in-band phase noise will not be affected with a reasonable η, especially for high M-factor SSPLLs, since the in-band PN is dominated by the reference, instead of the SS-CP.

As for the loop filter phase noise, it can be shown that the LF noise transfer function remains unchanged, i.e.,

$$H_{LF} = \frac{\Phi_{n,OUT}}{v_{n,LF}} = \frac{s \cdot K_{VCO}}{s^2 + 2\zeta_{SS} \cdot \omega_n \cdot s + \omega_n^2} \tag{5.33}$$

However, the proposed loop filter has a higher voltage noise,

$$\overline{v_{n,\text{conventional}}^2} = 4k_B T R_1 \tag{5.34a}$$

$$\overline{v_{n,\text{proposed}}^2} = 2k_B T R_1' = (1 + \eta) \cdot 4k_B T R_1 \tag{5.34b}$$

Again, the LF does introduce a slight noise penalty, but remains non-dominant in the PLL output noise spectrum for most cases.

Overall, although in the proposed topology both SS-CP and LF contribute roughly $(1 + \eta)$ more phase noise (worst case scenario), it is hardly visible in the PLL output phase noise spectrum, since its in-band PN is dominated by the reference while the out-band PN mostly comes from the VCO. On the other hand, it substantially reduces the FLL-CP power and improves it phase margin. The benefits outweigh the costs considerably.

5.4.4 Circuit Implementation

Fig. 5.22 provides the schematic of the proposed SS-CP which implements a current ratio of $\eta = 4$. The sampler uses $C_S = 10$ fF and the overall sampling capacitor is around 25 fF including the SS-CP input parasitics. In the main path, the sampled VCO waveform is converted to current by a source degenerated g_m stage for a better linearity. The current is mirrored into five copies, four of which ($k = 1 - 4$) have their output nodes $O\langle k \rangle$ and dump nodes $D\langle k \rangle$ connected respectively to create one SS-CP, whereas the remaining copy ($k = 0$) forms the other SS-CP. In each SS-CP, the dump node tracks the output node through a rail-to-rail unity gain buffer, which eliminates disruptive charge redistribution from $D\langle k \rangle$ to $O\langle k \rangle$ at the steady state. Fig. 5.23 provides the schematic of the unity gain buffer. Note that the accuracy of the split ratio η is determined by the random transistor mismatch, since no current flows through R_3' at the steady state so that the dc voltages of all the $O\langle k \rangle$ and $D\langle k \rangle$ are identical. In addition, a dummy path is included to prevent the BFSK modulation of the VCO tank and to improve the reference spur.

In terms of the noise performance, since M_{N1} and M_{P1} belongs to the input amplifier stage, which is shared by all five copies, their noise current are considered 'correlated' and thereby will not add more phase noise because of the split. On the other hand, noise from M_{N2} and M_{P2} in the mirrored sides are uncorrelated, which will contribute around five times more phase noise after the split.

The SS-CP fractional on-time can be tuned in the range of $\text{T}_{PUL}/\text{T}_{REF} \in (1/60, 1/15)$, which allows to change the PLL loop bandwidth as needed. The nominal loop bandwidth is set at around 2 MHz (= $f_{REF}/15$). Fig. 5.24 shows the component values used in the loop filter. With LGR = 64, the phase margin of the two loops are both 53°.

The PLL utilizes a Class-B LC VCO with an additional tail LC tank as the noise filter. The fundamental tank inductor is implemented using the top copper layer (M10) with a patterned ground shield (M1) to reduce the dielectric loss from the substrate. EM simulations were performed, based on which it realizes L = 767 pH, Q = 15.8 at 14.5 GHz and a self resonance frequency (SRF) of 40 GHz. The tail tank has a single-ended inductor which sits on the M10 layer as well but without the patterned shield for a higher SRF. EM simulations show that it exhibits L = 250 pH, Q = 16 at 29 GHz and SRF = 82 GHz. The VCO consumes around 3 mA current from a 0.8 V supply. Post-layout simulations indicate that the VCO can be tuned from 13.32 GHz to 17.07 GHz, with K_{VCO} varying from 150−280 MHz/V over the entire tuning range.

In the frequency lock loop, it employs a differential C^2MOS master-slave latch to perform the first stage divide-by-2 [147], and the output is further divided down by DFF-based static dividers. A conventional dead-zone PFD and charge pump as in [148] are implemented to bring the phase of the divider output and the reference clock close enough for the SSPLL to lock.

Fig. 5.25 shows the simulated PLL phase noise along with the contribution breakdown from 1 kHz to 100 MHz. The reference phase noise is measured data from the signal generator R&S® SMA100A at 29.6 MHz.

5.5   Sensor Core

The EPR spectrum is measured using a capacitively coupled passive LC resonator due to its superior sensitivity and power performance [149]. Fig. 5.5 shows its block diagram. The signal readout circuit consists of a passive mixer and a VGA. To avoid flicker noise from the baseband circuits, the sensor driver is modulated at 50 kHz, which is derived from the reference clock, as shown in Fig. 5.26. Details about the sensor core and the signal readout circuits have been provided in Chapter 4.

5.6   Electrical Characterization

The prototype is fabricated in the TSMC 28-nm bulk CMOS process. Fig. 5.27 shows the chip micrograph, which includes two EPR sensors driven by one single SSPLL. It consumes 9.6 mW with one sensor turned on and 11.4 mW with both sensors turned on. This section provides electrical characterization results of the SSPLL since the sensor has been characterized in Chapter 4.
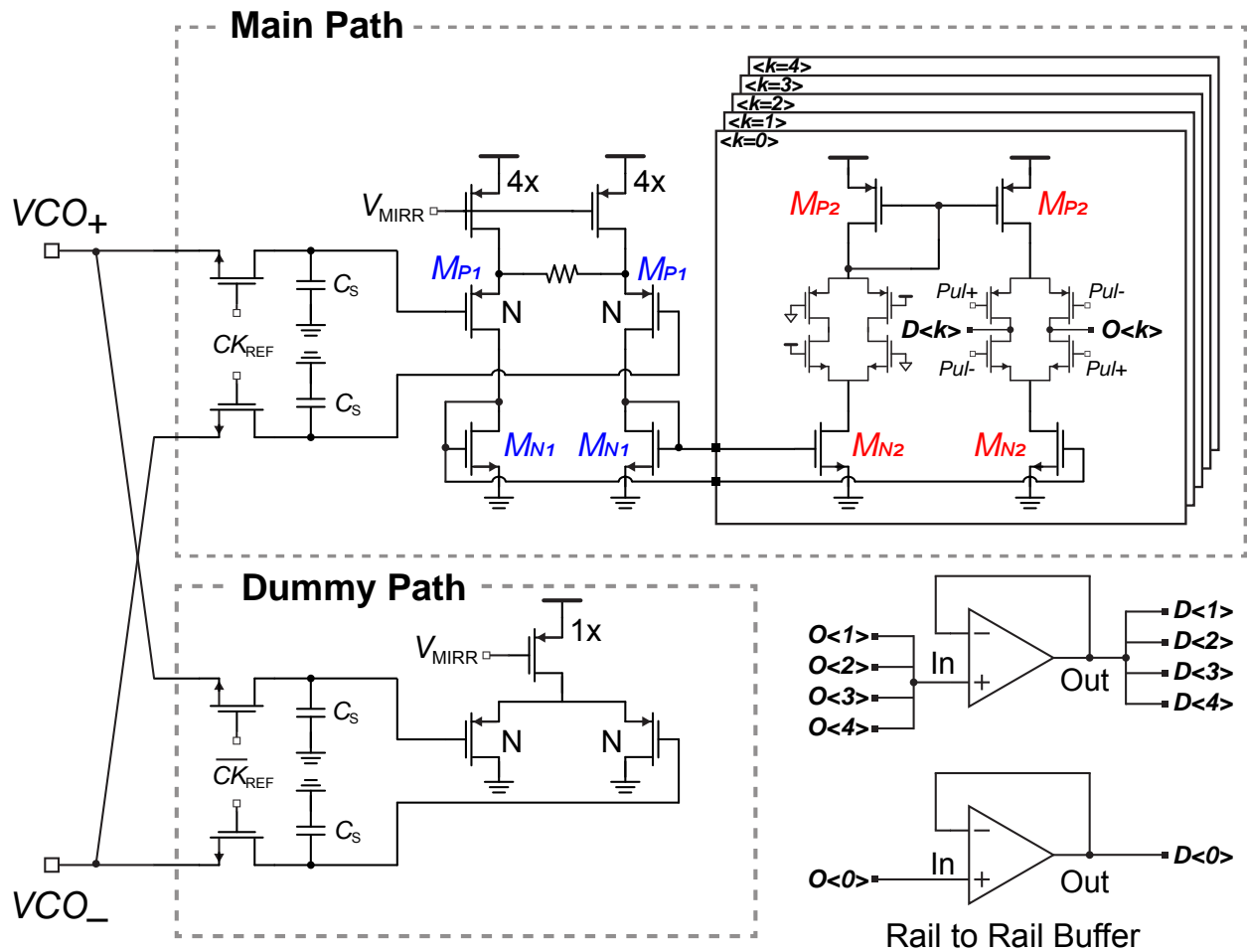
Figure 5.22: Schematic of the proposed subsampling charge pump, realizing a current ratio of $\eta = 4$.

5.6.1   VCO

The VCO consumes 2.4 mW power with V_{DD} = 0.8 V. To characterize its frequency tuning range and phase noise, the VCO varactor control node V_{CTRL} is disconnected from the PLL loop filter and biased by an external DAC. The VCO output is divided by 2 and connected to the spectrum analyzer (Agilent N9030A) through a CML buffer. Fig. 5.28 shows the measured oscillation frequency for V_{CTRL} = 0.2 − 1 V across all capacitor bank combinations. The VCO covers a frequency range of 13.23 − 17.27 GHz, exhibiting a 26.5% tuning capability. The measured phase noise at the divider output is given in Fig. 5.29, which corresponds to -108.51 dBc/Hz at 1 MHz offset. The VCO FoM is thereby estimated to be -187.7 dBc/Hz.
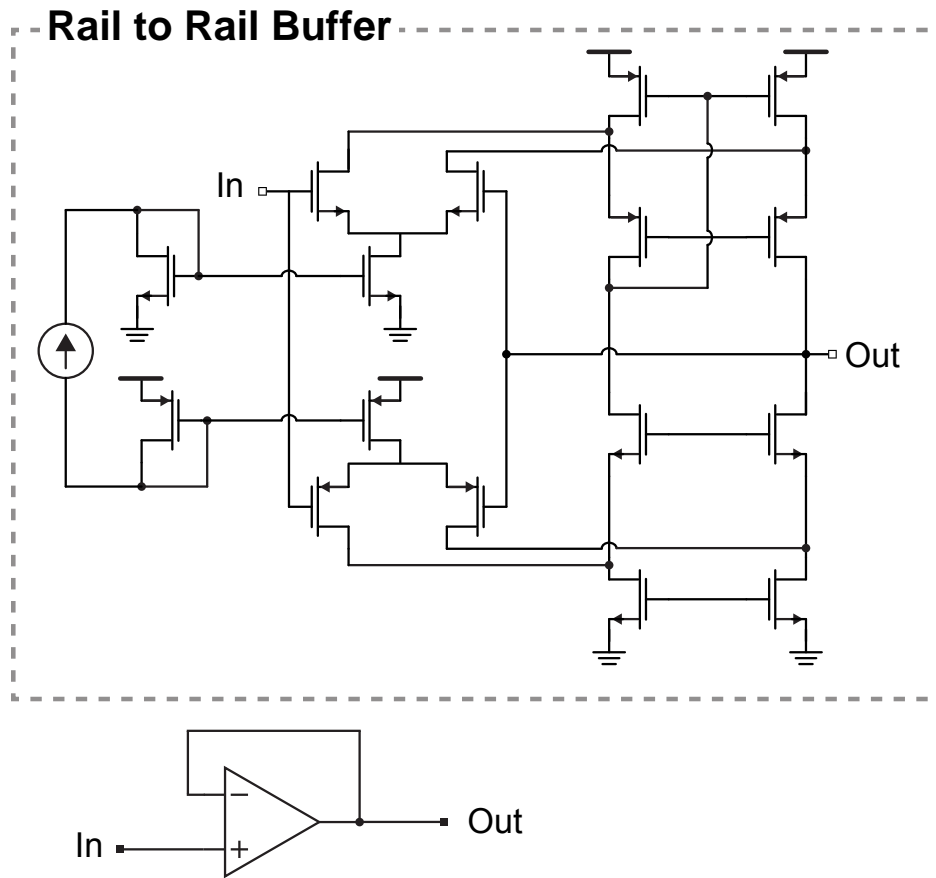
Figure 5.23: Schematic of the rail to rail unity gain buffer used in the SS-CP.
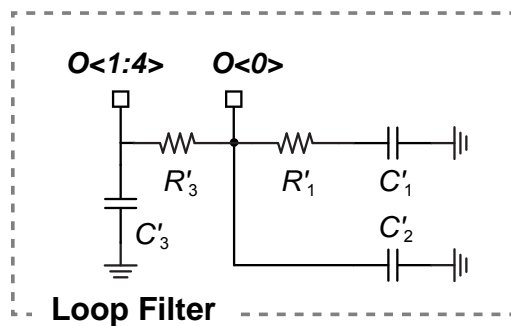
C'_1	R'_1	PM_{SS}
47.86 pF	24.4 kΩ	52.1°
C'_2	R'_3	PM_{FLL}
2.3 pF	24.4 kΩ	52.6°
C'_3		
47.86 pF		

Figure 5.24: Schematic and component values of the loop filter.

5.6.2 SSPLL

The SSPLL occupies 0.24 mm^2, with most area taken by the VCO and the loop filter. The detailed floorplan can be found in Fig. 5.27. The PLL consumes 6.6 mW power in total (excluding the output
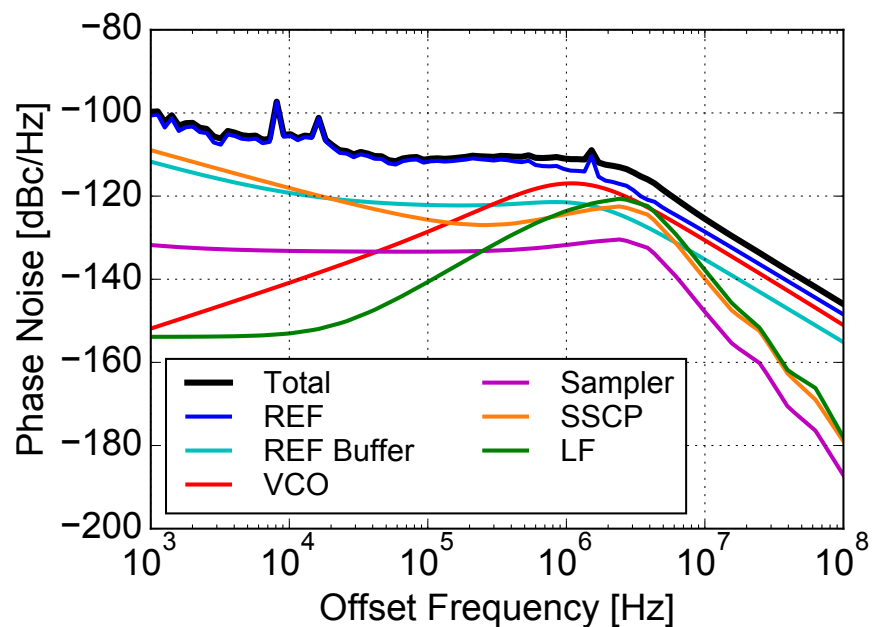
Figure 5.25: Simulated SSPLL phase noise with sub-block contribution breakdown.
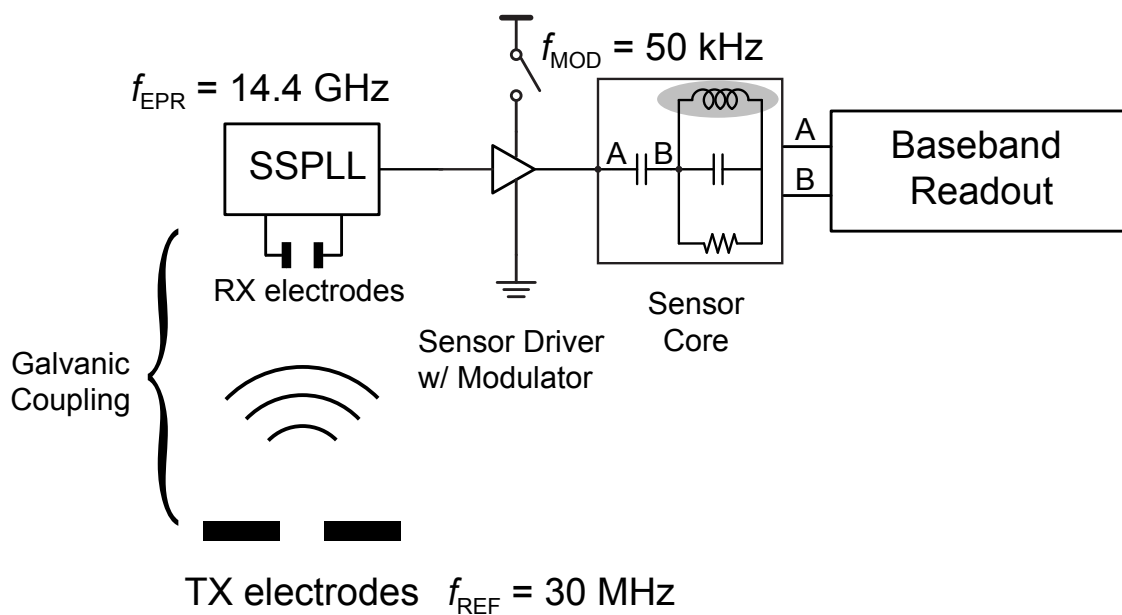
Figure 5.26: Simplified block diagram of the EPR spectrometer.
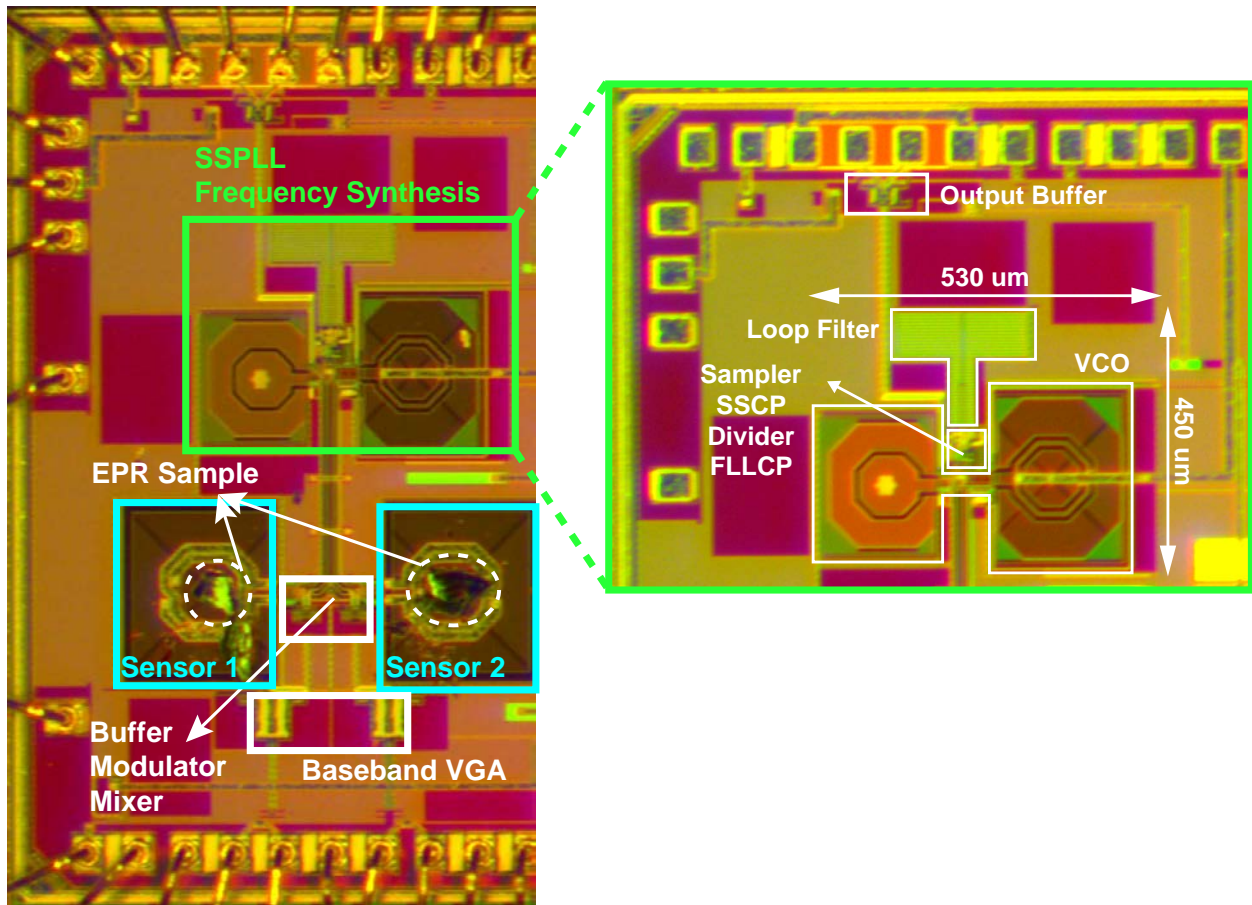
Figure 5.27: Chip micrograph.

CML pad driver), with V_{DDA} = 1.2 V for all the analog blocks and V_{DD} = 0.8 V for the VCO, VCO buffer and the frequency divider. Note that the VCO supply is separated from the other building blocks. Power contribution from each building block is given in Fig. 5.30.

The PLL has a multiplication factor of 480 with an input reference frequency at 30 MHz, which is provided by a signal generator (R&S® SMA100A) for the phase noise and spur measurements. The output of the signal generator is converted to a square wave by a clock buffer (TI's LMK1C110x) to suppress the impact from the power supply noise. Fig. 5.31 and Fig. 5.32 shows the measured phase noise and power spectrum at the divider output. The measured PN at 1 MHz offset is -112 dBc/Hz, which corresponds to -106 dBc/Hz at the PLL output. The integrated jitter (1 kHz − 100 MHz) is 153.4 fs and the in-band PN is dominated by the reference. The reference spur is -62.3 dBc when translated to 14.23 GHz.

The jitter and spur performance across the PLL tuning range are characterized. Fig. 5.33 and Fig. 5.34 provide the phase noise and spur measurements at 13.6 GHz and 16.8 GHz carrier, respectively. Measured jitter (1 kHz − 100 MHz) and spur at other frequencies are summarized in Fig. 5.35. It can be seen that the PLL jitter is relatively constant over the entire tuning range
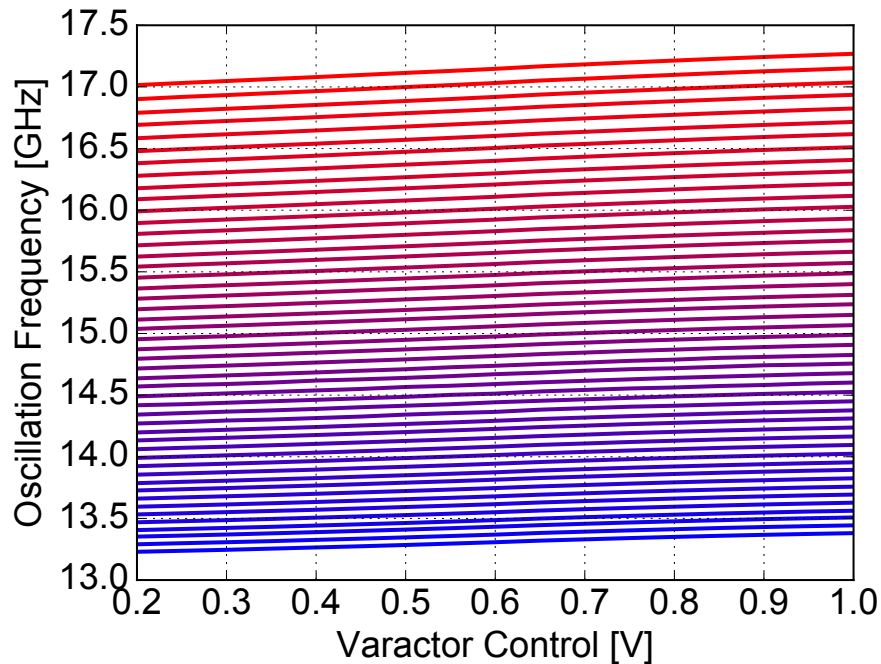
Figure 5.28: Measured VCO tuning range.

(146−159 fs), with a small improvement at the upper frequency band, which could be a result of a better source noise performance. On the other hand, the reference spur increases from -66 dBc to -54 dBc when the carrier frequency moves to the high side, since the VCO becomes more prone to the periodic disturbances from the sampler and the SS-CP as its effective tank capacitance reduces.

Table 5.4 benchmarks the proposed SSPLL with recent prior-art beyond-10GHz PLLs with M-factor > 300. It achieves the best jitter, FoM$_{JIT}$ and FoM$_{JIT,M}$.

It worth mentioning that although FoM$_{JIT}$ is the most widely used figure of merit for PLL performance benchmarking, FoM$_{JIT,M}$, which accounts for the multiplication factor, suits better for PLLs with f_{REF} < 100 MHz. This is based on the observation that the phase noise of sub-100 MHz high performance crystal oscillators and signal generators do not scale with the operation frequency by M^2. Instead, their phase noise only increases by 3 dB or even less when the frequency doubles. For instance, the same SSPLL can be locked to $2f_{REF}$ (i.e., $M = 240$), under which circumstance it exhibits almost 3 dB better FoM$_{JIT}$, while FoM$_{JIT,M}$ remains the same, as shown in Table 5.4. This provides a strong support for using FoM$_{JIT,M}$. In fact both FoM$_{JIT,M1}$ and FoM$_{JIT,M2}$ have been used in many prior works [150–152] for PLL comparison.

5.6.3   Galvanically Coupled SSPLL

To understand how galvanic coupling influences the SSPLL performance. A 29.76 MHz reference source is galvanically coupled to the SSPLL using the configuration described in Fig. 5.7 through a

Table 5.4: PERFORMANCE COMPARISON WITH HIGH MULTIPLICATION FACTOR PLLs

	This Work		VLSI'21 [153]	JSSC'20 [154]	ISSCC'18 [155]	ISSCC'17 [156]	ISSCC'16 [157]
COMS Tech.	**28 nm**		28 nm	45 nm	65 nm	65 nm	28 nm
Architecture	**Analog SSPLL**		Digital ROSPLL	Analog RSPLL + ILFM	Digital BBPLL	ADPLL	Analog SSPLL
f_{REF} [MHz]	**30**	**60**	50	80	52	100	40
f_{OUT} [GHz]	**13.2-16.5**		24-31	33.6-36	20.4-24.6	50.2-66.5	10.1-12.4
Multiplication Factor	**480**	**240**	576	448*	446	653	300
Power [mW]	**6.6**		11.55	20.6	19.7	46	5.6**
RMS jitter [fs] (Integration Range [Hz])	**153.4 (1k-100M)**	**116.5 (1k-100M)**	199 (10k-30M)	251 (10k-10M)	213 (10k-26M)	258.4 (1k-40M)	197.8 (10k-40M)
Reference Spur [dBc]	**-62.3**	**-57.2**	-65	-60	-	<-59.1	-69
PLL FoM$_{JIT}$ [dB]	**-248.1**	**-250.5**	-243.3	-238.9	-240.5	-235.1	-246.6**
PLL FoM$_{JIT,M1}$ [dB]	**-274.9**	**-274.3**	-270.9	-265.4	-267.0	-263.3	-271.3**
PLL FoM$_{JIT,M2}$ [dB]	**-248.1**	**-247.5**	-241.1	-234.6	-238.1	-229.9	-245.4**
Area [mm²]	**0.24**		0.3	0.41	0.48	0.45	0.77

$FoM_{JIT} = 10\log_{10}\left(\frac{Jitter^2}{(1s)^2} \cdot \frac{Power}{1mW}\right)$ $FoM_{JIT,M1} = FoM_{JIT} - 10\log_{10}\left(\frac{f_{OUT}}{f_{REF}}\right)$ $FoM_{JIT,M2} = FoM_{JIT} + 10\log_{10}\left(\frac{f_{REF}}{30\,MHz}\right)$

* Use cascaded PLL.

** FLL power not included.
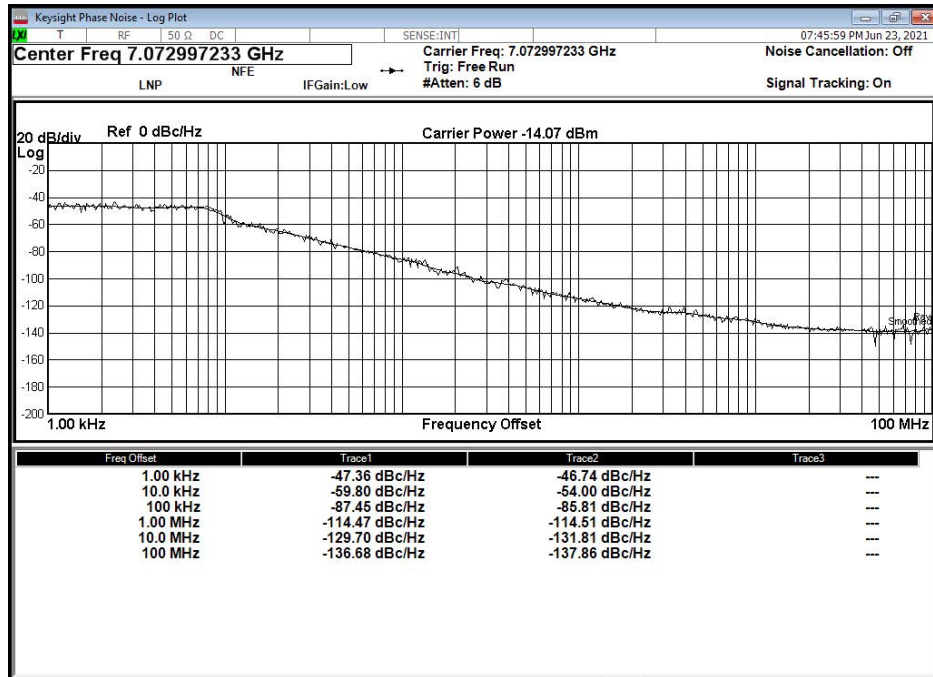
Figure 5.29: Measured VCO phase noise (after an on-chip divide-by-2).
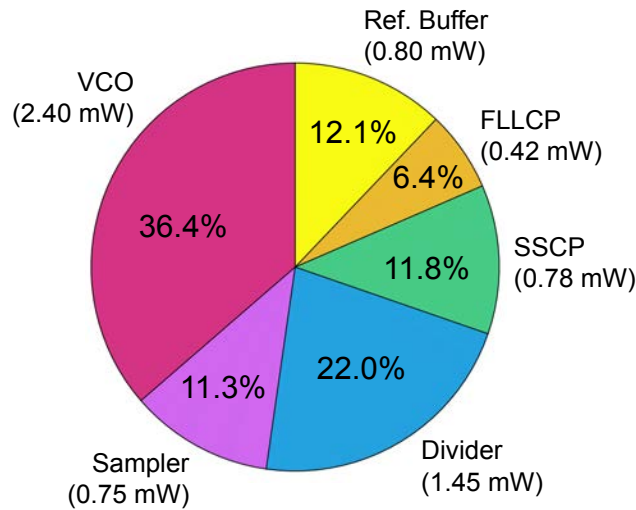
Figure 5.30: SSPLL power consumption breakdown.

$D = 5$ cm tissue phantom specified by Fig. 5.9. With 20 dBm input power, the measured phase noise and power spectrum are provided in Fig. 5.36. Even with up to 15 dB channel loss, the measured phase noise is still much worse than predicted in Fig. 5.11. This unpleasant surprise partially arises from the extra noise in the tissue phantom, but the majority is caused by the single-ended
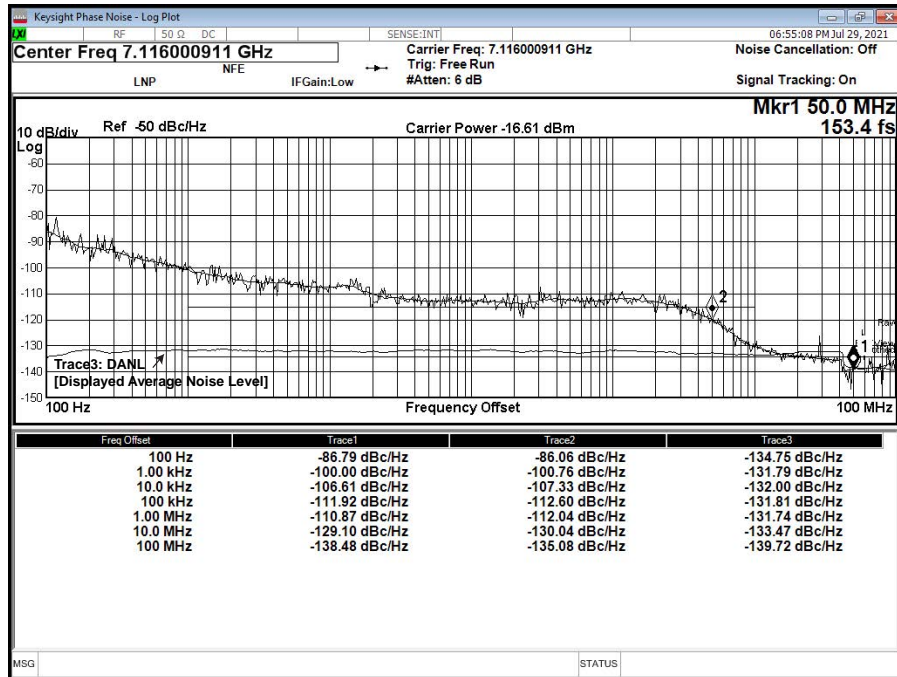
Figure 5.31: Measured SSPLL phase noise at the center frequency (after an on-chip divide-by-2). Integrated jitter from 1 kHz to 100 MHz is annotated at the top right. The spectrum analyzer noise level is plot as *Trace3*.

configuration of the reference input. As shown in Fig. 5.10, the $RX-$ electrode will inject to the chip ground some reference tone. Since $f_{REF} = 29.76$ MHz already exceeds the SRF of most of the SMD capacitors, the chip power supply, bias current and bias voltage do not follow exactly with the chip ground. On the other hand, the single-ended reference from $RX+$ needs a well defined voltage level to compare with as it propagates to the PLL. As a consequence, the 'zero-crossing' for the reference clock is ill-conditioned, which severely affect the phase noise performance. For the same reason, the reference spur degrades by 20 dB.

Even though the SSPLL sampler (see Fig. 5.22) only takes one clock phase, it is still a better configuration to apply a differential reference input to $RX+$ and $RX-$ electrodes, so that the chip ground is clean and that the 'zero-crossing' of the reference buffer is well defined since the reference only needs to compare with itself.

5.7 Biomolecular Experiments

Fig. 5.37 shows the setup for the *in vitro* experiment. The EPR spectrum of crystalline BDPA is re-measured in this *in-vitro* bio-experiment. The measurement procedure has been described in Chapter 4. In this experiment, the clock source power is set to 15 dBm and coupled to the chip galvanically through the aforementioned $D = 5$ cm tissue phantom. Battery sets are used as the
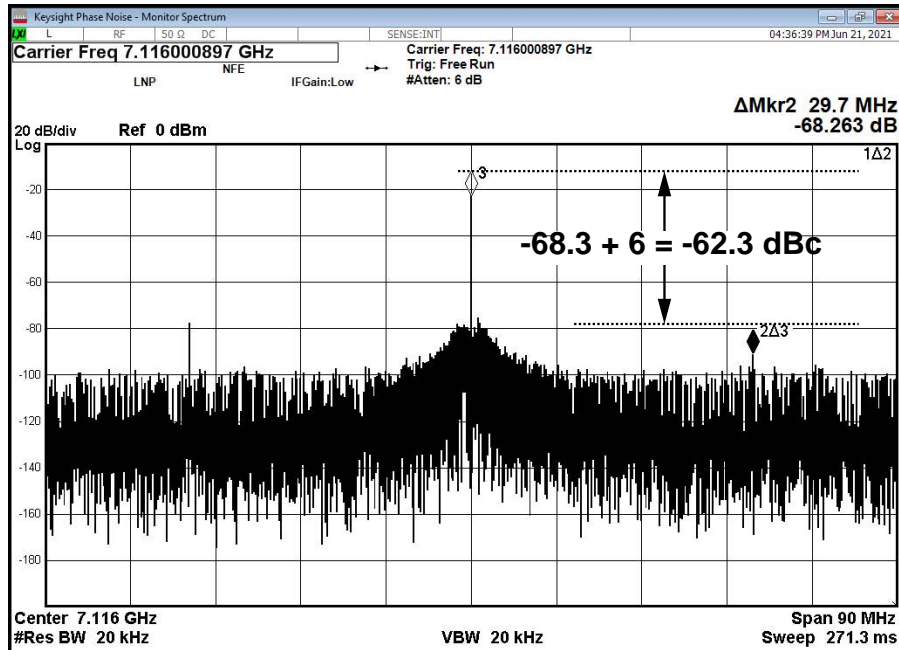
Figure 5.32: Measured SSPLL spur at the center frequency (after an on-chip divide-by-2).
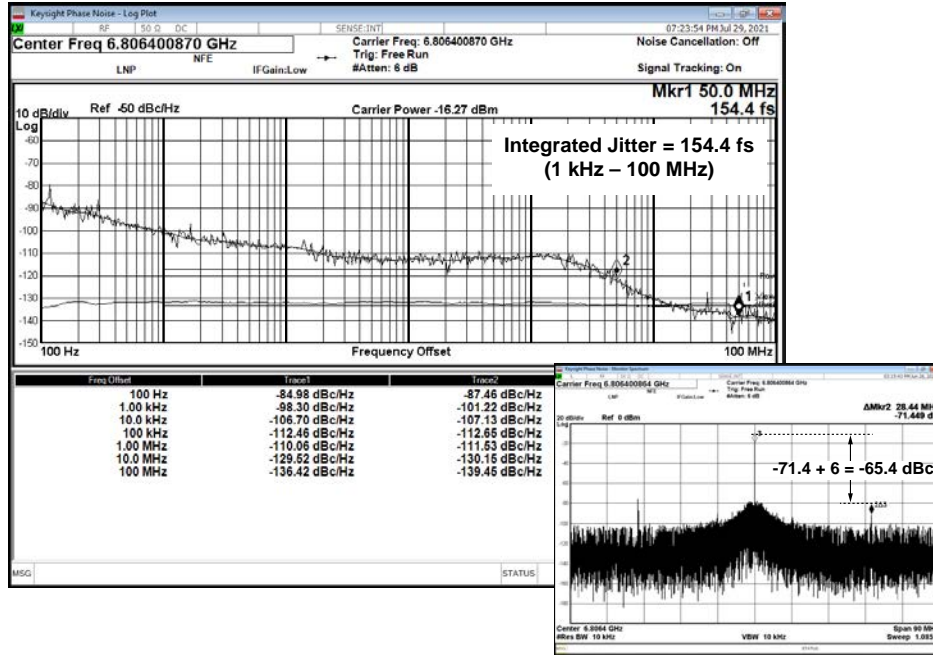
Figure 5.33: Measured SSPLL phase noise and spur at 13.6 GHz carrier.
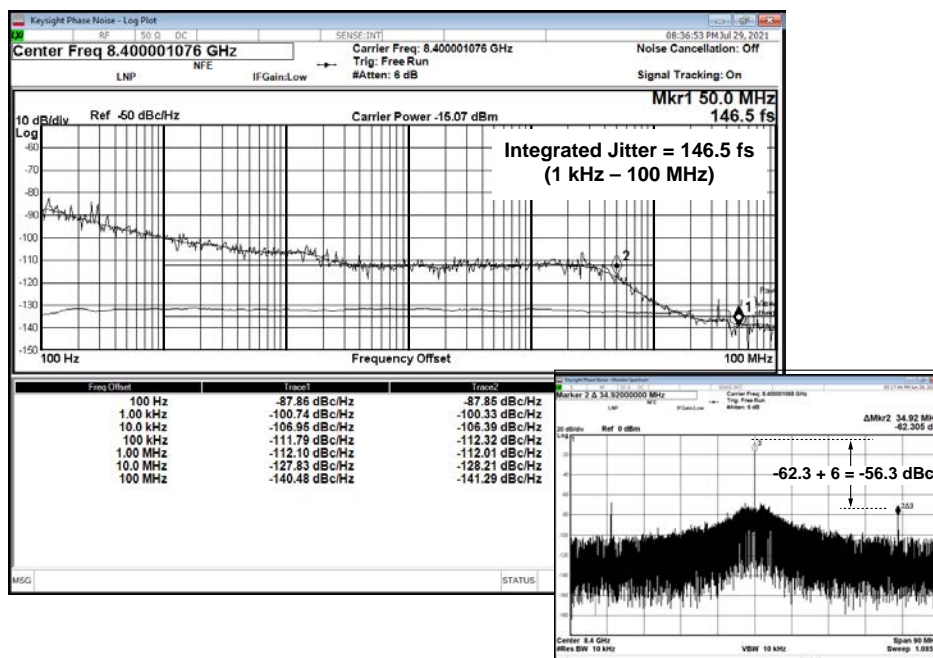
Figure 5.34: Measured SSPLL phase noise and spur at 16.8 GHz carrier.

power supply and the PCB/chip has no connection to the earth ground. The electric field level at the TX and RX electrodes comply with the FCC regulations without duty-cycling.

Unlike Chapter 4, this experiment modifies the dc field intensity of the PM-1055 magnet by applying a current bias through a coaxial Lemo at the side of the magnet mass. Two consecutive measurements were taken at distinct B_0 values, as shown in Fig. 5.38(a), where $B_L < B_H$. By taking the difference between the two measurements, the EPR spectrum is successfully detected, despite a considerable degradation of the source phase noise. More importantly, if $B_H - B_L$ is known, one can calculate the g-factor of the BPDA sample, which is considered as the fingerprint of any given molecule.

5.8 Chapter Summary

The 2019 Nobel Prize in Physiology or Medicine was awarded to hypoxia researchers, for their discoveries on how cells sense and adapt to O_2 variations. Considering the clinical potential that EPR spectroscopy can offer, it deserves much more recognition than what it is received now. However, the substantial signal loss due to tissue absorption hinders its further development.

To address this issue, this chapter aims at making a high frequency (> 10 GHz) EPR spectrometer implantable by exploring the possibility of (1) wirelessly coupling a subharmonic of the Larmor frequency through the human body and (2) exciting the paramagnetic resonance by a frequency multiplier. Specifically, galvanic coupling at 30−35 MHz was identified as a promising coupling
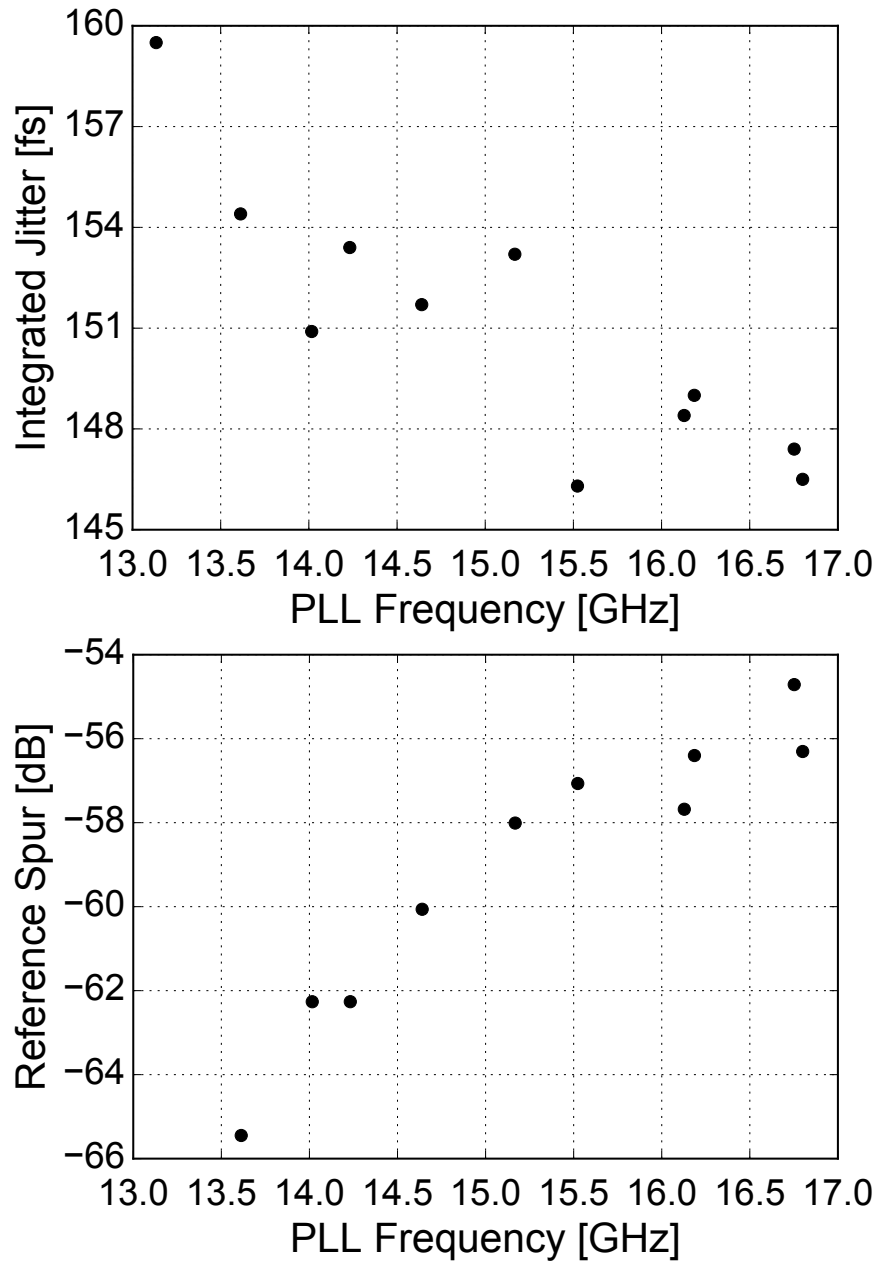
Figure 5.35: Measured SSPLL jitter (1 kHz − 100 MHz) and reference spur across the tuning range.

scheme and frequency range. EPR frequency synthesis demands a PLL with a very high multiplication factor, very low phase noise, very low power and very high robustness against disturbances. In response to such need, a SSPLL with proportionally divided charge pump was proposed which

Figure 5.36: Measured SSPLL phase noise and spur when it is galvanically coupled to the reference clock.
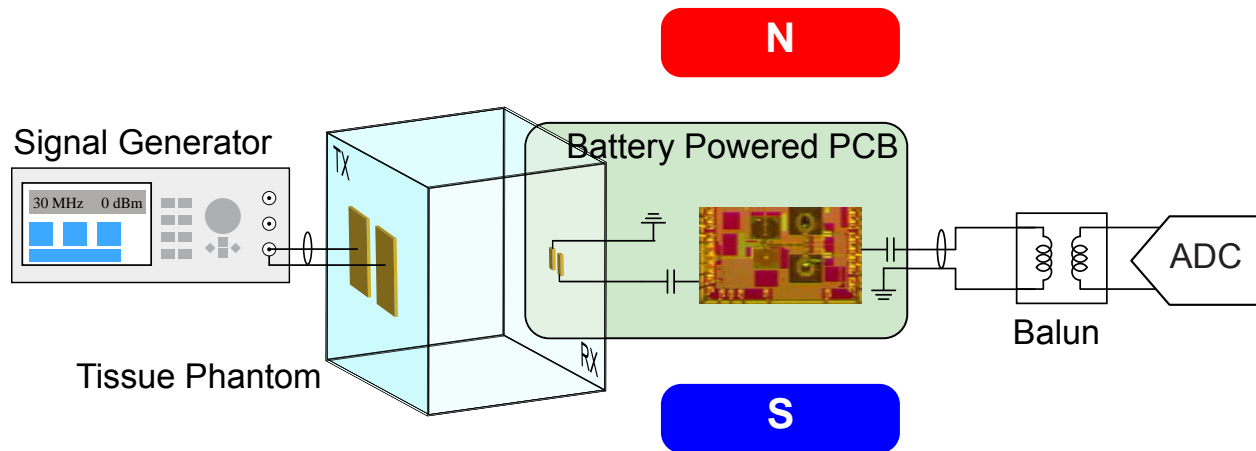
Figure 5.37: *In vitro* experiment setup.

achieves the best jitter, FoM_{JIT} and $FoM_{JIT,M}$ compared with state-of-the-art frequency synthesizers with $M > 300$. *In vitro* experiments were performed to validate the effectiveness of the proposed solution. The author hopes that this work helps the advancement of EPR spectrometry in clinical practices.
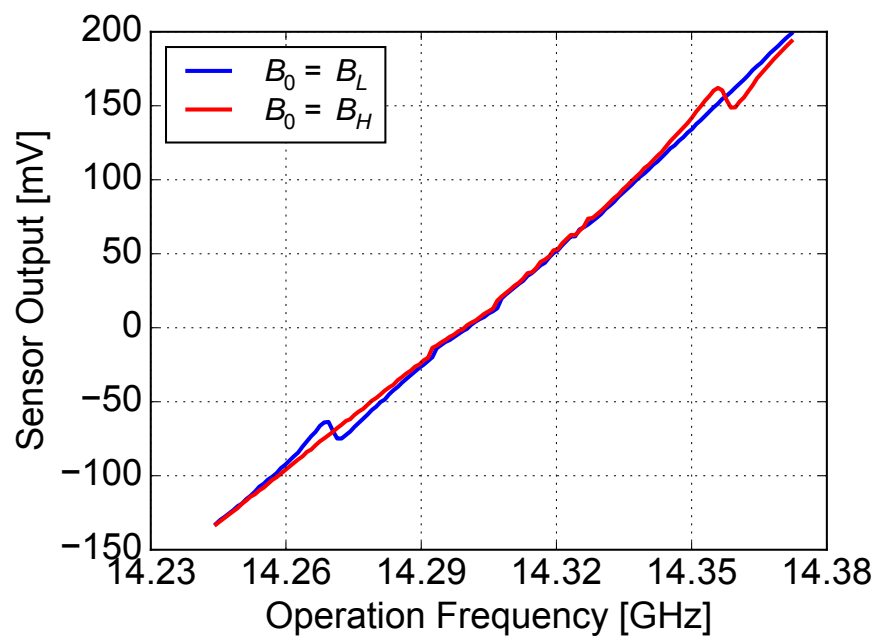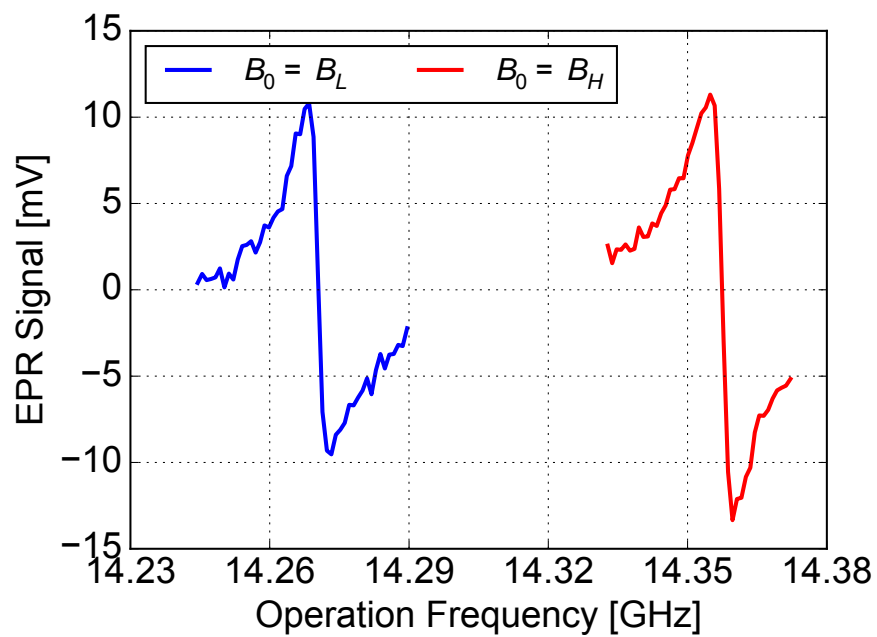
Figure 5.38: Measured EPR spectrum of a BDPA crystal at two distinct B_0 fields.

Chapter 6

Conclusion

6.1   Thesis Summary

This thesis focuses on the development of mmWave frequency impedance spectrometers for biomolecular sensing. Various techniques have been explored to achieve high sensitivity and high selectivity. These techniques include device-level innovations, such as the first-time demonstration of single photon avalanche diodes in 28 nm bulk CMOS, circuit-level innovations, such as the superharmonic coupled quadrature oscillator and the high multiplication-factor low-power low-noise subsampling PLL, and system-level innovations, such as combining multiple sensing modalities and exploiting resonance-based single sensing modality. As an interdisciplinary study, many interesting biomolecular experiments were involved.

In Chapter 2 and Chapter 3, a dual-modality dielectric-optical biosensor was implemented, which measures the permittivity change, bioluminescence intensity and fluorescence lifetime. The dielectric sensor employs a quadrature oscillator as the sensing frontend. Accompanied by a novel chopping technique, a sensitivity level as high as $0.2 \text{ ppm}/\sqrt{\text{Hz}}$ was achieved. The optical sensor, which utilizes an array of single photon avalanche diodes, improves the system selectivity by adding additional sensing modalities to create a high dimensional fingerprint for the biomolecules. As a first time implementation in the 28 nm bulk CMOS process, the SPAD exhibits better DCR, equivalent PDE and jitter performance without any process modifications compared with other SPADs in sub-100 nm CMOS nodes. A protein thermal denaturation experiment confirms the sensitivity and selectivity enhancement of the dual-modality biosensing platform.

In Chapter 4, the fundamental mechanism that enables high selectivity sensing is identified, based on which electron paramagnetic spectroscopy is explored as a powerful sensing technique with supreme selectivity. Bloch equations establish a connection between the quantum behaviors of unpaired electrons and the macroscopic magnetic properties of materials, which makes it possible to measure EPR spectrum using the impedance spectroscopic methods. A ultra-low-power inductance sensor was thereby designed for clinical EPR spectroscopy, which achieved the best energy efficiency and almost the highest spin sensitivity compared with the state-of-the-art integrated EPR spectrometers.

Built upon the study in Chapter 4, Chapter 5 delved into the exciting field of *in vivo* EPR spectroscopy. Strong absorption of microwave energies by the human body hinders the clinical adoption of *in vivo* EPR despite the enormous benefits. To date the EPR spectrometer operates at 1.2 GHz can only reach 1 cm depth in tissue. To address this issue, a 14 GHz implantable EPR spectrometer was demonstrated with more than 5 cm detection depth. The 14 GHz operation frequency is generated *in-situ* using a subsampling PLL, which is galvanically coupled to an external 30 MHz signal generator through the human body to minimize energy loss due to the tissue absorption. EPR frequency synthesis demands a PLL with a very high multiplication factor, very low phase noise, very low power and very high robustness against disturbances. In response to such need, a SSPLL with proportionally divid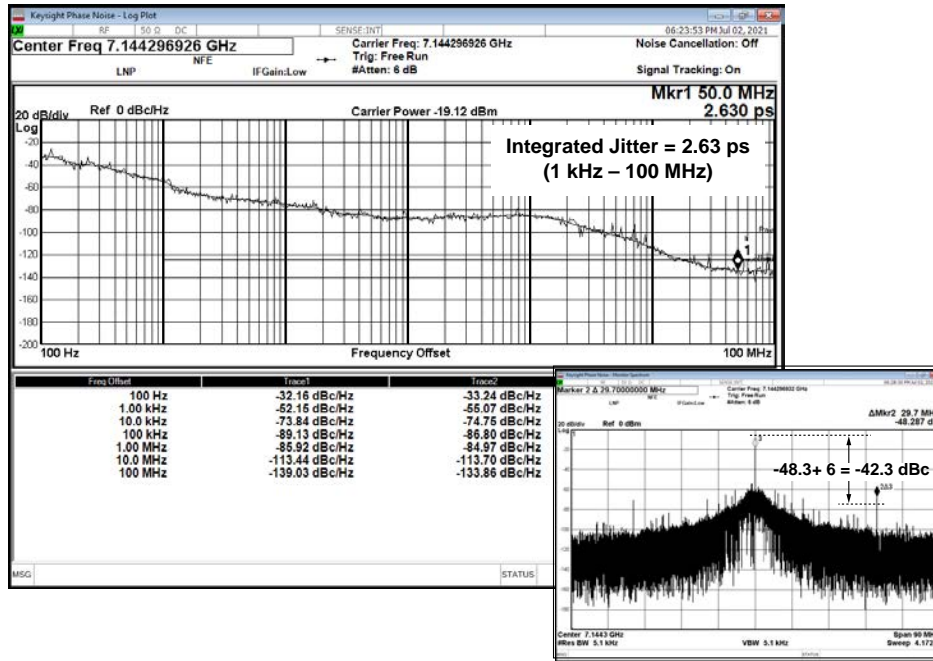ed charge pump was proposed which achieves the best jitter and FoM compared with state-of-the-art frequency synthesizers with $M > 300$. *In vitro* experiments were performed to validate the effectiveness of the proposed solution.

6.2   Future Directions

'Faster, higher, stronger'. The Olympic motto also fits here. Pushing the sensing frequency up towards the terahertz band will open up more possibilities. From the perspective of the dielectric spectroscopy, the terahertz frequency range contains rich spectral features which originates from the intermolecular vibrations of the biological macromolecules such as amino acids, proteins and nucleic acids. Detection of these vibrational modes is conventionally conducted via terahertz time-domain spectroscopy (THz-TDS) which relies on femtosecond laser sources. Now that the cutoff frequency of CMOS transistors is approaching half terahertz, it is definitely an important research thrust to replace the expensive bulky THz-TDS with a highly integrated solution for the exploration of biomolecular vibrational properties. In terms of paramagnetic resonance spectroscopy, it goes without saying that moving towards terahertz is always preferred since the fundamental detection limit scales proportionally with the operation frequency.

The combination of galvanic coupling and subsampling PLL enables the use of mmWave frequency sources inside the human body at almost arbitrary depth, based on which a vast variety of biosensors can be made implantable. Dielectric relaxation sensors and paramagnetic resonance sensors are only two examples given in this thesis. Building a network of high frequency implantable devices and (even) making them synchronized will definitely be an interesting research direction to pursue.

Bibliography

[1]   P. Bergveld, "Development of an ion-sensitive solid-state device for neurophysiological measurements," *IEEE Transactions on Biomedical Engineering*, vol. BME-17, no. 1, pp. 70–71, Jan. 1970.

[2]   Grand View Research, Inc., "Blood glucose monitoring devices market size, share & trends analysis report by product (self-monitoring, continuous), by end-use (hospitals, home care, diagnostic centers), by region, and segment forecasts, 2021 - 2028," Tech. Rep. 5263846, Dec. 2020.

[3]   S. Joo and R. B. Brown, "Chemical sensors with integrated electronics," *Chem. Rev.*, vol. 108, no. 2, pp. 638–651, Feb. 2008.

[4]   A. Manickam, A. Chevalier, M. McDermott, A. D. Ellington, and A. Hassibi, "A CMOS electrochemical impedance spectroscopy biosensor array for label-free biomolecular detection," in *2010 IEEE International Solid-State Circuits Conference - (ISSCC)*, Feb. 2010, pp. 130–131.

[5]   J. Dragas *et al.*, "In vitro multi-functional microelectrode array featuring 59 760 electrodes, 2048 electrophysiology channels, stimulation, impedance measurement, and neurotransmitter detection channels," *IEEE Journal of Solid-State Circuits*, vol. 52, no. 6, pp. 1576–1590, Jun. 2017.

[6]   F. Widdershoven *et al.*, "A CMOS pixelated nanocapacitor biosensor platform for high-frequency impedance spectroscopy and imaging," *IEEE Transactions on Biomedical Circuits and Systems*, vol. 12, no. 6, pp. 1369–1382, Dec. 2018.

[7]   V. Viswam *et al.*, "Impedance spectroscopy and electrophysiological imaging of cells with a high-density CMOS microelectrode array system," *IEEE Transactions on Biomedical Circuits and Systems*, vol. 12, no. 6, pp. 1356–1368, Dec. 2018.

[8]   A. Hassibi, N. Wood, and A. Manickam, "CMOS biochips: Challenges and opportunities," in *2018 IEEE Custom Integrated Circuits Conference (CICC)*, Apr. 2018, pp. 1–7.

[9]   A. Charkhesht, C. K. Regmi, K. R. Mitchell-Koch, S. Cheng, and N. Q. Vinh, "High-precision megahertz-to-terahertz dielectric spectroscopy of protein collective motions and hydration dynamics," *J. Phys. Chem. B*, vol. 122, no. 24, pp. 6341–6350, Jun. 2018.

[10] F. Artis *et al.*, "Microwaving biological cells: Intracellular analysis with microwave dielectric spectroscopy," *IEEE Microwave Magazine*, vol. 16, no. 4, pp. 87–96, May 2015.

[11] Wikipedia contributors, "Sensitivity and specificity," *Wikipedia*, Jul. 2021.

[12] F. Kremer and A. Schönhals, Eds., *Broadband Dielectric Spectroscopy*. Berlin, Heidelberg: Springer Berlin Heidelberg, 2003.

[13] P. Debye, *Polar Molecules*. Dover Publ., 1970.

[14] L. Onsager, "Electric moments of molecules in liquids," *J. Am. Chem. Soc.*, vol. 58, no. 8, pp. 1486–1493, Aug. 1936.

[15] J. L. Oncley, "Studies of the dielectric properties of protein solutions. I. carboxyhemoglobin1,2," *J. Am. Chem. Soc.*, vol. 60, no. 5, pp. 1115–1123, May 1938.

[16] G. Smith, A. P. Duffy, J. Shen, and C. J. Olliff, "Dielectric relaxation spectroscopy and some applications in the pharmaceutical sciences," *Journal of Pharmaceutical Sciences*, vol. 84, no. 9, pp. 1029–1044, Sep. 1995.

[17] K.-H. Lee *et al.*, "A CMOS impedance cytometer for 3D flowing single-cell real-time analysis with $\Delta\Sigma$ error correction," in *2012 IEEE International Solid-State Circuits Conference*, Feb. 2012, pp. 304–306.

[18] M. M. Bajestan, A. A. Helmy, H. Hedayati, and K. Entesari, "A 0.62–10 GHz complex dielectric spectroscopy system in CMOS," *IEEE Transactions on Microwave Theory and Techniques*, vol. 62, no. 12, pp. 3522–3537, Dec. 2014.

[19] D. Bianchi, G. Ferrari, A. Rottigni, and M. Sampietro, "CMOS impedance analyzer for nanosamples investigation operating up to 150 MHz with sub-aF resolution," *IEEE Journal of Solid-State Circuits*, vol. 49, no. 12, pp. 2748–2757, Dec. 2014.

[20] M. Bakhshiani, M. A. Suster, and P. Mohseni, "A broadband sensor interface IC for miniaturized dielectric spectroscopy from MHz to GHz," *IEEE Journal of Solid-State Circuits*, vol. 49, no. 8, pp. 1669–1681, Aug. 2014.

[21] J.-C. Chien, M. Anwar, E.-C. Yeh, L. P. Lee, and A. M. Niknejad, "A 6.5/11/17.5/30-GHz high throughput interferometer-based reactance sensors using injection-locked oscillators and ping-pong nested chopping," in *2014 Symposium on VLSI Circuits Digest of Technical Papers*, Jun. 2014, pp. 1–2.

[22] A. A. Helmy *et al.*, "A self-sustained CMOS microwave chemical sensor using a frequency synthesizer," *IEEE Journal of Solid-State Circuits*, vol. 47, no. 10, pp. 2467–2483, Oct. 2012.

[23] O. Elhadidy, M. Elkholy, A. A. Helmy, S. Palermo, and K. Entesari, "A CMOS fractional-N PLL-based microwave chemical sensor with 1.5% permittivity accuracy," *IEEE Transactions on Microwave Theory and Techniques*, vol. 61, no. 9, pp. 3402–3416, Sep. 2013.

[24] T. Mitsunaka *et al.*, "CMOS biosensor IC focusing on dielectric relaxations of biological water with 120 and 60 GHz oscillator arrays," *IEEE Journal of Solid-State Circuits*, vol. 51, no. 11, pp. 2534–2544, Nov. 2016.

[25] ——, "CMOS biosensor IC with 360-sensing elements using 63-GHz LC-oscillator and DEP for label-free single-cell detection," in *2018 Asia-Pacific Microwave Conference (APMC)*, Nov. 2018, pp. 243–245.

[26] L. Zhang and A. M. Niknejad, "Design and analysis of a microwave-optical dual modality biomolecular sensing platform," *IEEE Journal of Solid-State Circuits*, vol. 55, no. 3, pp. 639–649, Mar. 2020.

[27] F. Behbahani, Y. Kishigami, J. Leete, and A. Abidi, "CMOS mixers and polyphase filters for large image rejection," *IEEE Journal of Solid-State Circuits*, vol. 36, no. 6, pp. 873–887, Jun. 2001.

[28] A. Natarajan, A. Komijani, X. Guan, A. Babakhani, and A. Hajimiri, "A 77-GHz phased-array transceiver with on-chip antennas in silicon: transmitter and local LO-path phase shifting," *IEEE Journal of Solid-State Circuits*, vol. 41, no. 12, pp. 2807–2819, Dec. 2006.

[29] J. Savoj and B. Razavi, "A 10-Gb/s CMOS clock and data recovery circuit with a half-rate binary phase/frequency detector," *IEEE Journal of Solid-State Circuits*, vol. 38, no. 1, pp. 13–21, Jan. 2003.

[30] U. Decanis, A. Ghilioni, E. Monaco, A. Mazzanti, and F. Svelto, "A low-noise quadrature VCO based on magnetically coupled resonators and a wideband frequency divider at millimeter waves," *IEEE Journal of Solid-State Circuits*, vol. 46, no. 12, pp. 2943–2955, Dec. 2011.

[31] B. Razavi, "A millimeter-wave circuit technique," *IEEE Journal of Solid-State Circuits*, vol. 43, no. 9, pp. 2090–2098, Sep. 2008.

[32] A. Musa *et al.*, "A low phase noise quadrature injection locked frequency synthesizer for mm-wave applications," *IEEE Journal of Solid-State Circuits*, vol. 46, no. 11, pp. 2635–2649, Nov. 2011.

[33] F. Piri, M. Bassi, N. R. Lacaita, A. Mazzanti, and F. Svelto, "A PVT-tolerant >40-dB IRR, 44% fractional-bandwidth ultra-wideband mm-wave quadrature LO generator for 5G networks in 55-nm CMOS," *IEEE Journal of Solid-State Circuits*, vol. 53, no. 12, pp. 3576–3586, Dec. 2018.

[34] P. Andreani and X. Wang, "On the phase-noise and phase-error performances of multiphase LC CMOS VCOs," *IEEE Journal of Solid-State Circuits*, vol. 39, no. 11, pp. 1883–1893, Nov. 2004.

[35] A. Rofougaran, J. Rael, M. Rofougaran, and A. Abidi, "A 900 MHz CMOS LC-oscillator with quadrature outputs," in *1996 IEEE International Solid-State Circuits Conference. Digest of Technical Papers, ISSCC*, Feb. 1996, pp. 392–393.

[36] K. Scheir, S. Bronckers, J. Borremans, P. Wambacq, and Y. Rolain, "A 52 GHz phased-array receiver front-end in 90 nm digital CMOS," *IEEE Journal of Solid-State Circuits*, vol. 43, no. 12, pp. 2651–2659, Dec. 2008.

[37] C. Hsieh, H. Chen, H. Pan, and J. Y. Liu, "A 67 GHz dual injection quadrature VCO with -182.9 dBc/Hz FOM in 90-nm CMOS," in *2017 IEEE Asian Solid-State Circuits Conference (A-SSCC)*, Nov. 2017, pp. 101–104.

[38] H. Chang *et al.*, "Design and analysis of CMOS low-phase-noise low quadrature error V-band subharmonically injection-locked quadrature FLL," *IEEE Transactions on Microwave Theory and Techniques*, vol. 66, no. 6, pp. 2851–2866, Jun. 2018.

[39] P. Andreani, A. Bonfanti, L. Romano, and C. Samori, "Analysis and design of a 1.8-GHz CMOS LC quadrature VCO," *IEEE Journal of Solid-State Circuits*, vol. 37, no. 12, pp. 1737–1747, Dec. 2002.

[40] H. Chang *et al.*, "65-nm CMOS dual-gate device for Ka-band broadband low-noise amplifier and high-accuracy quadrature voltage-controlled oscillator," *IEEE Transactions on Microwave Theory and Techniques*, vol. 61, no. 6, pp. 2402–2413, Jun. 2013.

[41] X. Yi, C. C. Boon, H. Liu, J. F. Lin, and W. M. Lim, "A 57.9-to-68.3 GHz 24.6 mW frequency synthesizer with in-phase injection-coupled QVCO in 65 nm CMOS technology," *IEEE Journal of Solid-State Circuits*, vol. 49, no. 2, pp. 347–359, Feb. 2014.

[42] N. Kuo, J. Chien, and A. M. Niknejad, "Design and analysis on bidirectionally and passively coupled QVCO with nonlinear coupler," *IEEE Transactions on Microwave Theory and Techniques*, vol. 63, no. 4, pp. 1130–1141, Apr. 2015.

[43] A. W. L. Ng and H. C. Luong, "A 1-V 17-GHz 5-mW CMOS quadrature VCO based on transformer coupling," *IEEE Journal of Solid-State Circuits*, vol. 42, no. 9, pp. 1933–1941, Sep. 2007.

[44] L. Wu and H. C. Luong, "A 49-to-62 GHz quadrature VCO with bimodal enhanced-magnetic-tuning technique," *IEEE Transactions on Circuits and Systems I: Regular Papers*, vol. 61, no. 10, pp. 3025–3033, Oct. 2014.

[45] T. Xi *et al.*, "Low-phase-noise 54-GHz transformer-coupled quadrature VCO and 76-/90-GHz VCOs in 65-nm CMOS," *IEEE Transactions on Microwave Theory and Techniques*, vol. 64, no. 7, pp. 2091–2103, Jul. 2016.

[46] M. Vigilante and P. Reynaert, "Analysis and design of an E-band transformer-coupled low-noise quadrature VCO in 28-nm CMOS," *IEEE Transactions on Microwave Theory and Techniques*, vol. 64, no. 4, pp. 1122–1132, Apr. 2016.

[47] S. L. J. Gierkink, S. Levantino, R. C. Frye, C. Samori, and V. Boccuzzi, "A low-phase-noise 5-GHz CMOS quadrature VCO using superharmonic coupling," *IEEE Journal of Solid-State Circuits*, vol. 38, no. 7, pp. 1148–1154, Jul. 2003.

[48] V. Szortyka *et al.*, "A 42mW 230fs-jitter sub-sampling 60Ghz PLL in 40nm CMOS," in *2014 IEEE International Solid-State Circuits Conference Digest of Technical Papers (ISSCC)*, Feb. 2014, pp. 366–367.

[49] T. M. Hancock and G. M. Rebeiz, "A novel superharmonic coupling topology for quadrature oscillator design at 6 GHz," in *2004 IEE Radio Frequency Integrated Circuits (RFIC) Systems. Digest of Papers*, Jun. 2004, pp. 285–288.

[50] D. Guermandi, P. Tortori, E. Franchi, and A. Gnudi, "A 0.83-2.5-GHz continuously tunable quadrature VCO," *IEEE Journal of Solid-State Circuits*, vol. 40, no. 12, pp. 2620–2627, Dec. 2005.

[51] E. Hegazi, H. Sjoland, and A. Abidi, "A filtering technique to lower LC oscillator phase noise," *IEEE Journal of Solid-State Circuits*, vol. 36, no. 12, pp. 1921–1930, Dec. 2001.

[52] A. Hajimiri and T. Lee, "Design issues in CMOS differential LC oscillators," *IEEE Journal of Solid-State Circuits*, vol. 34, no. 5, pp. 717–724, May 1999.

[53] L. Zhang *et al.*, "A 37.5-45.1Ghz superharmonic-coupled QVCO with tunable phase accuracy in 28nm bulk CMOS," in *2018 IEEE Asian Solid-State Circuits Conference (A-SSCC)*, Nov. 2018, pp. 223–226.

[54] I. R. Chamas and S. Raman, "Analysis and design of a CMOS phase-tunable injection-coupled LC quadrature VCO(PTIC-QVCO)," *IEEE Journal of Solid-State Circuits*, vol. 44, no. 3, pp. 784–796, Mar. 2009.

[55] A. Hajimiri and T. H. Lee, "A general theory of phase noise in electrical oscillators," vol. 33, no. 2, p. 16, 1998.

[56] P. Andreani, X. Wang, L. Vandi, and A. Fard, "A study of phase noise in Colpitts and LC-tank CMOS oscillators," *IEEE Journal of Solid-State Circuits*, vol. 40, no. 5, pp. 1107–1118, May 2005.

[57] P. Andreani, "A time-variant analysis of the $1/f^2$ phase noise in CMOS parallel LC-tank quadrature oscillators," *IEEE Transactions on Circuits and Systems I: Regular Papers*, vol. 53, no. 8, pp. 1749–1760, Aug. 2006.

[58] M. Garampazzi, P. M. Mendes, N. Codega, D. Manstretta, and R. Castello, "Analysis and design of a 195.6 dBc/Hz peak FoM P-N class-B oscillator with transformer-based tail filtering," *IEEE Journal of Solid-State Circuits*, vol. 50, no. 7, pp. 1657–1668, Jul. 2015.

[59] F. Pepe *et al.*, "An efficient linear-time variant simulation technique of oscillator phase sensitivity function," in *2012 International Conference on Synthesis, Modeling, Analysis and Simulation Methods and Applications to Circuit Design (SMACD)*, Sep. 2012, pp. 17–20.

[60] M. Shahmohammadi, M. Babaie, and R. B. Staszewski, "A 1/f noise upconversion reduction technique for voltage-biased RF CMOS oscillators," *IEEE Journal of Solid-State Circuits*, vol. 51, no. 11, pp. 2610–2624, Nov. 2016.

[61] B. Wang, J. R. Hellums, and C. G. Sodini, "MOSFET thermal noise modeling for analog integrated circuits," *IEEE Journal of Solid-State Circuits*, vol. 29, no. 7, pp. 833–835, Jul. 1994.

[62] H. Wang, S. Kosai, C. Sideris, and A. Hajimiri, "An ultrasensitive CMOS magnetic biosensor array with correlated double counting noise suppression," in *2010 IEEE MTT-S International Microwave Symposium*, May 2010, pp. 616–619.

[63] A. Chu, B. Schlecker, K. Lips, M. Ortmanns, and J. Anders, "An 8-channel 13GHz ESR-on-a-Chip injection-locked VCO-array achieving 200μM-concentration sensitivity," in *2018 IEEE International Solid - State Circuits Conference - (ISSCC)*, Feb. 2018, pp. 354–356.

[64] M. Gal-Katziri and A. Hajimiri, "Analysis and design of coupled inductive bridges for magnetic sensing applications," *IEEE Journal of Solid-State Circuits*, pp. 1–12, 2019.

[65] H. Wang, C. Weng, and A. Hajimiri, "Phase noise and fundamental sensitivity of oscillator-based reactance sensors," *IEEE Transactions on Microwave Theory and Techniques*, vol. 61, no. 5, pp. 2215–2229, May 2013.

[66] R. Adler, "A study of locking phenomena in oscillators," *Proceedings of the IRE*, vol. 34, no. 6, pp. 351–357, Jun. 1946.

[67] R. A. York and R. C. Compton, "Quasi-optical power combining using mutually synchronized oscillator arrays," *IEEE Transactions on Microwave Theory and Techniques*, vol. 39, no. 6, pp. 1000–1009, Jun. 1991.

[68] R. A. York, "Nonlinear analysis of phase relationships in quasi-optical oscillator arrays," *IEEE Transactions on Microwave Theory and Techniques*, vol. 41, no. 10, pp. 1799–1809, Oct. 1993.

[69] B. Razavi, "A study of injection locking and pulling in oscillators," *IEEE Journal of Solid-State Circuits*, vol. 39, no. 9, pp. 1415–1424, Sep. 2004.

[70] Heng-Chia Chang, Xudong Cao, U. K. Mishra, and R. A. York, "Phase noise in coupled oscillators: theory and experiment," *IEEE Transactions on Microwave Theory and Techniques*, vol. 45, no. 5, pp. 604–615, May 1997.

[71] J. v. d. Tang, P. v. d. Ven, D. Kasperkovitz, and A. v. Roermund, "Analysis and design of an optimally coupled 5-GHz quadrature LC oscillator," *IEEE Journal of Solid-State Circuits*, vol. 37, no. 5, pp. 657–661, May 2002.

[72] A. Mirzaei, M. E. Heidari, R. Bagheri, S. Chehrazi, and A. A. Abidi, "The quadrature LC oscillator: a complete portrait based on injection locking," *IEEE Journal of Solid-State Circuits*, vol. 42, no. 9, pp. 1916–1932, Sep. 2007.

[73] A. Mirzaei and H. Darabi, "Mutual pulling between two oscillators," *IEEE Journal of Solid-State Circuits*, vol. 49, no. 2, pp. 360–372, Feb. 2014.

[74] J. Chien and A. M. Niknejad, "Oscillator-based reactance sensors with injection locking for high-throughput flow cytometry using microwave dielectric spectroscopy," *IEEE Journal of Solid-State Circuits*, vol. 51, no. 2, pp. 457–472, Feb. 2016.

[75] ——, "Design and analysis of chopper stabilized injection-locked oscillator sensors employing near-field modulation," *IEEE Journal of Solid-State Circuits*, vol. 51, no. 8, pp. 1851–1865, Aug. 2016.

[76] M. Elkholy and K. Entesari, "A wideband low-power LC-DCO-based complex dielectric spectroscopy system in 0.18- $\mu \textm$ CMOS," *IEEE Transactions on Microwave Theory and Techniques*, vol. 65, no. 11, pp. 4461–4474, Nov. 2017.

[77] C. Sideris, P. P. Khial, and A. Hajimiri, "Design and implementation of reference-free drift-cancelling CMOS magnetic sensors for biosensing applications," *IEEE Journal of Solid-State Circuits*, vol. 53, no. 11, pp. 3065–3075, Nov. 2018.

[78] J. M. Cyphert, C. S. Trempus, and S. Garantziotis, "Size matters: Molecular weight specificity of hyaluronan effects in cell biology," *Int J Cell Biol*, vol. 2015, p. 563818, 2015.

[79] Y. Han *et al.*, "Impact of refractive index increment on the determination of molecular weight of hyaluronic acid by muti-angle laser light-scattering technique," *Scientific Reports*, vol. 10, no. 1, p. 1858, Feb. 2020.

[80] J. Chen *et al.*, "Classification of cell types using a microfluidic device for mechanical and electrical measurement on single cells," *Lab Chip*, vol. 11, no. 18, pp. 3174–3181, Sep. 2011.

[81] A. Y. Zhu, F. Yi, J. C. Reed, H. Zhu, and E. Cubukcu, "Optoelectromechanical multimodal biosensor with graphene active region," *Nano Lett.*, vol. 14, no. 10, pp. 5641–5649, Oct. 2014.

[82] N. Apichitsopa, A. Jaffe, and J. Voldman, "Multiparameter cell-tracking intrinsic cytometry for single-cell characterization," *Lab Chip*, vol. 18, no. 10, pp. 1430–1439, May 2018.

[83] J. Seok Park *et al.*, "Multi-parametric cell profiling with a CMOS quad-modality cellular interfacing array for label-free fully automated drug screening," *Lab on a Chip*, vol. 18, no. 19, pp. 3037–3050, 2018.

[84] C. M. Lopez *et al.*, "A multimodal CMOS MEA for high-throughput intracellular action potential measurements and impedance spectroscopy in drug-screening applications," *IEEE Journal of Solid-State Circuits*, vol. 53, no. 11, pp. 3076–3086, Nov. 2018.

[85] M. A. Al-Rawhani *et al.*, "Multimodal integrated sensor platform for rapid biomarker detection," *IEEE Transactions on Biomedical Engineering*, Jun. 2019.

[86] B. Miccoli *et al.*, "High-density electrical recording and impedance imaging with a multi-modal CMOS multi-electrode array chip," *Front. Neurosci.*, vol. 13, 2019.

[87] D. Jung *et al.*, "A 21952-pixel multi-modal CMOS cellular sensor array with 1568-pixel parallel recording and 4-point impedance sensing," in *2019 Symposium on VLSI Circuits*, Jun. 2019, pp. C62–C63.

[88] H. Eltoukhy, K. Salama, and A. E. Gamal, "A 0.18-μm CMOS bioluminescence detection lab-on-chip," *IEEE Journal of Solid-State Circuits*, vol. 41, no. 3, pp. 651–662, Mar. 2006.

[89] A. Manickam *et al.*, "A fully integrated CMOS fluorescence biochip for DNA and RNA testing," *IEEE Journal of Solid-State Circuits*, vol. 52, no. 11, pp. 2857–2870, Nov. 2017.

[90] U. Kaatze, "Complex permittivity of water as a function of frequency and temperature," *J. Chem. Eng. Data*, vol. 34, no. 4, pp. 371–374, Oct. 1989.

[91] D. E. Schwartz, E. Charbon, and K. L. Shepard, "A single-photon avalanche diode array for fluorescence lifetime imaging microscopy," *IEEE Journal of Solid-State Circuits*, vol. 43, no. 11, pp. 2546–2557, Nov. 2008.

[92] A. Rochas *et al.*, "Single photon detector fabricated in a complementary metal-oxide-semiconductor high-voltage technology," *Review of Scientific Instruments*, vol. 74, no. 7, pp. 3263–3270, Jul. 2003.

[93] M. A. Karami, H. Yoon, and E. Charbon, "Single-photon avalanche diodes in sub-100nm standard CMOS technologies," 2011.

[94] E. Charbon, H. Yoon, and Y. Maruyama, "A Geiger mode APD fabricated in standard 65nm CMOS technology," in *2013 IEEE International Electron Devices Meeting*, Dec. 2013, pp. 27.5.1–27.5.4.

[95] S. Pellegrini *et al.*, "Industrialised SPAD in 40 nm technology," in *2017 IEEE International Electron Devices Meeting (IEDM)*, Dec. 2017, pp. 16.5.1–16.5.4.

[96] T. C. de Albuquerque *et al.*, "Integration of SPAD in 28nm FDSOI CMOS technology," in *2018 48th European Solid-State Device Research Conference (ESSDERC)*, Sep. 2018, pp. 82–85.

[97] Q. S. Hanley, V. Subramaniam, D. J. Arndt-Jovin, and T. M. Jovin, "Fluorescence lifetime imaging: multi-point calibration, minimum resolvable differences, and artifact suppression," *Cytometry*, vol. 43, no. 4, pp. 248–260, 2001.

[98] R. G. Geyer, "Dielectric characterization and reference materials," *NIST Technical Note 1338*, p. 128, Apr. 1990.

[99] A. Abragam, *The Principles of Nuclear Magnetism*. Clarendon Press, 1983.

[100] J. A. Weil and J. R. Bolton, *Electron Paramagnetic Resonance: Elementary Theory and Practical Applications*. John Wiley & Sons, Jan. 2007.

[101] X. Yang and A. Babakhani, "A single-chip electron paramagnetic resonance transceiver in 0.13-μm SiGe BiCMOS," *IEEE Transactions on Microwave Theory and Techniques*, vol. 63, no. 11, pp. 3727–3735, Nov. 2015.

[102] J. Handwerker *et al.*, "28.2 A 14GHz battery-operated point-of-care ESR spectrometer based on a 0.13μm CMOS ASIC," in *2016 IEEE International Solid-State Circuits Conference (ISSCC)*, Jan. 2016, pp. 476–477.

[103] J. Anders, A. Angerhofer, and G. Boero, "K-band single-chip electron spin resonance detector," *Journal of Magnetic Resonance*, vol. 217, pp. 19–26, Apr. 2012.

[104] T. Yalcin and G. Boero, "Single-chip detector for electron spin resonance spectroscopy," *Review of Scientific Instruments*, vol. 79, no. 9, p. 094105, Sep. 2008.

[105] A. V. Matheoud, "Electron spin resonance detectors from 400 MHz to 360 GHz," Ph.D. dissertation, EPFL, 2019.

[106] A. A. Bobko, T. D. Eubank, B. Driesschaert, and V. V. Khramtsov, "In vivo EPR assessment of pH, pO2, redox status, and concentrations of phosphate and glutathione in the tumor microenvironment," *J Vis Exp*, no. 133, p. 56624, Mar. 2018.

[107] V. V. Khramtsov, "In vivo molecular electron paramagnetic resonance-based spectroscopy and imaging of tumor microenvironment and redox using functional paramagnetic probes," *Antioxid Redox Signal*, vol. 28, no. 15, pp. 1365–1377, May 2018.

[108] E. B. Rankin and A. J. Giaccia, "Hypoxic control of metastasis," *Science*, vol. 352, no. 6282, pp. 175–180, Apr. 2016.

[109] M. Höckel *et al.*, "Tumor hypoxia in pelvic recurrences of cervical cancer," *International Journal of Cancer*, vol. 79, no. 4, pp. 365–369, 1998.

[110] J. L. Tatum, "Hypoxia: Importance in tumor biology, noninvasive measurement by imaging, and value of its measurement in the management of cancer therapy," *International Journal of Radiation Biology*, vol. 82, no. 10, pp. 699–757, Jan. 2006.

[111] L. H. Gray, A. D. Conger, M. Ebert, S. Hornsey, and O. C. Scott, "The concentration of oxygen dissolved in tissues at the time of irradiation as a factor in radiotherapy," *Br J Radiol*, vol. 26, no. 312, pp. 638–648, Dec. 1953.

[112] R. H. Thomlinson and L. H. Gray, "The histological structure of some human lung cancers and the possible implications for radiotherapy," *Br J Cancer*, vol. 9, no. 4, pp. 539–549, Dec. 1955.

[113] J. C. Walsh *et al.*, "The clinical importance of assessing tumor hypoxia: Relationship of tumor hypoxia to prognosis and therapeutic opportunities," *Antioxidants & Redox Signaling*, vol. 21, no. 10, pp. 1516–1554, Oct. 2014.

[114] L. C. Clark, R. Wolf, D. Granger, and Z. Taylor, "Continuous recording of blood oxygen tensions by polarography," *Journal of Applied Physiology*, vol. 6, no. 3, pp. 189–193, Sep. 1953.

[115] X. Sun, G. Niu, N. Chan, B. Shen, and X. Chen, "Tumor hypoxia imaging," *Mol Imaging Biol*, vol. 13, no. 3, pp. 399–410, Jun. 2011.

[116] D. S. Vikram, A. Bratasz, R. Ahmad, and P. Kuppusamy, "A comparative evaluation of EPR and OxyLite oximetry using a random sampling of pO2 in a murine tumor," *Radiat Res*, vol. 168, no. 3, pp. 308–315, Sep. 2007.

[117] B. Gallez, C. Baudelet, and B. F. Jordan, "Assessment of tumor oxygenation by electron paramagnetic resonance: Principles and applications," *NMR in Biomedicine*, vol. 17, no. 5, pp. 240–262, 2004.

[118] K. J. Liu *et al.*, "Lithium phthalocyanine: A probe for electron paramagnetic resonance oximetry in viable biological systems," *PNAS*, vol. 90, no. 12, pp. 5438–5442, Jun. 1993.

[119] H. M. Swartz *et al.*, "Clinical EPR: Unique opportunities and some challenges," *Acad Radiol*, vol. 21, no. 2, pp. 197–206, Feb. 2014.

[120] H. Hou *et al.*, "Monitoring oxygen levels in orthotopic human glioma xenograft following carbogen inhalation and chemotherapy by implantable resonator-based oximetry," *Int J Cancer*, vol. 136, no. 7, pp. 1688–1696, Apr. 2015.

[121] A. B. Flood, V. A. Wood, and H. M. Swartz, "Using india ink as a sensor for oximetry: Evidence of its safety as a medical device," *Adv Exp Med Biol*, vol. 977, pp. 297–312, 2017.

[122] H. Hou, N. Khan, S. Gohain, M. L. Kuppusamy, and P. Kuppusamy, "Pre-clinical evaluation of OxyChip for long-term EPR oximetry," *Biomed Microdevices*, vol. 20, no. 2, p. 29, Mar. 2018.

[123] P. E. Schaner *et al.*, "OxyChip implantation and subsequent electron paramagnetic resonance oximetry in human tumors is safe and feasible: First experience in 24 patients," *Front Oncol*, vol. 10, p. 572060, 2020.

[124] P. Kuppusamy, "Sense and sensibility of oxygen in pathophysiology using EPR oximetry," in *Measuring Oxidants and Oxidative Stress in Biological Systems*, L. J. Berliner and N. L. Parinandi, Eds. Cham (CH): Springer, 2020.

[125] J. Guo *et al.*, "The design of X-band EPR cavity with narrow detection aperture for in vivo fingernail dosimetry after accidental exposure to ionizing radiation," *Sci Rep*, vol. 11, no. 1, p. 2883, Feb. 2021.

[126] J. Charthad, M. J. Weber, T. C. Chang, and A. Arbabian, "A mm-sized implantable medical device (IMD) with ultrasonic power transfer and a hybrid bi-directional data link," *IEEE Journal of Solid-State Circuits*, vol. 50, no. 8, pp. 1741–1753, Aug. 2015.

[127] J. Charthad *et al.*, "A mm-sized wireless implantable device for electrical stimulation of peripheral nerves," *IEEE Transactions on Biomedical Circuits and Systems*, vol. 12, no. 2, pp. 257–270, Apr. 2018.

[128] T. C. Chang, M. J. Weber, J. Charthad, S. Baltsavias, and A. Arbabian, "End-to-end design of efficient ultrasonic power links for scaling towards submillimeter implantable receivers," *IEEE Transactions on Biomedical Circuits and Systems*, vol. 12, no. 5, pp. 1100–1111, Oct. 2018.

[129] A. Andryieuski, S. M. Kuznetsova, S. V. Zhukovsky, Y. S. Kivshar, and A. V. Lavrinenko, "Water: Promising opportunities for tunable all-dielectric electromagnetic metamaterials," *Sci Rep*, vol. 5, no. 1, p. 13535, Aug. 2015.

[130] B. C. Johnson *et al.*, "StimDust: A 6.5mm^3, wireless ultrasonic peripheral nerve stimulator with 82% peak chip efficiency," in *2018 IEEE Custom Integrated Circuits Conference (CICC)*, Apr. 2018, pp. 1–4.

[131] M. M. Ghanbari *et al.*, "A sub-mm^3 ultrasonic free-floating implant for multi-mote neural recording," *IEEE Journal of Solid-State Circuits*, vol. 54, no. 11, pp. 3017–3030, Nov. 2019.

[132] "R&S SMA100A signal generator specifications," Tech. Rep., 2013.

[133] "Guidelines for evaluating the environmental effects of radiofrequency radiation," Tech. Rep., Aug. 1996.

[134] "IEEE standard for safety levels with respect to human exposure to radio frequency electromagnetic fields, 3 kHz to 300 GHz," *IEEE Std C95.1-2005 (Revision of IEEE Std C95.1-1991)*, pp. 1–238, Apr. 2006.

[135] Center for Devices and Radiological Health, "Marketing clearance of diagnostic ultrasound systems and transducers," Tech. Rep., Thu, 06/27/2019 - 15:00.

[136] T. R. Nelson, J. B. Fowlkes, J. S. Abramowicz, and C. C. Church, "Ultrasound biosafety considerations for the practicing sonographer and sonologist," *Journal of Ultrasound in Medicine*, vol. 28, no. 2, pp. 139–150, 2009.

[137] S. Ozeri and D. Shmilovitz, "Ultrasonic transcutaneous energy transfer for powering implanted devices," *Ultrasonics*, vol. 50, no. 6, pp. 556–566, May 2010.

[138] T. C. Chang *et al.*, "Design of tunable ultrasonic receivers for efficient powering of implantable medical devices with reconfigurable power loads," *IEEE Transactions on Ultrasonics, Ferroelectrics, and Frequency Control*, vol. 63, no. 10, pp. 1554–1562, Oct. 2016.

[139] P. Röschmann, "Radiofrequency penetration and absorption in the human body: Limitations to high-field whole-body nuclear magnetic resonance imaging," *Medical Physics*, vol. 14, no. 6, pp. 922–931, 1987.

[140] "EMF-portal | radio frequency (10 MHz - 300 GHz)," https://www.emf-portal.org/en/cms/page/home/effects/radio-frequency.

[141] Q. Duan *et al.*, "Characterization of a dielectric phantom for high-field magnetic resonance imaging applications," *Medical Physics*, vol. 41, no. 10, p. 102303, 2014.

[142] C.-K. Chou, "Phantoms for electromagnetic heating studies," in *Physics and Technology of Hyperthermia*, ser. NATO ASI Series, S. B. Field and C. Franconi, Eds.   Dordrecht: Springer Netherlands, 1987, pp. 294–318.

[143] S. Gabriel, R. W. Lau, and C. Gabriel, "The dielectric properties of biological tissues: II. Measurements in the frequency range 10 Hz to 20 GHz," *Phys. Med. Biol.*, vol. 41, no. 11, pp. 2251–2269, Nov. 1996.

[144] H. Rategh, H. Samavati, and T. Lee, "A CMOS frequency synthesizer with an injection-locked frequency divider for a 5-GHz wireless LAN receiver," *IEEE Journal of Solid-State Circuits*, vol. 35, no. 5, pp. 780–787, May 2000.

[145] H. Liu *et al.*, "16.1 A 265μW fractional-N digital PLL with seamless automatic switching subsampling/sampling feedback path and duty-cycled frequency-locked loop in 65nm CMOS," in *2019 IEEE International Solid- State Circuits Conference - (ISSCC)*, Feb. 2019, pp. 256–258.

[146] Y. Lim *et al.*, "17.8 A 170MHz-lock-in-range and -253dB-FoMjitter 12-to-14.5GHz sub-sampling PLL with a 150μW frequency-disturbance-correcting loop using a low-power unevenly spaced edge generator," in *2020 IEEE International Solid- State Circuits Conference - (ISSCC)*, Feb. 2020, pp. 280–282.

[147] B. Razavi, *Design of CMOS Phase-Locked Loops: From Circuit Level to Architecture Level*. Cambridge University Press, Jan. 2020.

[148] X. Gao, E. A. M. Klumperink, G. Socci, M. Bohsali, and B. Nauta, "Spur reduction techniques for phase-locked loops exploiting a sub-sampling phase detector," *IEEE Journal of Solid-State Circuits*, vol. 45, no. 9, pp. 1809–1821, Sep. 2010.

[149] L. Zhang and A. M. Niknejad, "An ultrasensitive 14-GHz 1.12-mW EPR spectrometer in 28-nm CMOS," *IEEE Microwave and Wireless Components Letters*, vol. 31, no. 6, pp. 819–822, Jun. 2021.

[150] K. M. Megawer *et al.*, "A 5GHz 370fsrms 6.5mW clock multiplier using a crystal-oscillator frequency quadrupler in 65nm CMOS," in *2018 IEEE International Solid - State Circuits Conference - (ISSCC)*, Feb. 2018, pp. 392–394.

[151] J. Kim *et al.*, "16.2 A 76fsrms jitter and –40dBc integrated-phase-noise 28-to-31GHz frequency synthesizer based on digital sub-sampling PLL using optimally spaced voltage comparators and background loop-gain optimization," in *2019 IEEE International Solid-State Circuits Conference - (ISSCC)*, Feb. 2019, pp. 258–260.

[152] Z. Yang, Y. Chen, S. Yang, P.-I. Mak, and R. P. Martins, "16.8 A 25.4-to-29.5 GHz 10.2 mW isolated sub-sampling PLL achieving -252.9 dB jitter-power FoM and -63 dBc reference spur," in *2019 IEEE International Solid- State Circuits Conference - (ISSCC)*, Feb. 2019, pp. 270–272.

[153] J. Du, "A 24-31 GHz reference oversampling ADPLL achieving FoM$_{\text{jitter-N}}$ of -269.3 dB," in *2021 IEEE Symposium on VLSI Circuits*, Jun. 2021, pp. 1–2.

[154] D. Liao, Y. Zhang, F. F. Dai, Z. Chen, and Y. Wang, "An mm-Wave synthesizer with robust locking reference-sampling PLL and wide-range injection-locked VCO," *IEEE Journal of Solid-State Circuits*, vol. 55, no. 3, pp. 536–546, Mar. 2020.

[155] D. Cherniak *et al.*, "A 23GHz low-phase-noise digital bang-bang PLL for fast triangular and saw-tooth chirp modulation," in *2018 IEEE International Solid - State Circuits Conference - (ISSCC)*, Feb. 2018, pp. 248–250.

[156] A. Hussein, S. Vasadi, M. Soliman, and J. Paramesh, "19.3 A 50-to-66GHz 65nm CMOS all-digital fractional-N PLL with 220fsrms jitter," in *2017 IEEE International Solid-State Circuits Conference (ISSCC)*, Feb. 2017, pp. 326–327.

[157] N. Markulic *et al.*, "9.7 a self-calibrated 10Mb/s phase modulator with -37.4dB EVM based on a 10.1-to-12.4GHz, -246.6dB-FoM, fractional-N subsampling pll," in *2016 IEEE International Solid-State Circuits Conference (ISSCC)*, Jan. 2016, pp. 176–177.